DOPING DEPENDENCE OF SURFACE AND BULK PASSIVATION OF MULTICRYSTALLINE SILICON SOLAR CELLS

A Dissertation
Presented to
The Academic Faculty

By

Jed Brody

In Partial Fulfillment
of the Requirements for the Degree
Doctor of Philosophy in Electrical and Computer Engineering

Georgia Institute of Technology
November 2003

DOPING DEPENDENCE OF SURFACE AND BULK PASSIVATION OF MULTICRYSTALLINE SILICON SOLAR CELLS

Approved by:

Dr. Ajeet Rohatgi, Advisor

Dr. Alan Doolittle

Dr. Christiana Honsberg

Dr. Miroslav Begović

Dr. Philip First

Date Approved ____/____/____

ACKNOWLEDGEMENT

I would like to begin by acknowledging my advisor, Dr. Ajeet Rohatgi. His unflagging encouragement, support, and enthusiasm sustained me through long months of doubting that I would ever complete my degree. Next, Dr. Miroslav Begovic deserves special recognition for tirelessly guiding me through dozens of revisions of computational strategy. Dr. Alan Doolittle evaluated the research proposal with remarkable thoroughness and rigor. Dr. Christiana Honsberg made many useful and much appreciated suggestions. I also benefited immeasurably from Dr. Stuart Bowden's assistance with the photoconductance system. Dr. Dong Seop Kim, Ajay Upadhyaya, and Brian Rounsaville were a reliable and helpful presence in lab. Denise Taylor and Dean Sutter expertly maintained the office and laboratory facilities, respectively. Their priceless contributions to the success of our research are all too often unacknowledged.

Among the many, many students who contributed to my work in innumerable ways, several merit special recognition: Vijay Yelundur, who is an exemplary researcher and assisted me in lab more times than I can remember; Alan Ristow, who not only seems to know the answer to any question about anything but also has the inexhaustible patience to answer it; Aleksandar Pregelj, who generously shared with me his Matlab expertise; Mohamed Hilali, who brings a remarkable combination of determination and tranquility to the group; Ben Damiani, who offers his technical insights and boundless wit to all the newer students; and Michael Finnegan, who listened so attentively to my restless dream of transferring to UW-Madison that he carried out such a course of action instead of me. Best wishes for all of you at Georgia Tech and beyond.

TABLE OF CONTENTS

LIST OF TABLES

LIST OF FIGURES

SUMMARY

Solar-cell efficiency is a very strong function of bulk lifetime (τ_b) and surface recombination velocity (S). In low-cost multicrystalline silicon (mc-Si), τ_b and S can be a strong function of doping level. This research focuses on experimental and theoretical investigation of the doping dependence of τ_b and S in low-cost materials.

The base doping level of solar cells is an inexpensively adjusted parameter. To make an informed selection of doping level, we must know the doping dependence of τ_b and S. The doping dependence of τ_b and S in string ribbon and cast multicrystalline silicon (mc-Si) is investigated in this research using a combination of device modeling, the derivation of useful and pertinent equations, and experiments based on test structures and complete devices.

Detailed model calculations are performed in Chapter 3 to show that optimal bulk resistivity varies considerably as a function of back surface passivation quality, wafer thickness, emitter sheet resistance, and the degree of dopant-defect interaction. In all cases, the optimal resistivity for a device with an aluminum back-surface field is found to be greater than that for a device with rear oxide/nitride-stack passivation, and a device with no rear surface passivation at all has an even lower optimal resistivity (less than 0.5 Ω-cm in the absence of dopant-defect interaction).

Experimentally, investigators frequently make effective-lifetime (τ_{eff}) measurements that satisfy quasi-steady-state conditions. In fact, these are the conditions most frequently encountered when working with low-cost, solar-grade materials. Surprisingly, until now most researchers have used the simple equation $1/\tau_{eff} = 1/\tau_b +$

2S/W or other equations derived assuming transient, high-lifetime conditions, although an equation derived assuming steady-state conditions would presumably be more accurate and useful. The steady-state relationship among S, τ_b, and τ_{eff} has not appeared in the literature. Therefore, in Chapter 4 we derive the steady-state relationship among S, τ_b, and τ_{eff} for illumination of arbitrary spectral content.

A general equation, also derived in this research, is used to investigate the accuracy of the new steady-state equation, as well as the accuracy of the widely used simple equation and a frequently cited transient equation. It is shown in Chapter 4 that the simple equation is accurate whenever the average excess carrier concentration over the wafer equals the average excess carrier concentration at the two surfaces. This occurs at small S in transient conditions; however, in quasi-steady-state, the lower τ_b is, the higher S must be for the simple equation to be valid. We show that the steady-state equation is the only equation that matches the general equation over the entire range of τ_{eff} for slowly decaying illumination, but any equation may be used when $\tau_{eff} > 20$ µs. When $\tau_{eff} < 10$ µs and a popular flash lamp is the illumination source, the steady-state equation derived in this research must be used to avoid error that can exceed 100%.

Having established the correct relationship among measured τ_{eff} and the two parameters of interest, S and τ_b, techniques for separating the effects of S and τ_b on τ_{eff} are investigated. We confirm that the conventional method of iodine passivation can reduce S below 2 cm/s on float zone; however, in Chapter 5 we demonstrate for the first time that the same iodine solution can fail to passivate low-cost materials well enough to determine S for a dielectric. Additionally, a sensitivity analysis is performed to show that a two-spectrum method to obtain information about τ_b and S has serious limitations: only

a lower bound can be placed on τ_b for τ_b greater than about 10 μs, and only an upper bound can be placed on S for S less than about 1000 cm/s. Thus, both τ_b and S must be somewhat poor in order for their values to be extracted within about an order of magnitude. It is shown that although monocrystalline τ_b is too good to be extracted with precision using the two-spectrum method, it can be accurately determined by the conventional iodine passivation method.

In the original two-spectrum method, an uncertainty of ±10% is arbitrarily assumed for each τ_{eff} measurement. In this research, two improvements over the original method are introduced. First, instead of using arbitrary 10% uncertainty, repeated measurements are made for each wavelength, and statistical tolerance intervals based on the data are used to set upper and lower bounds to τ_{eff}. Second, a third wavelength is used to narrow the region in the S-τ_b plane consistent with all measurements. Applying this modified method to measured lifetimes, we find that upper S limits for float zone are often under 100 cm/s. However, for identically passivated cast mc-Si samples, the upper S limit often approaches 500 cm/s or higher. For identically passivated string ribbon, the upper S limit is extremely high. This suggests, but does not conclusively prove, that different materials may respond differently to identical passivation. For float zone and cast mc-Si, higher resistivity tends to have better upper limits to S. For string ribbon, no resistivity trend is apparent.

To study the impact of cell processing on τ_b, in Chapter 6 we investigate processing schemes combining oxide, nitride, or oxide/nitride dielectric coatings with full or partial aluminum coverage on the rear. It is found that for Eurosolare cast mc-Si, τ_b increases strongly with increasing resistivity. Processing tends to reduce this trend,

raising τ_b for the lowest resistivity and often lowering τ_b for higher resistivity. In most cases, nitride-coated wafers give the highest τ_b, while stack-coated wafers give the lowest. For the 2 Ω-cm material, full aluminum gives higher τ_b than partial aluminum. With full aluminum on the back, 2 Ω-cm cast mc-Si gives the highest final lifetime, followed by 0.5 Ω-cm and 0.3 Ω-cm materials, regardless of the front dielectrics. In string ribbon, all processing combinations improve τ_b, with improvement usually highest for full aluminum and sometimes exceeding 1000%.

In Chapter 7, device simulations are performed using S and τ_b obtained experimentally in this research. Complete solar cells are fabricated for comparison with the simulations. The open-circuit voltage (V_{oc}) is fairly well predicted by the simulations. The predictions for cast mc-Si are more closely matched than those for string ribbon. In particular, the highest V_{oc} is predicted for the highest resistivity (2.2-2.3 Ω-cm) studied in cast mc-Si, whereas the highest V_{oc} is predicted for the intermediate resistivity (1.4-1.7 Ω-cm) in string ribbon. Experimentally, the highest V_{oc} is measured on the highest resistivity for both materials.

Experimentally, it is found in Chapter 8 that the resistivity giving the best measured short-circuit current (J_{sc}) also gives the best measured efficiency. Specifically, for both nitride- and stack-passivated string ribbon wafers, the intermediate resistivity (1.4-1.7 Ω-cm) gives the best J_{sc} and efficiency. For the nitride-passivated cast mc-Si cells, the highest resistivity (2.2-2.3 Ω-cm) is the best, whereas the intermediate resistivity (0.44-0.45 Ω-cm) is the best for stack-passivated cast mc-Si cells. For cast mc-Si, J_{sc} tends to improve at higher resistivity, conforming with observations of τ_b and S. However, V_{oc} decreases at higher resistivity. This can be explained by recognizing

that V_{oc} decreases as resistivity increases whenever improvements in τ_b and S are insufficient to overcome increases in doping level.

CHAPTER 1

INTRODUCTION AND RESEARCH OBJECTIVES

1.1 Statement of the Problem

Photovoltaics (PV) is the direct conversion of sunlight into electricity using a semiconductor device called a solar cell. PV has the potential to solve energy and environmental problems simultaneously: sunlight or solar energy is essentially unlimited and can be converted into electrical energy without any direct, undesirable impact on the environment. Unfortunately, PV accounts for less than 0.1% of the current U.S. energy portfolio. This is primarily because the cost of solar electricity is about 2-4 times higher than the cost of conventional energy sources such as fossil and nuclear fuels [1, 2].

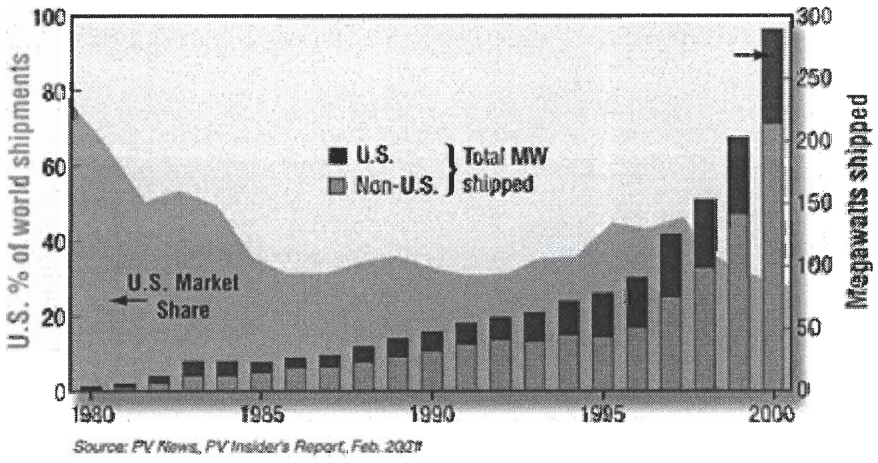

Figure 1. Annual shipments of PV modules (from [3]).

In spite of high costs, the PV industry has been growing at 15-20% a year, as illustrated in Figure 1 [3]. Industry leaders have set the ambitious goal of 25% annual growth in the future, shown in Figure 2. If this goal is achieved, then the domestic PV industry will provide 15% of new peak generating capacity by 2020; moreover, by 2030, PV may account of 10% of all the energy production in the U.S. [3]. The only way to achieve this goal is through significant cost reduction of PV energy.

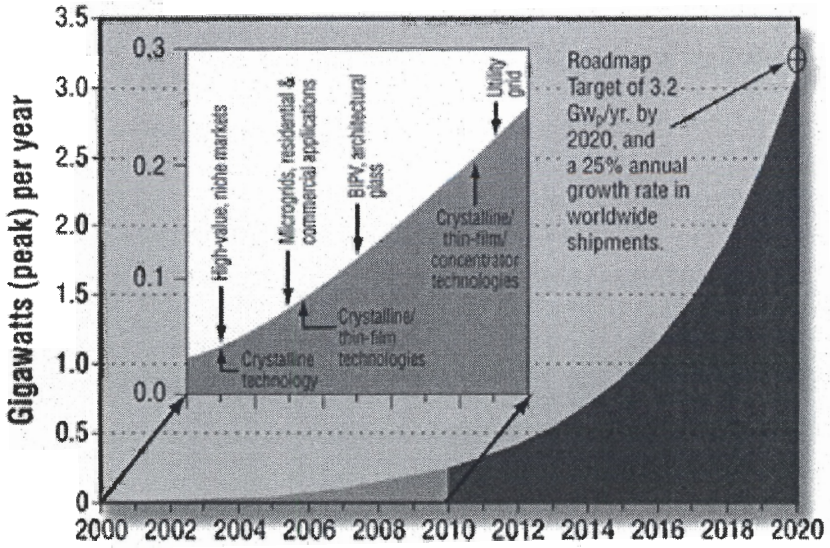

Figure 2. New peak generation capacity provided by the domestic PV industry, according the goals of the PV roadmap (from [3]).

The development of high efficiency cells on low-cost multicrystalline silicon (mc-Si) materials could have a significant impact on the cost reduction of PV, because about 45% of the cost of a PV module is related to the silicon substrate [1]. The substrate material for more than 85% of solar cells today is crystalline silicon: 35% is monocrystalline, and 53% is multicrystalline [4]. Though relatively inexpensive, mc-Si materials usually have defects and impurities, such as grain boundaries, dislocations,

metals, carbon, and oxygen. These imperfections lead to recombination centers that reduce bulk lifetime (τ_b) and efficiency. That is why mc-Si cell efficiencies are generally somewhat lower than those of monocrystalline cells. However, this gap can be reduced by carefully optimizing easily adjustable parameters such as thickness (W) and doping level (N_A). Device simulations show that optimization results are heavily dependent on the assumed doping dependence of τ_b and surface recombination velocity (S). Incomplete information about the doping dependence of these recombination parameters can dramatically affect simulation results.

To illustrate the impact of doping-dependent lifetime parameters on optimal resistivity, consider the empirical equation for a dopant-defect interaction [5]:

$$\tau_0 = \tau_{0\infty} / \left(1 + \frac{N_A}{N_{ref}} \right). \qquad (1)$$

τ_0 represents the electron and hole capture time constants (here assumed identical) in Shockley-Read-Hall (SRH) recombination. $\tau_{0\infty}$ gives the value of these constants in the absence of a dopant-defect interaction, and N_{ref} is an adjustable parameter determining the extent to which doping degrades lifetime. The lower N_{ref} is, the stronger the dopant-defect interaction. In high-quality monocrystalline materials like float zone, N_{ref} is expected to be infinity (no dopant-defect interaction). Equation (1) is used to accommodate the observation that some multicrystalline materials have lifetimes that decline dramatically at high doping levels. The impact of N_{ref} on τ_b is shown in Figure 3, where $N_{ref} = \infty$ for the monocrystalline cases, $N_{ref} = 3\times10^{14}$ cm^{-3} for the non-oxygenated edge-defined film-fed grown (EFG) multicrystalline material, and $N_{ref} = 2\times10^{15}$ cm^{-3} for the oxygenated EFG material [5]. Figure 4 shows the resulting cell efficiency curves

calculated using the simulation software PC-1D. The dopant-defect interaction degrades EFG lifetimes at low resistivities and causes EFG to have a significantly higher optimal resistivity than float zone [5].

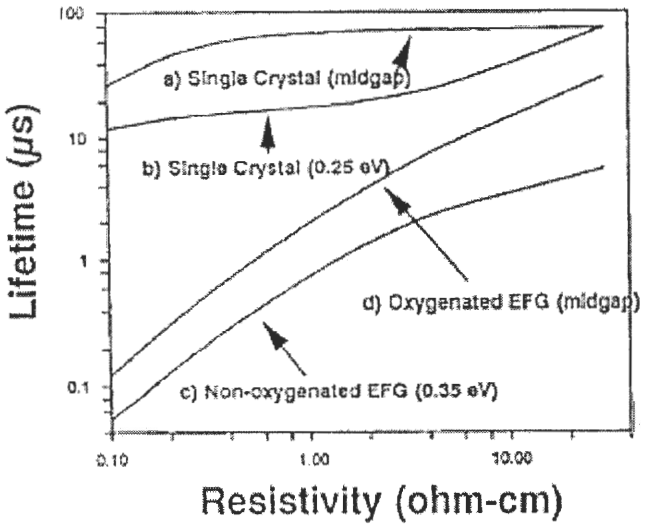

Figure 3. The calculated impact of N_{ref} on the resistivity dependence of τ_b. In cases (a) and (b), $N_{ref} = \infty$; in case (c), $N_{ref} = 3\times10^{14}$ cm^{-3}, and in case (d), $N_{ref} = 2\times10^{15}$ cm^{-3}. From [5].

Currently, the literature offers no clear model for the doping dependence of S_b and τ_b for multicrystalline materials. Limited data suggest that the doping dependence of S_b and τ_b for mc-Si may be different from that for monocrystalline silicon. If fully understood, this difference could be exploited to improve the performance of current mc-Si cells. Most cell manufacturers have no knowledge of the doping dependence of S and τ_b; for a given cell design, they try to empirically deduce the optimal resistivity, which is typically 1-3 Ω-cm. To predict the doping dependence of cell efficiency for an arbitrary cell design, the doping dependence of S and τ_b must be known.

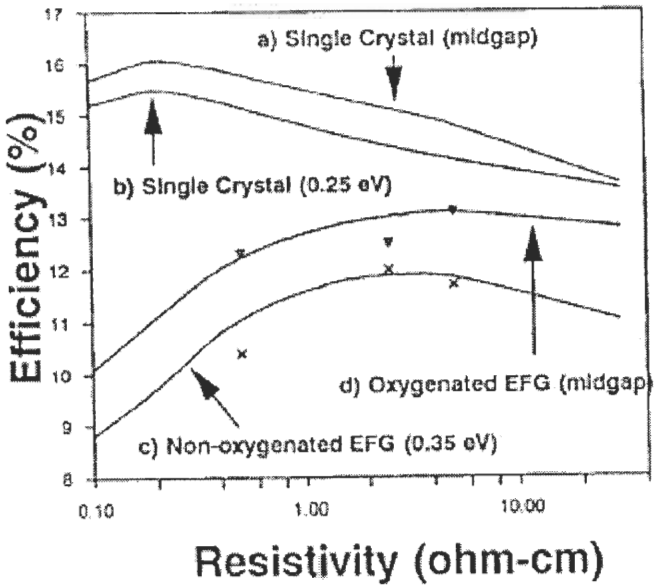

Figure 4. Simulation results using the lifetimes shown in Figure 3. From [5].

Therefore, the objective of the proposed research is to obtain experimentally the doping dependence of surface and bulk passivation in multicrystalline silicon and to apply the results to predict the resistivity dependence of cell efficiency for low-cost solar cells. Identifying the resistivity that tends to give the best efficiency may be an effective way to improve cell efficiency without increasing cost; the bulk resistivity of solar cells is an inexpensively adjusted parameter. To find the best resistivity accurately, the doping dependence of S and τ_b must be known with reasonable precision. While the doping dependence of S and τ_b of monocrystalline silicon is well documented in the literature [6], multicrystalline silicon remains to be thoroughly characterized. Since multicrystalline materials are non-uniform, S and τ_b must be measured at multiple positions for each resistivity to estimate the spread of possible values. Currently, resistivity optimization for multicrystalline silicon solar cells involves a number of

questionable assumptions about the doping dependence of S and τ_b. These assumptions may reduce the accuracy of the resistivity optimization, resulting in lower efficiency solar cells. The motivation of this research is to improve multicrystalline solar cell efficiency through improved understanding of the doping dependence of recombination parameters.

1.2 Specific Research Objectives

The research is in this dissertation is divided into six tasks, culminating in the experimental testing of the predicted resistivity dependence of the efficiency of multicrystalline silicon solar cells. The first task involves device simulations to demonstrate how the doping dependence of S and τ_b influences the doping dependence of cell efficiency. This provides the motivation for the rest of the work: the doping dependence of S and τ_b must be measured for use in realistic simulations of the doping dependence of cell efficiency. Since the doping dependence of S and τ_b is obtained experimentally using quasi-steady-state photoconductance measurements, the second task looks into the derivation and investigation of the solution to the continuity equation for time-dependent, non-uniform generation. The third task deals with the experimental extraction of S and which has five subtasks: a thorough and systematic experimental investigation of the effectiveness of the conventional iodine/methanol method for multicrystalline materials; the development of a novel empirical calibration of the lifetime characterization tool for arbitrary spectra of illumination; a sensitivity analysis of the two-spectrum method, whose limitations had not previously been elucidated; the development of a three-wavelength method in which we discard an arbitrary assumption from the original two-wavelength method; and the derivation of analytical

approximations to explain the doping dependence of S. The fourth task involves the measurement of the doping dependence of τ_b after various gettering and passivation treatments on string ribbon and cast mc-Si materials. In the fifth task, the doping dependence information obtained from Tasks 3 and 4 is used to predict the doping dependence of cell efficiency for the specified materials and cell designs. Finally, the sixth task includes the fabrication of complete silicon solar cells on these materials to test the predictions of Task 5.

1.2.1 Task 1: Device Simulations To Investigate the Impact of the Doping Dependence of S and τ_b on the Efficiency of Screen-Printed Solar Cells on Low-Cost Materials

Device simulations are performed to elucidate the importance and impact of base doping optimization for different back-surface passivation schemes, cell thicknesses, emitter profiles, and degrees of dopant-defect interaction. The simulations highlight the need to substitute measured values for arbitrary assumptions about the doping dependence of S and τ_b.

1.2.2 Task 2: Establishment of General and Steady-State Relationships among τ_{eff}, S, and τ_b for Flash-Lamp Illumination To Evaluate the Validity of Approximate Expressions

The relationship among τ_{eff}, τ_b, and S must be established in order to interpret the results of photoconductance measurements. Commonly, approximate equations derived assuming either impulse generation or uniform carrier concentration are used in the

literature. However, there are situations in which neither of these assumptions is appropriate, particularly when using the flash lamp favored in many laboratories. The intensity of the flash lamp decays nearly exponentially. Therefore, in this task the continuity equation is solved for exponentially decaying optical excitation of arbitrary spectral content. The solution is used to evaluate the accuracy of widely used approximate expressions, as well as the previously unpublished and very useful steady-state solution.

1.2.3 Task 3: Investigation of the Doping Dependence of S for Dielectric-Passivated String Ribbon and Cast mc-Si

Task 3.1 Comparison of Iodine/Methanol and Dielectric Surface Passivation of Monocrystalline and Multicrystalline Silicon

Widely used photoconductance measurements, either transient photoconductance decay (TPCD) or quasi-steady-state photoconductance (QSSPC), yield τ_{eff}, which depends on both S and τ_b. A well-known method to identify τ_b for monocrystalline silicon is the immersion of the wafer in an iodine/methanol solution that reduces S to negligible values. The iodine/methanol solution must passivate a wafer more effectively than the dielectric under investigation in order to extract S. It will be demonstrated in this task that this criterion may not be reliably satisfied for some multicrystalline materials; consequently, S cannot be determined by the QSSPC technique. This motivates subsequent investigation of alternative techniques for extracting S.

Task 3.2 Empirical Calibration of Lifetime Characterization Tool for Arbitrary Spectra

In a QSSPC lifetime measurement, τ_{eff} is inversely proportional to the average generation rate in the wafer. This generation rate is determined through its proportionality, K, with the current of the reference solar cell. K is a complicated function of illuminating spectrum, wafer thickness, wafer reflectance, and reference cell spectral response. The analytical determination of K assumes identical photon flux on both the reference cell and the test wafer. The assumption is surely false when light from the lamp is allowed to emerge only through a small-area optical bandpass filters. This section introduces a novel, empirical method for determining K that discards the unreasonable assumption of equal photon flux.

Task 3.3 Sensitivity Analysis of Quasi-Steady-State, Two-Spectrum Separation of Surface and Bulk Components of Electron-Hole Pair Recombination

An adaptation of the new quasi-steady-state, two-spectrum method will be used in this task to determine S. This new method has recently been proposed by Bail and Brendel [7] but has not yet been thoroughly researched. In particular, the sensitivity of the method will be elucidated as a function of S and τ_b of the test wafer. Analytical results will be illustrated by experiment.

Task 3.4 Development of a Three-Wavelength Method for the Extraction of S

The two-spectrum method has never before been used as a research tool. In fact, some of the assumptions of the original authors [7] appear problematic. For example, without any experimental justification, they assume 10% uncertainty in each τ_{eff}

measurement. The precision of the results depend critically on this assumption. This dubious assumption can be discarded in the three-wavelength method developed herein: instead of making a single τ_{eff} measurement and assuming 10% uncertainty, each τ_{eff} measurement will be repeated 15 times to experimentally obtain a range of possible values. As an additional improvement over the original two-wavelength method, a third wavelength will be used to provide additional information. This method is used to investigate the doping dependence of S for string ribbon and cast mc-Si passivated by each of three promising dielectrics: silicon dioxide, silicon nitride, and an oxide/nitride stack. This information will be subsequently used to predict the doping dependence of solar cell efficiency for these materials.

Task 3.5 Novel Analytical Approximations to Extended SRH Formalism To Understand Doping Dependence of S

Analytical approximations to the extended Shockley-Read-Hall (SRH) formalism are derived to better understand experimental results. The numerical procedure to determine S as a function of doping level is well known; however, the explicit influence of material parameters on the doping dependence of S may not be apparent. Thus, order-of-magnitude approximations are developed to estimate the influence of material parameters on S.

1.2.4 Task 4: Impact of Dielectric, Back Al Coverage, and Bulk Resistivity on Process-Induced Bulk-Lifetime Enhancement in Cast and Ribbon mc-Si

It is well-known that the bulk lifetime of multicrystalline silicon can be improved through various gettering and passivation steps. Some or all of these steps are incorporated in solar cell fabrication, depending on cell design. Since different cell process sequences may thus result in different final lifetimes, the optimal resistivity may correspondingly depend on cell design. To optimize resistivity for a given cell design, the doping dependence of τ_b following processing must first be established. The doping dependence of τ_b will be determined for cast and string ribbon silicon following phosphorous gettering, aluminum gettering, hydrogen passivation, and combinations of the three. The lifetime data will be used to predict the resistivity dependence of solar cells with various rear surface passivation schemes (Al BSF, SiO_2, SiN, or SiO_2/SiN).

1.2.5 Task 5: Simulation of the Doping Dependence of Cell Efficiency Based on Experimentally Determined Doping Dependence of S and τ_b

The doping dependence of S and τ_b obtained in Tasks 3 and 4 will be used in this task to predict the resistivity dependence of cast mc-Si and string ribbon solar cells. Device simulations are performed using the PC-1D software. Simulation results will be compared with the experimental results of Task 6.

1.2.6 Task 6: Fabrication and Characterization of Multicrystalline Silicon Solar Cells To Test Results of Device Simulations

To test the results of Task 5, complete solar cells are fabricated and characterized in this task. The doping dependence of efficiency, open-circuit voltage, and short-circuit current are compared with simulation.

CHAPTER 2

HISTORY AND MOTIVATION

2.1 Solar Cell Operating Principles

The power conversion efficiency η of a solar cell can be written as follows [8]:

$$\eta = \frac{V_{oc} J_{sc} FF}{P_{in} / A}, \tag{2}$$

where V_{oc} is the open-circuit voltage, J_{sc} is the short-circuit current, FF is the fill factor, P_{in} is the incident power (of the light illuminating the cell), and A is the cell area. The goal of PV device engineering is the maximization of V_{oc}, J_{sc}, and FF, within the economic constraints of fabrication and substrate costs. J_{sc} and V_{oc} will each be analyzed in order to understand the dependence of cell efficiency on surface and bulk passivation; recombination does not directly affect FF.

Since the equations for J_{sc} are complicated, it is helpful to look at the wavelength-dependent internal quantum efficiency (IQE), the fraction of absorbed photons generating carriers that contribute to J_{sc} [9]:

$$IQE(\lambda) = \frac{J_{sc}(\lambda)}{qN_{ph}(\lambda)[1 - R(\lambda)]}. \tag{3}$$

Here, λ is the wavelength, q is the electronic charge, N_{ph} is the photon flux, and R is the cell reflectance. Poor front surface passivation reduces short-wavelength IQE, since short-wavelength photons are mostly absorbed in the emitter and are drawn away from the collecting junction by a poorly passivated front surface. Similarly, a poorly passivated back surface tends to reduce long-wavelength IQE, especially for thin cells;

however, rear surface recombination has no effect on IQE if the cell's thickness is much greater than the minority carrier diffusion length in the base [10]. The effects of surface passivation on IQE are shown in Figure 5; a lower IQE corresponds with a lower J_{sc} and lower efficiency. J_{sc} at moderate and high wavelengths also depends strongly on base τ_b.

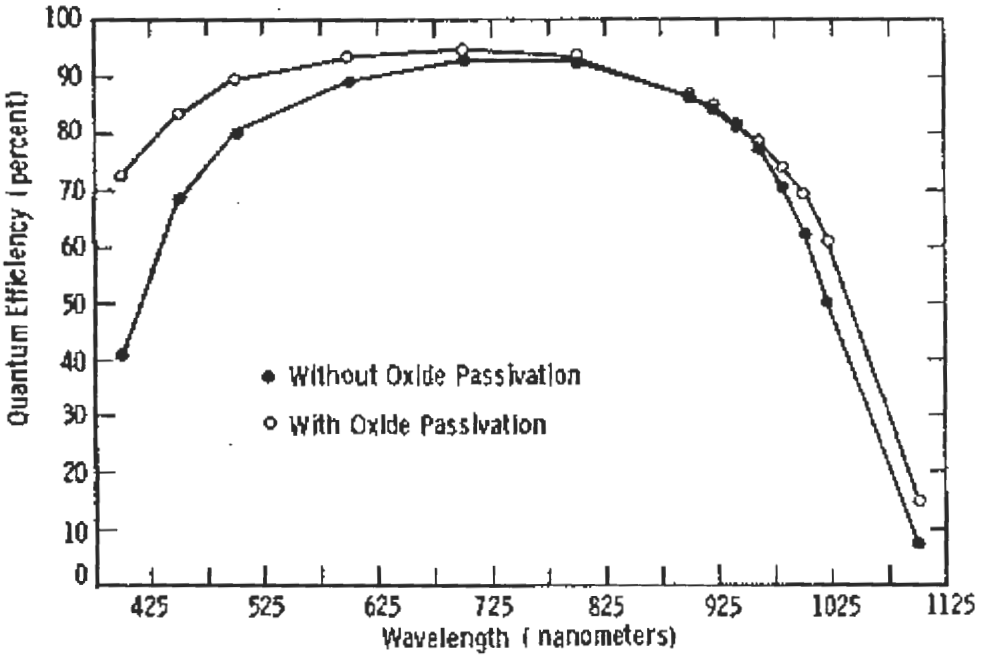

Figure 5. The impact of surface passivation on IQE (from [10]).

The other important cell parameter, V_{oc}, can be derived by setting the current J = 0 in the illuminated diode equation,

$$J = J_0(e^{qV/kT} - 1) - J_{sc}\,, \tag{4}$$

where k and T have their standard meanings, and J_0 is the dark saturation current [8]. Then

$$V_{oc} = \frac{kT}{q}\ln(\frac{J_{sc}}{J_0} + 1)\,. \tag{5}$$

J_0 is elaborated as follows:

$$J_0 = \frac{qD_n n_i^2}{L_n N_A} F_P + \frac{qD_p n_i^2}{L_p N_D} F_N , \tag{6}$$

where D_n and D_p are the diffusion coefficients for holes and electrons respectively, n_i is the intrinsic carrier concentration, and L_n and L_p are the minority carrier diffusion lengths. Assuming a p-type base with an n^+ emitter, N_A is the base doping level and N_D is the (assumed constant) emitter doping level. F_P and F_N are defined as follows [8]:

$$F_P = \frac{S_b \cosh(W_P / L_n) + (D_n / L_n)\sinh(W_P / L_n)}{(D_n / L_n)\cosh(W_P / L_n) + S_b \sinh(W_P / L_n)} \tag{7.a}$$

$$F_N = \frac{S_f \cosh(W_N / L_p) + (D_p / L_p)\sinh(W_N / L_p)}{(D_p / L_p)\cosh(W_N / L_p) + S_f \sinh(W_N / L_p)} . \tag{7.b}$$

W_P and W_N are the widths of the base and the emitter, respectively, and S_b and S_f are the surface recombination velocities in the base (back) and emitter (front), respectively. All of the surface dependence of J_0 is contained in the factors F_P and F_N.

Good solar cells have low values of F_P and F_N, which lead to low J_0, and therefore high V_{oc} and η. It is instructive to examine limiting cases of F_P and F_N in order to understand the influence of S_b and S_f on J_0. Consider Equation (7.a). If the cell is very thick or the lifetime is very low, and $W_P >> L_n$, then Equation (7.a) reduces to $F_P = 1$. In this case, S_b has no influence whatsoever on cell performance, because any carriers generated near the back surface are more than a diffusion length away from the junction.

Consider limiting values of S_b [8]. When S_b is very high, Equation (7.a) reduces to

$$F_P = \coth(W_P/L_n) . \tag{8}$$

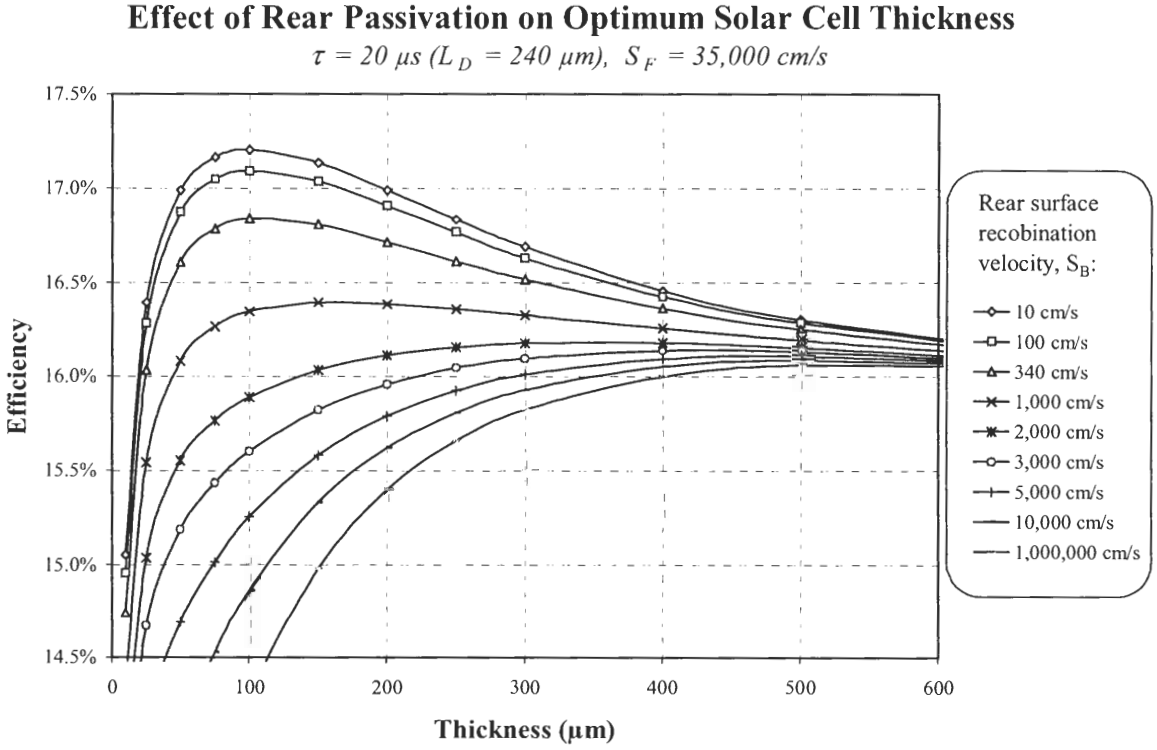

Figure 6. Influence of S_b on optimal thickness (from [2]).

In this case of poor S_b, the thinner the cell is, the worse F_P, J_0, and V_{oc} are. Conversely, if S_b is very low, then

$$F_P = \tanh(W_P/L_n) \, . \tag{9}$$

In this case of excellent surface passivation, the thinner the cell is, the better. Simulations show that efficiency improves with decreasing thickness all the way down to 25-50 μm, provided that both surfaces are textured for optical confinement and that $S_b < 100$ cm/s and $S_f < 1000$ cm/s [11]. Below 25-50 μm, too many photons pass right through the silicon without getting absorbed. Simulations performed for non-textured cells suggest an optimal thickness of 100 μm [2], as shown in Figure 6. Observe that thinning the cell

from 300 μm to 100 μm improves efficiency if $S_b < 2000$ cm/s and reduces efficiency otherwise. Clearly, the choice of thinner substrates in an industrial setting demands that surface passivation be carefully examined and, preferably, improved.

2.2 Recent Advances in Quasi-steady-state, Quasi-transient Measurements of Minority Carrier Lifetime

2.2.1 The Generalized Equation for Effective Lifetime

Over the course of this research, many measurements of S and τ_b are made. Neither of these parameters is directly accessible to measurement; instead, the measured effective lifetime (τ_{eff}) depends on both. Therefore, the relationship among τ_{eff}, S, and τ_b will be established in this research by solving the continuity equation for an optically excited semiconductor wafer.

Until recently, transient photoconductance decay (TPCD) and quasi-steady-state photoconductance (QSSPC) were considered two entirely separate techniques for the measurement of the effective lifetime of a semiconductor wafer [12-14]. Each technique uses a different equation for the determination of effective lifetime from measured photoconductance, a different duration of light pulse, a different range of effective lifetimes suitable for measurement, and a different equation for the extraction of surface recombination velocity from the effective lifetime (τ_{eff}) measured. Table 1, drawn from information in [12, 13], summarizes the differences between TPCD and QSSPC for the case of the popular flash-lamp tester. The flash-lamp tester is favored for its affordability and the ease with which it can be used to perform both TPCD and QSSPC measurements.

Table 1. Distinctions formerly drawn between TPCD and QSSPC for the popular lifetime tester with flashlamp illumination.

	TPCD	**QSSPC**
A. Determination of τ_{eff} [12]	$\tau_{eff} = -\dfrac{\Delta n(t)}{d\Delta n(t)/dt}$	$\tau_{eff} = \dfrac{\Delta n}{G}$
B. Typical light pulse time constant [13, 14]	18 μs	2.3 ms
C. Range of suitable τ_{eff} [13]	$\tau_{eff} > 50$ μs	$\tau_{eff} < 60$ μs

Recently, it was demonstrated that both TPCD and QSSPC are limiting cases of the measurement of τ_{eff}, with the generalized equation given as [12, 14]

$$\tau_{eff}(\Delta n_{av}) = \frac{\Delta n_{av}(t)}{G_{av}(t) - \dfrac{d\Delta n_{av}(t)}{dt}}, \tag{10}$$

where G_{av} is the average generation rate, and Δn denotes excess carrier concentration. Equation (10) is valid for all flash lamp time constants and all effective lifetimes, eliminating the restrictions indicated in rows B and C of Table 1.

At first glance, Equation (10) may appear to be an arbitrary definition chosen to reduce to $\Delta n_{av}/G_{av}$ for nearly steady-state illumination ($d\Delta n/dt = 0$) and to $-\Delta n_{av}/(d\Delta n_{av}/dt)$ for very brief illumination ($G_{av} = 0$). However, Equation (10) follows from the continuity equation. The derivation is sketched in [12] and provided in greater detail here. First we recognize that the recombination current J_{recom} (the total recombination rate per unit area, multiplied by q) is [12, 15]

$$J_{recom} = q\left[\int_{-W/2}^{W/2} \frac{\Delta n(x)}{\tau_b}\,dx + S_{front}\Delta n(-W/2) + S_{back}\Delta n(W/2)\right], \tag{11}$$

where q is the electronic charge, and W is the thickness of the wafer. The first term is the total bulk recombination, per unit area, over the thickness of the wafer. The other terms give the recombination currents at the two surfaces. To convert J_{recom} into an effective volume recombination rate, U_{eff}, divide by qW. Next τ_{eff} is defined via $U_{eff} = \Delta n_{av}/\tau_{eff}$, which yields

$$\frac{\Delta n_{av}}{\tau_{eff}} = \frac{1}{W}\left[\int_{-W/2}^{W/2} \frac{\Delta n(x)}{\tau_b} dx + S_{front}\Delta n(-W/2) + S_{back}\Delta n(W/2)\right]. \quad (12)$$

Equation (12) can be reduced to Equation (10) using the low-level-injection continuity equation [12]

$$\frac{\partial \Delta n(x,t)}{\partial t} = G(x,t) - \frac{\Delta n(x,t)}{\tau_b} + D\frac{\partial^2 \Delta n(x,t)}{\partial x^2} \quad (13)$$

and the boundary conditions

$$D\frac{\partial \Delta n(x,t)}{\partial x}\bigg|_{x=-W/2} = S_{front}\Delta n(-W/2,t) \quad (14)$$

and

$$-D\frac{\partial \Delta n(x,t)}{\partial x}\bigg|_{x=W/2} = S_{back}\Delta n(W/2,t). \quad (15)$$

Equation (13) is integrated from –W/2 to W/2 and divided by W:

$$\frac{1}{W}\int_{-W/2}^{W/2} \frac{\partial \Delta n(x,t)}{\partial t} dx = \frac{1}{W}\int_{-W/2}^{W/2} G(x,t)dx - \frac{1}{W}\int_{-W/2}^{W/2} \frac{\Delta n(x,t)}{\tau_b} dx + \frac{D}{W}\int_{-W/2}^{W/2} \frac{\partial^2 \Delta n(x,t)}{\partial x^2} dx. \quad (16)$$

The first two terms are easily simplified through the definitions of Δn_{av} and G_{av}:

$$\frac{\partial \Delta n_{av}}{\partial t} = G_{av} - \frac{1}{W}\int_{-W/2}^{W/2} \frac{\Delta n(x,t)}{\tau_b} dx + \frac{D}{W}\int_{-W/2}^{W/2} \frac{\partial^2 \Delta n(x,t)}{\partial x^2} dx. \quad (17)$$

The last term can be integrated to yield

$$\frac{\partial \Delta n_{av}}{\partial t} = G_{av} - \frac{1}{W}\int_{-W/2}^{W/2} \frac{\Delta n(x,t)}{\tau_b} dx + \frac{D}{W}\left(\left.\frac{\partial \Delta n(x,t)}{\partial x}\right|_{x=W/2} - \left.\frac{\partial \Delta n(x,t)}{\partial x}\right|_{x=-W/2} \right). \quad (18)$$

Using Equations (14) and (15), this becomes

$$\frac{\partial \Delta n_{av}}{\partial t} = G_{av} - \frac{1}{W}\int_{-W/2}^{W/2} \frac{\Delta n(x,t)}{\tau_b} dx + \frac{1}{W}\left(- S_{back}\Delta n(W/2) - S_{front}\Delta n(-W/2) \right). \quad (19)$$

Now Equation (12) is used to make this

$$\frac{\partial \Delta n_{av}}{\partial t} = G_{av} - \frac{\Delta n_{av}}{\tau_{eff}}. \quad (20)$$

Simple rearrangement produces Equation (10), derived from the continuity equation and the definition $U_{eff} = \Delta n_{av}/\tau_{eff}$.

Despite its great versatility, Equation (10) does not give the true bulk lifetime and surface recombination velocity. Therefore, the relationship among the experimentally interesting quantities τ_{eff}, S, and τ_b must be carefully derived and examined. The simplest expression for S [16],

$$\frac{1}{\tau_{eff}} = \frac{1}{\tau_b} + \frac{2S}{W}, \quad (21)$$

has been recognized as valid whenever the excess carrier concentration is approximately uniform. Under transient conditions (brief illumination of a wafer with moderate to high lifetime; see Table 1), the excess carrier profile rapidly becomes a single, concave-down, sinusoidal arch [17]. Low S is all that is necessary to make this profile approximately uniform; specifically, if $SW/D < 0.25$ [16], Equation (21) determines τ_{eff} within 4% of its true value, where W is the thickness of the wafer, and D is the diffusion coefficient. Thus for large S, Equation (21) is not expected to be valid. However, Luke and Cheng [17] developed an equation that is always true under transient conditions [9, 17]:

$$S = \sqrt{D\left(\frac{1}{\tau_{eff}} - \frac{1}{\tau_b}\right)} \tan\left[\frac{W}{2}\sqrt{\frac{1}{D}\left(\frac{1}{\tau_{eff}} - \frac{1}{\tau_b}\right)}\right], \qquad (22)$$

which reduces to Equation (21) when S is small. This equation is equally valid for uniform and non-uniform generation, because τ_{eff} under transient conditions is independent of the initial generation profile [14, 17].

It is important to note that Equation (22) is derived assuming transient conditions; the requirement that $\tau_{eff} > 50$ μs [13] (shown in Table 1 for flashlamp illumination with a time constant of 18 μs) can only be satisfied by high-quality, high lifetime silicon materials. However, the bulk lifetimes of many low-cost photovoltaic-grade materials are lower than 50 μs. Thus, while transient conditions cannot be satisfied for these low-cost materials, QSSPC conditions (slowly decaying illumination of a low-lifetime wafer; see Table 1) can be satisfied when the flash lamp is set to its longest time constant. Clearly, Equation (22), derived assuming transient conditions, is not valid in the QSSPC case. However, Equation (21) is known to be valid whenever carrier concentration is uniform, regardless of the time dependence of the illumination. Under QSSPC conditions, the excess carrier concentration is approximately uniform when two restrictions are satisfied: the diffusion length (L) is much greater than W, and the surfaces are well passivated [18]. The precise conditions under which Equation (21) can be used to extract τ_b and S from a QSSPC measurement are not well documented in the literature. This provided the motivation to derive a completely general equation for flashlamp illumination and elucidate the conditions under which Equations (21) and (22) are valid.

Equations (21) and (22) are widely cited in the literature. A third simple formula that relates the measured τ_{eff} to S and τ_b may be obtained by following the suggestion of [18], for the case of steady-state, uniform generation. The resulting expression is as follows:

$$S = \frac{W\left(\tau_b - \tau_{eff}\right)\sqrt{\frac{D}{\tau_b}}\sinh\zeta}{2\tau_b\sqrt{D\tau_b}\sinh\zeta + W\left(\tau_{eff} - \tau_b\right)\cosh\zeta} \tag{23}$$

where

$$\zeta \equiv \frac{W}{2\sqrt{D\tau_b}}. \tag{24}$$

Equation (23) may be used under QSSPC conditions, with the additional restriction that generation must be uniform. In practice, the use of an infra-red (IR) filter to achieve uniform generation [7, 18] may introduce a new problem. By blocking all wavelengths below about 1000 nm, the IR filter reduces generation and limits the range of achievable injection levels [7]. This is undesirable, because low-lifetime materials typically exhibit non-recombinative trapping behavior (induced by shallows traps) unless the injection level is much greater than the trap density [7, 19]. Trapping behavior has been observed and theoretically explained in both transient and steady-state conditions [19]. Non-recombinative trapping results in the measurement of erroneously high lifetime. While using an IR filter that blocks all wavelengths below about 1000 nm to illuminate a multicrystalline wafer with τ_b = 7.7 μs, Bail and Brendel just barely achieved a sufficiently high injection level [7]. Thus, the IR filter, while enabling uniform generation, may prevent the achievement of sufficiently high injection levels in solar-

grade silicon wafers. The general restrictions on Equations (21-23) are summarized in Table 2.

Table 2. Restrictions placed on the use of Equations (21-23) with flash lamp illumination, as stated or implied in the literature.

Measurement conditions	**Equation (21)**	**Equation (22)**	**Equation (23)**
TPCD conditions ($\approx$ 18 μs illumination, $\tau_{eff} > 50$ μs), any generation profile [16]	SW/D < 0.25	Always valid	Not valid
QSSPC conditions ($\tau_f \approx 2.3$ ms, $\tau_{eff} <$ 60 μs), non-uniform generation [18]	Low S, L >> W	Not valid	Not valid
QSSPC conditions ($\tau_f \approx 2.3$ ms, $\tau_{eff} <$ 60 μs), uniform generation [18]	Low S, L >> W	Not valid	Valid as long as IR filter transmits enough light to saturate traps

Consider a solar-grade silicon wafer with low bulk lifetime and/or poor surface passivation. Its short diffusion length and/or high surface recombination cause the excess carrier concentration to be non-uniform, prohibiting the conventional use of Equation (21). Since its effective lifetime is too low to satisfy standard transient conditions, Equation (22) is not expected to be valid. Finally, the use of an IR filter to produce uniform generation, necessary for the validity of Equation (23), may restrict injection levels to values insufficiently high to overcome trapping phenomena. Thus, Equations (21-23) are not expected to be useful or accurate for many promising low-cost, low-lifetime materials. For these materials, the relationship among S, τ_b, and the measured

τ_{eff} is unclear. Without being able to extract S and τ_b, it is difficult to optimize the cell design for highest efficiency.

The above problem provided the motivation to solve the continuity equation with time-dependent generation to derive equations that will be applicable without restriction to wafers of any effective lifetime illuminated by a flash lamp of any time constant and wavelength. The results will predict not only effective lifetime as a function of S and τ_b, but also the excess carrier concentration as a function of position and time. The general analysis will be used to evaluate the accuracy of the standard Equations (21-23), extending, for the first time, the use of Equation (21) beyond the restriction of approximately uniform excess carrier concentration.

2.2.2 Separation of Surface and Bulk Components of Effective Lifetime through the Use of Two Illumination Spectra

While τ_{eff} determined by a photoconductance measurement is influenced by both S and τ_b, it is important to be able to separate their effects in order to deduce their values. One method for the isolation of bulk recombination is the application of an extremely effective temporary surface passivation, such as corona discharge [20] or immersion in a passivating solution [21, 22], which causes S to approach 0. With surface recombination practically eliminated, a measurement of τ_{eff} yields τ_b. Before or after this measurement of τ_b, τ_{eff} is measured with the wafer having the surface passivation of interest. Knowledge of τ_b allows S for the surface passivation of interest to be calculated from the measured τ_{eff}; Equation (21) can be used for this purpose if S is sufficiently small. A disadvantage of this method is the extra experimental work required to apply the

temporary surface passivation. Additionally, while the iodine solution has been shown to provide extremely effective surface passivation for monocrystalline wafers [21, 22], multicrystalline materials may be less effectively passivated. Other techniques would then be required to separate S and τ_b in multicrystalline materials.

Two recent methods have been suggested for the separation of surface and bulk recombination by two different photoconductance measurements of the same wafer; no temporary surface passivation is required. Nagel *et al.* [14] showed that for S > 1000 cm/s and τ_b < 10 μs, S and τ_b can be extracted from two 400 nm illumination τ_{eff} measurements: one steady-state and one transient. However, a transient measurement (in which generation can be approximated as an impulse function) cannot be made when τ_{eff} is less than the smallest flash lamp time constant (18 μs), and τ_{eff} indeed falls below 18 μs when S > 1000 cm/s and τ_b < 10 μs. In fact, whether the lamp time constant is set to its smallest (18 μs) or largest (2.3 ms) value, the measurement of a wafer whose τ_{eff} < 10 μs will approximate a steady-state condition. Thus the method of extracting S and τ_b by making a steady-state and a transient measurement is limited to theoretical interest, unless a laser pulse with duration much less than 10 μs is used instead of the standard flash lamp for the transient measurement. An alternative method is investigated in this research.

The method described by Bail and Brendel [7] uses two quasi-steady-state photoconductance (QSSPC) measurements performed under different illumination spectra: blue and infrared (IR). Based on an exact calculation of the generation profiles and the excess carrier distributions throughout the wafer, they determined which values of S and τ_b yield the measured photoconductances under blue and IR illumination. While

their method is meticulously precise, it requires knowledge of the spectral dependence of the following: the photon flux, the external quantum efficiency (EQE) of the reference cell used to measure the photon flux, and the front and rear reflectance of the test wafer.

Bail and Brendel's method differs in two ways from earlier two-wavelength methods [23, 24], coined "multi-color methods" (MCM) in [24]. Bail and Brendel appear to be the first to use MCM with a filtered flashlamp instead of a laser. This is significant because the flash lamp tester has become a popular method of measuring lifetime, as a result of the flash lamp's ability to produce either rapidly or slowly decaying light pulses [13]. The second new feature of Bail and Brendel's method is that it is both contactless (unlike [24]) and effectively steady-state (unlike [23]). The steady-state, open-circuit solution to the continuity equation suitable for Bail and Brendel's method is different from the formulas derived for earlier techniques [23, 24].

The novelty of Bail and Brendel's method and its largely unexplored promise and unspecified limitations provide the motivation to assess the sensitivity of this method for various combinations of S and τ_b. In this research, two improvements will be made to the method. First, the unjustified assumption of 10% uncertainty will be replaced with statistical tolerance intervals based on repeated measurements. Also, a third wavelength will be used to provided additional information. Moreover, the failure of the conventional iodine passivation solution for some multicrystalline materials will be demonstrated, justifying interest in the refinement of Bail and Brendel's method.

2.3 Doping Dependence of Surface Recombination Velocity for Multicrystalline Silicon

2.3.1 Experimental Determination of S for Multicrystalline Silicon

S has been experimentally determined on monocrystalline materials for a number of resistivities and dielectric surface passivation schemes, as shown in Figures 7 [25] and 8 [6]. However, far less data is available in the literature for multicrystalline materials. In fact, the doping dependence of S for multicrystalline materials is not established; however, multicrystalline cells are being fabricated under the assumption that they follow the same patterns as monocrystalline cells. The available data commonly consist of record-low S values reported for a single resistivity, typically about 1 Ω-cm. For example, the following results are reported for multicrystalline silicon: the aluminum back surface field can produce S of about 1000 cm/s on 1 Ω-cm material [26], a boron surface field yields S = 830 cm/s on 1 Ω-cm material [26], a thermal oxide produces S from 70-120 cm/s on 1.5 Ω-cm material [27], a thermal oxide followed by an "alneal" (an anneal of the oxidized wafer coated by pure aluminum) gives S as low as 40 cm/s on 1.5 Ω-cm material [27], and silicon nitride reduces S to 30 cm/s on 1 Ω-cm material [26]. Table 3 compares these values with the lowest monocrystalline S values found in the literature [28-30]. However, significantly higher values are also reported; for example, up to 800 cm/s due to thermal oxide with partial metal coverage [31]. Moreover, S values seem to be reported mostly for cast mc-Si, not ribbon materials. One exception reports the high value of 950 cm/s for nitride-coated ribbon material of 1.5 Ω-cm resistivity [32].

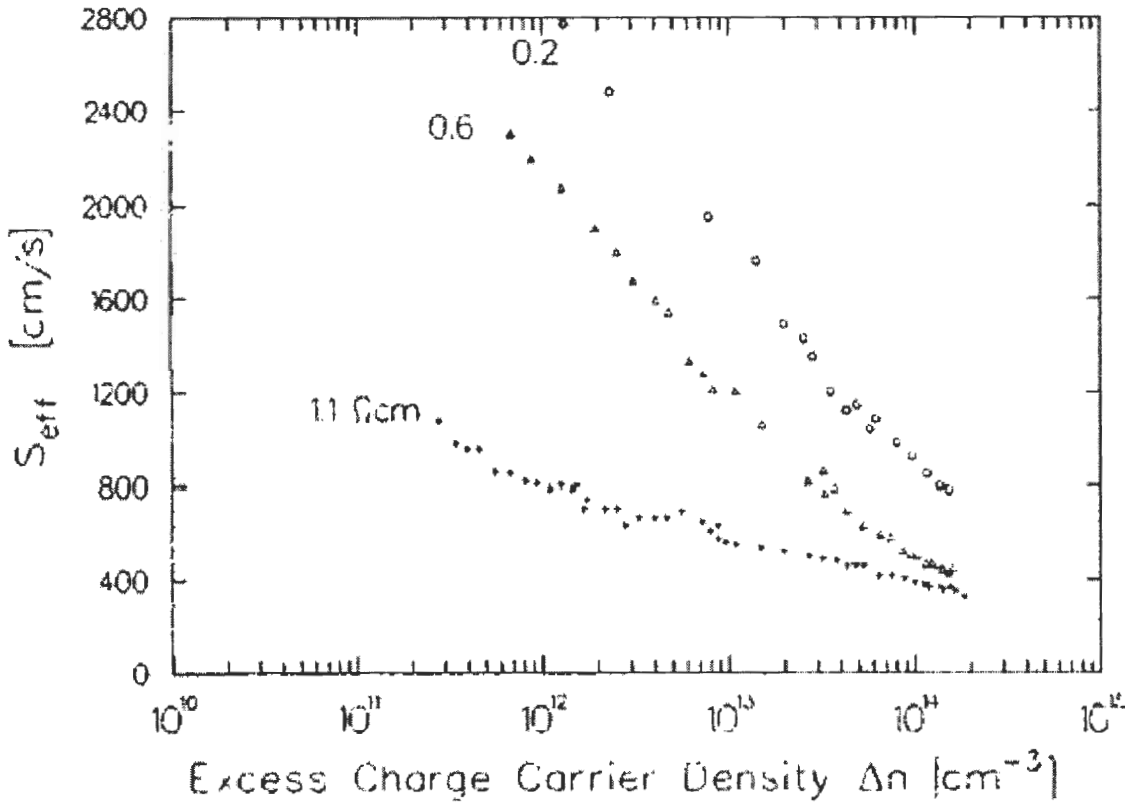

Figure 7. Example from the literature [25] of experimental resistivity dependence of S for oxide passivation on float zone.

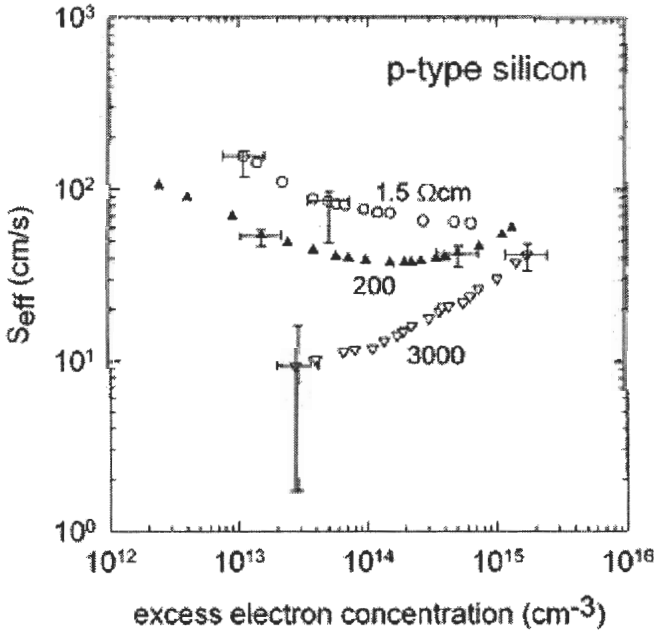

Figure 8. Example from the literature [6] of resistivity dependence of S for nitride passivation on float zone.

Table 3. Comparison of record-low S (cm/s) on monocrystalline and multicrystalline silicon. All wafers are p-type of 1-2.3 Ω-cm resistivity. The reference is given in brackets.

Passivation technique	**Monocrystalline Si**		**Multicrystalline Si**	
Al BSF	200	[28]	~1000	[26]
Thermal oxide	22	[29]	70-120	[27]
Silicon nitride	4	[30]	30	[26]

The literature appears to offer little experimental information about the dependence of S on doping level for multicrystalline silicon. This provided the motivation to experimentally investigate S as a function of doping level. The consequences will be an improved understanding of the limitations on the surface passivation of solar-grade materials, as well as the ability to accurately model S when simulating the resistivity dependence of solar cells.

2.3.2 Analytical Approximation to the Extended SRH Formalism

The dependence of S on doping level for multicrystalline silicon cannot be found in the literature. Further, it is difficult to predict S theoretically. The analytical model of S on a dielectric-passivated surface requires knowledge of the density of surface states (D_{it}) and the capture cross sections σ_p and σ_n. As charge may be stored in the dielectric, the effects of the resulting electric field must taken into account in the calculation of S. This is accomplished through the use of a method called the extended SRH formalism. The extended SRH formalism begins with analytical equations and provides an algorithm for numerical calculations of the surface carrier concentrations n_s and p_s. These results are used to compute effective S (S_{eff}) at the edge of the space-charge region below the

surface [9]. Following the convention of many authors [18], *S throughout this text refers to the effective surface recombination velocity at the virtual surface at the edge of the surface space-charge region* (x = w in Figure 9); we will not refer to the surface recombination velocity at the physical surface (x = 0).

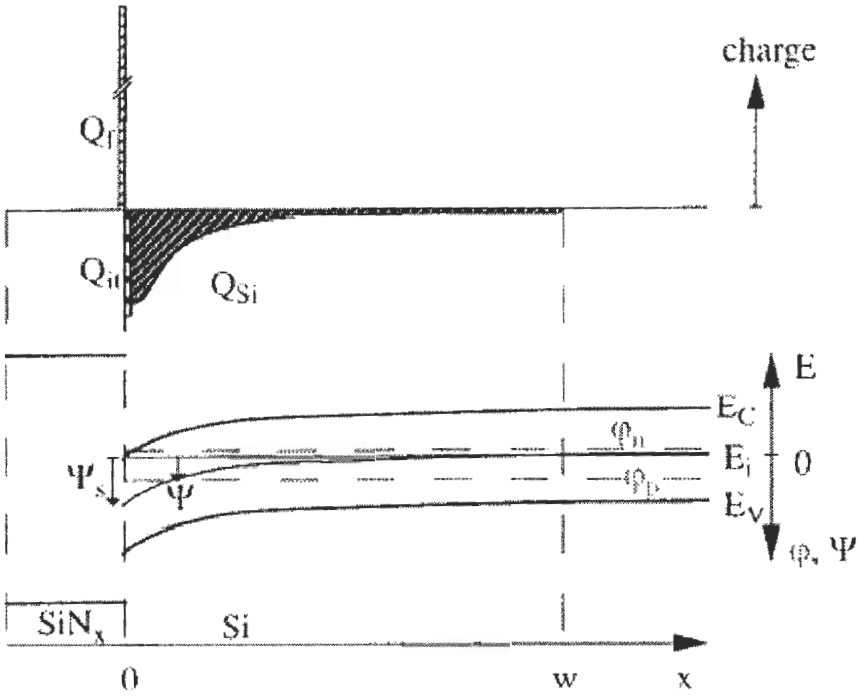

Figure 9. Charge density and energy bands at the illuminated SiN_x/Si interface (from [20]).

The calculation of S at the illuminated SiN_x/p-Si is described as an illustration of the extended SRH formalism. The charge distribution and band diagram are given in Figure 9. Q_f is the fixed, positive charge density in the nitride; Q_{it} is the charge density trapped in the interface states; Q_{Si} is the charge density of the silicon space-charge region below the surface; x = w is the edge of the space-charge region; φ_n and φ_p are the quasi-Fermi levels; E_C and E_V are the conduction and valence band edges; ψ is the potential

relative to the intrinsic Fermi level; and ψ_s is the surface potential [20]. The band diagram implies low-level injection, since φ_n is much closer to midgap than φ_p. The goal of the extended SRH formalism is to determine the effective surface recombination velocity, S_{eff}, at the edge of the depletion layer.

For simplicity, this discussion considers the case of single-level, midgap states [9]. This approximation is inspired by the fact that the recombinative effect of interface states declines exponentially with their distance from midgap [33], for constant capture cross sections. In fact, even though the number of interface states increases towards the band edges at the Si/SiO_2 interface, midgap states still tend to make the most significant contributions to surface recombination [9]. The surface recombination rate can be expressed as follows, for the mid-gap trap, assuming flat quasi-fermi levels in the surface space-charge region [9, 20, 34] (which will be justified below):

$$U_s = \frac{v_{th} N_{st}[(n_0 + \Delta n)(N_A + \Delta n) - n_i^2]}{\frac{(n_0 + \Delta n)e^{q\Psi_s / kt}}{\sigma_p} + \frac{(N_A + \Delta n)e^{-q\Psi_s / kT}}{\sigma_n}} \tag{25}$$

for a p-type semiconductor. n_0 is the equilibrium electron concentration, and Ψ_s is the surface band-bending that results from the charge at the silicon surface. Equation (25) has deliberately been put in terms of the experimentally accessible quantities N_A, n_0, and Δn, instead of the surface carrier concentrations:

$$n_s = (n_0 + \Delta n)e^{q\Psi_s / kT} \tag{26.a}$$

$$p_s = (N_A + \Delta n)e^{-q\Psi_s / kT} \tag{26.b}$$

where $n_0 + \Delta n$ and $N_A + \Delta n$ are electron and hole concentrations deep in the bulk where the energy bands are flat. These equations are easily derived under the assumption of flat

quasi-fermi levels in the surface space-charge region, one of the key assertions of the extended SRH formalism [34].

At first, the assumption of flat quasi-fermi levels in the surface space-charge region seems improper, because electron current is given as [35]

$$J_n = -q\mu_n n \frac{d\varphi_n}{dx}. \tag{27}$$

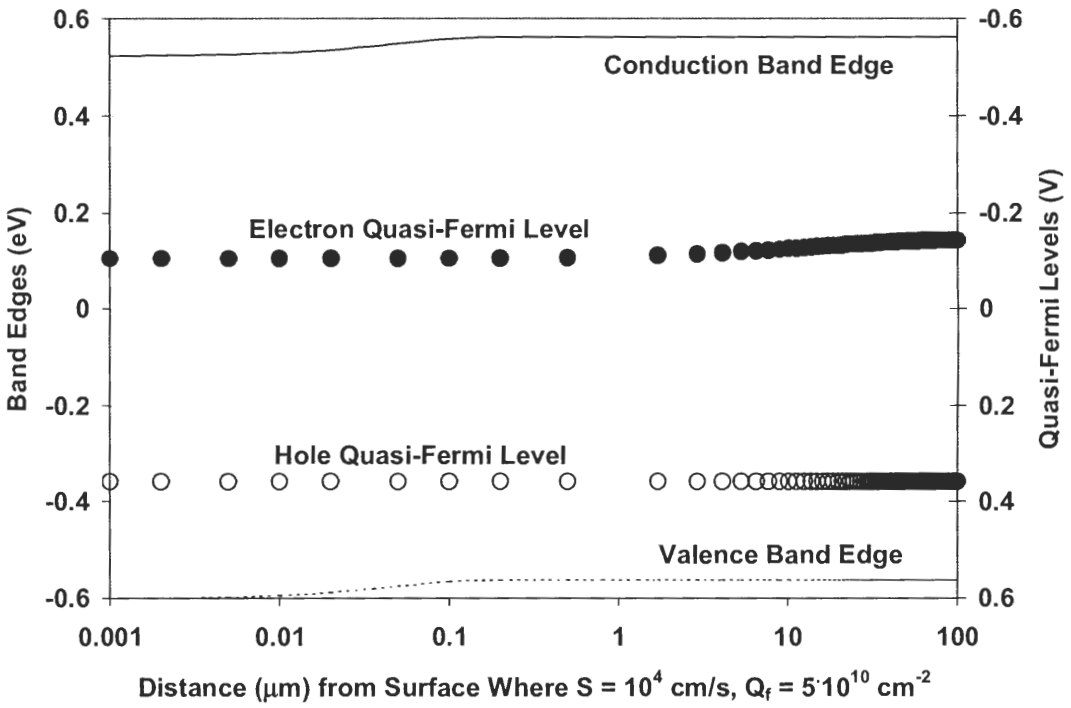

Figure 10. Energy band edges and quasi-fermi levels for an illuminated structure with one charged, recombinative surface.

If φ_n is perfectly flat, then recombination current into the surface must be zero, implying that S_{eff} must be 0 as well. Although flat quasi-fermi levels in the surface space-charge region are frequently assumed [9, 20, 34], little attempt has been made to quantitatively justify the assumption. To investigate the legitimacy of the assumption of flat quasi-

fermi levels in the surface space-charge region, we simulated a recombinative surface with the PC-1D software, which allows quasi-fermi levels to vary.

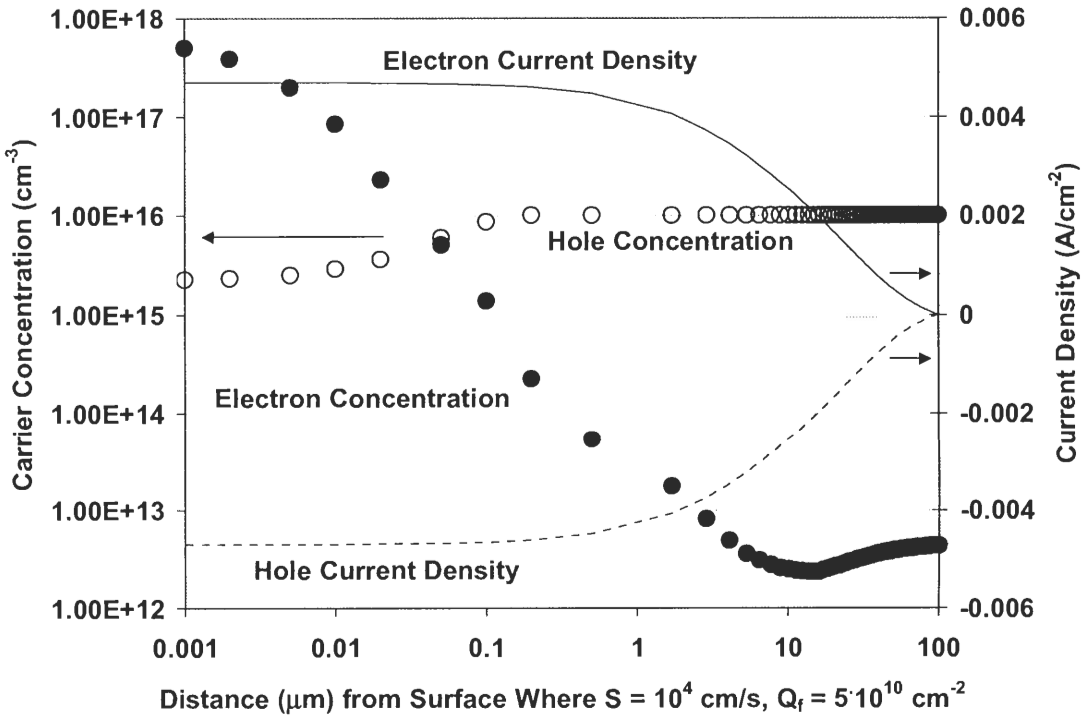

Figure 11. Current concentrations and carrier densities for same structure represented in Figure 10.

In the simulation, we chose a very high S of 10^4 cm/s at one surface. High S should produce a high surface recombination current, for which Equation (27) seems to predict a high φ_n gradient. A fixed dielectric charge of $Q_f = 5\times10^{10}$ cm^{-2} is placed at this surface. There is no recombination at the other surface. Other parameters chosen include W = 100 μm, τ_b = 1 ms, and a light intensity of 100 mW/cm^2. Results are shown in

Figures 10 and 11. The logarithmic scale of the x-axis focuses on the recombinative surface.

In Figure 10, we observe that in the surface space-charge region (where the band edges are bending), the quasi-fermi levels indeed appear flat. However, Figure 11 shows that the current densities are not zero but actually highest in these regions. Although this seems to violate Equation (27), an order-of-magnitude calculation can explain the result. Rearranging Equation (27), we find $d\varphi_n/dx = -J_n/(q\mu_n n)$. Figure 11 shows that J_n is on the order of 10^{-3} A/cm^2, while q and μ_n are well known to be on the order of 10^{-19} C and 10^3 cm^2/(sV) respectively. Figure 11 also shows that the lowest order of magnitude of n is 10^{12} cm^{-3}. The highest order of magnitude of $d\varphi_n/dt$ is then $10^{-3}/(10^{-19}\times10^{3}\times10^{12}) = 10$ V/cm or 10^{-3} V/μm. Thus within the surface space-charge region, which is about 1 μm thick, the electron quasi-fermi level only needs to vary about 10^{-3} V. Indeed, the simulation shows that φ_n at the surface is –0.107 V, while half a micron from the surface φ_n = -0.109 V.

Within a couple percent, the quasi-fermi level is indeed flat in the surface space-charge region, even in this case of very high S = 10^4 cm/s. However, the quasi-fermi levels appear in exponents; we must consider whether the small approximation of flat quasi-fermi levels brings about a large error in U_s. φ_n enters Equation (25) through Δn, the excess carrier concentration deep in the bulk [35]:

$$\Delta n = n_i e^{-q\varphi_n/kT} - n_0 . \qquad (28)$$

Since kT/q ≈ 0.025 V, an error of 0.002 V in φ_n causes the exponential term to be off by a factor of $e^{0.002/0.025} = 1.08$. In other words, the assumption of flat quasi-fermi levels

appears to cause about an 8% error in Δn. Thus the central approximation of the extended SRH formalism appears accurate within 10%.

When capture cross-sections are given, Equation (25) can be used to determine U_s as a function of Δn and N_A, once Ψ_s is known. The exact determination of Ψ_s cannot be done by hand, and a numerical method is therefore used. Assuming charge neutrality [34]:

$$Q_{it} + Q_f + Q_{Si} = 0 \tag{29}$$

where the trapped interface charge Q_{it} is often negligible (as justified in Section 5.7) and will not be further examined. Q_f, the fixed dielectric charge density, can be measured or estimated as an adjustable parameter. By solving the Poisson equation under the assumption of flat quasi-fermi levels, the total silicon space-charge density Q_{Si} can be expressed as a function of Ψ_s [36]:

$$Q_{Si} = -\sqrt{\frac{2kTn_i\varepsilon_{Si}}{q^2}F(\Psi_s,\varphi_n,\varphi_p)} \tag{30}$$

where

$$F(\Psi_s,\varphi_n,\varphi_p) = e^{q(\varphi_p-\Psi_s)/kT} - e^{q\varphi_p/kT} + e^{q(\Psi_s-\varphi_n)/kT} - e^{-q\varphi_n/kT} + \frac{q\Psi_s N_A}{kTn_i} \tag{31}$$

with the quasi-fermi levels given as [34]

$$\varphi_n = -\frac{kT}{q}\ln\left(\frac{n_0+\Delta n}{n_i}\right) \tag{32.a}$$

$$\varphi_p = \frac{kT}{q}\ln\left(\frac{N_A+\Delta n}{n_i}\right). \tag{32.b}$$

In the standard numerical method, Ψ_s is determined by minimizing the sum on the left side of Equation (29). Then U_s is calculated by Equation (25) and S_{eff} is given by [9]

$$S_{eff} = \frac{U_s}{\Delta n} = \frac{v_{th} N_{st} [(n_0 + \Delta n)(N_A + \Delta n) - n_i^2]}{\Delta n \left(\frac{(n_0 + \Delta n) e^{q\Psi_s / kt}}{\sigma_p} + \frac{(N_A + \Delta n) e^{-q\Psi_s / kT}}{\sigma_n} \right)}. \quad (33)$$

Equation (33) is complicated, and Ψ_s must be determined numerically. As an example of the variety of S_{eff} vs. Δn curves generated by following the full numerical procedure of the extended SRH formalism, consider Figure 12, reproduced from Aberle [9]. One interesting feature is the charge dependence of S. At an injection level of 10^{12} cm^{-3}, S does not decrease monotonically as Q_f increases. In fact, $Q_f = 0$ gives the median S value. As Q_f increases to 5×10^{10} cm^{-2} and again to 10^{11} cm^{-2}, S increases. The additional increases of Q_f to 2×10^{11} cm^{-2} reduces S below its $Q_f = 0$ value, and the final increase of Q_f to 5×10^{11} cm^{-2} reduces S to its lowest value.

The explanation for the dependence of S on Q_f is important, because a positive dielectric charge is often considered beneficial for surface passivation. However, if Q_f is too small, it does more harm than good. The impact of Q_f on surface recombination can be understood by studying Equations (25) and (26). The numerator in Equation (25) is constant at a given injection level. The application of a dielectric charge can only affect ψ_s in the denominator; a higher Q_f creates a higher ψ_s. To minimize U_s, ψ_s should be chosen to maximize one of the terms in the denominator. As ψ_s increases, the first term in the denominator increases, while the second decreases.

In p-type material, the second term in the denominator is much larger than the first when $\psi_s = 0$. At first, increasing ψ_s raises U_s: the larger term in the denominator decreases. Later, a turning point is reached when the two terms are equal, and subsequent increases in ψ_s reduce U_s, eventually below its flatband level. Thus positive dielectric

charge should be as large as possible, and a small dielectric charge should be avoided especially. However, for n-type materials, S improves monotonically as positive dielectric charge increases.

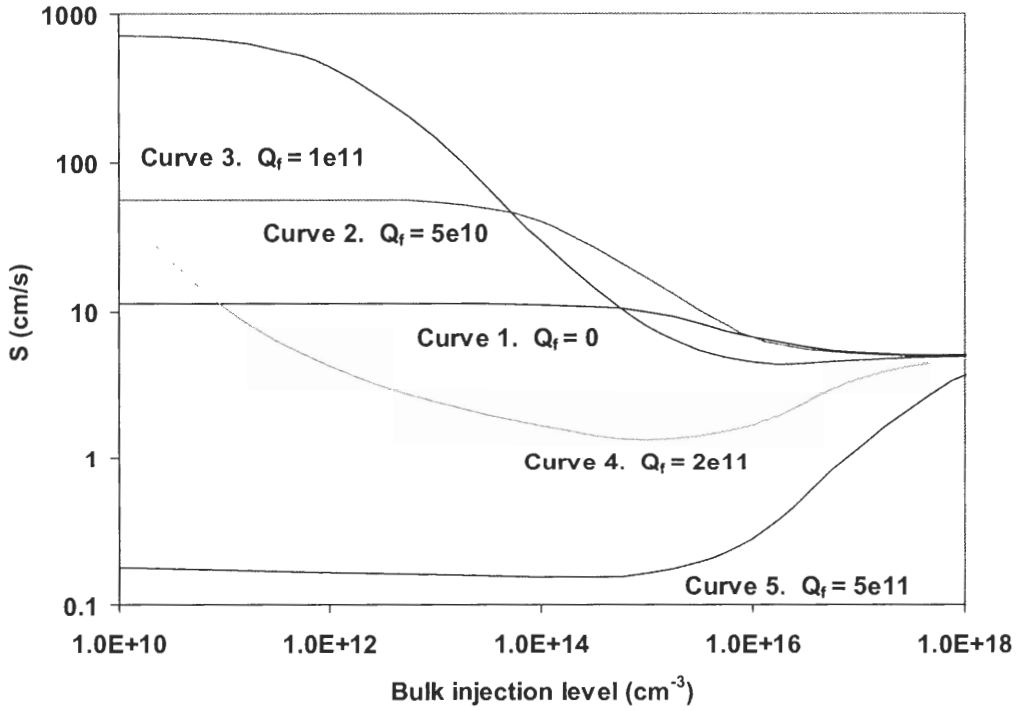

Figure 12. Numerical simulation of surface recombination velocity as a function of injection level for p-type silicon, reproduced from Aberle [9]. Here, $N_A = 1\times10^{16}$ cm^{-3}, $N_{st} = 1\times10^{10}$ cm^{-2} (evenly divided between acceptor and donor states), and $\sigma_n = \sigma_p = 1\times10^{-16}$ cm^2.

As useful and accurate as the numerical method is for generating curves such as those in Figure 12, the underlying physics is obscured. This provided the motivation to derive analytical approximations to the numerical solutions in order to clarify the underlying physics. This research will answer, on the basis of equations derived from first principles, the following four questions: (A) Why are curves 2 and 3 in Figure 12 flat at low injection levels, and why do they decline at higher injection? (B) Why does

curve 4 drop sharply at low injection levels, and why is it alone in this behavior? (C) Why is curve 5 flat in low-level injection (LLI)? (D) And why is curve 5 increasing in high-level injection (HLI)?

Kuhlmann [37] was the first to answer question C with an analytical approximation. For the case of inversion due to large Q_f, he derived the approximate equation

$$S_{eff} = \frac{2v_{th}kT\varepsilon_{Si}\sigma_p N_{st} N_A}{q^2 Q_f^2}. \tag{34}$$

This equation indicates the dependence of S_{eff} on N_A, but only in low-level injection (LLI), when $n_s >> p_s$ (due to strong band bending caused by high Q_f), and when Q_{Si} is due primarily to mobile electrons in the space-charge region. These conditions are met in the LLI range of curve 5, where the curve is flat. As predicted by Equation (34), there is no injection level dependence.

While Kulhmann's Equation (34) answers question C, more work is needed to answer questions A, B, and D associated with Figure 12. To answer these questions, three new analytical approximations will be derived. The motivation for these derivations is to gain insight into the approximate doping and injection level dependence of S under various conditions, without needing to refer to a numerical procedure upon every change of parameters.

2.4 Doping Dependence of τ_b for Multicrystalline Silicon

Unlike monocrystalline silicon, multicrystalline silicon materials have high concentrations of metallic impurities and crystallographic defects, resulting in low

minority-carrier lifetimes [27, 38-40]. The lifetime can be improved by using atomic hydrogen to passivate dangling bonds at vacancies, dislocations [41, 42], and grain boundaries [43]. Technologically feasible sources of hydrogen include forming gas anneal [44, 45], remote plasma [46, 47], or plasma-enhanced chemical vapor deposited (PECVD) SiN [45, 48, 49] followed by an anneal at 600°C or higher [40]. Recently it has been reported that bulk passivation is enhanced by the simultaneous anneal of SiN on the front surface and aluminum on the back surface of the wafer [38, 50]. The proposed mechanism is the injection of vacancies from molten aluminum into silicon at the rear of the wafer. Vacancies can form pairs with hydrogen atoms, providing an added chemical potential, thereby increasing the hydrogen flux through the bulk from its source at the front surface.

In order to optimize resistivity, it is necessary to predict the bulk lifetime of the passivated multicrystalline material as a function of resistivity. Accurate models of the doping dependence of lifetime are considerably more difficult to obtain for multicrystalline materials than for monocrystalline materials, given the significant concentrations of impurities and defects in the former. Two models have been proposed to account for the observation that optimal resistivity is higher for multicrystalline solar cells than for monocrystalline solar cells [5]. In the first model, a dopant-defect interaction is assumed to increase the effective trap density of point defects as a function of doping level, according to the following empirical equation for p-type substrates [51]:

$$\tau_0 = \tau_{0\infty} / \left(1 + \frac{N_A}{N_{ref}} \right), \qquad (1)$$

where N_{ref} is a measure of the dopant-defect interaction.

In contrast, the second model assumes a distribution of levels in the bandgap, which may be caused by extended defects such as dislocations and precipates. In this model, doping concentration influences recombination only indirectly, through the position of the Fermi level [42]. Only those levels closer to midgap than the Fermi level participate in recombination, for the following reasons. Consider a p-type semiconductor. All trap levels below the Fermi level are predominantly occupied by electrons. These filled traps cannot capture conduction band electrons and thus do not participate in recombination. Symmetrically, in the upper half of the bandgap, all states farther from midgap than ($E_i - E_F$) cannot participate in recombination. [42] asserts without proof that these states emit captured electrons with greater probability than they capture holes to complete the recombination process. To understand this fact, compare the emission rate of an electron [52]

$$R_{en} = \sigma_n N_t f(E_t) n_1 \tag{35}$$

with the capture rate of a hole [52]

$$R_{cp} = \sigma_p N_t f(E_t) p\,, \tag{36}$$

where E_t is the trap level and f is the Fermi-Dirac distribution. In the case of identical capture cross sections, for example, the higher rate is clearly determined by comparing n_1 and p. It is well known that

$$n_1 = n_i \exp[(E_t - E_i)/kT] \tag{37.a}$$

and

$$p = n_i \exp[(E_i - E_F)/kT]. \tag{37.b}$$

Thus we arrive at the conclusion that upper-bandgap states farther from midgap than (E_i - E_F) emit captured electrons back into the conduction band and do not participate in

recombination. This is illustrated in Figure 13. As the Fermi level moves away from midgap with rising doping level, the "window" of energy levels that participate in recombination widens, decreasing lifetime [42].

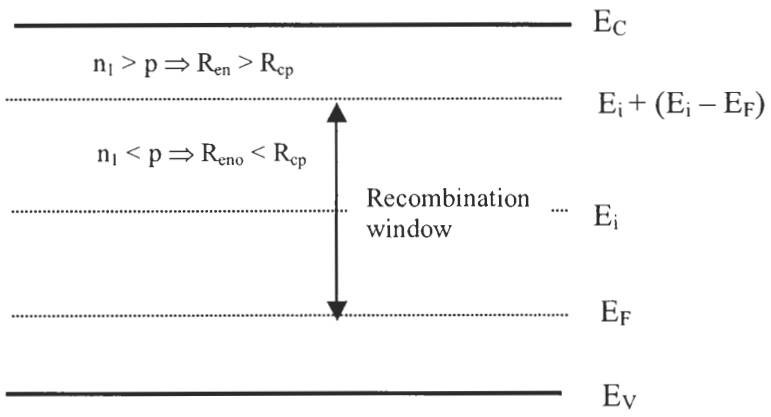

Figure 13. Illustration of the "recombination window" of energy levels participating in recombination for extended defects.

The two models are associated with different physical causes. The dopant-defect interaction is associated with point defects, such as metallic impurities. Data consistent with this view have been obtained for edge-defined film-fed grown (EFG) ribbon silicon [5]. On the other hand, extended defects lead to the distribution of levels assumed in the Fermi level analysis [42]. Data consistent with this model have been obtained for dendritic web silicon [42]. Some investigators have succeeded in separating the influence of metallic impurities and crystallographic defects in the same cast multicrystalline wafers as follows: to study the role of metallic impurities, high-temperature processing was used to cross-contaminate high-purity float zone silicon. To study crystallographic defects, $POCl_3$ gettering was performed on the multicrystalline wafers to extract as many metallic impurities as possible [27].

While it is clear that that doping-dependence of lifetime is material-specific, it is not obvious how to quantitatively model lifetime vs. doping for all solar-grade multicrystalline materials. It appears that a systematic investigation of the doping dependence of bulk passivation has only been done for dendritic web silicon, but even in this case, no clear trend emerges from the data of Figure 14 [53]. To predict the doping dependence of solar cell performance, the doping dependence of τ_b following any gettering and passivation steps must be known. This information cannot be found in the literature. This provided the motivation for investigating the doping dependence of τ_b for processed string ribbon and cast multicrystalline silicon.

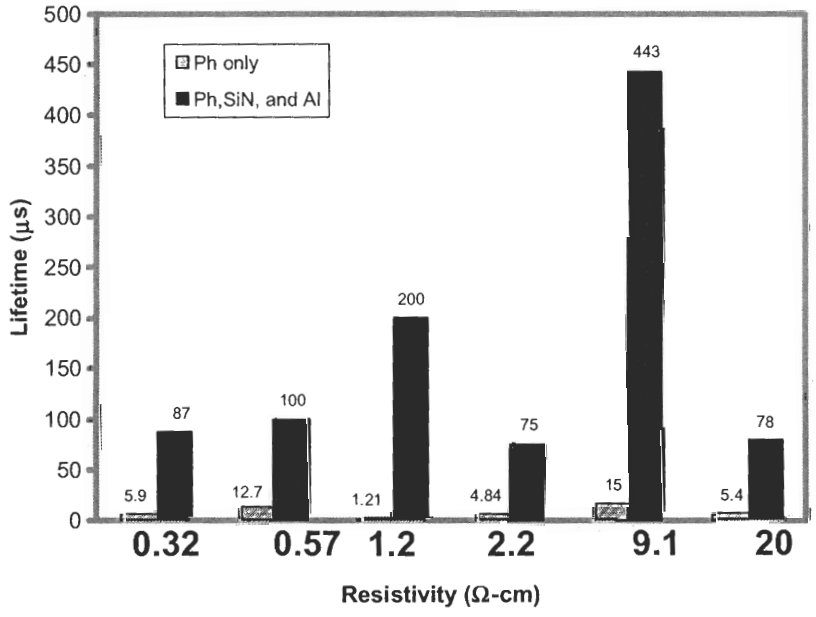

Figure 14. Doping dependence of gettering and bulk passivation on dendritic web silicon (from [53]).

2.5 Solar Cell Resistivity Optimization

Solar cell resistivity optimization can be performed empirically by fabricating statistically significant quantities of devices over a wide resistivity range [54]. While this optimization method is impeccably convincing, it suffers an important drawback. Since all theory is circumvented in this empirical method, it is necessary to repeat the resistivity optimization experiment whenever any other device parameter is varied. For example, optimization would have to be repeated for new choices of wafer thickness, emitter profile, anti-reflection coating, or front or rear passivation scheme. The goal of theoretical resistivity optimization is to predict the optimal resistivity for any arbitrary combination of device parameters.

Numerical resistivity optimization is commonly performed using the device simulation software PC-1D [51, 55-58]. Although one-dimensional, PC-1D can account for such phenomena as high-level injection, heavy doping effects, arbitrary doping profiles, and flexible boundary conditions [56]. Shockley-Read-Hall (SRH) recombination [59] is frequently the dominant recombination mechanism, and the trap level can be easily adjusted in the software. The user can provide a sequence of doping-dependent lifetimes according to Equation (1) to incorporate the effect of a dopant-defect interaction [51]. However, N_{ref} must first be experimentally established for the material under investigation in order for the simulation to be valid.

The doping dependence of S must also be incorporated in the optimization. In the case of a back surface field, PC-1D may be used to determine S, given that the concentration profile of the back surface field is known. If the rear surface is passivated by a dielectric, which is typical in bifacial cells [60], the extended SRH formalism

outlined earlier is the appropriate theoretical tool for modeling the doping dependence of S on monocrystalline materials. On multicrystalline materials, however, S depends locally on crystal orientation [61], and an average S over a given area may depend on the grain distribution in a complicated way. Thus, it is not clear how C-V measurements should be used on multicrystalline materials to obtain the dielectric parameters necessary in the extended SRH formalism. In the literature, the doping dependence of S for a dielectric has apparently not been used in resistivity optimization, even for monocrystalline materials. For example, in some simulations S has been held constant over all doping levels [62] or neglected entirely [63].

To more accurately predict the resistivity dependence of solar cell performance, the doping dependence of S and of τ_b will be incorporated in device simulations. The simulations will use the doping dependence of S and τ_b experimentally determined in this research for multicrystalline materials.

CHAPTER 3

DEVICE SIMULATIONS TO INVESTIGATE THE IMPACT OF THE DOPING DEPENDENCE OF S AND τ_b ON THE EFFICIENCY OF SCREEN-PRINTED SOLAR CELLS ON LOW-COST MATERIALS

This chapter presents guidelines to achieve planar solar cell efficiencies as high as 17.5% using existing fabrication technologies and silicon substrates with lifetimes as low as 20 μs. Device simulations are performed to elucidate the importance and impact of base doping optimization for different back surface passivation schemes, cell thicknesses, emitter profiles, and degrees of dopant-defect interaction. Simulation results in this chapter will highlight the need to use experimentally determined values for τ_b and S at different resistivities; assumed values or trends are used in this chapter. It is also important to recognize that the doping dependence of τ_b and S in high-quality silicon materials is much better understood and quantified, but there is very limited data for low-cost silicon materials.

The search for cheaper materials that reduce the cost of PV module fabrication has led researchers to investigate ribbon silicon substrates such as dendritic web silicon, string ribbon silicon, and edge-defined film fed growth (EFG) silicon. These materials eliminate kerf loss associated with wafer sawing and can be grown with a variety of thicknesses. The choice of base doping during growth greatly influences cell performance. Since manufacturers can adjust base doping inexpensively, the

optimization of this parameter could provide a very cost-effective way to achieve higher cell efficiency. Although the base doping level of mc-Si materials cannot be adjusted with complete precision, device simulations performed in this task will show that small deviations from the optimal doping level have little impact on efficiency.

It has been shown that the optimal base doping for high-quality monocrystalline Si, in the absence of appreciable dopant-defect interaction, is 0.2-0.3 Ω-cm [5, 8, 64]. However, there are no clear guidelines for establishing the optimal bulk resistivity for a low-cost PV-grade material, where dopant-defect interaction may be significant. The dopant-defect interaction reduces bulk lifetime at lower resistivities, thereby elevating the optimal resistivity. Most PV manufacturers use 1-3 Ω-cm as an empirically determined optimal resistivity. Since the empirically determined optimal resistivity for PV-grade materials (1-3 Ω-cm) is greater than the optimal resistivity in the absence of dopant-defect interaction (0.2-0.3 Ω-cm), we infer that a dopant-defect interaction occurs in PV-grade materials.

The optimal bulk resistivity of a PV device depends on many factors, including back surface passivation, thickness, and emitter doping profile of the device. This chapter provides guidelines for the proper selection of bulk resistivity for three choices of back surface passivation (a dielectric stack passivation, unpassivated ohmic contact, and aluminum back surface field). In addition, it shows how cell thickness, emitter doping, and dopant-defect interaction affect optimal doping level for each of the three back surface passivation schemes.

Device modeling is performed with the device simulation software PC-1D. While this is a one-dimensional model whose output may not precisely match that of a more

detailed two-dimensional model, the trends observed in the influence of various cell parameters on optimal resistivity are expected to be the same.

3.1 Guidelines for Achieving High Efficiency with Low Bulk Lifetime

Current screen printed solar cell efficiencies in production are in the range of only 12-15%. In this section, the simulation of over 17% screen-printed devices using 20 μs bulk lifetime material is illustrated by systematic improvements to the device design. Six devices are modeled, each with a bulk lifetime of 20 μs. The device parameters for this simulation are shown in Table 4. All values of front surface recombination velocity (S_f) are extracted from published values of J_{oe} [65], assuming a doping profile given by the error function. The internal reflectance for all devices is assigned to 70% at the rear surface and 92% at the front surface; without adequate internal reflectance, the benefits of thinner cells would not be observed. The doping dependence of carrier mobilities is calculated automatically by PC-1D. As modeled, the junction leakage current J_{02} is fixed at 5×10^{-9} A/cm^2.

Table 4. PC-1D inputs for high efficiency simulation.

Device Para-meter	Device 1	Device 2	Device 3	Device 4	Device 5	Device 6
τ (μs)	20	20	20	20	20	20
S_b (cm/s)	10^6	340	340	340	340	340
Thickness (μm)	300	300	100	100	100	100
Emitter sheet res. (Ω/sq)	40	40	40	90	90	90
Junction depth (μm)	0.586	0.586	0.586	0.550	0.550	0.550
S_f (cm/s)	94620	52840	52840	7269	7269	7269
ARC	SLAR	SLAR	SLAR	SLAR	DLAR	DLAR
N_A (cm^{-3})	9.14×10^{15}	9.14×10^{15}	9.14×10^{15}	9.14×10^{15}	9.14×10^{15}	5.46×10^{16}
R_s ($\Omega \cdot cm^2$)	0.6	0.6	0.6	0.6	0.6	0.6
R_{sh} ($\Omega \cdot cm^2$)	10000	10000	10000	10000	10000	10000
J_{02} (A/cm^2)	$5 \cdot 10^{-9}$	$5 \cdot 10^{-9}$	$5 \cdot 10^{-9}$	$5 \cdot 10^{-9}$	$5 \cdot 10^{-9}$	$5 \cdot 10^{-9}$

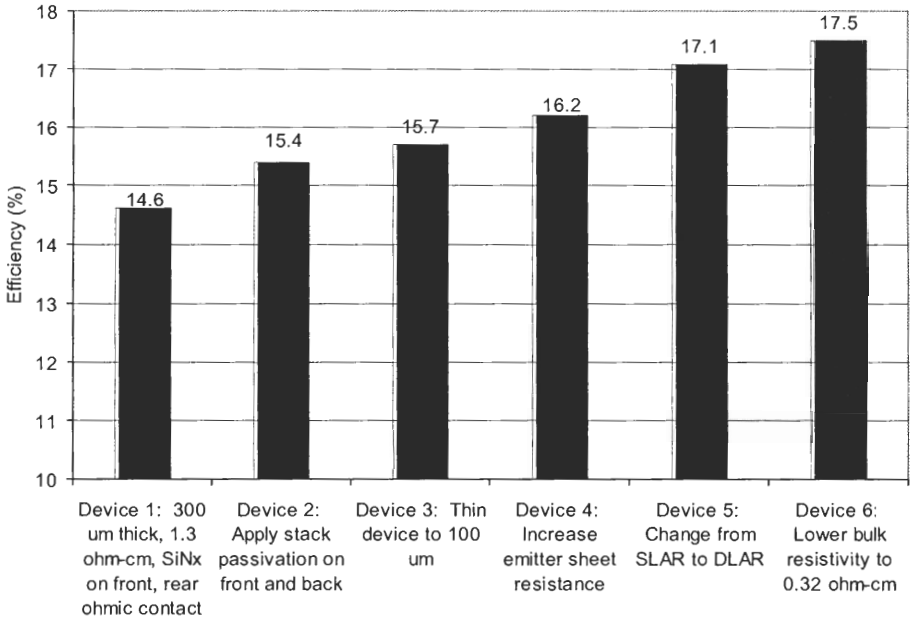

Figure 15. Systematic improvements in cell performance.

Device 1 represents a 300 μm thick cell with no rear passivation and only a single layer silicon nitride ARC on the front. It has a typical commercial cell bulk resistivity of 1.6 Ω-cm. Figure 15 shows that a series of incremental improvements, all theoretically achievable with existing commercial technologies, raises the cell efficiency from 14.6% to 17.5%.

The 0.8% increase in efficiency when going from Device 1 to Device 2 is a result of improved surface passivation. Both surfaces in Device 2 have the rapid thermal oxide (RTO)/SiN_x stack passivation. The RTO/SiN_x stack has been shown to provide better passivation than either of its constituent dielectrics alone [66]. The rear recombination velocity of 340 cm/s used in this model includes the contribution of an ohmic gridded back contact [67]. An additional 0.3% augmentation in absolute efficiency is achieved in Device 3, simply by thinning the device from 300 μm to 100 μm. This reduces the dependence of efficiency on bulk lifetime and improves device performance because the surfaces are well passivated. Device 4 adds the benefit of a more lightly doped emitter, which, in combination with the corresponding higher quality surface passivation (S = 7269 cm/s), improves the blue response. While screen-printed contacts with low contact resistance have not yet been demonstrated on such a lightly doped surface, a selective emitter structure, which combines a high sheet resistance profile as a field diffusion and a heavier diffusion under the contacts, is expected to yield similar results. Device 5 adds the significant benefit of a double layer anti-reflective (DLAR) coating. The 0.4% improvement of efficiency in shifting from Device 5 to Device 6 is achieved simply by selecting the optimal bulk resistivity, which is 0.32 Ω-cm in this case where lifetime is independent of doping concentration prior to Auger recombination. This can happen

when there is no dopant-defect interaction and a midgap trap controls lifetime [64]. The optimal selection of base doping results in a final device efficiency of 17.5%. A dopant-defect interaction or a shallow lifetime-limiting trap would have the effect of raising optimal resistivity while lowering efficiency, as detailed below. The simulation demonstrates that high efficiency screen-printed cells can be fabricated on 20 μs material if a high quality surface passivation scheme is applied and combined with a selective emitter structure, a DLAR coating, and the optimal base resistivity.

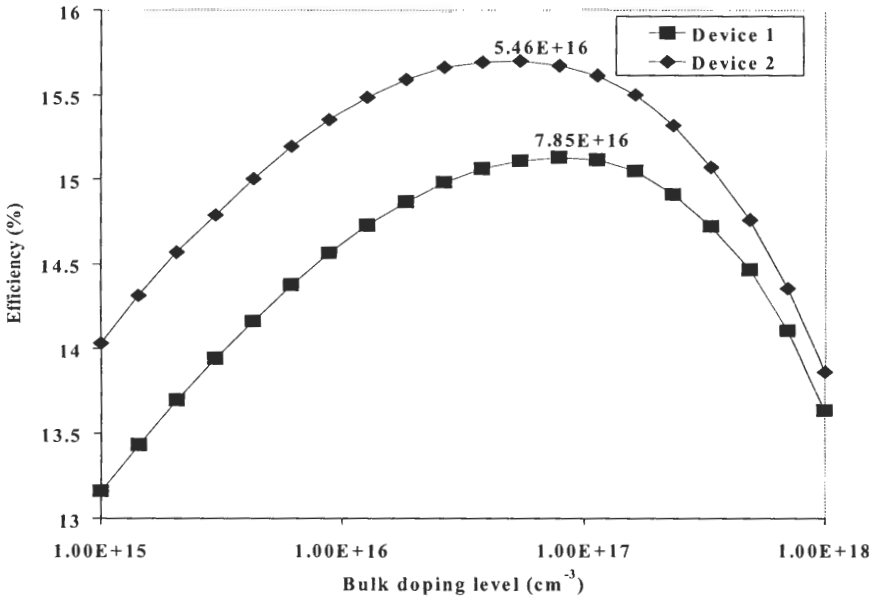

Figure 16. Variation in performance of Device 1 and 2 with base doping. Optimal doping level is indicated.

3.2 Understanding of Base Doping Optimization

To determine the optimum base resistivity for various device structures, it is necessary to understand which device characteristics compete as a function of base resistivity to result in an optimal base doping level. Figure 16 shows how the

performance of Devices 1 and 2 from Table 4 varies with the doping level. The figure shows that device efficiency increases with the doping level up to $7.85 \cdot 10^{16}$ cm^{-3} and $5.46 \cdot 10^{16}$ cm^{-3} for Device 1 and Device 2 respectively, and decreases beyond these doping levels. Figure 17 illustrates how the device parameters J_{sc}, J_{0b}, and J_{0e} of Devices 1 and 2 vary with base doping to result in the optimal base doping levels. In these simulations, realistic values were chosen for the parameters J_{02}, R_s, and R_{sh} (see Table 4), yielding fill factors in the range of 0.77-0.78. These are close to the fill factors we typically obtain experimentally for screen-printed devices. Since the variation of fill factor as a function of resistivity is very slight, compared with the variation of J_0 and V_{oc}, it can be inferred from Figure 17 that the optimal resistivity is a result of the competition between the decrease of J_0 (and thus increase of Voc) and the decrease of J_{sc} with doping level. Figure 17 also shows that the J_{0e} of Devices 1 and 2 are insensitive to the variation in base doping until a base doping level of 10^{17} cm^{-3}, but beyond that, J_{0e} increases for the following reason: the depletion region thickness on the emitter side of the junction increases at higher base doping levels, in accordance with standard junction equations. The emitter is therefore effectively thinner. A thinner emitter is more sensitive to front surface passivation. Since front surface passivation is generally poor on a heavily doped 40 Ω/sq emitter used for manufacturable screen-printed cells, a thinner emitter for a given doping profile results in higher J_{0e}. As illustrated by Device 1 in Figure 17, in the absence of dopant-defect interaction, J_{0b} decreases with doping level until about N_A = 1×10^{17} cm^{-3} according to the following equation [8]:

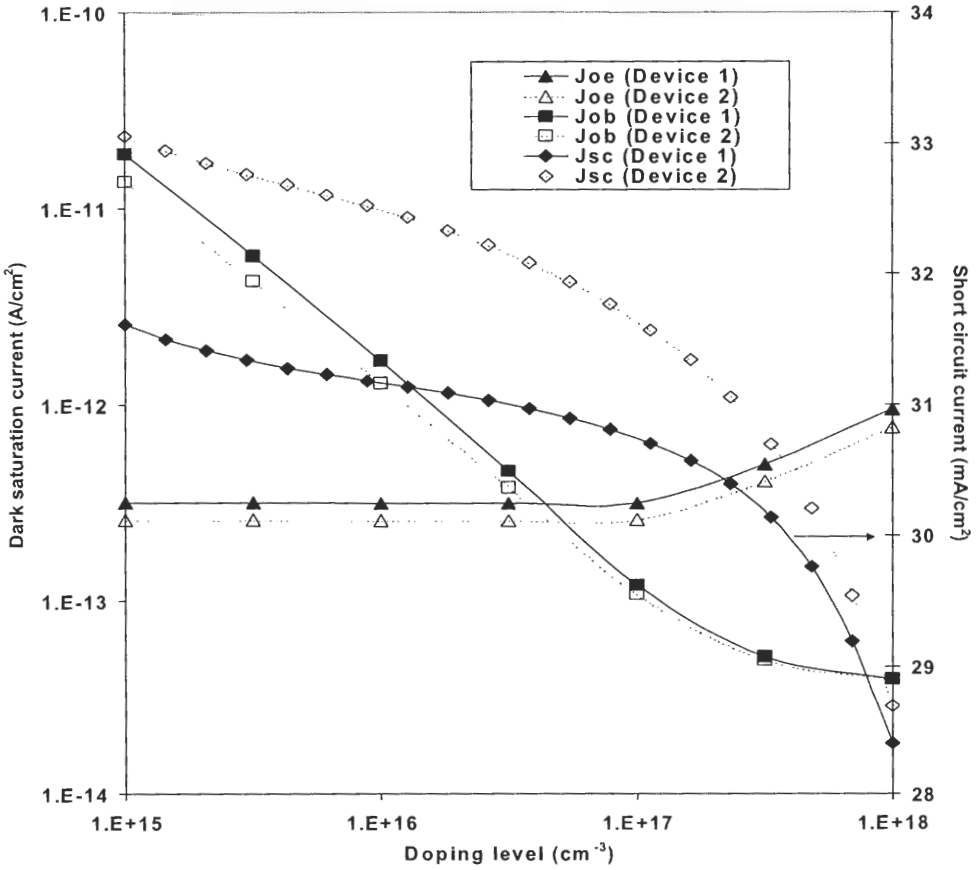

Figure 17. Variation of J_{0b}, J_{0e}, and J_{sc} with base doping for Device 1 (S_f = 94620 cm/s, $S_b = 10^6$ cm/s) and Device 2 (S_f = 52840, S_b = 340 cm/s).

$$J_{0b} = \frac{qD_n n_i^2}{L_n N_A} F_p \tag{38}$$

where

$$F_p = \frac{S_b L_n / D_n + \tanh(W / L_n)}{1 + (S_b L_n / D_n)\tanh(W / L_n)}. \tag{39}$$

Beyond $N_A = 1x10^{17}$ cm^{-3}, J_{0b} becomes relatively insensitive to increases in base doping as the reduction of the $1/N_A$ term is balanced by a decrease is minority carrier lifetime. At these very high doping levels, the lifetime is dominated by Auger recombination, which varies with doping level according the well-known equation shown below.

$$\frac{1}{\tau_{Auger}} \approx C_p N_A^2 . \tag{40}$$

Then since

$$L_n = \sqrt{D_n \tau} \approx \frac{1}{N_A}\sqrt{\frac{D_n}{C_p}}, \tag{41}$$

the N_A terms cancel out in Equation (38), resulting in $J_{ob} = qn_i^2 F_p \sqrt{C_p D_n}$.

Equations (38) and (39) also indicate that a reduction in the back surface recombination velocity will decrease J_{0b}, for $W \leq L$, as verified by the difference in J_{0b} for Devices 1 and 2 in Figure 17.

J_{sc} for both devices decreases sharply beginning at a doping level of about $1x10^{17}$ cm^{-3} due to the onset of Auger recombination. The difference between the J_{sc} curves of Device 1 and Device 2 is a result of the difference in effective diffusion length due to the different back surface recombination velocity.

Since both surfaces of Device 2 are better passivated than those of Device 1, Figure 17 summarizes the roles of front and rear surface passivation and doping level in determining cell efficiency: improved front surface passivation reduces J_{0e}, while improved back surface recombination reduces J_{0b} and boosts J_{sc}. Prior to the Auger recombination ($N_A \geq 10^{17}$ cm^{-3}), as doping level increases, the three parameters behave as follows: J_{0e} stays constant, J_{0b} drops according to Equation (38), and J_{sc} declines because the net bulk lifetime, as well as carrier mobility, decreases as doping level increases. Below the optimal doping level, an increase in doping level results in a gain in V_{oc} that is greater than the loss in J_{sc}; therefore, cell efficiency increases with doping concentration. After $N_A \approx 7 \cdot 10^{16}$ cm^{-3}, J_{0e} dominates J_0 and limits V_{oc}, while J_{sc} continues to decrease, resulting in a decrease in efficiency and an optimum doping concentration of $5\text{-}8 \cdot 10^{16}$ cm^{-3}.

3.3 Impact of Cell Thickness and Surface Passivation on the Optimal Bulk Resistivity

Reducing the cell thickness without sacrificing cell efficiency can significantly reduce the cost of silicon photovoltaics, because silicon material alone accounts for 40-50% of the cost of current commercial silicon PV modules [1]. This section shows that the quality and knowledge of surface passivation combined with the appropriate selection of doping level can actually produce cells with higher efficiency on thinner materials, continuing to assume a low-cost, defective material with a 20 μs bulk lifetime.

While the RTO/SiN_x rear stack passivation scheme is a promising technology for the next generation of silicon solar cells, it is not currently used in commercial silicon PV

cells, due to the lack of a continuous rapid thermal processing (RTP) machine. The most common rear passivation and contact schemes in PV module manufacturing are an Al back surface field (BSF) or simply an ohmic contact. However the RTO/SiN_x rear stack passivation scheme is a promising technology particularly for high efficiency thin bifacial devices [66]. A reduction in device thickness and surface recombination improves J_{ob}, which may change the optimal doping level. In this section, the optimal base resistivity is determined as a function of rear surface passivation and device thickness. In these simulations, the back surface recombination velocity was fixed at 340 cm/s for all base doping levels for the stack passivation, consistent with published results [67] of devices fabricated on 0.6 Ω-cm FZ silicon with screen-printed gridded Ag ohmic contacts, and 10^6 cm/s for the unpassivated ohmic contact. For devices with an Al BSF with thickness ≥ 5μm formed by firing screen-printed aluminum at 850°C, S_b was modeled as a parabolic function of doping concentration (N_A) according to the following quadratic fit to the surface recombination velocity at a p/p+ interface calculated by an S model [68]:

$$S_b = 4\times10^{-31} N_A^2 + 2\times10^{-14} N_A + 25 \quad (42)$$

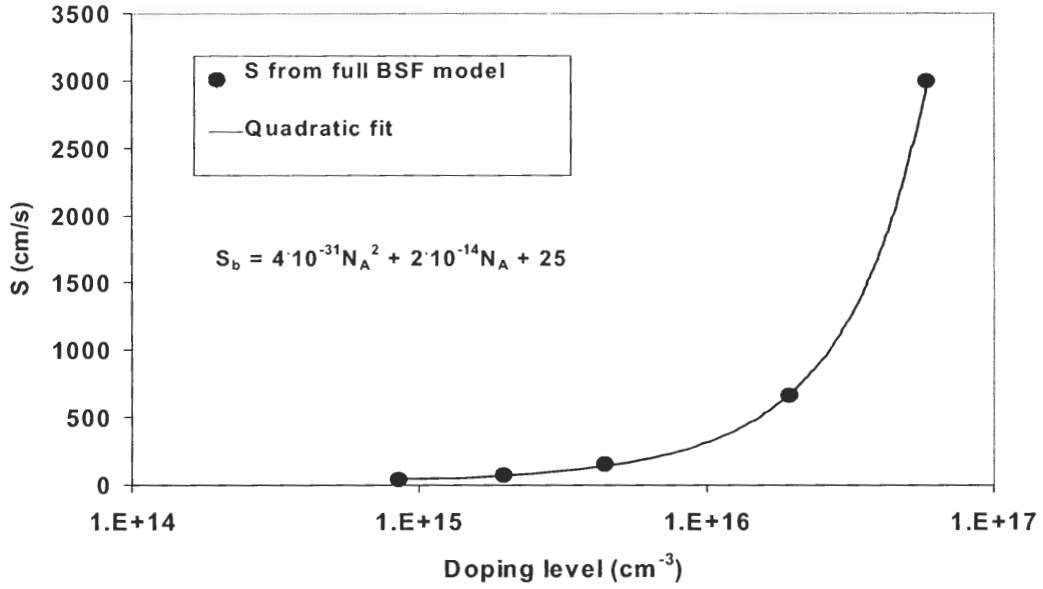

Figure 18. Curve indicating quadratic fit to S values calculated from a model of the Al BSF.

where S_b is in cm/s and N_A is in cm^{-3}. Figure 18 shows that Equation (42) fits very well to the S values calculated by the full model of an Al BSF [68]. Equation (42) gives S_b values of 241 cm/s for 1.6 Ω-cm material and 2580 cm/s for 0.3 Ω-cm material. The remaining device parameters used in the simulation are identical to those given for Device 3 in Table 4.

Device simulations were performed to determine optimum resistivity for each of the three back surface conditions and two device thicknesses (100 μm and 300 μm). In Figure 19, cell efficiency is plotted for a typical commercial cell resistivity of 1.6 Ω-cm and also for the calculated optimal resistivity. The optimal resistivity was found to be highest (0.6 Ω-cm or 1.2 Ω-cm for 300 μm or 100 μm thick cells, respectively) for the Al BSF, lower for the stack passivation (0.32 Ω-cm for both thicknesses), and lowest for the ohmic contact (0.24 Ω-cm or 0.13 Ω-cm), for this cell design with 20 μs lifetime. This trend is observed for both thicknesses. Figure 19 demonstrates that optimal resistivity, in

the absence of a dopant-defect interaction, is lower than the typical industrial cell resistivity (1.6 Ω-cm) for all back surface passivation schemes.

Note in Figure 19 that the efficiency difference between the typical resistivity (1.6 Ω-cm) device and the optimal resistivity device is greatest (≥0.6% absolute) for the ohmic contact cells and least (≤0.1%) for the BSF cells. This is because the typical resistivity (1.6 Ω-cm) is closest to the optimal resistivities for the BSF cells (1.2 Ω-cm and 0.6 Ω-cm for 100 μm and 300 μm thick cells, respectively), and farthest from the optimal resistivities for ohmic contact cells (0.13 Ω-cm and 0.24 Ω-cm for 100 μm and 300 μm thick cells, respectively). The most common commercial cell design uses

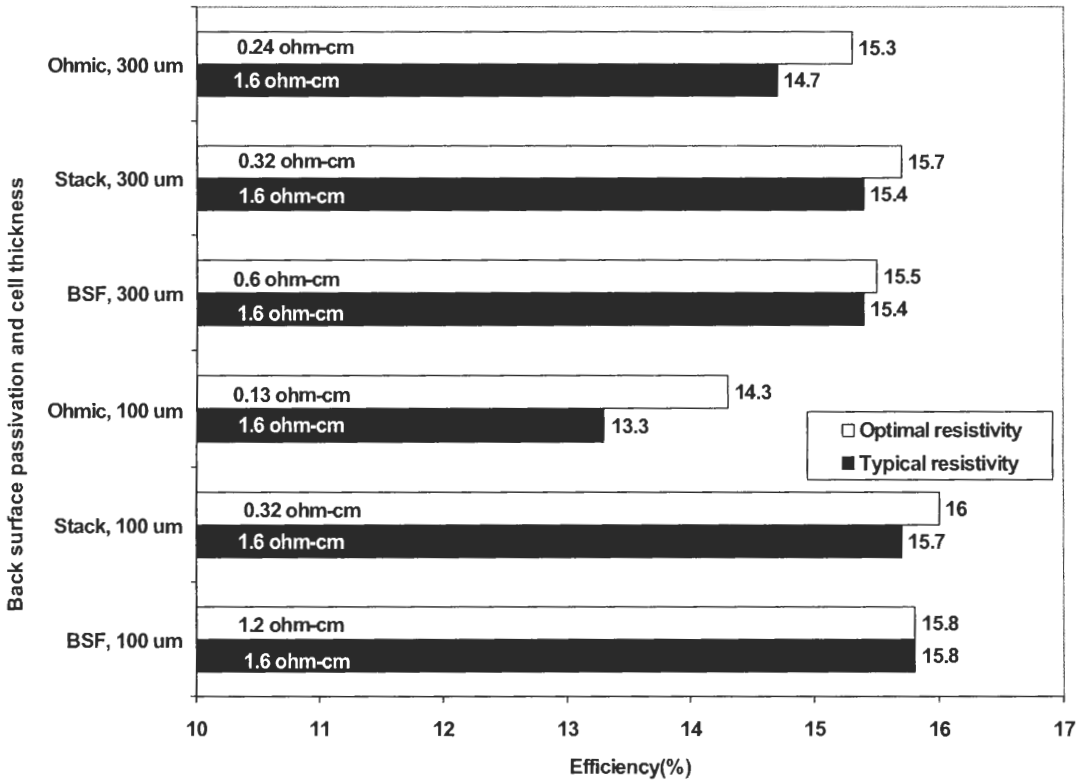

Figure 19. Efficiency of cells with optimal and typical resistivity for three surface passivation schemes and two cell thicknesses.

roughly 300 μm thick, 1.6 Ω-cm silicon and a rear ohmic contact, yet our results show that the optimal base resistivity is 0.24 Ω-cm, if the lifetime is independent of bulk resistivity in that range. An explanation for this discrepancy is that common low-cost silicon materials may have a dopant-defect interaction, which lowers lifetime at higher doping levels. The presence of a shallow trap or a dopant-defect interaction can lower bulk lifetime at higher doping levels, and, therefore, raise optimal base resistivities, as shown in a later section.

Since thinner cells are more sensitive to surfaces, two trends observed in the 300 μm cells in Figure 19 are magnified in the 100 μm cells. First, the difference in efficiency between the poorly passivated cell (ohmic contact) and the well-passivated cells (stack and BSF) is greater for the thinner cells. Second, the difference in optimal resistivity between the unpassivated and BSF cells is greater in the 100 μm cells (0.13 Ω-cm and 1.2 Ω-cm for ohmic contact and BSF respectively) than the 300 μm cells (0.24 Ω-cm and 0.6 Ω-cm for ohmic contact and BSF respectively), for the doping-independent

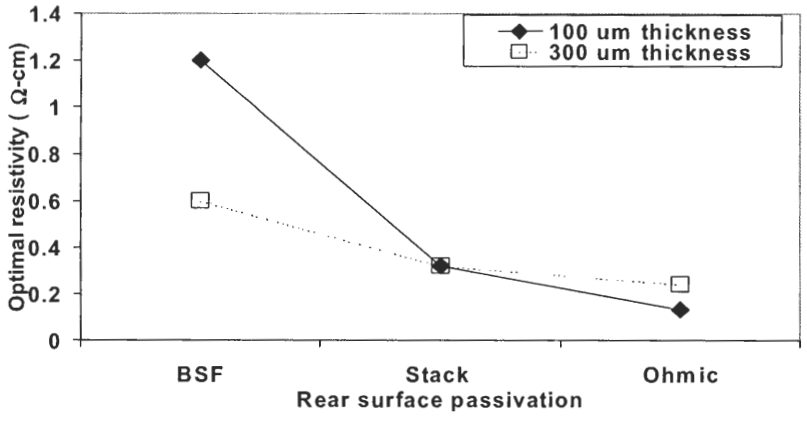

Figure 20. Optimal resistivity of 100 μm and 300 μm devices with three different back surface passivation schemes.

bulk lifetime case.

In Figure 20, the essential data is extracted from Figure 19, demonstrating clearly that optimal resistivities are highest for the Al BSF and lowest for the rear ohmic contact. In order to understand why the Al BSF is associated with the highest optimal bulk resistivity, S_b values were plotted as a function of doping level for all three back surface conditions, as shown in Figure 21. Since S_b for the Al BSF increases as resistivity decreases according to Equation (42), optimal resistivity is highest for the Al BSF. (S_b values are assumed constant for ohmic contact and stack passivation cases.)

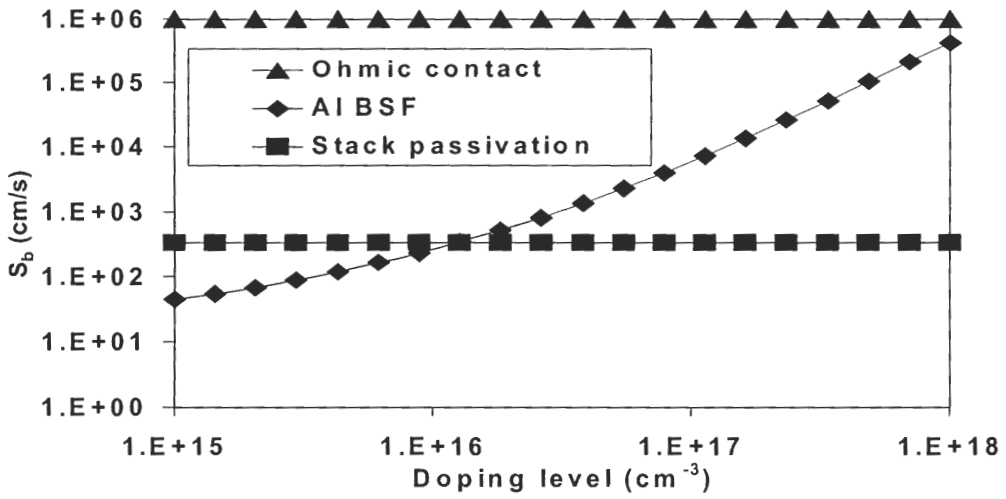

Figure 21. Back surface recombination velocity as a function of doping level for the three back surface passivation schemes simulated.

To explain why the optimal resistivity for cells with a stack-passivated rear surface is higher than for cells with an unpassivated ohmic contact, J_{0e} and J_{0b} values were determined by model calculations and plotted in Figure 22. As doping level increases, the dark saturation current due to the base (J_{0b}) improves (decreases) because it

is proportional to $1/N_A$. This improvement in J_{0b} ceases to benefit the device as soon as J_{0e} begins to dominate J_0. Figure 22 shows that J_{0e} begins to dominate J_0 at lower doping levels in the stack passivated cell, as compared with the ohmic contact cell; the latter has a crossover point at higher doping levels. Since the ohmic contact cell continues to benefit from J_{ob} improvements at higher doping concentrations, its optimal doping level is higher than that of the stack passivated cell.

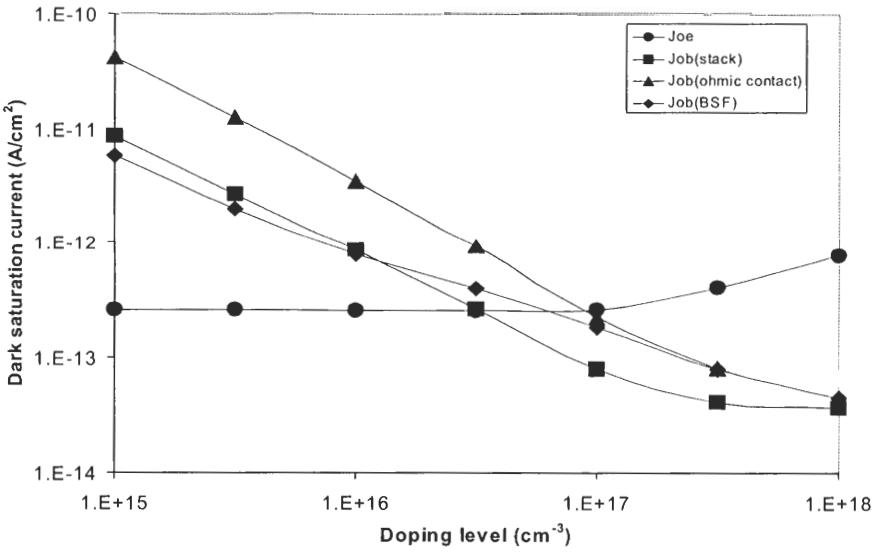

Figure 22. Variation in J_{0b}, J_{0e}, and J_{sc} with doping level for three back surface passivation schemes.

Though the Al BSF offers intermediate passivation between stack passivation and ohmic contact, the J_{0b} curves help explain why it is associated with the highest optimal resistivity. The J_{0b} curve of the Al BSF cell crosses that of the stack passivation cell near 10^{16} cm^{-3}. At higher doping levels, the Al BSF J_{0b} decreases more slowly than the stack J_{0b}, reducing the benefits of increased doping level (relative to the drawback of decreased J_{sc}) and resulting in a higher optimal resistivity for the Al BSF device.

3.4 Impact of Emitter Sheet Resistance on Optimal Bulk Resistivity

In this section, we seek to evaluate the impact, if any, of the emitter doping on the selection of the optimal base doping. These simulations, using a homogenous emitter with a 90 Ω/sq sheet resistance, approximate the performance of devices with selective emitters, which have emitter sheet resistance of 90 Ω/sq everywhere except under the contacts. Though a two-dimensional model may yield values that do not agree precisely with those of this one-dimensional model, the influence of different cell parameters on optimal resistivity is expected to be the same. The optimal base doping level and efficiency of this emitter design are compared to those of a typical screen-printed device emitter with a homogeneous sheet resistance of 40 Ω/sq for the three back surface passivation schemes described in previous sections. The front surface recombination velocities extracted from published J_{0e} results [65], 52840 cm/s and 7269 cm/s for 40 Ω/sq and 90 Ω/sq respectively, were used in these simulations.

The results of the simulation in Figure 23 show that the benefit of base doping optimization is greater when the selective emitter design is applied for all three passivation schemes. The results show that the optimum resistivity for devices with the three back surface passivation schemes is insensitive to the emitter design, for a fixed base lifetime of 20 μs ($\tau_{n0} = \tau_{p0}$ of 20 μs with a midgap trap) and a thickness of 100 μm. A change in emitter sheet resistance does not affect optimal resistivity, because J_{0b} dominates J_0 for low-lifetime material, so that J_{0e} plays no appreciable role in the competition between J_0 and J_{sc} in the determination of optimal resistivity. The optimal resistivities are shown in Figure 24, which are the same for the 40 Ω/sq and 90 Ω/sq

emitters. However, as found in the previous section, the optimal resistivity is highest for the Al BSF and lowest for the ohmic contact.

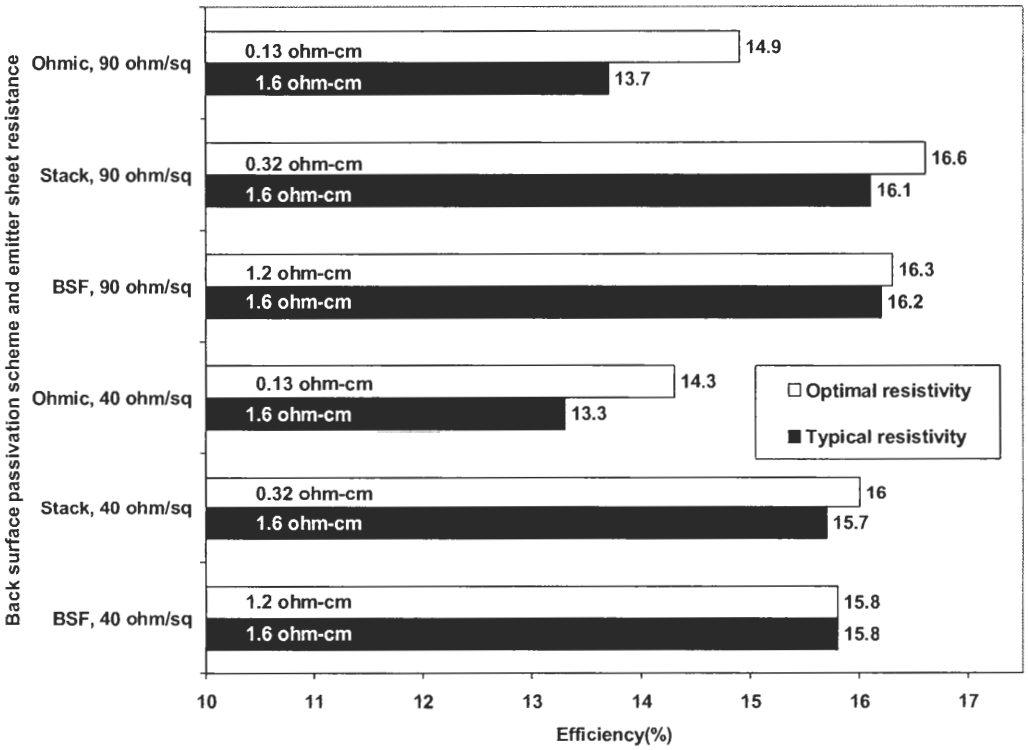

Figure 23. Efficiency of optimal resistivity and typical resistivity devices for homogeneous (40 Ω/sq) and selective (90 Ω/sq) emitter structures.

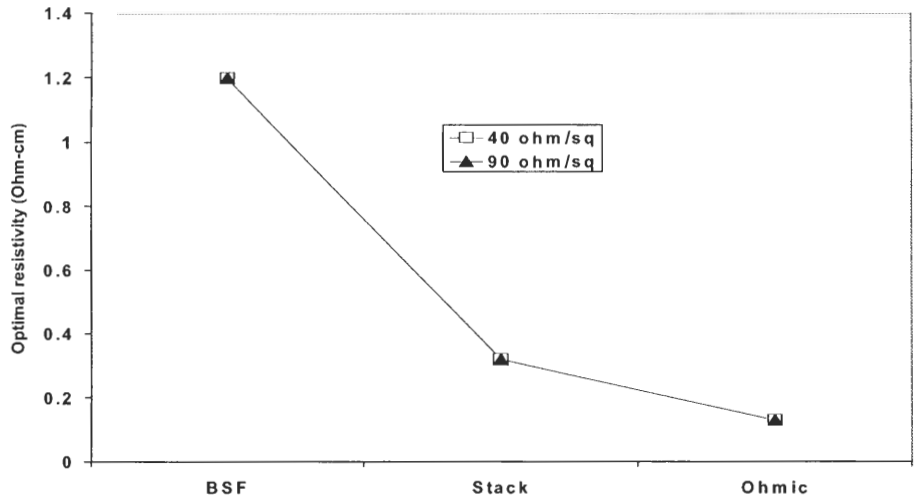

Figure 24. Optimal resistivity for both 40 ohm/sq and 90 ohm/sq emitters; for 20 μs τ_b, changing the emitter sheet resistance does not change optimal resistivity.

3.5 Impact of Dopant-Defect Interaction (N_{ref}) on Optimal Bulk Resistivity

Even though our calculations in the previous sections show optimal resistivities in the range 0.13-1.2 Ω-cm, the experience of the PV industry favors cells made on resistivities in the range of 1-3 Ω-cm for defective materials. The discrepancy is explained in this section by the doping dependence of bulk lifetime, which is not incorporated in most device simulation programs. In the above simulations, the bulk lifetime τ was assumed to be 20 μs ($\tau_{n0} = \tau_{p0} = 20$ μs) with a midgap trap. However, τ can be a function of doping level. For low-level injection, bulk lifetime is given by $\tau = \tau_{n0}(1+p_1/N_A)$. For a shallow trap, $p_1/N_A >> 1$, and τ is proportional to $1/N_A$, which would move the optimal bulk resistivity to a higher level. Since often midgap traps are the dominant lifetime killers, we have tried to simulate the dopant-defect interaction for midgap traps.

For the case of midgap traps, $p_1/N_A << 1$, and $\tau = \tau_0 \neq f(N_A)$. However, if dopants are involved in forming recombination centers and dopant-defect interaction changes the trap and N_t according to $N_t = N_t(1+N_A/N_{ref})$, then $\tau_{n0} = \tau_{p0} = \tau_{0\infty}/(1+N_A/N_{ref}) = f(N_A)$. N_{ref} is a measure of the doping-dependence of lifetime, and $\tau_{o\infty}$ is the value of τ_{no} and τ_{po} when $N_{ref} = \infty$ (no dopant-defect interaction). In these simulations, the maximum lifetime ($\tau_{0\infty}$) is still 20 μs. The optimal bulk doping level was sought in nine cases: three different back surface passivation schemes (stack passivation, unpassivated ohmic contact, and BSF) each combined with one of three values of N_{ref} (10^{99} cm^{-3}, 10^{15} cm^{-3}, and 10^{14} cm^{-3}). The N_{ref} values of 10^{15} cm^{-3} and 10^{14} cm^{-3} are in the range of

experimentally obtained values for EFG and dendritic web material [5, 53]. $N_{ref} = 10^{99}$ cm^{-3} is effectively $N_{ref} = \infty$, the case of no doping dependence of the SRH parameters. As N_{ref} is reduced, the doping dependence of τ_{no} and τ_{po} is more pronounced. N_{ref} causes these parameters to drop as doping level increases, an effect which is observed at all doping levels above roughly $N_{ref}/10$. The precise values of τ_{no} and τ_{po} are shown in Figure 25 as a function of doping level for three vales of N_{ref}. For all cells modeled in this section, thickness is 100 μm, emitter sheet resistance is 40 Ω/sq, $S_f = 52840$ cm/s, and S_b depends on the back surface passivation scheme as detailed in earlier sections. In all cases, $\tau_{o\infty} = 20$ μs. The N_{ref} equation is used simply to solve for τ_{no} and τ_{po} at every doping level to input into the PC-1D model. The results are shown in Figures 26-28. (Figure 28 is for the case of stack passivation.)

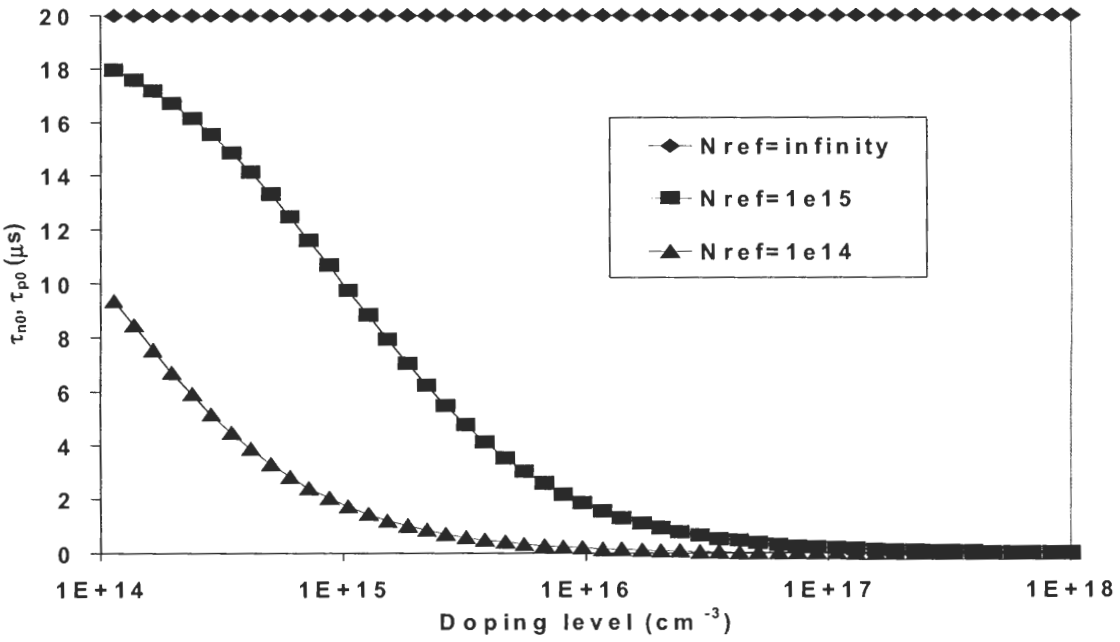

Figure 25. $\tau_{n0} = \tau_{p0}$ as a function of doping level for three values of N_{ref}.

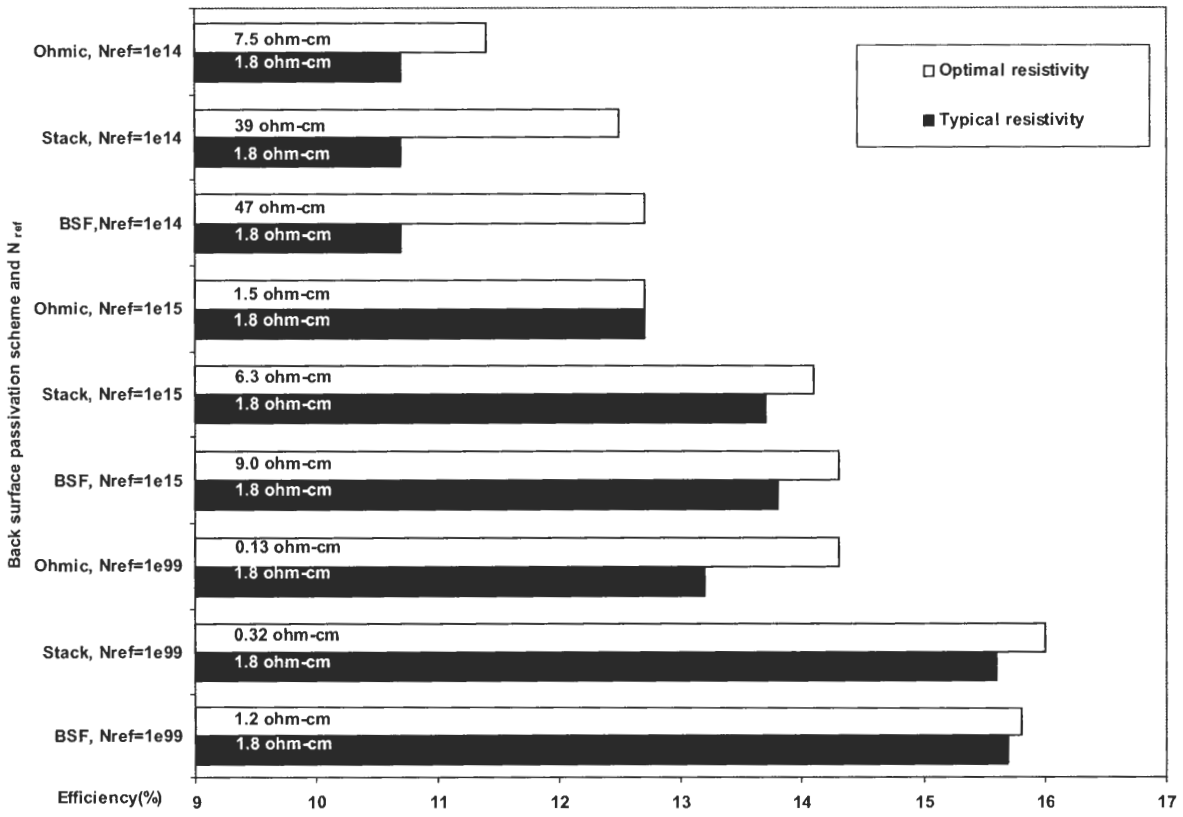

Figure 26. Impact of N_{ref} on the efficiency and optimal resistivity of screen-printed cells.

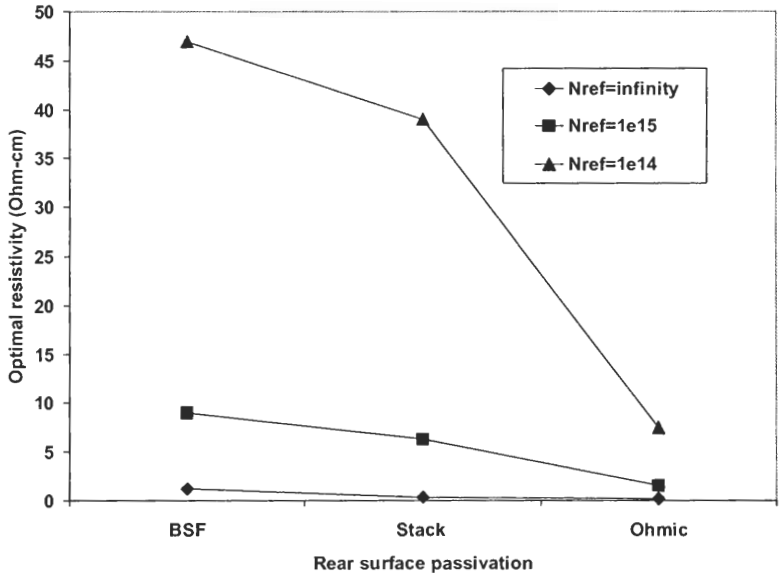

Figure 27. Optimal resistivity for three values of N_{ref} for three back surface passivation schemes. Note how optimal resistivity rises with increasing N_{ref}.

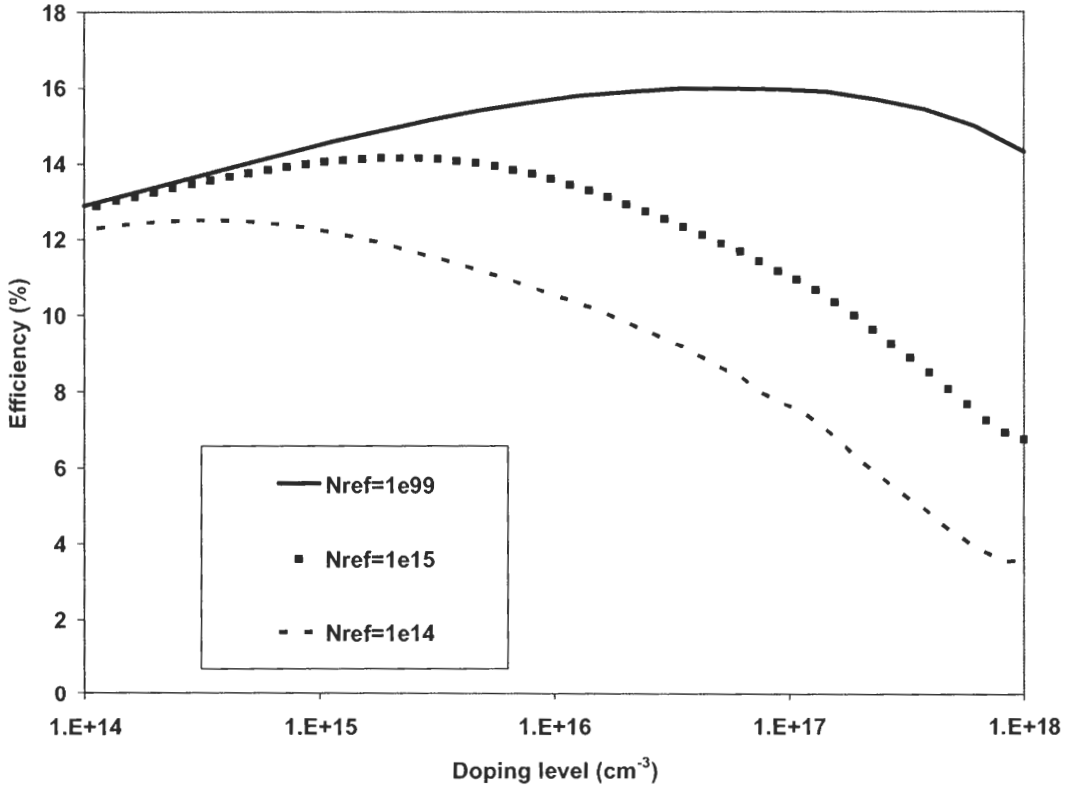

Figure 28. Efficiency vs. doping level for three levels of dopant-defect interaction, N_{ref}. This figure illustrates how a decrease in N_{ref} lowers both efficiency and optimal doping level.

Consistent with the previous calculations, the optimal bulk resistivity again tends to be greatest for the Al BSF and least for the ohmic contact. Note that as N_{ref} decreases, both efficiency and optimal doping level decrease as well. This is because lifetime decreases more rapidly at higher doping levels for lower values of N_{ref}. $N_{ref} = 10^{15}$ cm^{-3} may closely model the doping dependence of lifetime in some real materials, giving optimal resistivities of 9.0 Ω-cm for the cell with a BSF, 6.3 Ω-cm for the device given stack passivation, and 1.5 Ω-cm for the cell with very poor or no rear passivation.

3.6 Interdependence of Optimal Resistivity and Thickness

The simulation results in Figure 29 show the dependence of cell efficiency on W and N_A when τ_b and front and rear S (S_f and S_b) are assumed independent of N_A. S_b is set to 340 cm/s, representing high-quality surface passivation. The resulting optimal thickness is 100 μm, confirming the expectation that thin devices excel in this case: for low S_b, the device should be thin to take advantage of the good surface. Conversely, high S_b favors thick devices that are nearly insensitive to surfaces. In addition to W, N_A is also optimized in Figure 29. Optimal N_A here is high at 6.0×10^{16} cm^{-3}, but it would be lower if the simulation incorporated the tendency of τ_b and S to worsen with increasing doping level.

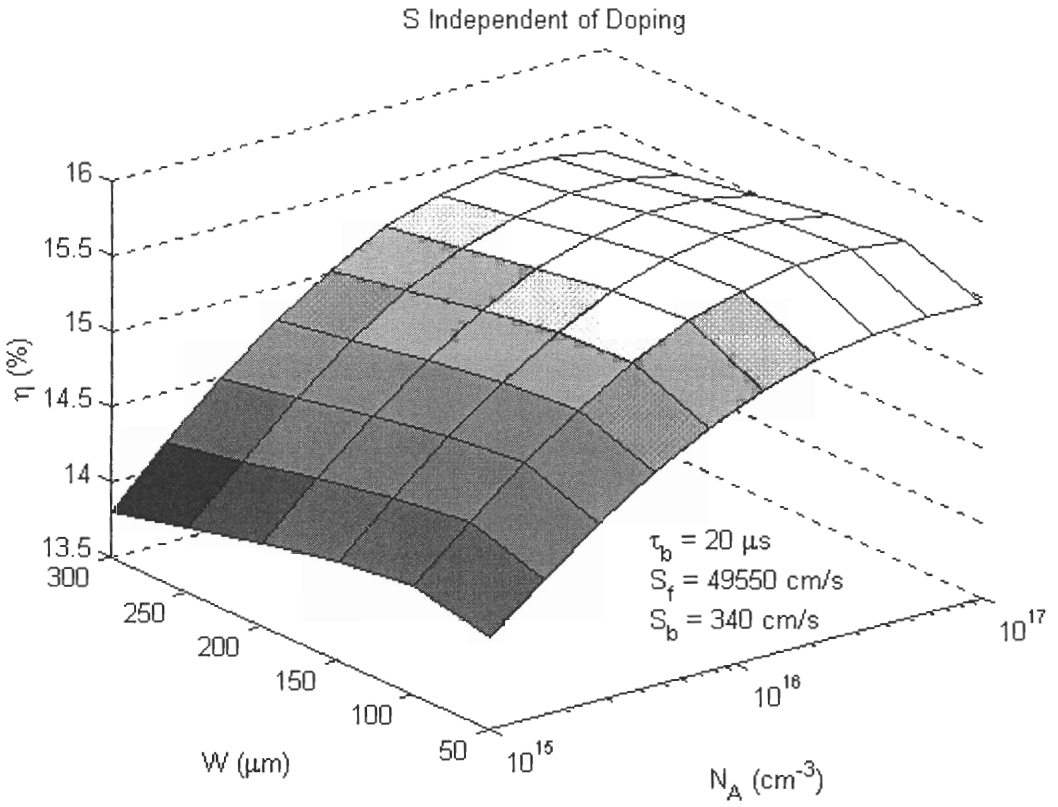

Figure 29. Simultaneous optimization of W and N_A for constant S and τ_b: W = 100 μm and $N_A = 6\times10^{16}$ cm^{-3}.

The tendency of S to worsen with increasing doping level is incorporated in Figure 30. Equation (42) is used here to be consistent with the aluminum back-surface field (BSF) [69]. Since the doping dependence of S_b favors lower N_A, the optimum is 1.3×10^{16} cm^{-3}, as opposed to 6.0×10^{16} cm^{-3} obtained for constant S_b in Figure 29. Optimal W is still 100 μm because S at moderate doping levels is still good. Finally, Figure 31 shows the results obtained when using a linear model for S_b, which may be appropriate for dielectric surface passivation [37]. In this case, optimal W and N_A are heavily interdependent. For low N_A, thin cells benefit most from the low S_b and perform best. For high N_A, S_b is very high, and optimal W is large to escape the effects of the poorly passivated surface (Figure 31). In fact, for this particular S_b model, optimal W is greater than 300 μm. In contrast, Figures 29 and 30 both indicate W = 100 μm. Thus,

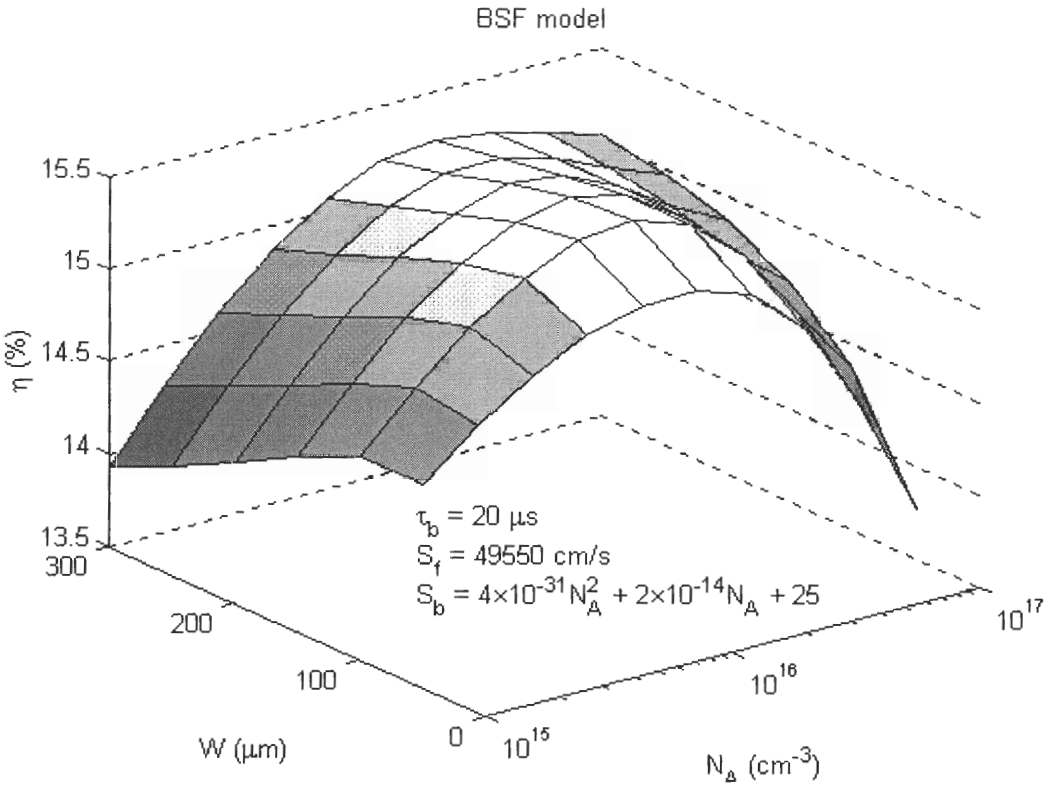

Figure 30. Simultaneous optimization of W and N_A for Al BSF: W = 100 μm and $N_A = 1.3\times10^{16}$ cm^{-3}.

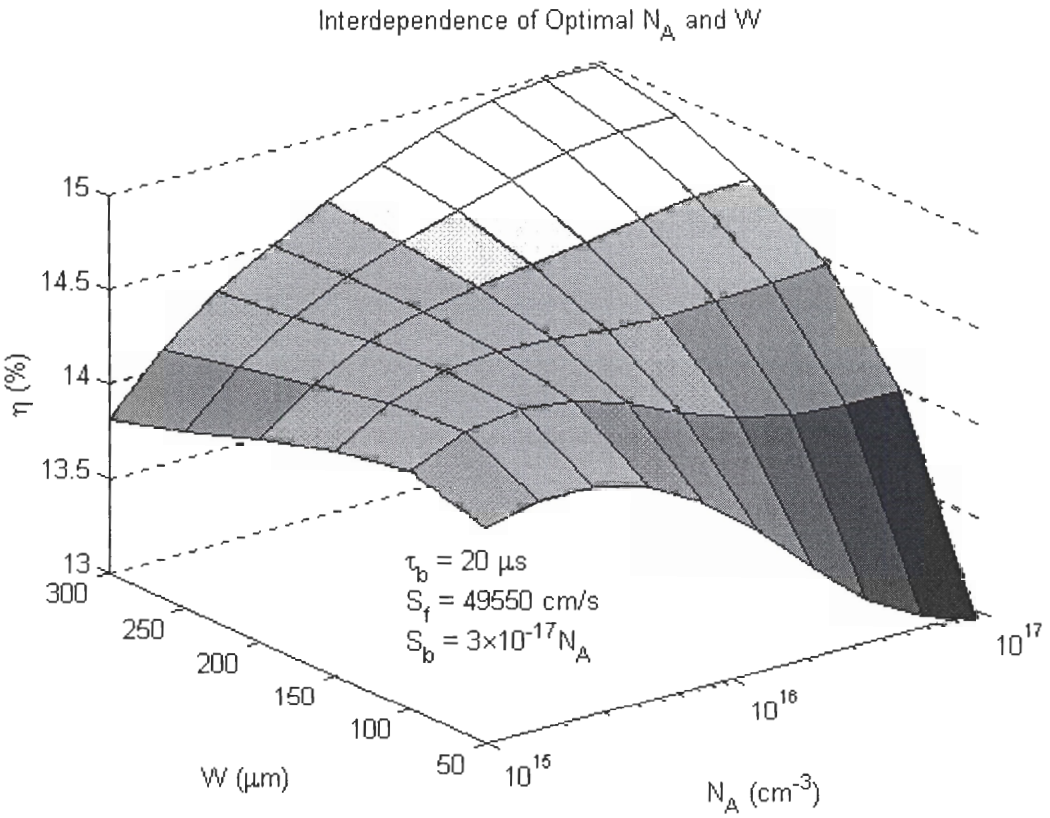

Figure 31. Interdependence of optimal W and N_A for S linearly dependent on N_A.

the model used for the doping dependence of S_b critically influences optimal W as well as optimal N_A.

3.7 Conclusions

This chapter uses extensive τ_b and device modeling to understand the impact of the doping dependence of lifetime and surface recombination velocity on optimal base doping, optimal thickness, and cell performance. It shows that a combination of informed understanding and cost-effective implementation of several advanced design features is required to achieve 17-18% efficient cells on low-cost PV material, even with

a bulk lifetime of 20 μs. Detailed model calculations were performed to show that optimal bulk resistivity varies considerably as a function of back surface passivation quality, thickness, emitter sheet resistance, and the degree of dopant-defect interaction, N_{ref}. In all cases, the optimal resistivity for a device with a BSF is greater than that for a device with rear stack passivation, and a device with no rear surface passivation at all has an even lower optimal resistivity (<0.5 Ω-cm in the absence of dopant-defect interaction). The optimal resistivity is greatest in the BSF case, because S_b due to a BSF increases greatly as resistivity decreases. Devices with unpassivated rear ohmic contacts need the lowest resistivity substrates because J_{oe} is highest for these cells, and the improvement in J_{ob} as doping level increases remains significant at higher doping levels. Finally, it was shown that dopant-defect interaction, which is observed in most low-cost PV grade materials and modeled through finite values of N_{ref}, reduces efficiency and pushes optimal bulk resistivities to higher values.

The motivation for the remaining research is to replace some of the arbitrary assumptions used in these simulations with experimentally obtained values. Specifically, the S = 340 cm/s value used here for stack passivation was measured only on float zone silicon, and only on 0.65 Ω-cm material [29]. Experimental data is needed to replace this value with measured S values for various resistivities of string ribbon and cast multicrystalline silicon. Additionally, τ_b must be measured as a function of resistivity for these materials to determine if the N_{ref} equation fits the measured lifetimes, and if so, what N_{ref} value should be used.

CHAPTER 4

UNDERSTANDING AND ESTABLISHMENT OF GENERAL AND STEADY-STATE RELATIONSHIPS AMONG τ_{eff}, S, AND τ_b FOR THE EVALUATION OF THE ACCURACY OF APPROXIMATE EXPRESSIONS

Photoconductance measurements are commonly used to characterize silicon materials. The measurement most readily yields τ_{eff}, which depends on both S and τ_b. Thus the relationship among τ_{eff}, τ_b, and S is crucial to the analysis of photoconductance measurements because τ_b and S are the quantities of interest. As discussed in Chapter 2, approximate equations derived assuming either impulse generation or uniform carrier concentration are typically cited in the literature. To evaluate the accuracy of these equations, the continuity equation is solved exactly in this chapter for a wafer illuminated by a flash lamp of arbitrary spectral content.

4.1 Solving the Continuity Equation for a Wafer Illuminated by a Flash Lamp of Arbitrary Spectral Content

The continuity equation governing excess minority carrier concentration (Δn) in a semiconductor wafer is as follows [12, 17]:

$$\frac{\partial \Delta n}{\partial t} = D\frac{\partial^2 \Delta n}{\partial x^2} - \frac{\Delta n}{\tau_b} + G(x,t), \tag{43}$$

with the boundary conditions at the surfaces (±W/2)

$$D\frac{\partial \Delta n(-W/2,t)}{\partial x} = S \times \Delta n(-\frac{W}{2},t) \tag{44.a}$$

and

$$-D\frac{\partial n(W/2,t)}{\partial x} = S \times \Delta n(\frac{W}{2},t), \tag{44.b}$$

when surface recombination velocity (S) is the same on both sides of the wafer. Although τ_b is a function of position in mc-Si, Equation (43) can only be solved analytically if τ_b is considered a local constant throughout the measured region. In fact, it is common to neglect any variation in τ_b over the thickness of mc-Si wafers when performing lifetime mapping [70, 71]. This is not unreasonable since grain boundaries are generally perpendicular to the surfaces, and lifetime variation within a grain is expected to be minimal.

Luke and Cheng [17] solved Equation (43) for $\Delta n(x,t)$ for the case of a delta function generation rate, thus eliminating G from the equation for $t > 0$. This approximates a transient PCD measurement. At the other extreme, Cuevas and Sinton [18] solved Equation (43) for uniform and steady state generation, when the time derivative is zero. This approximates a long-wavelength QSSPC measurement. However, if the illumination is of an intermediate duration, neither the assumption of $G = 0$ nor $d\Delta n/dt = 0$ is appropriate.

In order to explore measurements with intermediate lamp time constants, Equation (43) with boundary conditions given by Equations (44) will be solved exactly for $\Delta n(x,t)$, assuming neither delta function illumination nor steady-state illumination. As

exponentially decaying illumination is a good approximation for the light generated by flash lamps frequently used in lifetime measurements [12], G can be expressed as [17]

$$G(x,t) = \left[ke^{-\alpha x} + kRe^{\alpha(x-W)}\right]e^{-t/\tau_f}, \tag{45}$$

where τ_f is the decay time constant of the flash lamp, α is the absorption coefficient, R is the reflectance (assumed identical on both sides), and k is determined (by considering an infinite series of reflections from surface to surface) to be [17]

$$k \equiv \frac{N_{ph}\alpha(1-R)e^{-\alpha W/2}}{1-(Re^{-\alpha W})^2}. \tag{46}$$

N_{ph} is the initial photon flux, measured in units per square centimeter per second. (For convenience we make a number of notational modifications to Luke and Cheng's work [17], in which an impulse function is used instead of time-dependent generation.) The single value of α in Equations (45-46) implies monochromatic illumination. Later we will explain how to extend the analysis to illumination by a full spectrum of light.

Let the initial condition be equilibrium: excess carrier concentration $\Delta n(x,0)=0$. The expression for $\Delta n(x,t)$ may be obtained either by convolving Luke and Cheng's impulse response with the normalized generation time dependence [17], or by following the steps outlined below and detailed in Appendix A. First we take the Laplace transform of Equation (43), using Equations (45) and (46) for G(x,t):

$$s\overline{\Delta n} = D\frac{d^2\overline{\Delta n}}{dx^2} - \frac{\overline{\Delta n}}{\tau_b} + \frac{ke^{-\alpha x} + kRe^{\alpha(x-W)}}{s+1/\tau_f}. \tag{47}$$

We also take the Laplace transform of the boundary conditions, Equation (44):

$$\pm D\frac{\partial\overline{\Delta n}(\mp W/2,s)}{\partial x} = S\overline{\Delta n}(\mp\frac{W}{2},s). \tag{48}$$

Equation (47) is an ordinary differential equation in x whose solution is

$$\overline{\Delta n}(x,s)$$

$$= -\frac{\cosh\left[\left(\frac{s+1/\tau_b}{D}\right)^{1/2}x\right]\left[D\alpha\sinh\left(\frac{\alpha W}{2}\right)+S\cosh\left(\frac{\alpha W}{2}\right)\right]k(1+Re^{-\alpha W})}{\left(s+\frac{1}{\tau_f}\right)\left(s+\frac{1}{\tau_b}-D\alpha^2\right)\left\{D\left(\frac{s+1/\tau_b}{D}\right)^{1/2}\sinh\left[\left(\frac{s+1/\tau_b}{D}\right)^{1/2}\frac{W}{2}\right]+S\cosh\left[\left(\frac{s+1/\tau_b}{D}\right)^{1/2}\frac{W}{2}\right]\right\}}$$

$$+\frac{\sinh\left[\left(\frac{s+1/\tau_b}{D}\right)^{1/2}x\right]\left[D\alpha\cosh\left(\frac{\alpha W}{2}\right)+S\sinh\left(\frac{\alpha W}{2}\right)\right]k(1-Re^{-\alpha W})}{\left(s+\frac{1}{\tau_f}\right)\left(s+\frac{1}{\tau_b}-D\alpha^2\right)\left\{D\left(\frac{s+1/\tau_b}{D}\right)^{1/2}\cosh\left[\left(\frac{s+1/\tau_b}{D}\right)^{1/2}\frac{W}{2}\right]+S\sinh\left[\left(\frac{s+1/\tau_b}{D}\right)^{1/2}\frac{W}{2}\right]\right\}}$$

$$+\frac{ke^{-\alpha x}+kRe^{\alpha(x-W)}}{\left(s+\frac{1}{\tau_f}\right)\left(s+\frac{1}{\tau_b}-D\alpha^2\right)} \qquad (49)$$

after applying the boundary conditions, Equation (48). The inverse transform of the third term of Equation (49) may be found in a table [72]. The inverse transform of the first two terms in Equation (49) may be obtained by using the expansion theorem [72]

$$f(t)=L^{-1}\left[\frac{\varphi(s)}{\psi(s)}\right]=\sum_{n=1}^{\infty}\frac{\varphi(s_n)}{\psi'(s_n)}e^{s_n t}\,, \qquad (50)$$

which is valid whenever the Taylor series expansion

$$\frac{\varphi(s)}{\psi(s)}=\frac{A_0+A_1 s+A_2 s^2+\cdots}{B_0+B_1 s+B_2 s^2+\cdots} \qquad (51)$$

is such that $A_0 \neq 0$ and $B_0 = 0$. The first two terms of Equation (49) can be put in a suitable form by factoring out $(s+1/\tau_f)$ and using the shifting property to write the inverse Laplace transform of $\overline{n}(x,s-1/\tau_b+D\alpha^2)$ in terms of $\Delta n(x,t)$. The complete solution is eventually obtained as

$$\Delta n(x,t)$$

$$= \sum_{i=1}^{\infty} \frac{k(1+Re^{-\alpha W})\cos\left(\frac{2\mu_i x}{W}\right)\left[D\alpha\sinh\left(\frac{\alpha W}{2}\right)+S\cosh\left(\frac{\alpha W}{2}\right)\right]\left(e^{-4D\mu_i^2 t/W^2 - t/\tau_b} - e^{-t/\tau_f}\right)}{\left(\frac{1}{\tau_f}-\frac{1}{\tau_b}-\frac{4D\mu_i^2}{W^2}\right)\left(\frac{\mu_i}{2}+\frac{W^2\alpha^2}{8\mu_i}\right)\left(\frac{2D\mu_i}{W}\cos\mu_i+\left(S+\frac{2D}{W}\right)\sin\mu_i\right)}$$

$$+ \sum_{i=1}^{\infty} \frac{k(1-Re^{-\alpha W})\sin\left(\frac{2\nu_i x}{W}\right)\left[D\alpha\cosh\left(\frac{\alpha W}{2}\right)+S\sinh\left(\frac{\alpha W}{2}\right)\right]\left(e^{-4D\nu_i^2 t/W^2 - t/\tau_b} - e^{-t/\tau_f}\right)}{\left(\frac{1}{\tau_f}-\frac{1}{\tau_b}-\frac{4D\nu_i^2}{W^2}\right)\left(\frac{\nu_i}{2}+\frac{W^2\alpha^2}{8\nu_i}\right)\left(-\frac{2D\nu_i}{W}\sin\nu_i+\left(S+\frac{2D}{W}\right)\cos\nu_i\right)} \tag{52}$$

where μ_i and ν_i are the positive roots (which must be computed numerically) of

$$\cot\mu = \frac{2D}{WS}\mu \tag{53.a}$$

and

$$\tan\nu = -\frac{2D}{WS}\nu\,. \tag{53.b}$$

Equation (52) may be used to represent $\Delta n(x,t)$ for any flash decay time τ_f, ranging from a very short flash approaching a delta function to a very long flash approaching steady state. In order to extend Equation (52) to the case of illumination by a spectrum of wavelengths, simply sum the solutions obtained for all values of λ, each with a corresponding value of α, N_{ph} and R. This process can be represented by the equation

$$\Delta n(x,t) = \sum_{\lambda} \Delta n(x,t,\lambda)\,, \tag{54}$$

where the $\Delta n(x,t,\lambda)$ are given by Equation (52). The validity of Equation (54) is demonstrated in Appendix A.

Equation (52) may be modified to accommodate large values of α that cause $\cosh(\alpha W/2)$ and $\sinh(\alpha W/2)$ to exceed 10^{100}. In these cases, computation is facilitated by

replacing $\cosh(\alpha W/2)$ and $\sinh(\alpha W/2)$ with $e^{\alpha W/2}/2$, which then cancels with the $e^{-\alpha W/2}$ term in k.

The infinite series in Equation (52) may be truncated with less than one percent error after a small number of terms, often 5-40. Rapid convergence occurs because the numerators in Equation (52) decay exponentially with μ_n^2 (or ν_n^2), and the denominators become proportional to μ_n^4 (or ν_n^4) when μ_n (or ν_n) is large. The convergence of Equation (52) is slower when larger values of μ_n (or ν_n) are needed to make the denominators approach a multiple of μ_n^4 (or ν_n^4). The conditions for slow convergence may be described by examining each of the three factors in the denominators of Equation (52). The first factor in each denominator is less rapidly dominated by the μ_n^2 (or ν_n^2) term when the difference $(1/\tau_f - 1/\tau_b)$ is large; this occurs when τ_f and τ_b are significantly different from each other, and one is very small. The second factor in the denominator is less rapidly dominated by its first term when α is large. (W is assumed not to vary over orders of magnitude for cases of practical interest.) Finally, the third factor in the denominator is less rapidly dominated by its first term when S is high. A worst case scenario of low τ_b (with high τ_f), high α, and high S is shown in Figure 32, where 200 terms are required to obtain a reasonably smooth excess carrier concentration. Lowering α from 25500 cm^{-1} to 2050 cm^{-1} results in Figure 33, where convergence occurs within 40 terms. At still lower values of α, convergence is more rapid, often within several terms. Similarly, lower values of S and higher values of τ_b (with high τ_f) produce quicker convergence, even at high values of α.

The carrier concentration $\Delta n(x,t)$ obtained from Equation (52) is averaged over the thickness of the wafer to obtain $\Delta n_{av}(t)$ for use in Equation (10). The computation of

Δn_{av} may be done either analytically, by integrating Equation (52) over the thickness of the wafer, or numerically, by averaging $\Delta n(x,t)$ over a sufficiently large number of equally spaced points between -W/2 and W/2. The derivative $d\Delta n_{av}/dt$, also needed in Equation (10), can be computed from the resulting n_{av}. Thus Equation (10) can be used to determine the τ_{eff} that would be obtained in a measurement for a given set of parameters, including time t. The τ_{eff} values thus obtained may be compared with the simple Equation (21), regardless of the S, τ_b, and τ_f values. This procedure is illustrated in Figure 34.

We will now demonstrate that the general condition under which the widely used Equation (21) is valid, assuming constant τ_b and identical S on both surfaces, is that

$$\Delta n_{av} = \frac{\Delta n(-W/2) + \Delta n(W/2)}{2}, \tag{55}$$

which means that the average of the excess carrier concentration over the whole wafer must equal the average of the excess carrier concentration at the surfaces. This is different from the conventional wisdom that Equation (21) is valid only when the excess carrier concentration is approximately uniform. It is known that the most general expression for τ_{eff} is [12]

$$\frac{\Delta n_{av}}{\tau_{eff}} = \frac{1}{W}\left[\int_{-W/2}^{W/2} \frac{\Delta n(x)}{\tau_b(\Delta n)}\,dx + S_{front}\Delta n(-W/2) + S_{back}\Delta n(W/2)\right]. \tag{56}$$

When τ_b is independent of injection level and S is the same on each surface, Equation (56) reduces to

$$\frac{\Delta n_{av}}{\tau_{eff}} = \frac{\Delta n_{av}}{\tau_b} + \frac{S[\Delta n(-W/2) + \Delta n(W/2)]}{W}. \tag{57}$$

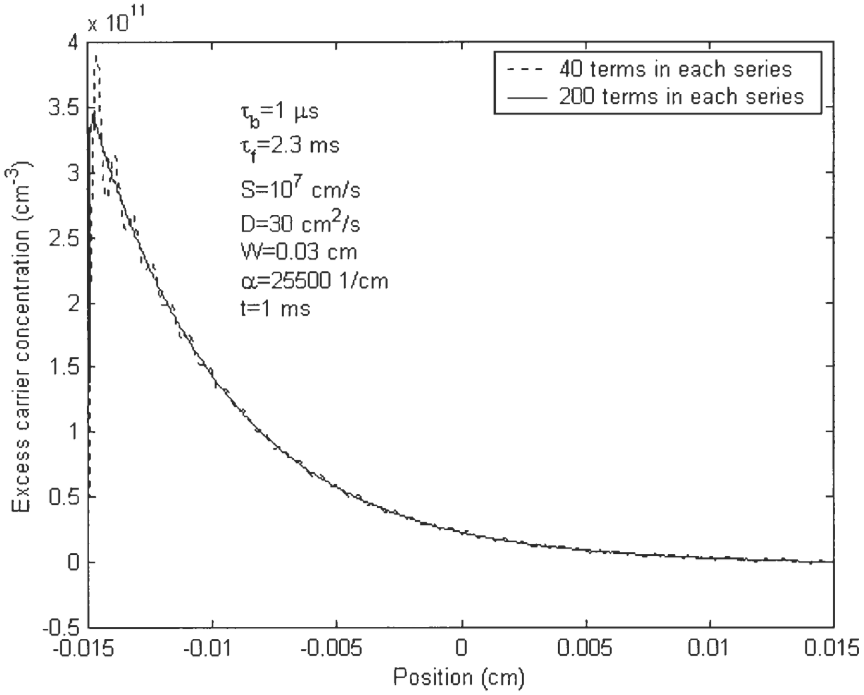

Figure 32. Theoretical calculations to show the convergence of Equation (52) using the first 40 and 200 terms for a wafer illuminated by 450 nm light. The convergence of Equation (52) is slowest when large values of μ_n are needed to make the denominator approach a multiple of μ_n^4, and this figure represents a worst case scenario of low τ_b (with high τ_f), high α, and high S.

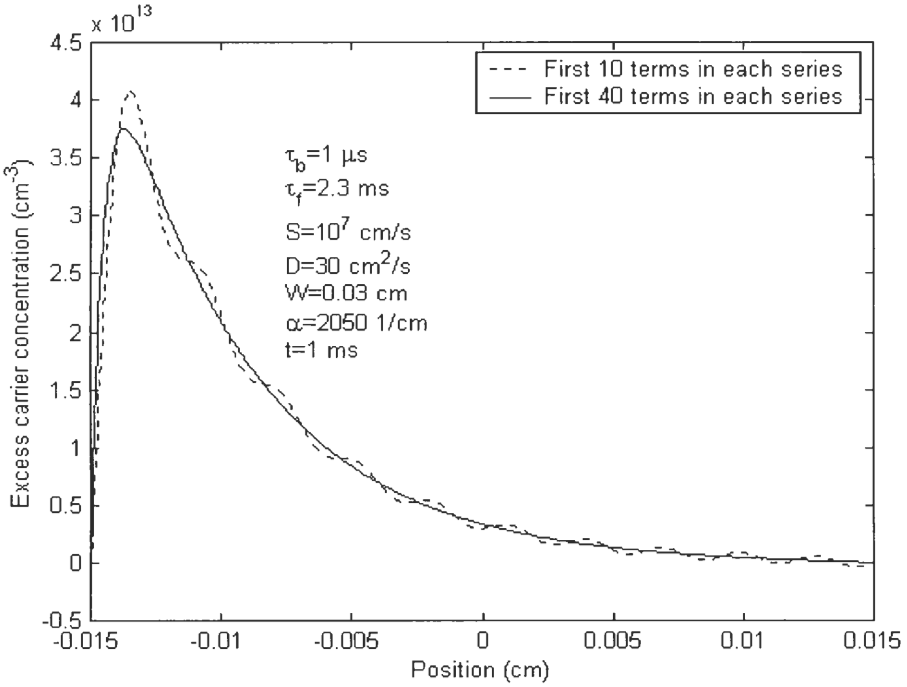

Figure 33. Convergence of Equation (52) for unpassivated wafer illuminated by 690 nm light. Addition of terms after the fortieth term in each series does not significantly change the result.

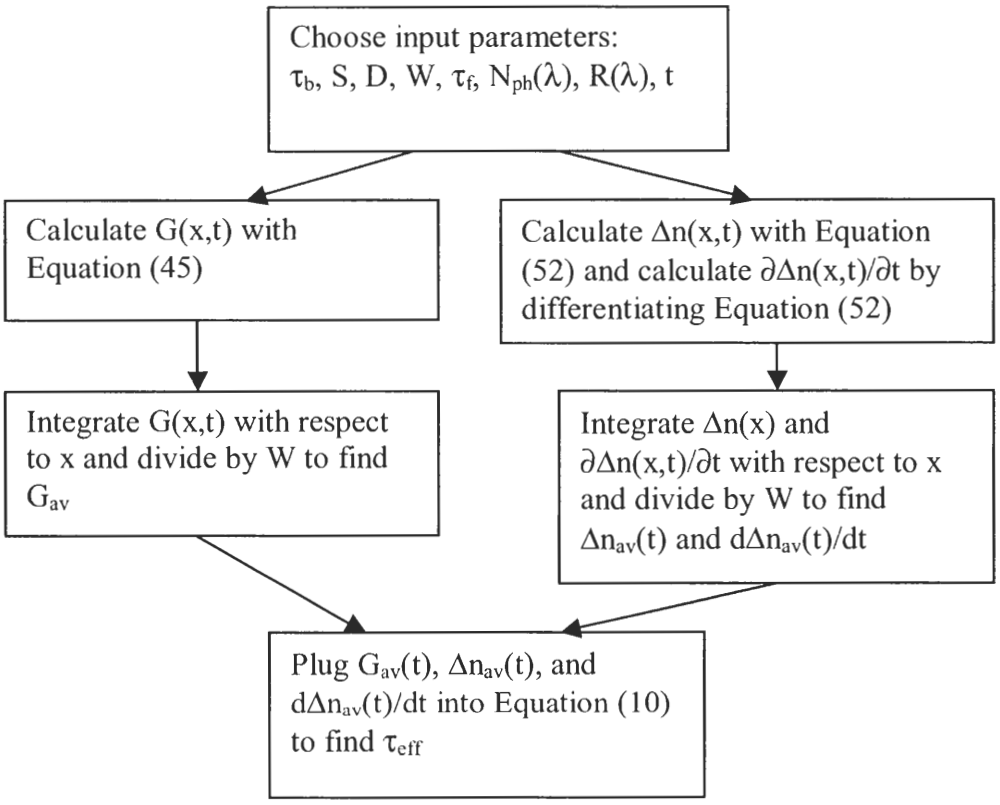

Figure 34. Demonstration of the use of Equation (52) to calculate τ_{eff}.

It is obvious that Equation (57) becomes Equation (21) when Equation (55) is valid. A special case that satisfies Equation (55) is uniform carrier concentration, which approximately occurs for low S, specifically $S < D/4W$ for transient illumination [16]. This case of low S is the only situation permitting the use of Equation (21) recognized in the literature and represented as curve A in Figure 35. However, another excess carrier profile that satisfies Equation (55) is a diagonal line, curve B, also shown in Figure 35. Curve C, though not linear, also satisfies Equation (55) within 3%; this result is obtained by using Equation (52) to determine $\Delta n(x,t)$, at t = 1 ms, for insertion in Equation (55). In curve C, the droop caused by very high S at the illuminated surface compensates for

the droop caused by low τ_b throughout the bulk and results in the satisfaction of Equation (55). Thus Equation (21), valid whenever Equation (55) is satisfied, is not restricted to the case of uniform carrier concentration, in contrast with the prevailing view in the literature. The excess carrier concentrations plotted in Figure 35 were obtained for non-uniform though monochromatic 700 nm wavelength generation. In subsequent sections, the full spectrum of the Qflash T2 flash lamp is used, based on measurements at the National Renewable Energy Lab.

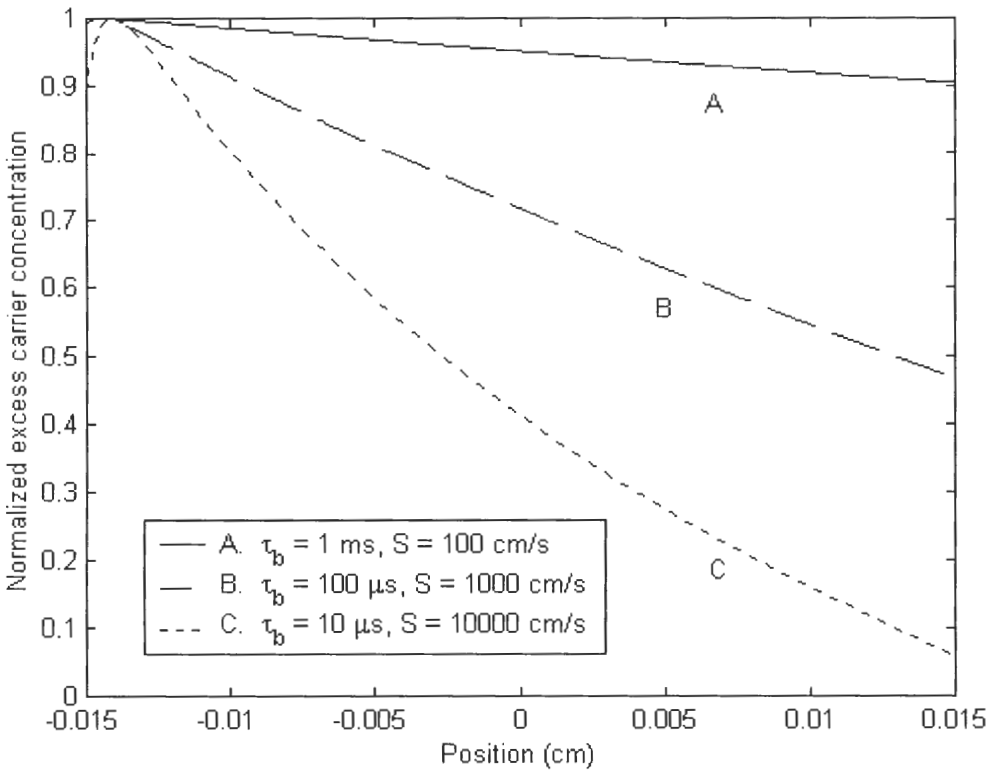

Figure 35. Three excess carrier profiles that satisfy Equation (55) within 3%, thereby permitting the use of Equation (21). These profiles were obtained using Equation (52) with τ_f = 2.3 ms (QSSPC), 700 nm wavelength illumination, W = 0.03 cm, D = 30 cm^2s^{-1}, and t = 1 ms after the onset of illumination.

4.2 Derivation of the Steady-State Relationship among τ_{eff}, τ_b, and S

Investigators frequently make lifetime measurements that satisfy quasi-steady-state conditions: $\tau_f >> \tau_{eff}$. In fact, these are the conditions most frequently encountered when working with low-cost, solar-grade materials. Surprisingly, until now researchers have used Equation (21) or other equations derived assuming transient, high-lifetime conditions, although an equation derived assuming steady-state conditions would presumably be more accurate and useful. The steady-state relationship among S, τ_b, and τ_{eff} has not appeared in the literature. We therefore must derive the steady-state relationship among S, τ_b, and τ_{eff} for illumination of arbitrary spectral content. The resulting expressions are implicitly applied in [7], yet not present in the literature.

The steady-state continuity equation [7], with $\partial\Delta n/\partial t = 0$, is

$$G(x) + D\frac{d^2\Delta n(x)}{dx^2} - \frac{\Delta n(x)}{\tau_b} = 0, \tag{58}$$

where D is the diffusion coefficient and n is the excess carrier concentration. The boundary conditions are again

$$Surface\ flux = \mp D\frac{d\Delta n(x)}{dx}\Big|_{x=\pm W/2} = S \times \Delta n(\pm W/2), \tag{59}$$

where W is the wafer thickness, and identical S on both surfaces is assumed. The generation rate in Equation (58) is an integral over all wavelengths, in principle. However, we represent it as a sum, because in practice the photon flux is measured at discrete intervals [7, 17]:

$$G(x) = \sum_{\lambda}\left[c_1(\lambda)e^{-\alpha(\lambda)x} + c_2(\lambda)e^{\alpha(\lambda)x}\right], \tag{60}$$

where $\alpha(\lambda)$ is the absorption coefficient, and k in Equations (45) and (46) has been rewritten to make the wavelength dependence explicit:

$$c_1(\lambda) \equiv k = \frac{N_{ph}(\lambda)\alpha(\lambda)[1-R(\lambda)](e^{-\alpha(\lambda)W/2})}{1-[R(\lambda)e^{-\alpha(\lambda)W}]^2} \tag{61}$$

and

$$c_2(\lambda) = c_1(\lambda)R(\lambda)e^{-\alpha(\lambda)W}, \tag{62}$$

where $N_{ph}(\lambda)$ is the photon flux, and $R(\lambda)$ is the reflectance.

The solution to the differential Equation (58) is

$$\Delta n(x) = A\cosh\left(\frac{x}{L}\right) + B\sinh\left(\frac{x}{L}\right) + \sum_{\lambda}\left[\frac{c_1(\lambda)e^{-\alpha(\lambda)x}}{1/\tau_b - D\alpha(\lambda)^2} + \frac{c_2(\lambda)e^{\alpha(\lambda)x}}{1/\tau_b - D\alpha(\lambda)^2}\right], \tag{63}$$

where $L = (D\tau_b)^{1/2}$,

$$A = -\frac{\sum_{\lambda}\frac{[c_1(\lambda)+c_2(\lambda)]\{D\alpha(\lambda)\sinh[\alpha(\lambda)W/2]+S\cosh[\alpha(\lambda)W/2]\}}{1/\tau_b - D\alpha(\lambda)^2}}{S\cosh(W/2L)+(D/L)\sinh(W/2L)}, \tag{64}$$

and

$$B = \frac{\sum_{\lambda}\frac{[c_1(\lambda)-c_2(\lambda)]\{D\alpha(\lambda)\cosh[\alpha(\lambda)W/2]+S\sinh[\alpha(\lambda)W/2]\}}{1/\tau_b - D\alpha(\lambda)^2}}{S\sinh(W/2L)+(D/L)\cosh(W/2L)}. \tag{65}$$

Using $\tau_{eff} = n_{av}/G_{av}$ [13], we find τ_{eff} in terms of S and τ_b:

$$\tau_{eff} = \frac{AL\sinh(W/2L)+\sum_{\lambda}\frac{[c_1(\lambda)+c_2(\lambda)]\sinh[\alpha(\lambda)W/2]/\alpha(\lambda)}{1/\tau_b - D\alpha(\lambda)^2}}{\sum_{\lambda}[c_1(\lambda)+c_2(\lambda)]\sinh[\alpha(\lambda)W/2]/\alpha(\lambda)}. \tag{66}$$

S enters into Equation (66) through A. Upon rearrangement, S may be obtained:

$$S = \frac{-L\sinh(\frac{W}{2L})\Sigma_1 + \frac{D}{L}\sinh(\frac{W}{2L})\Sigma_2 - WG_{av}\tau_{eff}D\sinh(\frac{W}{2L})/(2L)}{WG_{av}\tau_{eff}\cosh(\frac{W}{2L})/2 + L\sinh(\frac{W}{2L})\Sigma_3 - \cosh(\frac{W}{2L})\Sigma_2}, \quad (67)$$

where

$$\Sigma_1 = \sum_{\lambda}\frac{[c_1(\lambda)+c_2(\lambda)]D\alpha(\lambda)\sinh[\alpha(\lambda)W/2]}{1/\tau_b - D\alpha(\lambda)^2}, \quad (68)$$

$$\Sigma_2 = \sum_{\lambda}\frac{[c_1(\lambda)+c_2(\lambda)]\sinh[\alpha(\lambda)W/2]/\alpha(\lambda)}{1/\tau_b - D\alpha(\lambda)^2}, \quad (69)$$

$$\Sigma_3 = \sum_{\lambda}\frac{[c_1(\lambda)+c_2(\lambda)]\cosh[\alpha(\lambda)W/2]}{1/\tau_b - D\alpha(\lambda)^2}, \quad (70)$$

and

$$G_{av} = (2/W)\sum_{\lambda}[c_1(\lambda)+c_2(\lambda)]\sinh[\alpha(\lambda)W/2]/\alpha(\lambda). \quad (71)$$

Equation (67) is useful for plotting S vs. τ_b for measured values of τ_{eff}.

4.3 Comparison of General Equation with Steady-State Equation and Widely Used Approximations To Evaluate Their Accuracy

The general equation, Equation (52), is used to evaluate the accuracy of the three approximate equations: Equation (67) derived in this research assuming steady-state conditions, Equation (22) derived assuming transient conditions [17], and the simple equation, Equation (21) [16]. In Equation (52), τ_f was set either to 2.3 ms to represent slowly decaying light intensity, or to 18 μs to represent the brief pulse. The other parameters chosen were t = 2.3 ms if τ_f = 2.3 ms, t = 50 μs if τ_f = 18 μs, W = 300 μm, D = 30 cm^2s^{-1}, R = 0, and the spectrum of the Qflash T2 lamp. S vs. τ_{eff} was plotted using

all four equations for both τ_b = 1 μs and τ_b = 1 ms, representing the lowest and highest values typically encountered.

Results for τ_b = 1 μs are shown in Figure 36. As expected, the steady-state approximation, Equation (67), conforms exactly to the general equation, since the steady-state assumption is valid in this very low-lifetime case. Even for the brief light pulse τ_f = 18 μs, the steady-state assumption appears to be excellent, because $\tau_{eff} < \tau_f$. The simple equation, Equation (21), is about 100% too high over nearly the entire S range of interest, and the transient equation is worthless in these conditions.

In Figure 37, τ_b = 1 ms. The steady-state approximation remains in agreement with the general equation, even for τ_{eff} approaching 1 ms. In general, the steady-state equation, Equation (67), is found to be an excellent substitute for the general equation when τ_f = 2.3 ms and to a lesser extent when τ_f = 18 μs, over the entire range of τ_{eff} possible. The advantages of Equation (67), derived in this research, relative to the general equation are that Equation (67) has no infinite sum to truncate and no transcendental equations to solve. In Figure 37, the various equations converge for $\tau_{eff} >$ 20 μs, which is generally true [14]. This fact leads to the unexpected conclusion that Equation (67), though derived assuming steady-state conditions, is accurate even under transient conditions. Thus any equation may be used if $\tau_{eff} > 20$ μs, but for $\tau_{eff} < 10$ μs, Equation (67) must be used to avoid errors that can exceed 100%.

As seen in Figures 36 and 37, the various equations diverge the most dramatically at low τ_b and high S. Thus to best illustrate the importance of choosing the valid equation, an unpassivated string ribbon wafer was chosen. Under a slowly decaying light pulse (τ_f = 2.3 ms), τ_{eff} was measured to be 0.48 μs. Next τ_b was estimated by measuring

τ_{eff} after immersing the wafer in a passivating iodine/methanol solution [21]. τ_b was thereby determined to be 3.4 μs.

With τ_{eff} = 0.48 μs, τ_b = 3.4 μs, D = 27 cm^2s^{-1}, W = 0.021 cm, R(λ) of bare silicon, and the spectral content of the Qflash T2 lamp, S was calculated from each of Equations (67), (22), and (21). Equation (67), the steady-state equation, gave S = 1.4×10^5 cm/s. Since quasi-steady-state conditions are very well satisfied, this is the correct result, confirmed by the general solution Equation (52). Equation (22), the

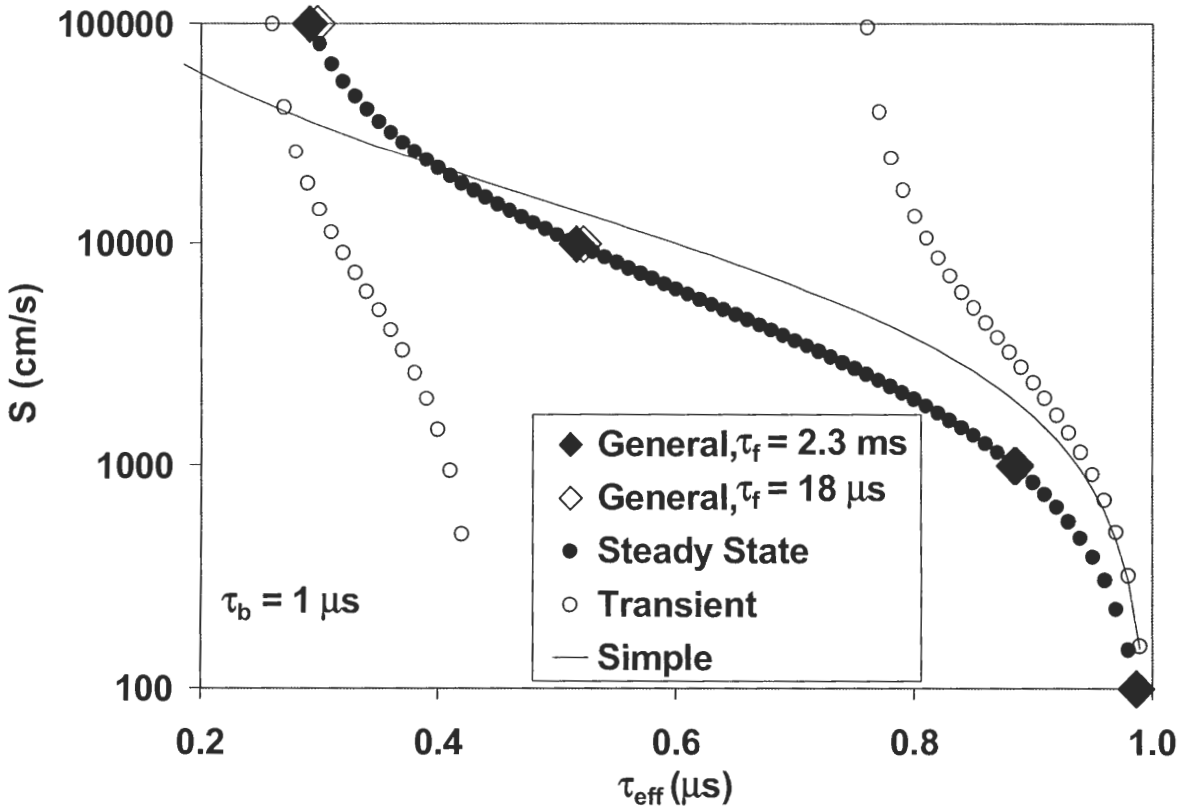

Figure 36. Comparison of the three approximate equations with the general equation, in which t = 2.3 ms if τ_f = 2.3 ms, and t = 50 μs if τ_f = 18 μs. The spectrum of the Qflash T2 lamp was used. Other parameters were τ_b = 1 μs, W = 300 μm, D = 30 cm^2s^{-1}, and R = 0.

transient equation, gave S = -3500 cm/s. As expected, this is meaningless, since the assumption of impulse generation leading to Equation (22) is not valid in this case. Equation (21), the simple equation, gave S = 19000 cm/s, which is an order of magnitude too low. This demonstrates the importance of using Equation (67) when τ_{eff} is low.

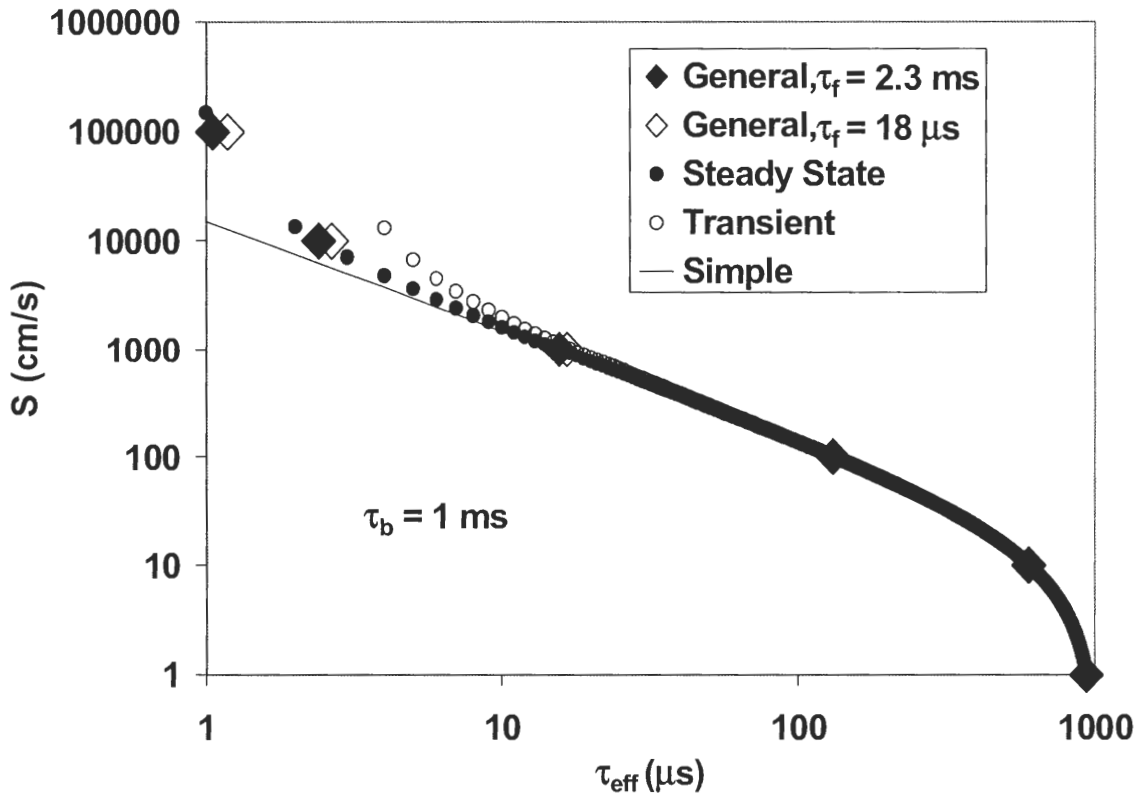

Figure 37. Same as Figure 36 but with τ_b = 1 ms.

4.4 Conclusions

A general equation for the excess carrier concentration of an optically excited semiconductor wafer has been derived for use with illumination that decays exponentially with time. A second important equation was derived assuming steady-state conditions to establish the relationship among S, τ_b, and τ_{eff}. The general equation was used to

investigate the accuracy of the steady-state equation, the transient equation, and the simple equation. The simple equation $1/\tau_{eff} = 1/\tau_b + 2S/W$ is accurate whenever the average excess carrier concentration over the wafer equals the average excess carrier concentration at the two surfaces. This occurs at small S in transient conditions; however, in QSSPC, the lower τ_b is, the higher S must be for the simple equation to be valid. The steady-state equation is the only equation that matches the general equation over the entire range of τ_{eff} when $\tau_f = 2.3$ ms, but any equation may be used when $\tau_{eff} >$ 20 μs. When $\tau_{eff} < 10$ μs, the steady-state equation must be used to avoid error that can exceed 100%. Prior to the introduction of Equation (67) derived in this research, no equation in the literature was available to link measured τ_{eff} with the desired quantities τ_b and S for QSSPC measurements. With the derivation of the transient and steady-state equations and the demonstration that the steady-state equation is valid for all lifetimes under slowly decaying illumination, this task is complete.

CHAPTER 5

INVESTIGATION OF THE DOPING DEPENDENCE OF S FOR DIELECTRIC-PASSIVATED STRING RIBBON AND CAST mc-Si

The contactless, quasi-steady-state, two-spectrum separation of S and τ_b is a new method that will be the experimental basis in this part of the research for the determination of the doping dependence of S in multicrystalline materials. To justify interest in this new method, the failure of the conventional iodine/methanol passivation method for the separation of S and τ_b on a multicrystalline material will be demonstrated. A sensitivity analysis indicates for the first time that the two-spectrum method can be used with reasonable sensitivity only over a limited range of τ_b and S. The sensitivity limitations are experimentally illustrated using high-quality float zone (FZ) silicon and lower-quality heat-exchanger method (HEM) multicrystalline silicon (mc-Si).

Bail and Brendel [7] were the first to describe the two-spectrum method. Two improvements over the original method are proposed and implemented in this section. First, we discard the unjustified assumption of 10% uncertainty in each τ_{eff} measurement. Instead, each measurement is repeated 15 times to experimentally obtain a range of possible τ_{eff} values. Second, a third wavelength is used to narrow the resulting ranges of S and τ_b values. These improvements are used for the experimental determination of S in 12 FZ wafers and three spots on each of nine string ribbon and nine cast mc-Si wafers. S

is determined on each of these 66 spots by repeating the measurement of τ_{eff} 15 times with each of three wavelengths, for a total of 2970 measurements.

5.1 Comparison of Iodine and Dielectric Passivation for Monocrystalline and Multicrystalline Silicon

If the iodine/methanol passivation frequently used to determine τ_b for monocrystalline silicon wafers were just as effective with low-lifetime materials, then there would be no need for a new method such as Bail and Brendel's. In order to investigate the effectiveness of iodine passivation of solar-grade silicon materials, string ribbon silicon wafers of three resistivities (0.7 Ω-cm, 1.5 Ω-cm, and 3 Ω-cm) were coated with passivating dielectrics. Three wafers of each resistivity were passivated with one of the following films: plasma-deposited nitride, thermal oxide, and an oxide/nitride stack. For comparison, a low-resistivity float zone wafer was treated with a thermal oxide. The effective lifetimes of all wafers were measured. Subsequently, the dielectric layers were removed, and the wafers were cleaned and immersed in the iodine/methanol solution described in [21]. The same iodine/methanol solution was used on the float zone and ribbon wafers. The effective lifetimes of all wafers were again measured. Results are shown in Figure 38.

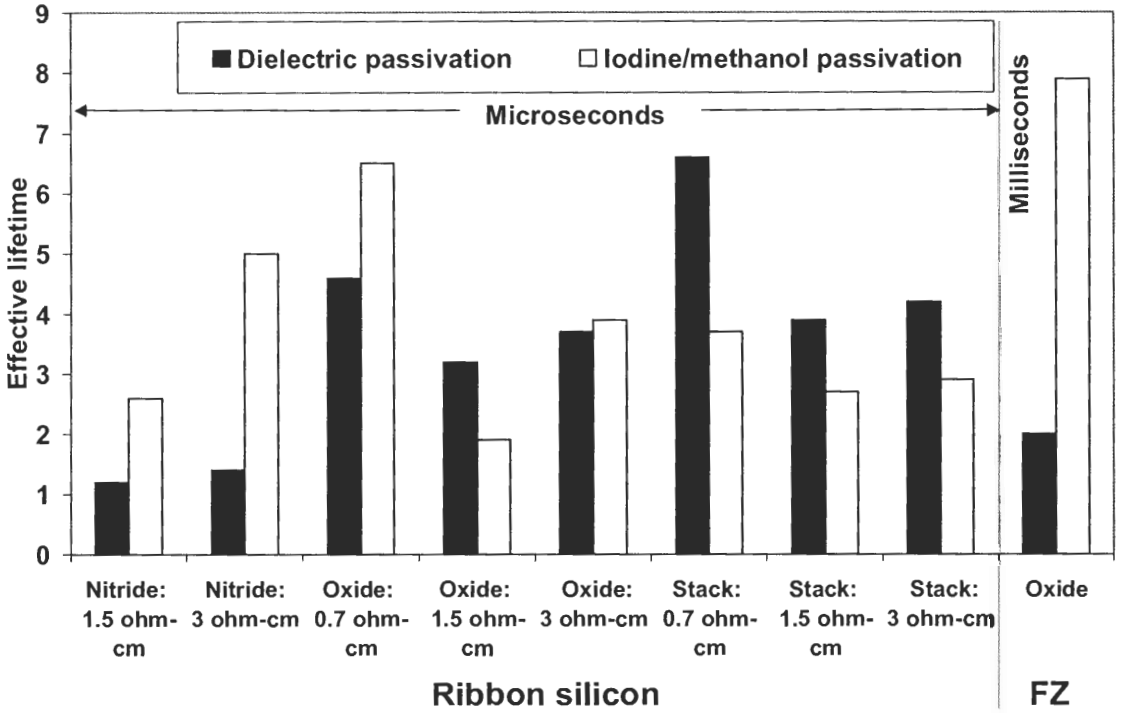

Figure 38. The effectiveness of iodine passivation of ribbon silicon. "Stack" refers to oxide/nitride stack passivation.

Using iodine, the measured effective lifetime of the float zone wafer was 7.9 ms, corresponding to a maximum S of less than 2 cm/s. This maximum S is obtained by ignoring τ_b in Equation (21): $\tau_{eff}^{-1} = 2S/W$, where W = 270 μm for this wafer. It is extremely difficult to exceed this level of surface passivation with a dielectric layer, and thus this method works well on monocrystalline materials. On the other hand, half of the eight ribbon wafers measured were less well passivated by iodine than by the dielectric layers; τ_{eff} (iodine) < τ_{eff} (dielectric). Thus the method of determining S by measuring τ_{eff} under dielectric passivation and extracting τ_b using iodine fails for this set of wafers; half the results would be meaningless (S < 0), and the other half would be suspect, given that iodine seems incapable of reducing S to insignificant values on ribbon silicon. We may

infer from Figure 38 that iodine passivates ribbon silicon more effectively than our nitride and less effectively than our oxide/nitride stack, but it is not clear how to determine quantitative values of S. This provided the motivation for the further study and application of the new two-spectrum method.

First, additional experiments were performed to compare the iodine and dielectric passivation on monocrystalline and multicrystalline materials were done. One cast mc-Si wafer of 2 Ω-cm, three string ribbon wafers of 3.3-4.9 Ω-cm, and three FZ wafers of 2.4 Ω-cm were oxidized all at the same time in a tube furnace. The wafers underwent a forming-gas anneal. The effective lifetimes (τ_{oxide}) were measured on all wafers. The

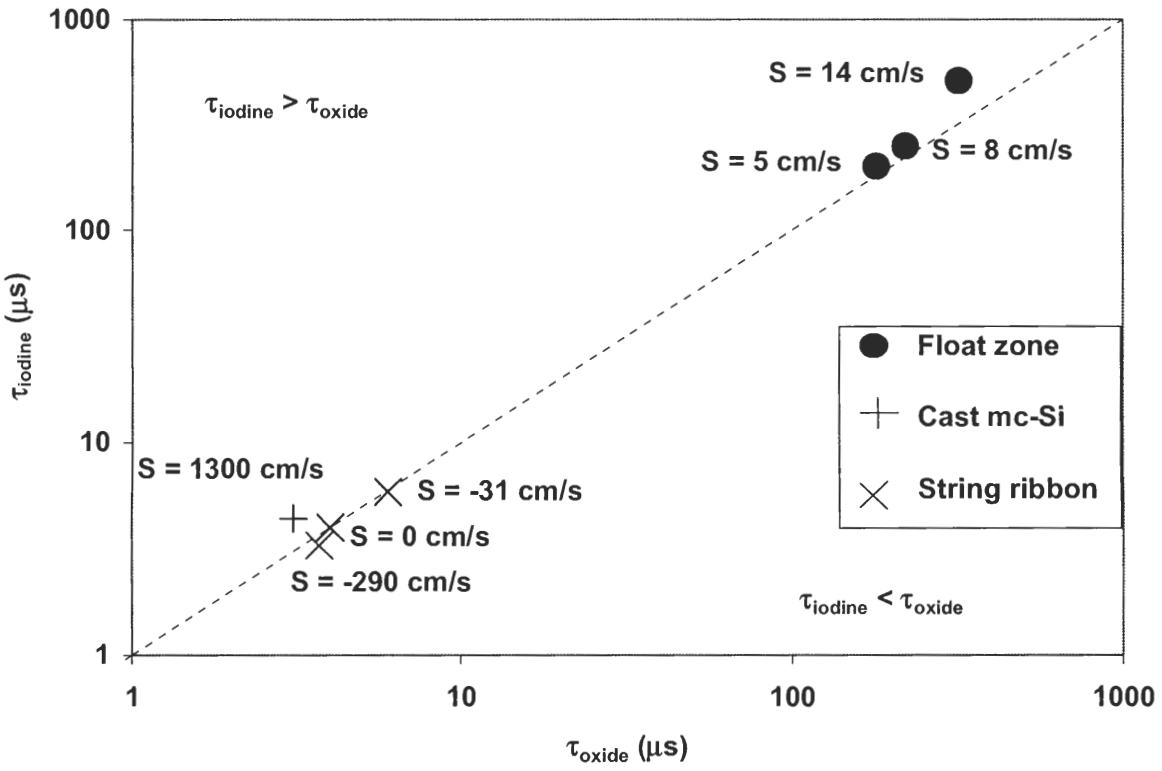

Figure 39. Experimental comparison of lifetimes measured under oxide and iodine passivation on different materials. Physically impossible S values for string ribbon result because the oxide passivates these wafers at least as well as the iodine in this experiment.

oxide was removed, the wafers were cleaned and passivated in the iodine/methanol solution, and the lifetimes (τ_{iodine}) were again measured. Results are shown in Figure 39, where S is calculated by assuming $\tau_b = \tau_{iodine}$ and using Equation (21) for the FZ wafers and the full steady-state Equation (67) for the multicrystalline wafers.

The S values shown in Figure 39 are lower limits on S because τ_{iodine} is a lower limit on τ_b [6]. An upper limit on S is determined by neglecting bulk recombination ($\tau_b = \infty$), which is reasonable for the FZ wafers [6]. The S ranges thus determined for the three FZ wafers were found to be narrow, within about 60 cm/s: 14-38 cm/s, 8-69 cm/s, and 5-50 cm/s.

For the identically passivated cast mc-Si wafer, a much higher S of 1300 cm/s is determined. Worse yet, all three string ribbon wafers were at least as well passivated by the oxide as by the iodine solution. Thus the assumption that $\tau_b = \tau_{iodine}$ resulted in physically meaningless $S \leq 0$ for string ribbon. Once again, the iodine method clearly failed to permit the determination of S on string ribbon.

Two possible reasons may explain why τ_{iodine} is sometimes lower than $\tau_{dielectric}$ on string ribbon. It may be that string ribbon, in contrast with float zone, truly is better passivated by dielectrics than iodine in some cases. Alternatively, it may be that τ_b in these as-grown string ribbon samples is so low that both τ_{iodine} and $\tau_{dielectric}$ are bulk-dominated and are insensitive to the surface passivation. Then, apparent differences between τ_{iodine} and $\tau_{dielectric}$ are due to measurement error instead of differences in surface passivation.

To elucidate this point, the experiment summarized in Figure 39 was repeated with a much larger number of wafers: 30 wafers of various types and resistivities were

coated according to one of several standard dielectric passivation schemes. A forming-gas anneal was performed on all wafers. Next, τ_{eff} was measured on one spot on each monocrystalline wafer and three spots on each multicrystalline wafer. Finally, the dielectrics were removed, and the wafers were cleaned in standard chemical solutions, passivated in the iodine solution, and measured once again. To confirm the quality of the iodine solution used for all wafers, the lifetime of a high-resistivity float-zone wafer was measured during immersion in the solution, yielding 1.8 ms. This guarantees a maximum S of 8.5 cm/s at the iodine-passivated surface of this wafer. Results for all wafers (whether the dielectric coating was nitride, oxide, or stack) are shown in Figure 40.

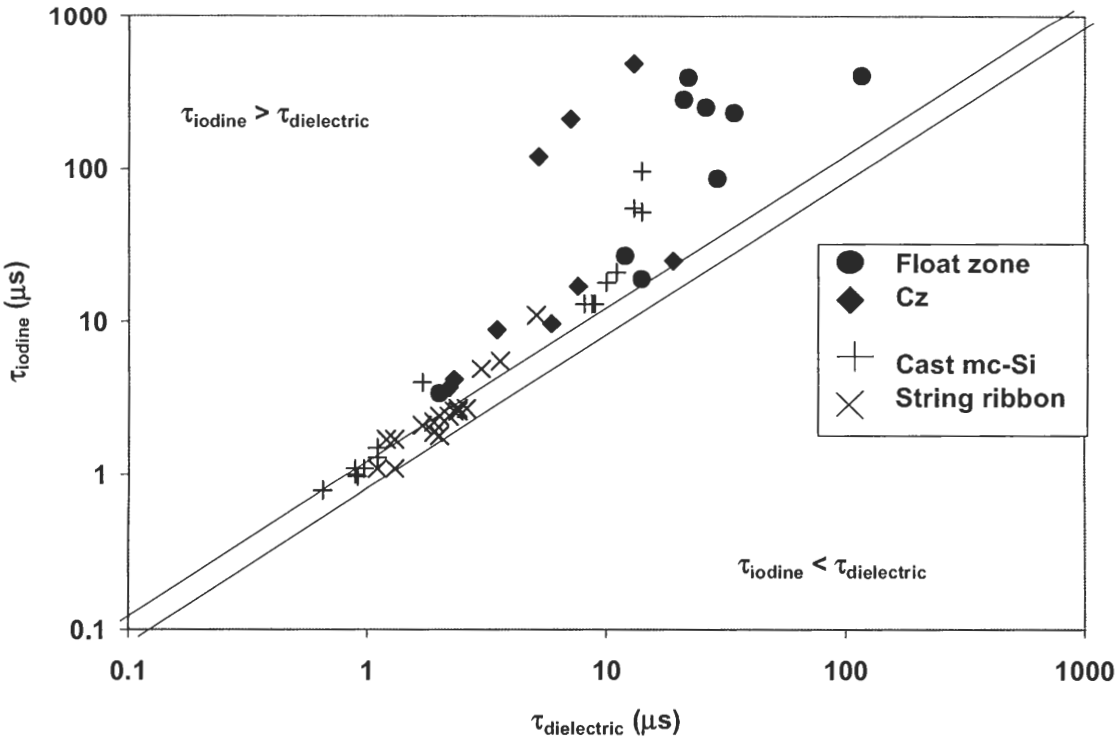

Figure 40. Comparison of iodine with various dielectric coatings for a variety of monocrystalline and multicrystalline materials. For points falling between the two diagonal lines, τ_{iodine} and $\tau_{dielectric}$ are the same within measurement error.

Based on a 10% uncertainty in lifetime measurements (as assumed in [7]), the two diagonal lines bound a region in which $\tau_{iodine} \approx \tau_{dielectric}$ within measurement error. All monocrystalline materials fall safely in the $\tau_{iodine} > \tau_{dielectric}$ region. However, one third of the measurements on cast mc-Si and two thirds of the measurements on string ribbon fall in the $\tau_{iodine} \approx \tau_{dielectric}$ region. This occurs for the wafers with the lowest lifetimes, less than about 3 μs. Additionally, none of the measurements fall in the $\tau_{iodine} < \tau_{dielectric}$ region. These observations suggest that low-lifetime wafers, instead of being better passivated by dielectrics than iodine, are insensitive to surface passivation within measurement precision. Figure 41 clarifies this point.

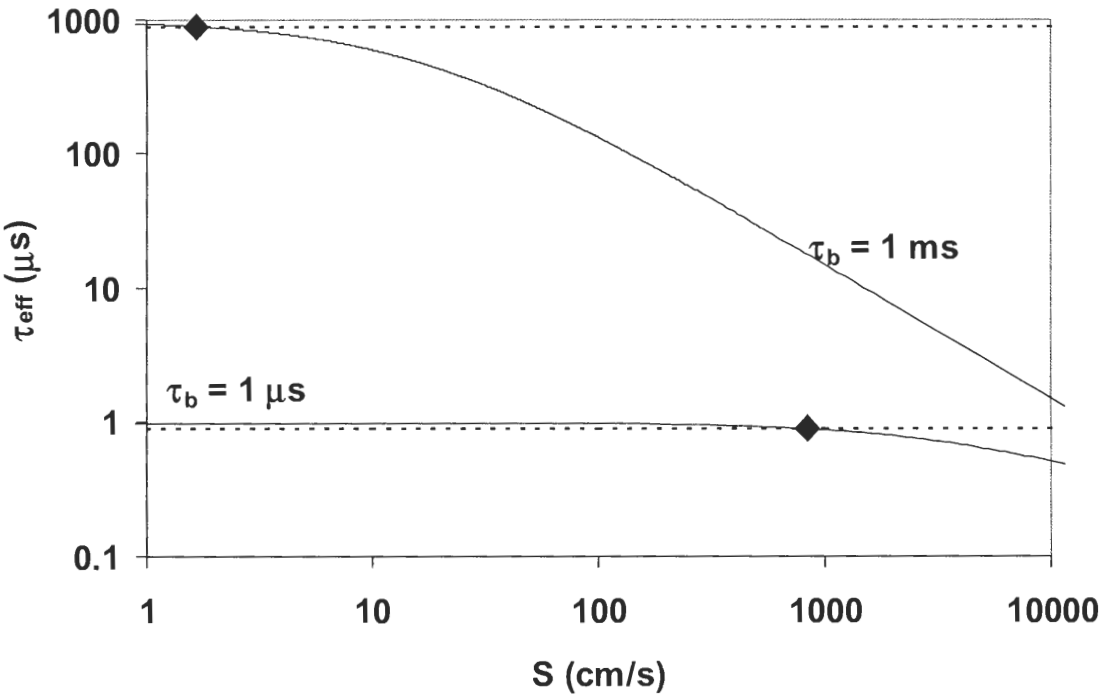

Figure 41. τ_{eff} as a function of S for τ_b = 1 ms and τ_b = 1 μs. The broken lines indicate $0.9\tau_b$, the τ_{eff} value above which the impact of S is undetectable for systems with 10% error. The diamonds indicate the lowest S for which the impact of S on τ_{eff} is detectable.

Figure 41 shows the calculated τ_{eff} vs. S for τ_b = 1 ms and τ_b = 1 μs using Equation (67) and W = 300 μm. The broken lines indicate $0.9\tau_b$, the τ_{eff} value above which the impact of S is undetectable for measurement systems with 10% error. The diamonds indicate the lowest S for which the impact of S on τ_{eff} is detectable. For τ_b = 1 ms, S as low as 2 cm/s has a greater than 10% impact on τ_{eff}. However, for τ_b = 1 μs, S must exceed 840 cm/s to have a detectable impact on τ_{eff}. Thus if S for both iodine and dielectrics is less than 840 cm/s on a material with τ_b = 1 μs, τ_{eff} in both cases is unaffected by S; apparent differences in τ_{eff} are due to error.

The lifetime measurements performed in most of this research use inductive coupling to detect photoconductance. These measurements are called area-integrated because the entire area that couples with the roughly 1-cm-diameter coil influences the measurement. Cast and especially ribbon silicon show rather inhomogeneous material properties within small wafer areas. As a consequence, area-integrated lifetime measurements might partly incorporate bulk-dominated areas that would falsify the results of S determination. To address these concerns, our area-integrated measurements were compared with lifetime mapping performed at the University of Konstanz. Three 1.5 Ω-cm, p-type string ribbon silicon wafers were coated according to different passivation schemes: ~100 Å thermal oxide, ~850 Å PECVD silicon nitride deposited at 300°C, and a stack of nitride on top of oxide. The τ_{eff} of each wafer was measured in two ways: area-integrated measurements of four spots, and high-resolution lifetime mapping (< 1 mm) performed with a microwave-detected PCD system under low-injection conditions using 1 sun bias light and a laser wavelength of 904 nm. Next, the dielectrics

were removed, and the wafers were cleaned and re-measured in an iodine solution. Area-integrated data are compared with average mapped values in Table 5.

Table 5. Mean τ_{eff} (μs) obtained by four area-integrated measurements (A) and lifetime map (B).

	Dielectric (A) τ_{eff} (μs)	**Iodine (A) τ_{eff} (μs)**		**Dielectric (B) τ_{eff} (μs)**	**Iodine (B) τ_{eff} (μs)**
Nitride	1.4	1.8		1.8	2.1
Stack	3.0	2.6		3.0	2.9
Oxide	2.7	3.1		2.9	3.0

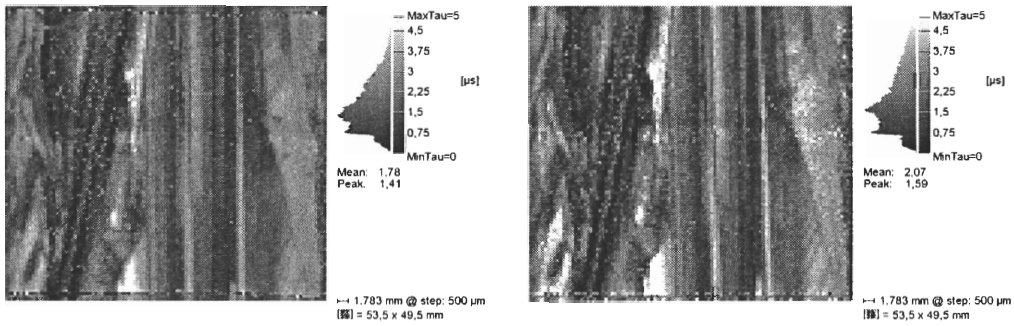

Figure 42. Lifetime maps obtained for a string ribbon wafer passivated by silicon nitride (left) and an iodine solution (right).

For typical as-grown lifetimes in the range of 1-10 μs, Table 5 suggests that oxide and the dielectric stack passivate string ribbon silicon as well as the iodine solution. In the case of silicon nitride, however, it can be seen that iodine tends to provide a better surface passivation than nitride. More detailed information can be obtained by analyzing the corresponding lifetime maps and histograms given in Figure 42. By comparing the

high end of the histograms, above 3.75 μs, it can be seen that differences between the two passivation methods are found especially in regions of higher lifetimes where bulk domination of τ_{eff} is less severe.

To get a more quantitative impression, local mean values have been calculated for the nearly homogeneous wafer areas indicated in Figure 43. In this way it is possible to compare the differences in effective lifetimes measured with both surface passivation techniques in regions with different bulk lifetime. As Table 6 shows, the differences get stronger with higher measured effective lifetime values. This is due to an increasing influence of surface recombination velocity on measured $\tau_{eff.}$ Consequently, it can be concluded from the mapping data that the iodine solution passivates ribbon silicon more efficiently than silicon nitride. This makes it possible to determine local S values without the disturbing influence of the whole wafer's inhomogeneity.

The full solution to the steady-state continuity equation is used to compute S for the nitride-coated ribbon surface in Table 6; τ_b is taken to be τ_{iodine} as the best available estimate. All four S values fall within 670-950 cm/s. Thus it appears that the surface quality is much more uniform than τ_b, which ranges from 0.84-5.6 μs over the same four areas. While S on nitride-passivated monocrystalline materials can be as low as 4 cm/s [30], the values in Table 6 are less than or equal to the 950 cm/s reported for a ribbon sample in [32]. A float zone wafer was processed along with the string ribbon sample studied in Table 6. Using the iodine solution to estimate τ_b, S for the nitride-passivated float zone wafer was calculated to be 410 cm/s. This is considered a lower bound to S [6] since the iodine solution determines a lower bound to τ_b and $S = W/2(1/\tau_{eff} - 1/\tau_b)$. The simple equation is valid because τ_{eff} was measured as 29 μs, which is higher than the 20

μs limit above which all equations converge; the agreement of the simple equation with the general equation for this situation was demonstrated in Fig. 37 of Chapter 4. The upper limit to S determined by setting $\tau_b = \infty$ is 500 cm/s, which is still significantly lower than the S values determined for the identically passivated string ribbon wafer.

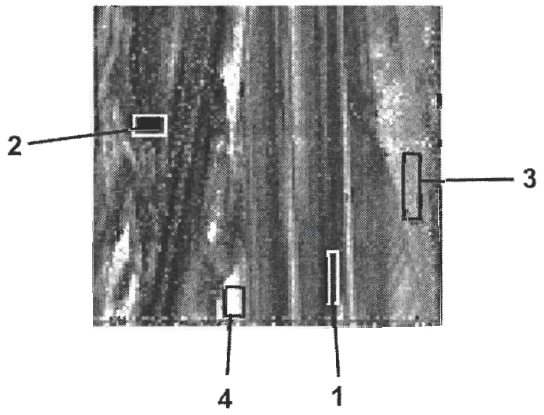

Figure 43. Location of the four areas in which local lifetimes are computed and listed in Table 6.

Table 6. Local effective lifetimes computed for four small, nearly homogeneous areas of a string ribbon wafer. Low-lifetime Areas 1 and 2 appear dominated by bulk recombination regardless of surface passivation, while higher-lifetime Areas 3 and 4 show significantly different lifetimes under nitride and iodine passivation.

	$\tau_{nitride}$ (μs)	τ_{iodine} (μs)	$\tau_{nitride}/\tau_{iodine}$	S (cm/s)
Area 1	0.77	0.84	.92	950
Area 2	1.0	1.1	.91	850
Area 3	3.0	3.6	.84	670
Area 4	4.1	5.6	.72	850

For the calculation of S it is necessary that the iodine solution provides a better surface passivation than the dielectrics. With the help of spatially resolved measurements

it could be shown that an iodine solution provides better surface passivation than silicon nitride on as-grown ribbon silicon wafers, whereas no significant differences were found in comparison to silicon oxide or nitride/oxide stacks in lifetime ranges of 1-10 μs. This suggests that oxide or stack passivation is better than nitride passivation and becomes comparable to or better than iodine passivation.

The evaluation of S in the case of silicon nitride is possible when effective lifetimes are determined with a higher resolution. Here effective lifetimes can be locally integrated in small areas of rather homogeneous quality and accurate results for S can be obtained.

5.2 Empirical Calibration of Lifetime Characterization Tool for Arbitrary Spectra

A quasi-steady-state photoconductance (QSSPC) measurement is made when the flash lamp time constant is much greater than τ_{eff}. In QSSPC, $\tau_{eff} = n_{av}/G_{av}$, where n_{av} is the average excess carrier concentration, and G_{av} is the average generation rate [13]. G_{av} is determined by its proportionality with the measured short-circuit current (J_{sc}) of the reference cell: $G_{av} = KJ_{sc}$. K, the constant of proportionality between G_{av} and J_{sc}, depends on the photon flux spectral density of the illumination [7]. This constant may be determined analytically from knowledge of the photon flux spectral density, the external quantum efficiency (EQE) of the reference cell, and the reflectance of the test wafer [7]. Specifically, J_{sc} is written as

$$J_{sc} = q\int N_{ph}(\lambda)EQE(\lambda)d\lambda, \tag{72}$$

and G_{av} is obtained by integrating Equation (60) over the thickness of the wafer and dividing by W:

$$G_{av} = \frac{1}{W}\sum_{\lambda}\frac{N_{ph}(\lambda)[1-R(\lambda)][1+R(\lambda)e^{-\alpha(\lambda)W}](1-e^{-\alpha(\lambda)W})}{1-[R(\lambda)e^{-\alpha(\lambda)W}]^2} = \frac{1}{W}\sum_{\lambda}\frac{N_{ph}(\lambda)[1-R(\lambda)](1-e^{-\alpha(\lambda)W})}{1-R(\lambda)e^{-\alpha(\lambda)W}} \quad (73)$$

K is then defined as the ratio of Equation (73) to Equation (72). Clearly K depends on the spectrum of illumination, which determines $N_{ph}(\lambda)$. K also depends on the test wafer because the thickness and reflectance of the test wafer appear in Equation (73).

A shortcoming of the analytical procedure to determine K is that the photon flux is assumed to be the same on both the reference cell and the test wafer: the same $N_{ph}(\lambda)$ is used in Equations (72) and (73). This assumption is questionable is in general and almost certainly false when small optical filters are used to obtain different spectra; we sometimes allow the lamp to shine only through a selected 2"-square filter. Since the analytical determination is thus inappropriate in this case, a rapid calibration procedure to determine K empirically is presently suggested.

A calibration wafer with S < 50 cm/s is chosen. When S < 50 cm/s, the difference between τ_{eff} measured using transient photoconductance decay (PCD) and QSSPC is less than 1% [14]. For a given illuminating spectrum, the calibration wafer is first measured using transient PCD. The resulting τ_{eff} does not depend on K, because K only affects the calculation of G_{av}, which is negligible in a transient measurement. The transient τ_{eff} is thus considered the true τ_{eff} because it is unaffected by a possibly erroneous K value. The same wafer is then measured using QSSPC. Since S < 50 cm/s, the QSSPC τ_{eff} should equal the transient τ_{eff}. If the two are not equal, the discrepancy results from an incorrect

value of K skewing the QSSPC calculations. K is chosen as the value that causes the QSSPC τ_{eff} to equal to transient τ_{eff}. Let this value of K determined for the calibration wafer be called K_{cal}, defined as $G_{av}(cal)/J_{sc}$; $G_{av}(cal)$ is the average generation in the calibration wafer for the chosen illumination. We need to determine $K_{test} = G_{av}(test)/J_{sc}$, the ratio between G_{av} and J_{sc} for a test wafer of arbitrary S illuminated by the same spectrum. J_{sc} depends only the illumination and not the test wafer; thus the same J_{sc} appears in $K_{test} = G_{av}(test)/J_{sc}$ and $K_{cal} = G_{av}(cal)/J_{sc}$. It thus becomes clear that $K_{test} = K_{cal} \times [G_{av}(test)/G_{av}(cal)]$. Using Equation (73) to find G_{av} in both cases, we find

$$K_{test} = K_{cal} \frac{1}{W_{test}} \sum_{\lambda} \frac{N_{ph}(\lambda)[1-R_{test}(\lambda)](1-e^{-\alpha(\lambda)W_{test}})}{1-R_{test}(\lambda)e^{-\alpha(\lambda)W_{test}}} \left[\frac{1}{W_{cal}} \sum_{\lambda} \frac{N_{ph}(\lambda)[1-R_{cal}(\lambda)](1-e^{-\alpha(\lambda)W_{cal}})}{1-R_{cal}(\lambda)e^{-\alpha(\lambda)W_{cal}}} \right]^{-1} \quad (74)$$

where $R_{test}(\lambda)$ and $R_{cal}(\lambda)$ are the reflectances of the test and calibration wafers, respectively, and W_{test} and W_{cal} are the respective thicknesses.

5.3 Sensitivity Analysis of Two-Spectrum Extraction of S and τ_b

Assuming knowledge of all optical properties (N_{ph}, R, and α) as well as W, D, and measured τ_{eff}, Equation (67) provides the relationship between S and τ_b. Small uncertainty in τ_{eff} can result in very large uncertainty in S and τ_b, depending on their actual values. This section investigates the sensitivity of the two-spectrum extraction of S and τ_b for various combinations of their values.

We choose two spectra of illumination easily achievable in the laboratory. The first is the unfiltered white light of the Qflash T2 flash lamp. The second spectrum is monochromatic 1140 nm light, chosen as an approximation to the light transmitted

through a 300 μm silicon wafer used as a filter in front of the lamp. Using $D = 30\ cm^2s^{-1}$, $W = 0.03$ cm, and $R = 0.1$, Figure 44 is obtained from the application of Equation (66) to calculate τ_{eff} as a function of S, τ_b, and illuminating spectrum. (Although $R = 0.1$ is an arbitrary choice, τ_{eff} under white-light illumination typically varies less than 5% as R is changed from 0 to 0.9; moreover, τ_{eff} under monochromatic illumination is completely independent of R.) As τ_{eff} increases to 10 μs, the difference between white and infra-red (IR) τ_{eff} becomes insignificant. When white and IR τ_{eff} differ insignificantly, a measurement using a single spectrum provides just as much information as two measurements using two spectra. Figure 44 also indicates that very little resolution is available for $\tau_b > 10$ μs or $S \leq 1000$ cm/s. It should be noted that Figure 44 resembles the comparison of steady-state and transient τ_{eff} in [14]. The similarity results from the fact that under transient illumination or steady-state IR illumination, the excess carrier concentration is relatively low near the surfaces, whereas under steady-state, short-wavelength illumination, the excess carrier concentration is very high near the front surface, and surface recombination is much more significant. Figure 45 illustrates the similarity between transient illumination (of any wavelength) and quasi-steady-state IR illumination; in contrast, short-wavelength, quasi-steady-state illumination causes the excess carrier profile to heavily favor the illuminated surface. The calculated τ_{eff} is correlated with the carrier profile and is higher for the concave-down, surface-shunning profiles. To fully understand why τ_{eff} is higher for the concave-down profiles, it is necessary only to rearrange Equation (57), which we recall is exact for any kind of illumination, provided τ_b is independent of injection level and S is identical on both surfaces:

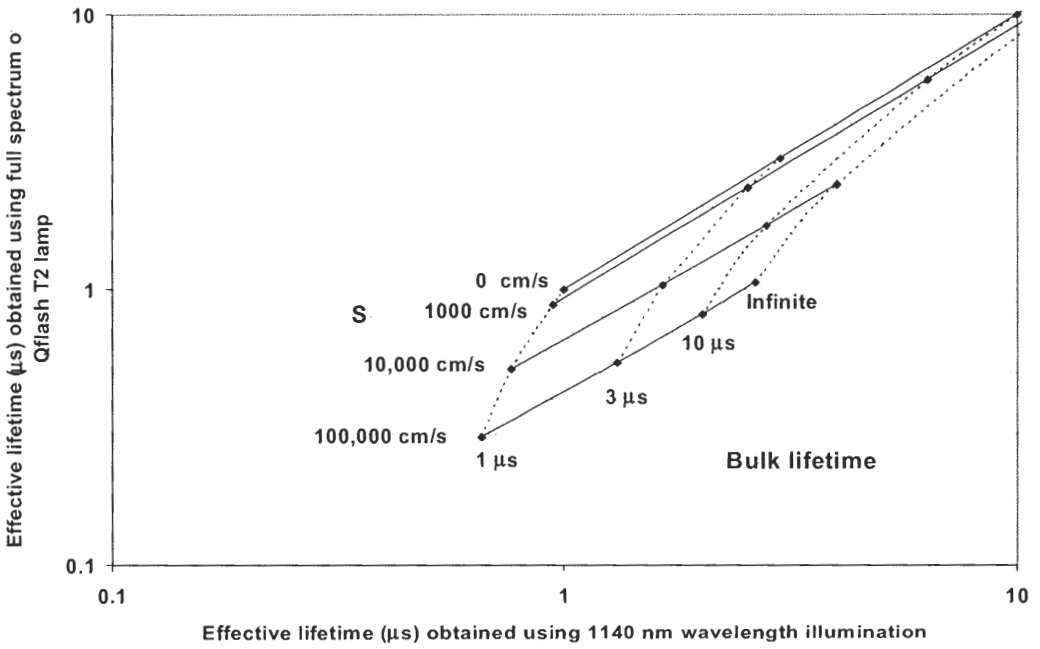

Figure 44. Comparison of τ_{eff} under white illumination with τ_{eff} under IR illumination.

$$\frac{1}{\tau_{eff}} = \frac{1}{\tau_b} + \frac{S[\Delta n(-W/2) + \Delta n(W/2)]}{W\Delta n_{av}}. \tag{75}$$

Every term on the right side of the equation is a constant parameter except the ratio $[\Delta n(-W/2)+\Delta n(W/2)]/\Delta n_{av}$. The highest τ_{eff} for a given τ_b and S will occur under illumination conditions that minimize this ratio. This ratio is minimized when Δn at the surfaces is as small as possible relative to Δn deep within the bulk. As the solutions to the continuity equation in Figure 45 demonstrate, this occurs under both transient illumination, which allows the excess carrier concentration to decay toward its fundamental mode, and steady-state IR generation, in which generation is not too concentrated at the front surface.

Having firmly established the reasons for which two spectra of illumination result in different τ_{eff} values in QSSPC, we further explore the ability of this method to specify S and τ_b. Figure 46 demonstrates how the information provided by the two-spectrum method is limited for different values of S and τ_b. This figure was constructed by applying Equation (66) to calculate τ_{eff} for each of the two spectra using the specified S and τ_b values. Next an experimental uncertainty of ±10% was assumed for τ_{eff}. The upper and lower values of τ_{eff} given by this uncertainty were used in Equation (67) to plot the S vs. τ_b curves. The intersection of the region bounded by the white light curves with the region bounded by the IR curves gives all the points in S-τ_b space consistent with the τ_{eff} that would be measured for a wafer having the specified S and τ_b. This area of intersection represents the information about S and τ_b that can be inferred using the two-spectrum method.

We observe that when τ_b = 100 μs, the intersection provides only a lower limit on τ_b: Figure 46.a (τ_b = 100 μs, S = 1000 cm/s) gives τ_b > 13 μs, and Figure 46.b (τ_b = 100 μs, S = 10000 cm/s) gives τ_b > 9 μs. However, when τ_b = 10 μs, the intersection provides upper and lower limits on τ_b: Figure 46.c (τ_b = 10 μs, S = 1000 cm/s) gives 6 μs < τ_b < 1000 μs, and Figure 46.d (τ_b = 10 μs, S = 10000 cm/s) gives 5 μs < τ_b < 100 μs. The fact that Figure 46 provides more information for τ_b = 10 μs than τ_b = 100 μs is consistent with the inference from Figure 44 that little resolution is available for τ_b > 10 μs. The inference from Figure 44 that little resolution is available for S ≤ 1000 cm/s is also confirmed in Figure 46. When S = 1000 cm/s, only an upper limit is placed on S: Figure 46.a gives S < 1300 cm/s, and Figure 46.c gives S < 3300 cm/s. However, when S =

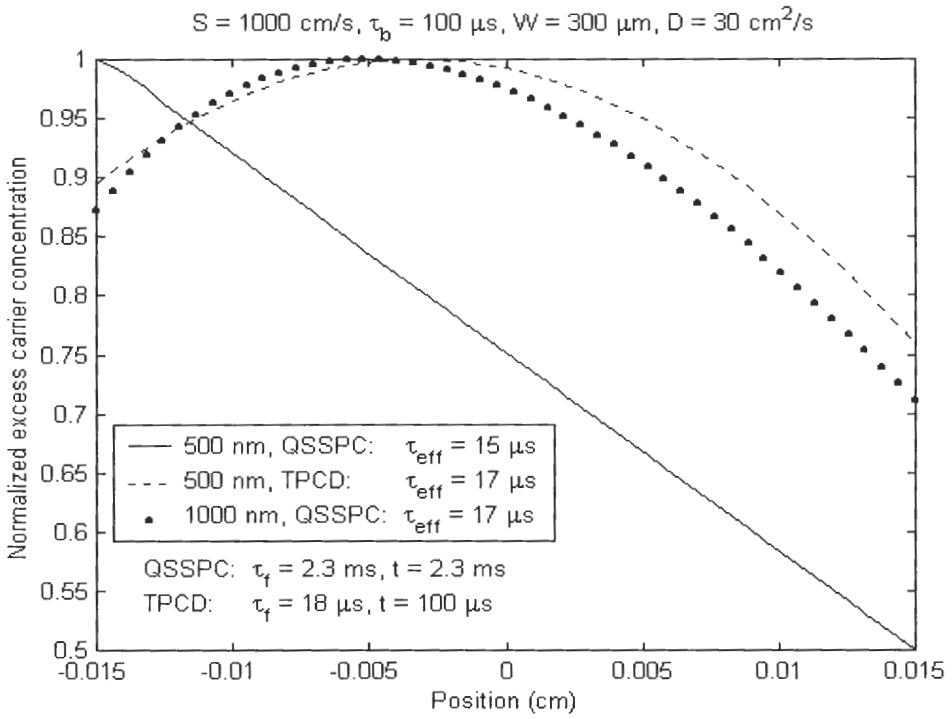

Figure 45. Contrast between excess carrier profile for short-wavelength (500 nm), quasi-steady-state illumination, and carrier profile for two conditions yielding similar results: short-wavelength TPCD and IR (1000 nm) QSSPC. For a given wafer under different illumination conditions, the carrier profile is correlated with τ_{eff}. (The parameter t is time after onset of illumination at which the results are calculated.)

10000 cm/s, both an upper and lower limit are placed on S: Figure 46.b gives 4000 cm/s < S < 12000 cm/s for τ_b = 100 μs, and Figure 46.d gives 4000 cm/s < S < 20000 cm/s for τ_b = 10 μs.

Since these results are a strong function of the assumed uncertainty in measured τ_{eff}, the influence of the uncertainty value will be investigated systematically in Section 5.5. Under the current assumption of 10% uncertainty, we conclude that using white light and IR light QSSPC measurements on a 300 μm wafer can provide the following information about τ_b and S: it will always be possible to infer a lower limit on τ_b and an upper limit on S. However, τ_b can be specified within an order of magnitude for low τ_b

only (τ_b no higher than about 10 μs), and S can be specified within an order of magnitude for high S only (S greater than about 1000 cm/s). To our knowledge, these limitations on the two-spectrum method have not previously been elucidated in the literature. Even though the two-spectrum method can only place an upper limit on S for low S, this information may be all that is necessary for many applications in photovoltaics. Conveniently, while this method specifies τ_b least precisely for high-lifetime materials, monocrystalline materials can be effectively passivated with iodine for the extraction of τ_b. Thus high-lifetime, monocrystalline materials are better suited for the conventional method of iodine passivation. Conversely, multicrystalline materials, which tend to have lower τ_b and higher S, are not reliably passivated by iodine; these materials are better suited for the two-spectrum method when S is sought as well as τ_b. Since gettering and passivation often elevate τ_b above 10 μs even in multicrystalline materials, the two-spectrum method is best suited for as-grown materials.

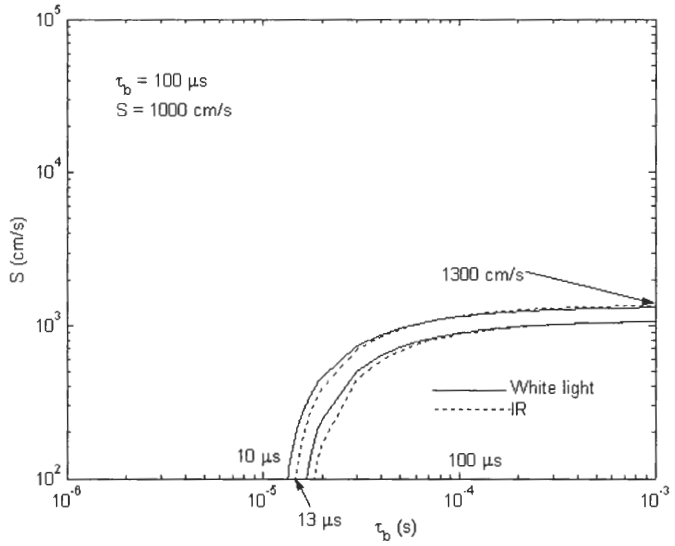

a.

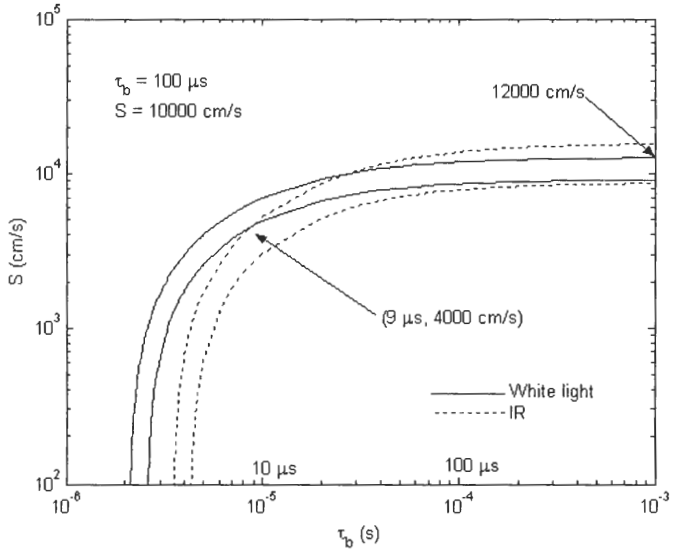

b.

Figure 46, a and b. S vs. τ_b curves obtained assuming ±10% of the calculated value of τ_{eff}, D = 30 cm^2s^{-1}, and W = 0.03 cm. τ_b = 100 µs.

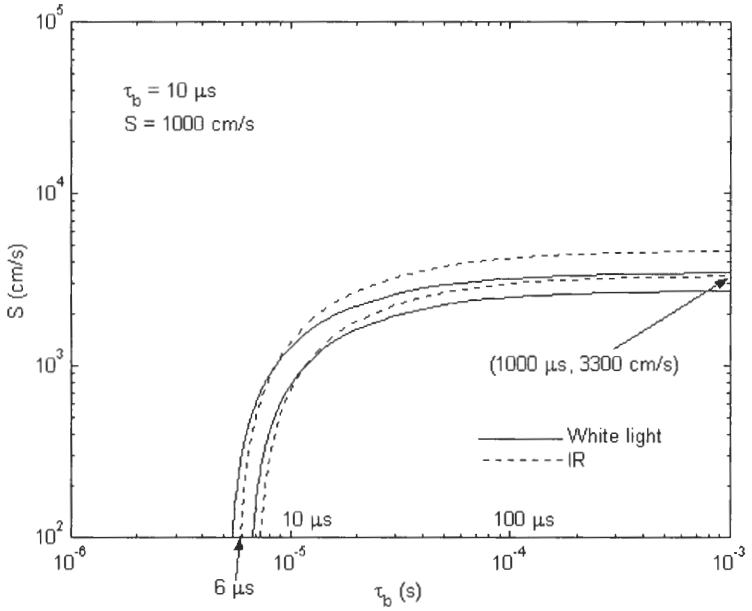

c.

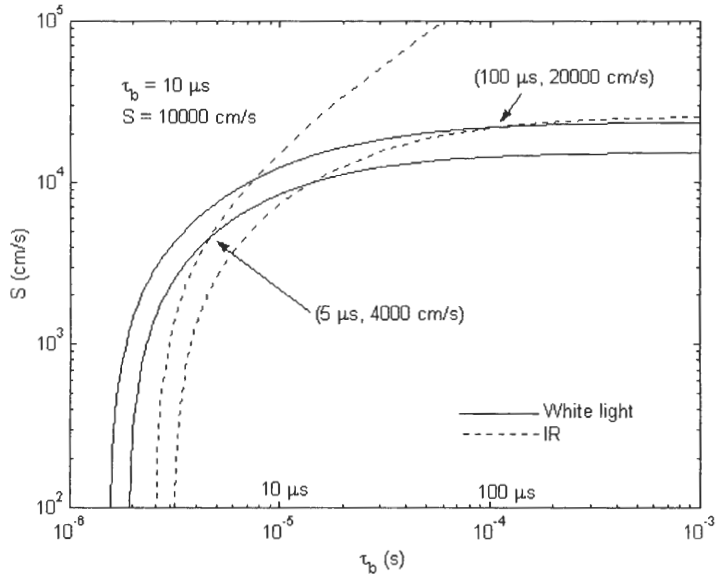

d.

Figure 46, c and d. S vs. τ_b curves obtained assuming ±10% of the calculated value of τ_{eff}, D = 30 cm^2s^{-1}, and W = 0.03 cm. τ_b = 10 μs.

5.4 Experimental Illustration and Validation of Two-Spectrum Method Using Float Zone and Multicrystalline Silicon Wafers of Different Resistivities

Three test wafers were used for experimental validation of the cases illustrated by the theoretical calculations in Figure 46.a, b, and d: a 1.3 Ω-cm float zone wafer, a 1.4 Ω-cm heat-exchanger method (HEM) multicrystalline wafer, and a 0.2 Ω-cm HEM wafer, respectively. SiN_x was deposited on all wafers and annealed. A calibration wafer was used according to the procedure described in Sec. 4.2.3, and τ_{eff} was measured on all test wafers using both white light and IR light. We estimate an uncertainty of ±10% for these experimentally determined τ_{eff}. The 0.2 Ω-cm HEM wafer was measured both before and after the anneal of the SiN_x to test the consistency of this two-spectra method.

Figure 47 shows the results for the float zone wafer. This wafer has high τ_b and low S and thus is similar to the case illustrated by Figure 46.a: only a lower bound can be inferred for τ_b (80 μs), and only an upper bound can be inferred for S (165 cm/s).

The 1.4 Ω-cm HEM wafer has moderately high τ_b and high S and thus is similar to the case illustrated by Figure 46.b, as shown in Figure 48: only a lower bound can be inferred for τ_b (9 μs), but both a lower bound (1200 cm/s) and an upper bound (4200 cm/s) are deduced for S.

Finally, Figure 49 show the results for the 0.2 Ω-cm HEM wafer, which has low τ_b and high S and is similar to the case of Figure 46.d. We are able to conclude 1.5 μs < τ_b < 2.5 μs, and 3000 cm/s < S < 20000 cm/s. In Figure 50, we show the results for the

measurements of the same point on the same wafer before the SiN_x was annealed in a belt furnace at 850°C for two minutes. As expected for this low-resistivity wafer coated with high-frequency silicon nitride, the τ_b range is nearly unchanged (within 10%); however, the S range is much higher, 8000 cm/s - 60,000 cm/s, for the as-deposited SiN_x. While Figures 48 and 49 show the results for a single point on the wafer, these results are typical for three other points measured on the same wafer.

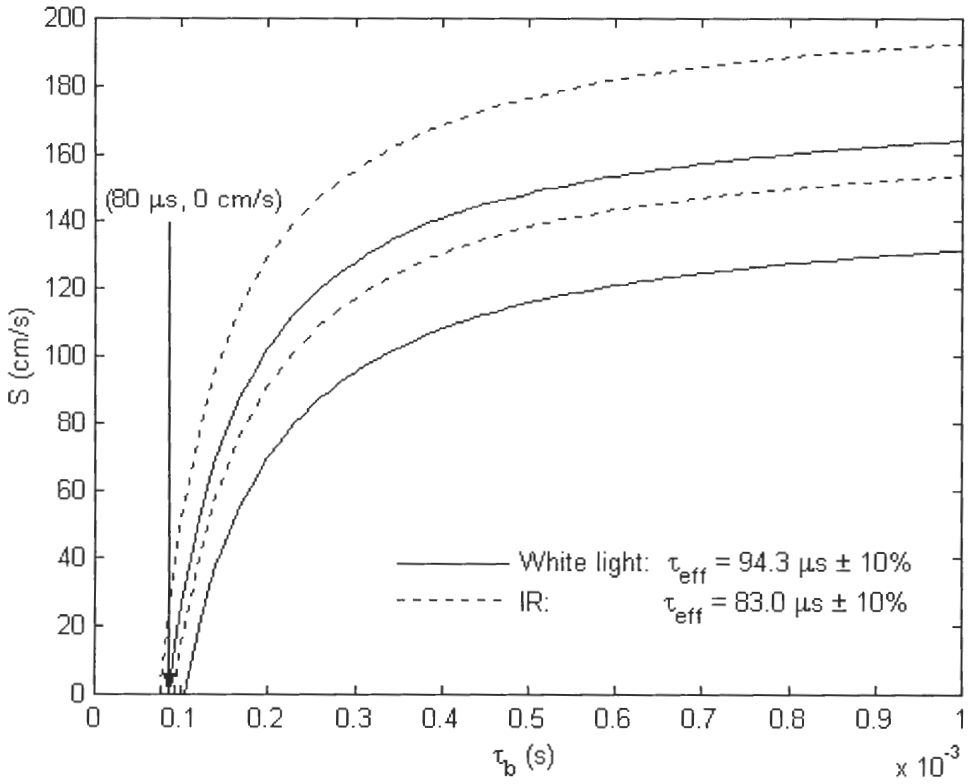

Figure 47. Two-spectrum method applied to measured τ_{eff} for a 1.3 Ω-cm float zone wafer coated with SiN_x.

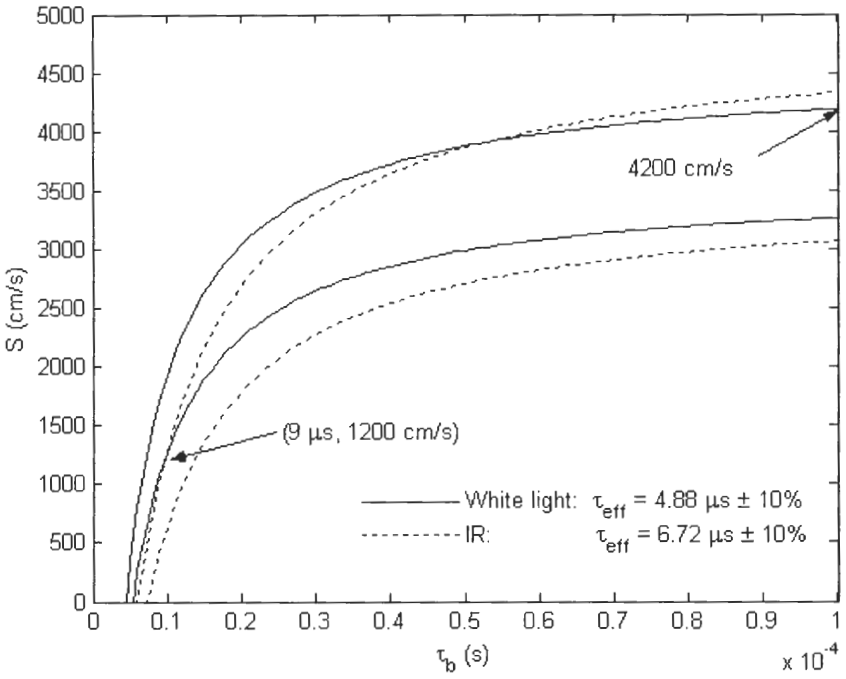

Figure 48. Two-spectrum method applied to measured τ_{eff} for a 1.4 Ω-cm HEM wafer coated with SiN_x.

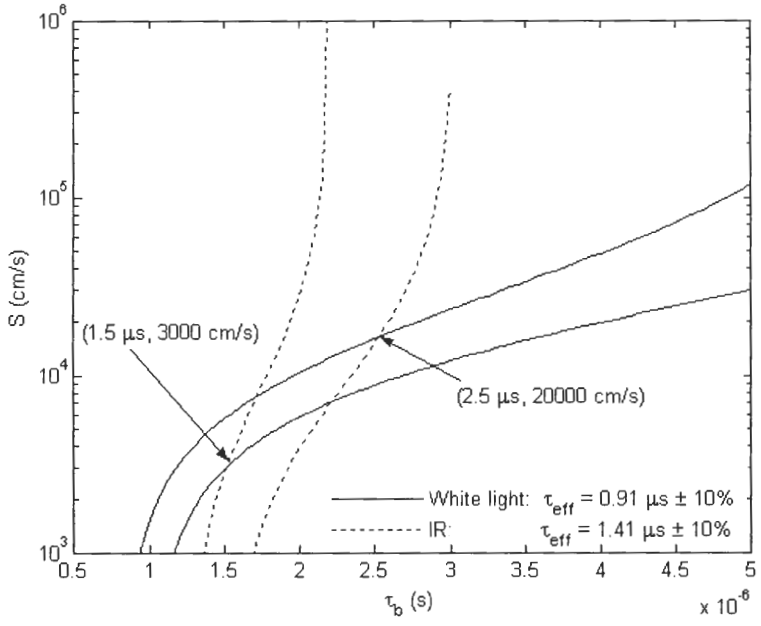

Figure 49. Two-spectrum method applied to measured τ_{eff} for a 0.2 Ω-cm HEM wafer coated with SiN_x and annealed at 850°C for two minutes.

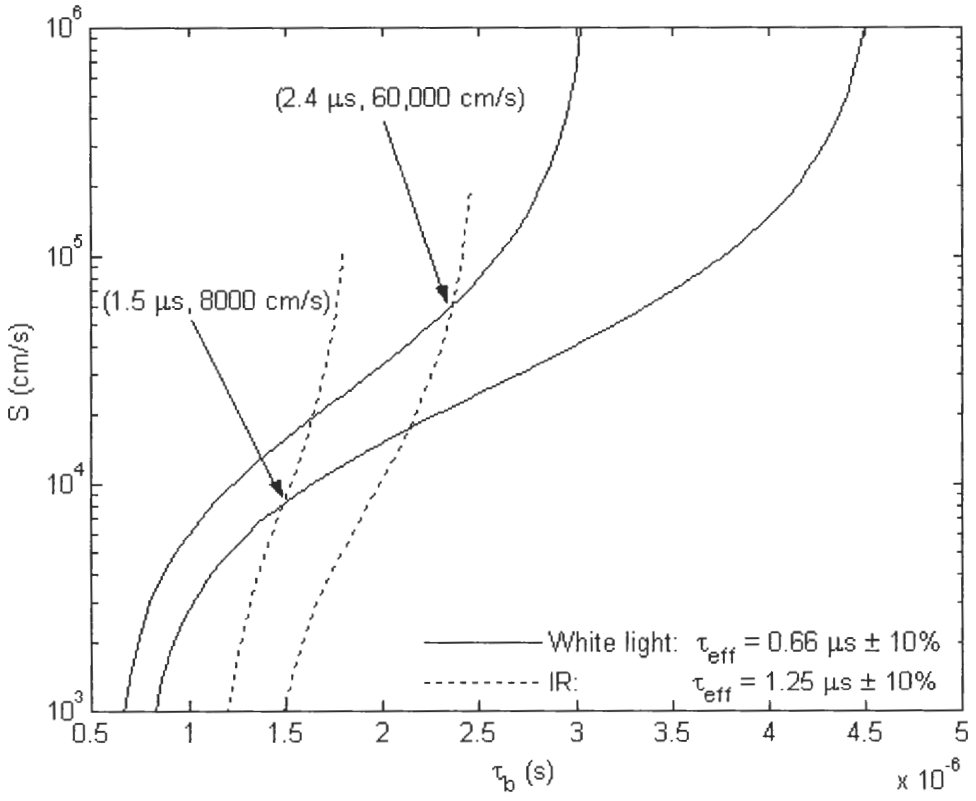

Figure 50. Two-spectrum method applied to measured τ_{eff} for the 0.2 Ω-cm HEM wafer of Figure 49, before the anneal of the SiN_x. As expected, the τ_b range is scarcely different (within about 10%), while the S range is much higher (by a factor of about 3).

5.5 Influence of Uncertainty on Two-Spectrum Results

Most of theoretical and experimental work thus far has used white light illumination and light filtered through a silicon wafer resulting in (approximately) uniform generation. In this section, 500 nm and 1000 nm illumination will be used instead. Experimentally, this light is produced by placing the appropriate monochromatic filters in front of the flash lamp. Although the filters have finite bandwidths (71.3 nm and 16.3 nm respectively), simulations using Equation (66) have shown that little error is introduced by assuming purely monochromatic illumination.

Switching from white and wafer-filtered light to 500 nm and 1000 nm light brings three important improvements. First, we avoid the unproven assumption that filtering light through a wafer results in uniform generation. Second, we achieve greater sensitivity because 500 nm light produces a generation profile that favors the front surface more strongly than white light; white light includes long wavelengths absorbed throughout the wafer. Therefore, 500 nm measurements are more closely linked to S than white light measurements, while 1000 nm measurements are linked to τ_b. Finally, we can eliminate from Equation (67) the complicated sums over wavelength:

$$S = \frac{(D/L)\sinh(W/2L)\left(\frac{1}{1/\tau_b - D\alpha^2} - \tau_{eff}\right) - \frac{DL\alpha^2 \sinh(W/2L)}{1/\tau_b - D\alpha^2}}{\cosh(W/2L)\left(\tau_{eff} - \frac{1}{1/\tau_b - D\alpha^2}\right) + \frac{\coth(\alpha W/2)\sinh(W/2L)L\alpha}{1/\tau_b - D\alpha^2}}. \quad (76)$$

The tedious algebra leading to Equation (76) has been omitted. Equation (66) can also be simplified to find τ_{eff} in monochromatic illumination. Using these equations, we can determine the influence of the uncertainty in τ_{eff} measurements on the ranges of S and τ_b obtained from the two-wavelength analysis. We expect that as the uncertainty increases from 0 to 20%, the ranges of S and τ_b will increase dramatically.

Simulations were performed as follows. First, fixed values of the S and τ_b were selected. Equation (66) was used to calculate the true τ_{eff} for both 500 nm and 1000 nm illumination. A variable uncertainty ranging from 0-20% was applied to each τ_{eff}; whatever uncertainty was applied to the 500 nm τ_{eff} was also applied to the 1000 nm τ_{eff}. Using the procedures described and illustrated previously, we determined the ranges of S and τ_b consistent with both τ_{eff} values within the given uncertainty. In addition to the

physical requirement that $S \geq 0$, we only search for solutions in the range $\tau_b \leq 1$ ms, because few materials of interest exceed this limit.

S results are given in Figure 51. As expected, zero uncertainty restricts S to a single value. The upper and lower limits on S diverge in a roughly linear fashion as the uncertainty increases. Figures 51.a and 51.c show that uncertainty must be less than 7% in order to extract a minimum value for S when S = 1000 cm/s. Figures 51.b and 51.d show that when S = 10000 cm/s, S is determined within a factor of 2-5 even for uncertainty as high as 20%.

Figure 52 shows the influence of τ_{eff} uncertainty on τ_b ranges. In Figures 52.a and 52.b, with $\tau_b = 100$ μs, a meaningful upper limit on τ_b (1 ms) is possible only for uncertainties less than 2%. $\tau_b = 10$ μs in Figures 52.c and 52.d. In Figure 46 for the case of $\tau_b = 10$ μs, reasonably narrow τ_b ranges were extracted assuming 10% uncertainty. Figures 52.c and 52.d show, however, that the upper limit on τ_b increases greatly between uncertainties of 10% and 20%.

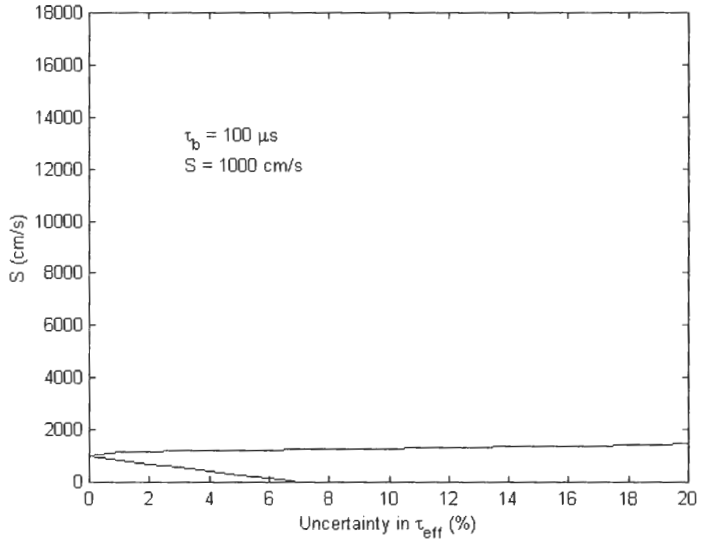

a.

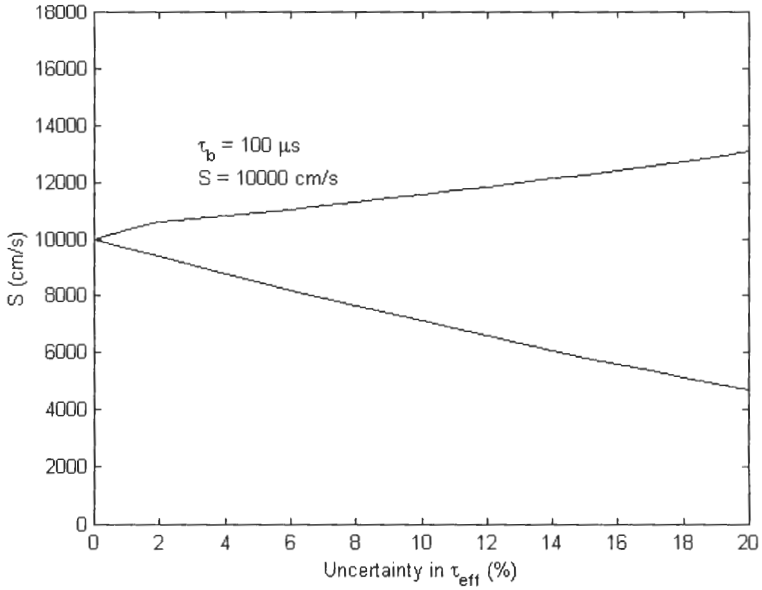

b.

Figure 51, a and b. Influence of uncertainty in τ_{eff} on S ranges obtained from two-spectrum analysis. S must lie between the two lines. For zero uncertainty in τ_{eff}, S is constrained to a single point. τ_b = 100 µs.

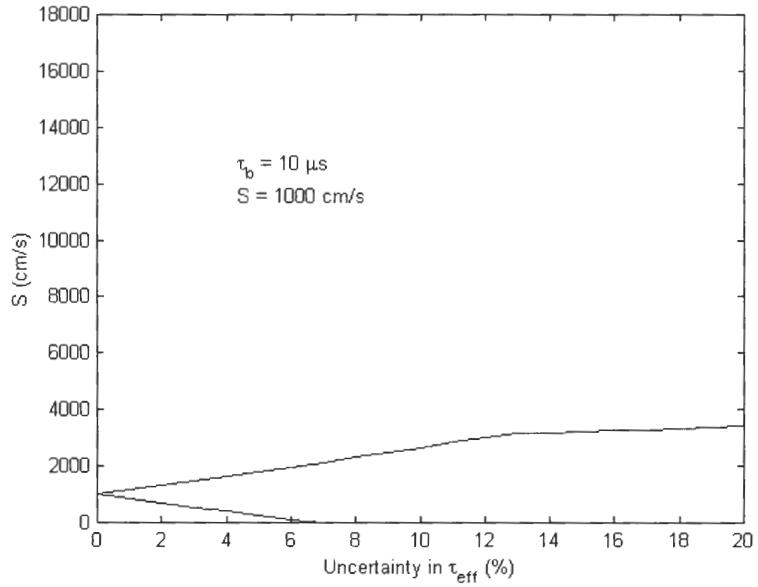

c.

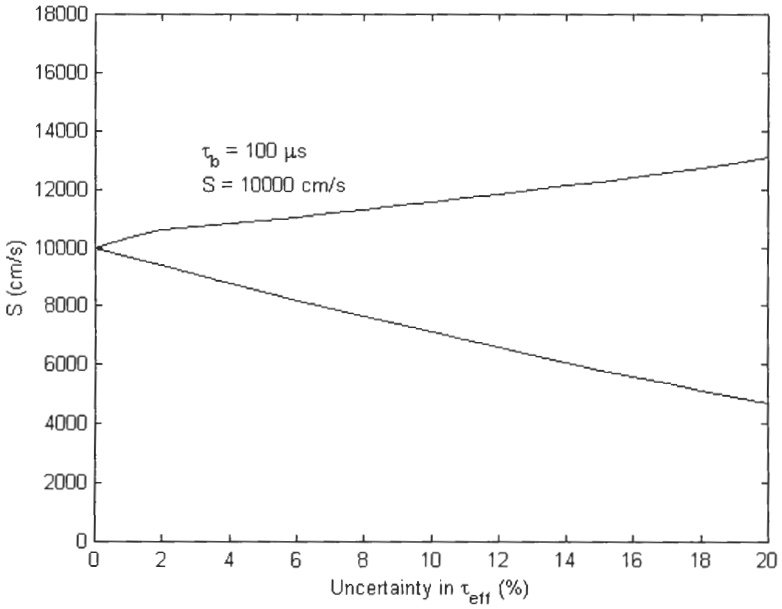

d.

Figure 51, c and d. Influence of uncertainty in τ_{eff} on S ranges obtained from two-spectrum analysis. S must lie between the two lines. For zero uncertainty in τ_{eff}, S is constrained to a single point. τ_b = 10 µs.

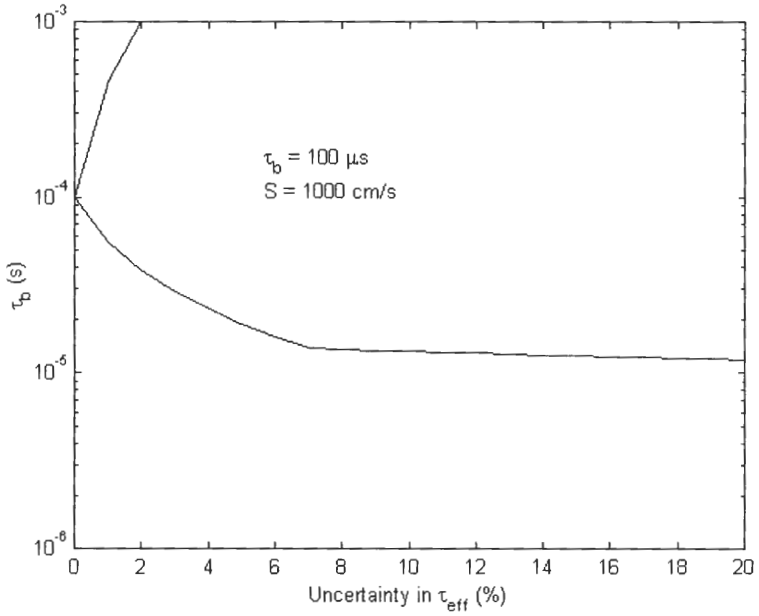

a.

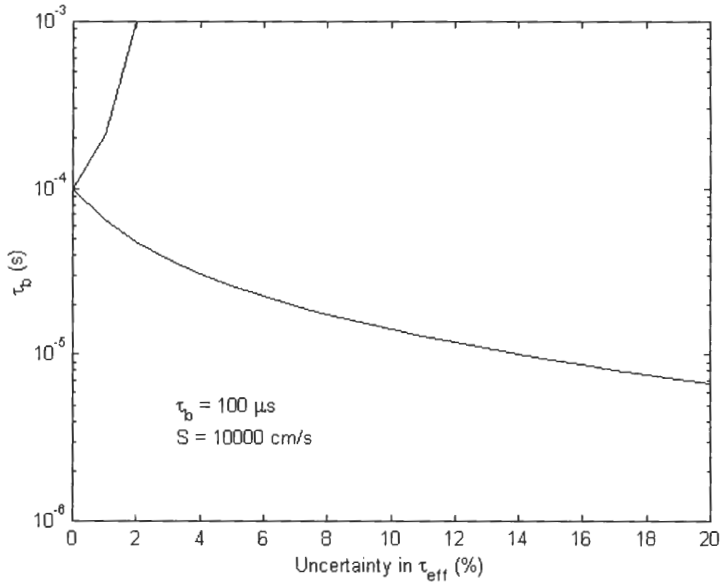

b.

Figure 52, a and b. Influence of uncertainty in τ_{eff} on ranges of τ_b determined by two-spectrum method. τ_b = 100 µs.

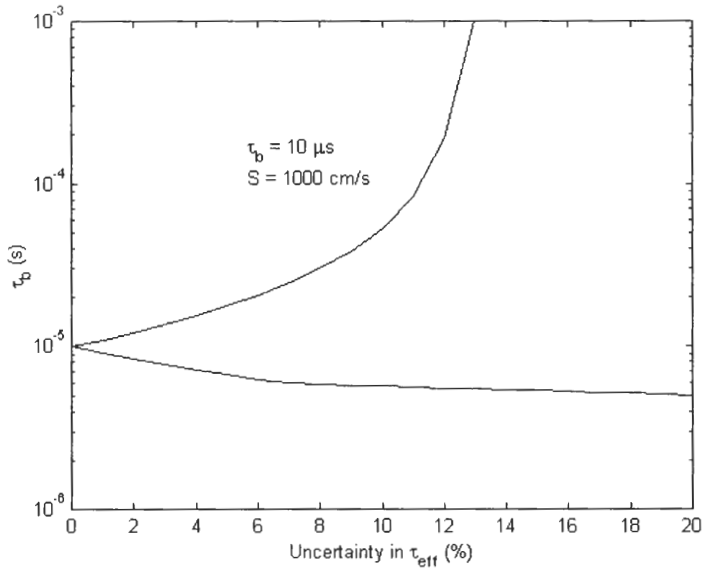

c.

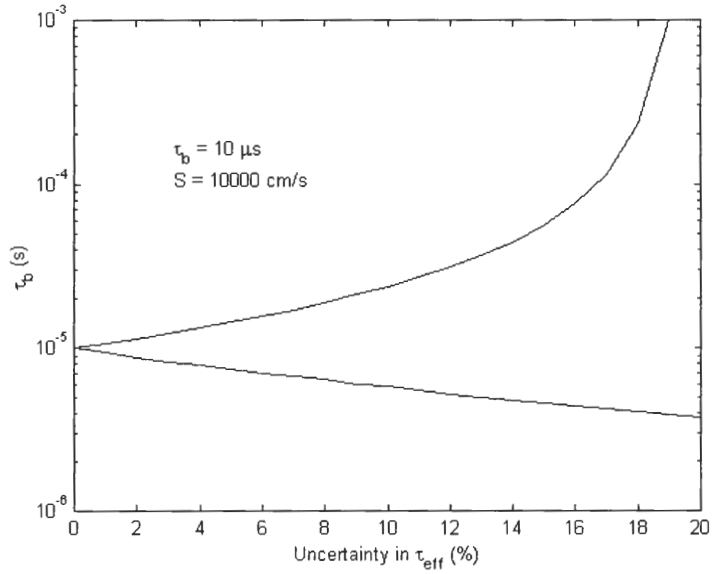

d.

Figure 52, c and d. Influence of uncertainty in τ_{eff} on ranges of τ_b determined by two-spectrum method. τ_b = 10 µs.

5.6 Development and Implementation of Three-Wavelength Method

Two improvements over the original two-wavelength method [7] will now be introduced. The most worrisome aspect of the original procedure is the assumption of a ±10% error in a single τ_{eff} measurement. We have demonstrated that the resulting S and τ_b ranges vary dramatically as the assumed error in τ_{eff} is changed. Instead of making arbitrary assumptions about the measurement error, we will use repeated measurements and distribution-free statistical intervals to experimentally infer upper and lower limits to τ_{eff}.

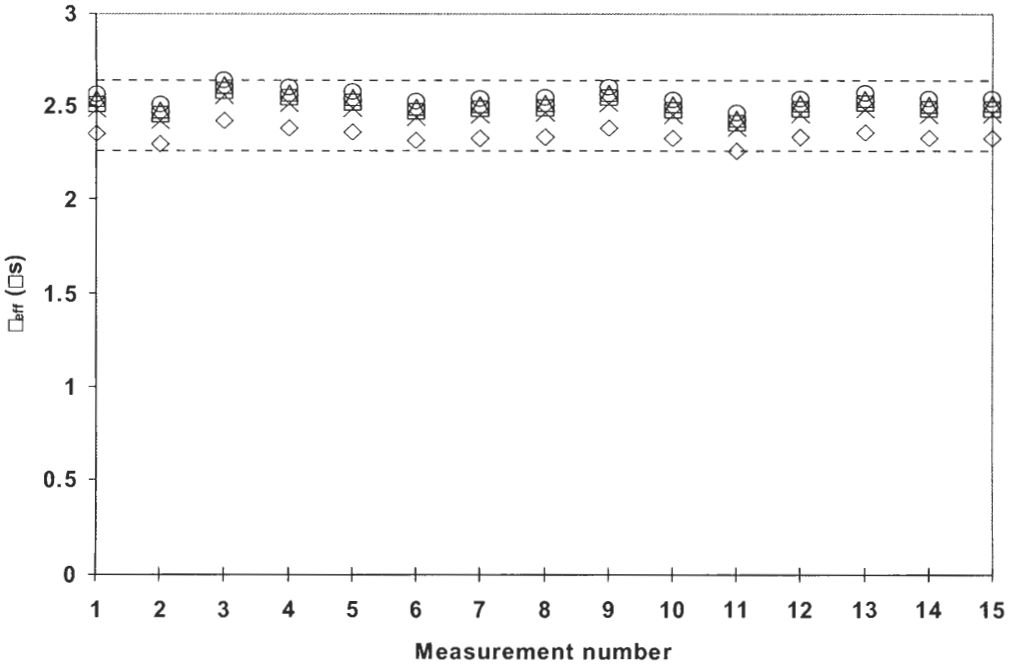

Figure 53. Fifteen repeated measurements of τ_{eff} calculated using each of five measured calibration constants, for a total of 75 possible experimental values of τ_{eff}. The broken lines indicate highest and lowest measured values.

For each wavelength used, we repeat five times the empirical procedure described in Sec. 5.2 to determine the constant of proportionality (K_{cal}) between J_{sc} of the reference cell and G_{av} in the calibration wafer. A sample of five values of K_{cal} is obtained. For each test wafer, K_{test} is computed from K_{cal} using Equation (74). Then we measure τ_{eff} for each test wafer 15 times on a chosen spot. If each of the five calibration constants is combined with each of the 15 τ_{eff} measurements, we obtain 75 possible τ_{eff} values as shown in Figure 53; the five different symbols represent the five different calibration constants. To obtain upper and lower limits to τ_{eff} based on our measurements, we seek a statistical tolerance interval with a high probability (β) of containing a large fraction (γ)

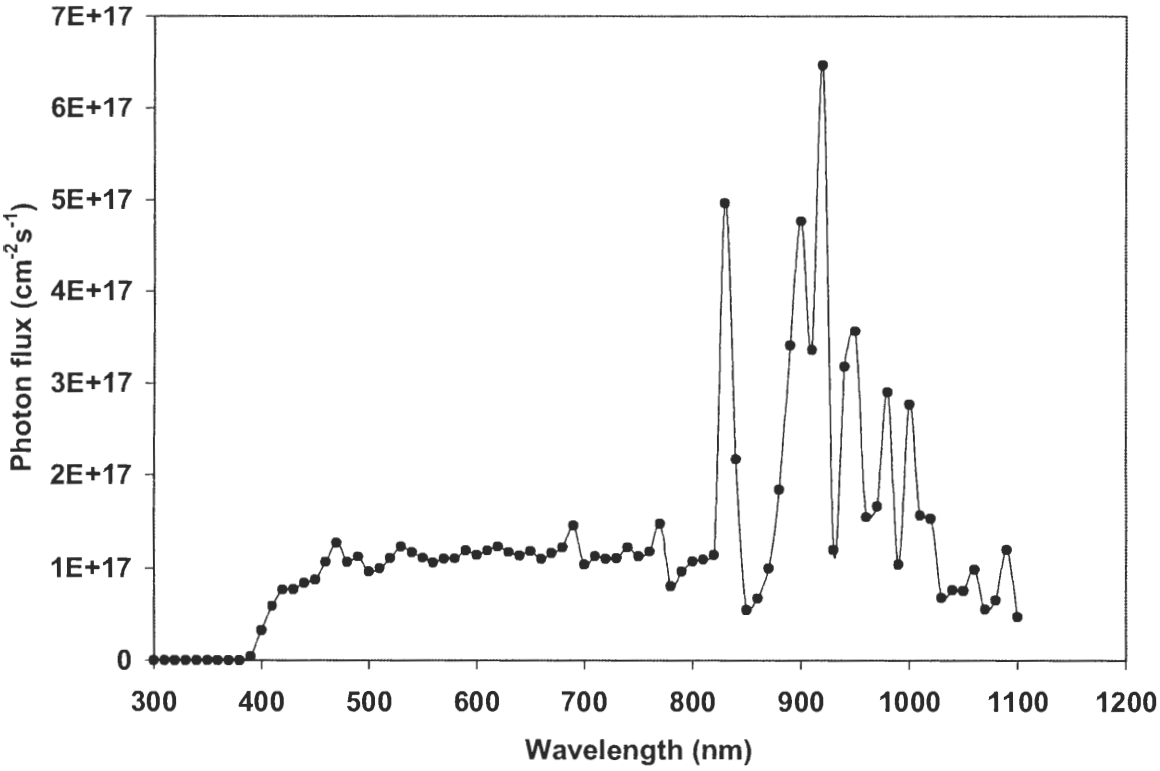

Figure 54. The photon flux for the flash lamp used in the lifetime measurements, calculated from the spectral irradiance measured at NREL. The diffusor plates through which the lamp shines block short-wavelength light.

of the population sampled.

A large number of techniques exist for establishing tolerance intervals [73]. Many of these assume an analytic form for the distribution of the sampled population. This dubious assumption, however, is unnecessary, and we will instead choose a distribution-free tolerance interval. If no assumptions at all are made about the population, then the distribution-free tolerance limits always fall within the set of measured values [73]. It seems prudent to prefer tolerance limits that can exceed the range of measured values; as the tolerance interval expands, the probability that it contains a high fraction of the population increases.

Let us assume that the population is symmetrical about the median. This is a much less restrictive assumption than the assignment of a particular analytical distribution, and it is a reasonable assumption because there is no reason random measurement error should be asymmetrical. For a continuous symmetrical population, a distribution-free tolerance interval can be defined as $[L_{low}, L_{high}]$, where [74]

$$L_{low} = \min[x(1), 2x(1)-x(n)] \tag{77}$$

and

$$L_{hi} = \max[x(n), 2x(n)-x(1)]; \tag{78}$$

x(1) and x(n) are the lowest and highest values, respectively, from the measured data set, and n is the number of values in the data set. For the data shown in Figure 53, n = 75, and x(1) and x(n) are indicated by the broken lines.

When Equations (77) and (78) define the tolerance interval, there is a known relationship [74] among the minimum n required so that the tolerance interval has a

probability of at least β of containing at least a fraction γ of the population. When β and γ are "not too small (say, $\beta \geq .8$ and $\gamma \geq .85$)" [74], that relationship is given by

$$n = \log(1-\beta)/\log\gamma. \qquad (79)$$

With $n = 75$ and choosing $\beta = 0.95$, Equation (79) gives $\gamma = 0.96$. Thus, Equations (77) and (78) provide tolerance limits that are at least 95% likely to contain at least 96% of the population. We then use these experimentally obtained τ_{eff} limits exactly the way the original method [7] used the (arbitrary) ±10% limits.

Our second improvement over the original method is to use a third wavelength to obtain a smaller region of common intersection than would be found using only two wavelengths. The three wavelengths we chose were 500 nm, 910 nm, and 1000 nm, and we obtained optical filters with bandwidths of 71 nm, 39 nm, and 16 nm, respectively. Below 500 nm, the lamp's photon flux is very low, as shown in Figure 54. (The photon flux was calculated from the spectral irradiance measured at NREL. The low-wavelength photon flux is low because the diffusor plates through which the lamp shines filter out the low wavelengths.) Above 1000 nm, the photon absorption in the wafer is very low. 910 nm is the wavelength whose S vs. τ_b curve tends to be about halfway between the 500 nm and 1000 nm curves, as shown in the simulation results of Figure 55. Thus, given 500 nm and 1000 nm illumination, 910 nm is the intermediate wavelength that provides the most additional information.

Nine string-ribbon multicrystalline wafers (three each of 0.6-0.8 Ω-cm, 1.3-1.5 Ω-cm, and 4-5.9 Ω-cm), nine cast multicrystalline wafers (three each of 0.3 Ω-cm, 0.5 Ω-cm, and 2 Ω-cm), and 12 float zone wafers (three of 0.7 Ω-cm, six of 1.3 Ω-cm, and three of 2.9 Ω-cm) were prepared for measurement. One third of the wafers were passivated

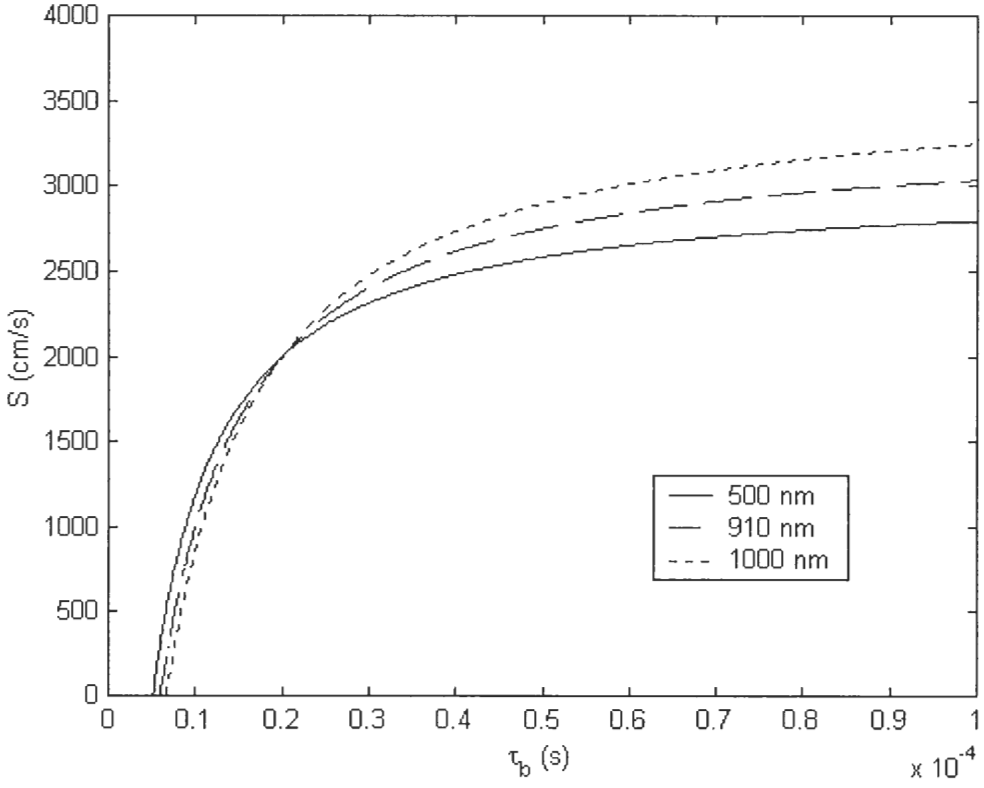

Figure 55. Calculations showing that the S vs. τ_b curve for 910 nm illumination is roughly midway between the curves for 500 nm and 1000 nm. Thus, 910 nm provides more information than other intermediate wavelengths.

with silicon nitride, one third with silicon dioxide, and one third with an oxide/nitride stack. Each of the 18 multicrystalline wafers was measured on three spots, and each of the 12 float zone wafers was measured on one spot, for a total of 66 spots measured. On each of these 66 spots, τ_{eff} was measured 15 times under 500 nm illumination, 15 times under 910 nm illumination, and 15 times and 1000 nm illumination. The 45 measurements of each spot yield a grand total of 2970 measurements.

Before τ_{eff} was measured, the calibration procedure to determine the constant of proportionality between J_{sc} in the reference cell and G_{av} in the calibration wafer was performed five times for each wavelength. One set of calibration factors was used for the

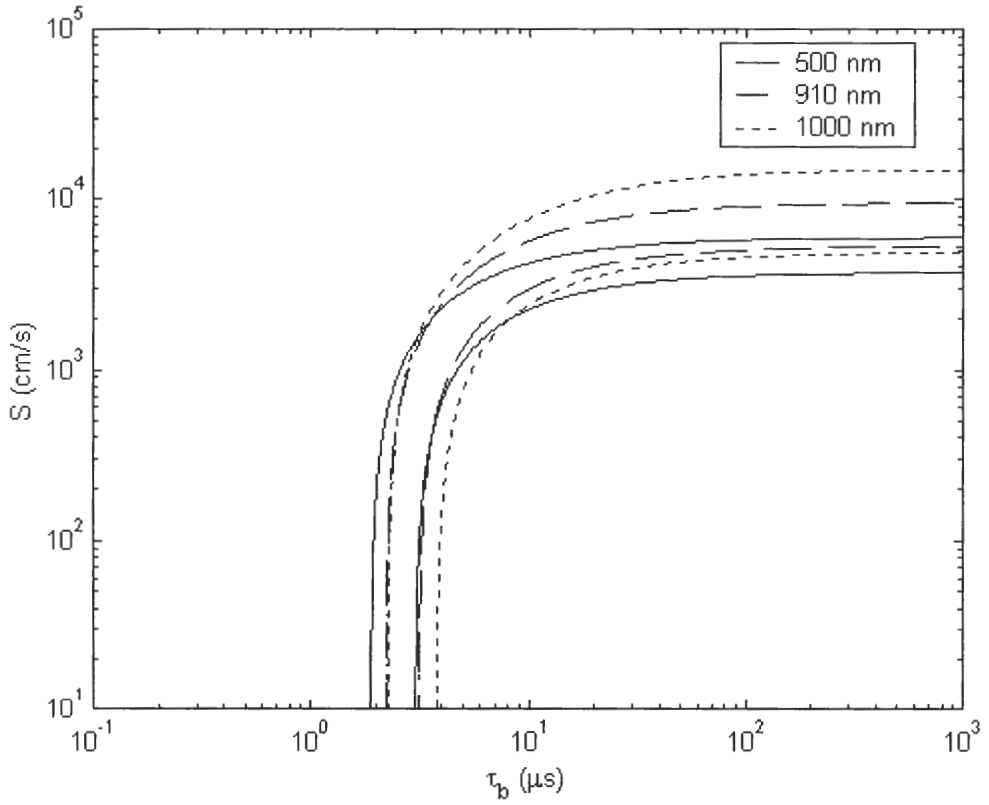

Figure 56. Results for one spot measured on a nitride-coated, 0.7 Ω-cm string ribbon wafer.

string ribbon wafers. Several weeks elapsed before the rest of the wafers were measured, so the calibration measurements were performed again for use in the measurements of the cast mc-Si and float zone wafers.

For each spot measured, upper and lower limits to τ_{eff} for each wavelength were determined using Equations (77) and (78). These upper and lower limits to τ_{eff} were then used to generate lower and upper S vs. τ_b curves for each of the three wavelengths, resulting in a figure such as Figure 56. The region of common intersection for all three wavelengths was then used to find ranges of S and τ_b consistent with experiment.

Following the three-wavelength measurements, the iodine/methanol method was attempted on the three spots of each of the 18 multicrystalline wafers and one spot each of nine of the float zone wafers: in each case, τ_{eff} with dielectric passivation was measured using the full spectrum of the lamp, the dielectrics were removed, and the wafers were cleaned and measured in the iodine solution. Results for this part of the experiment are shown in Figure 57. Consistent with Figures 38, 39, and 40, the float zone wafers are all better passivated by iodine than the dielectrics, whereas many multicrystalline wafers appear better passivated by the dielectrics.

Since the iodine method is considered reliable for float zone, the float zone data will be analyzed using all three methods discussed: the three-wavelength analysis introduced in this section (upper and lower limits to τ_{eff} determined through tolerance intervals based on experimental data sets), the original two-wavelength analysis (±10% and ±20% uncertainty are assumed for each 500 nm and 1000 nm τ_{eff}, which is determined in this case by the average of 15 measurements), and the iodine/methanol method (the lifetime measured during immersion in the passivating solution is assumed to give τ_b). Results are shown in Figure 58.

Figure 58.a indicates that the range of S values determined by the three-wavelength analysis is always wider than the range determined by the two-wavelength analysis, in which 10% uncertainty is arbitrarily assumed. Of course, the two-wavelength results depend critically on the choice of uncertainty. Figure 58.b shows results when ±20% is used for the two-wavelength calculations. These are very close to the results for the three-wavelength analysis. The three-wavelength analysis based on confidence

intervals has the advantage of a foundation in repeated measurements, rather than an arbitrary choice of uncertainty.

Three other facts are apparent in Figure 58. First, the iodine-method results show the expected trend for S to improve as resistivity increases. Second, the results indicate acceptably good S, often under 100 cm/s. Third, the higher the iodine-method S is, the higher the upper limit to S tends to be for the two- and three-wavelength analyses. This observation may aide in interpreting three-wavelength results for the multicrystalline materials, for which the iodine method does not reliably give meaningful ($S > 0$) results.

Three-wavelength results for the multicrystalline materials are shown in Figures 59 and 60. Recall that three points were measured on each of these wafers. Since the lower limit to S is 0 in every case, only the upper limits are shown. Though these multicrystalline materials were passivated identically to the float zone wafers, the upper limits to S are much higher. Cast multicrystalline silicon at least shows the expected resistivity trend, and $S < 500$ for stack- and oxide-passivated wafers of 0.5 Ω-cm and 2 Ω-cm resistivity. String ribbon, on the other hand, shows no resistivity trend, and the upper limits to S are extremely high. Since only upper limits to S are determined, these results merely suggest, rather than conclusively prove, that S for identically passivated materials is lowest for float zone, higher for cast mc-Si, and highest for string ribbon.

These limits on S, from Figures 59-60, will be used in device modeling in Task 5.

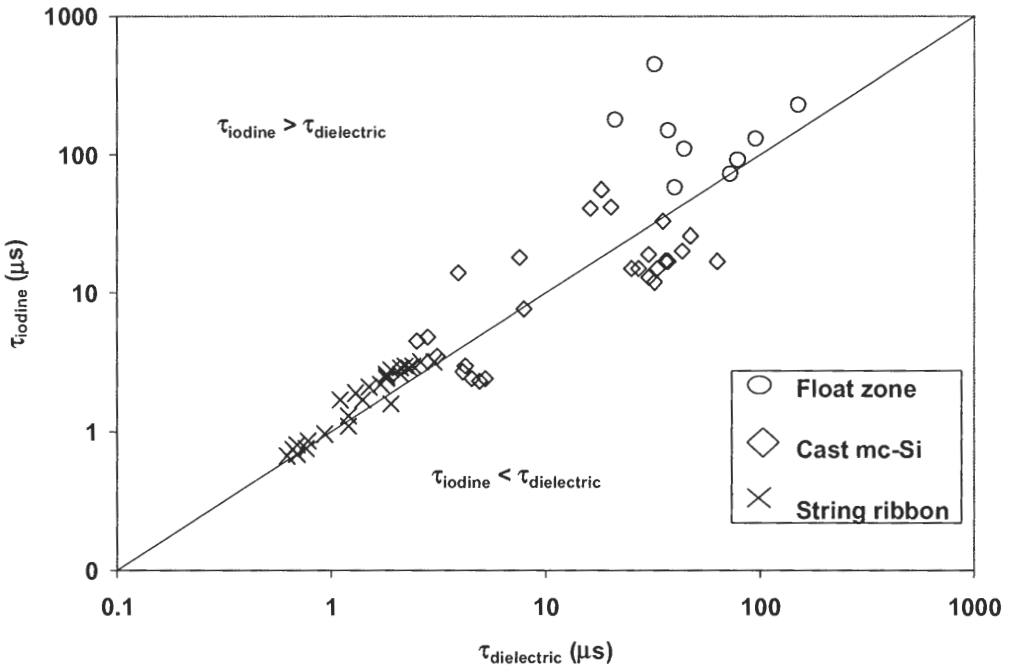

Figure 57. Comparison of lifetime measured for dielectric and iodine passivation.

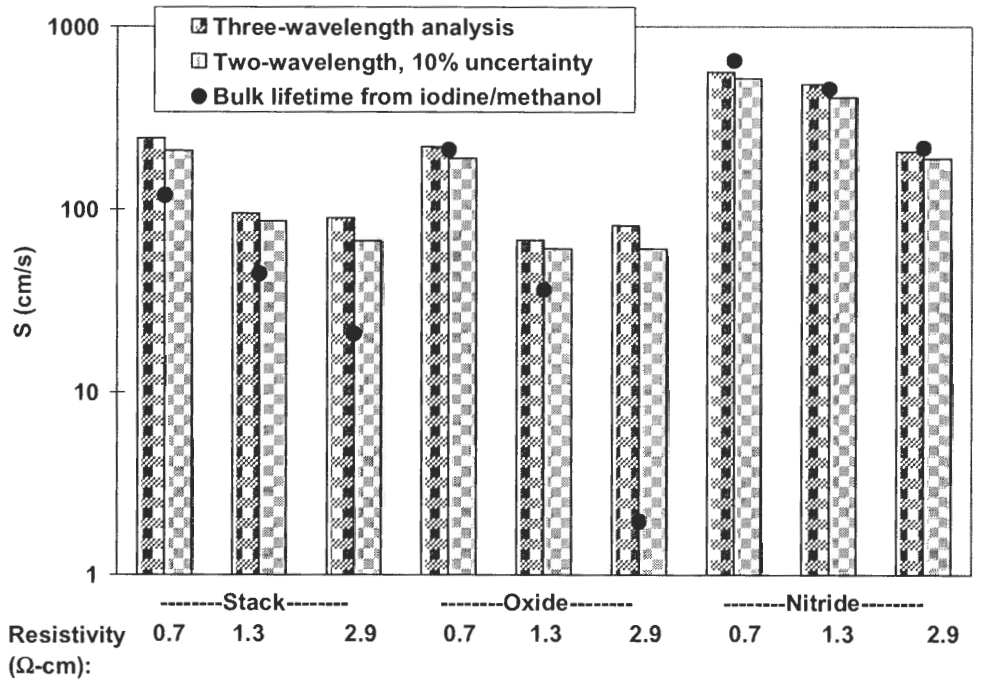

a.

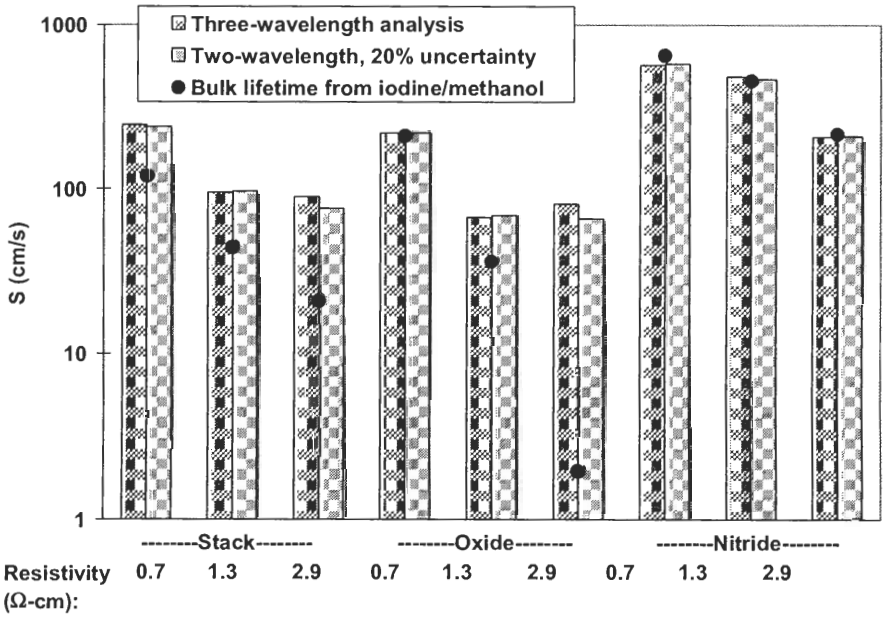

b.

Figure 58. S results, computed three different ways, for nine float zone wafers. The columns represent S ranges consistent with the indicated methods. The uncertainty used in the two-wavelength computations is either 10% (a) or 20% (b).

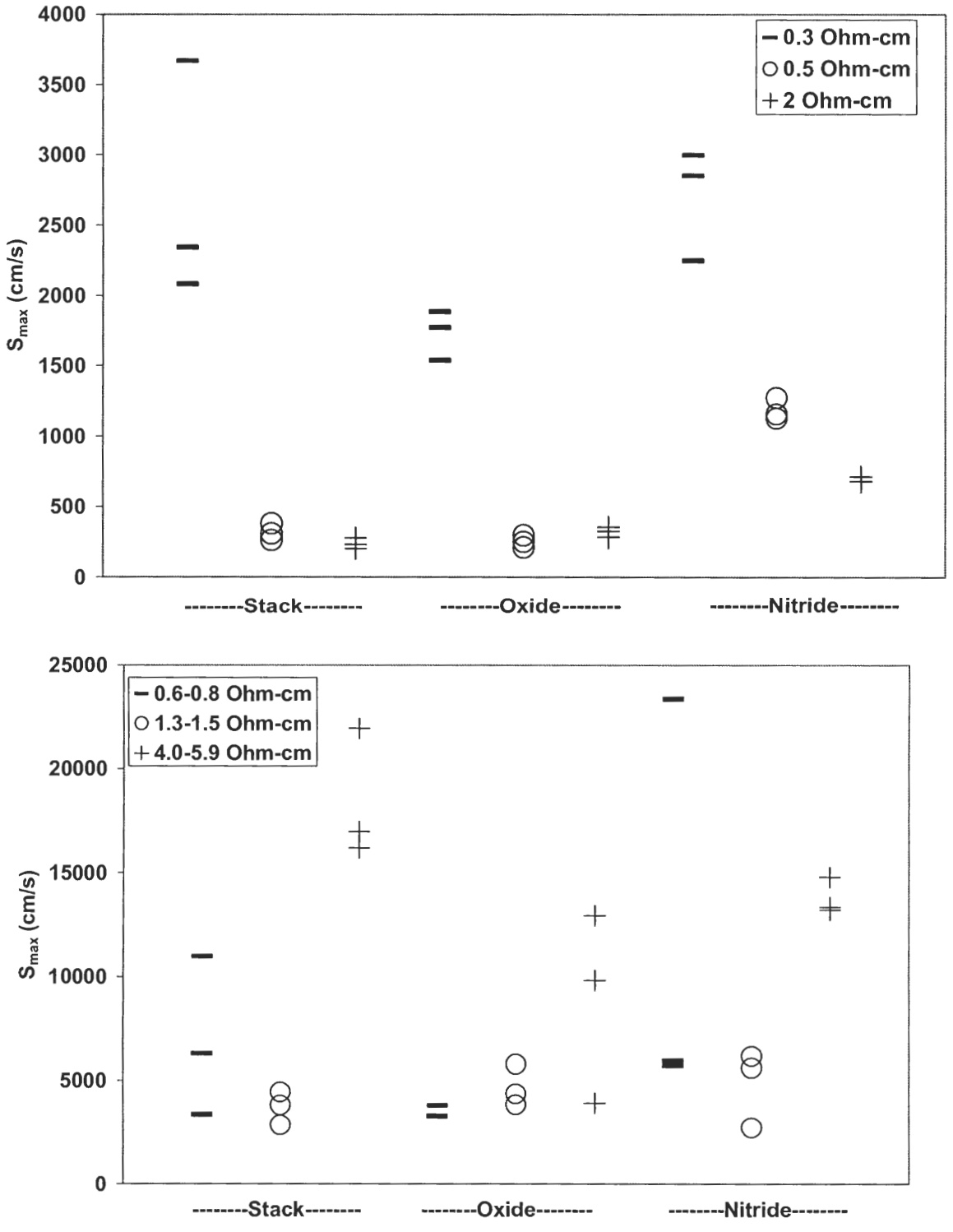

Figure 59. Upper limits to S determined by the three-wavelength analysis for three points measured on each cast multicrystalline wafer.

5.7 Novel Analytical Approximations to the Extended SRH Formalism To Explain Doping Dependence of S

In the previous section we saw that there was a doping dependence of S for float zone silicon, resulting in higher S for higher doping level. In addition, nitride passivation for this material was found to be worse than the oxide or stack dielectrics. This is largely attributed to a difference in dielectric charge and interface states. In this section, an attempt is made to understand the influence of dielectric properties, substrate doping, and injection level on S.

As reviewed in Section 2.3.2, exact, analytical expressions for S are not possible when charge stored in a dielectric passivation layer causes band bending. Thus, the extended SRH formalism involves a numerical procedure to calculate S as a function of doping level or injection level. The results of the extended SRH formalism are then families of curves whose physical causes and consequences are not immediately obvious. Accordingly, new analytical approximations to the extended SRH formalism will be derived to better understand the influence of such parameters as dielectric charge, interface state concentration, and capture cross-section on the doping dependence of S.

5.7.1 Theory and Modeling

Analytical approximations are derived by solving for Ψ_s under given conditions. The starting point is Equation (29) under the assumption that interface charge Q_{it} is negligible [37], resulting in

$$Q_{Si} = -Q_f. \tag{80}$$

The assumption of negligible Q_{it} is investigated in Figure 61, obtained by numerical simulation for the case of dielectric charge $Q_f = 2\times10^{11}$ cm^{-2}. To be consistent with Figure 12 (reproduced for convenience in this section), we have assumed $N_A = 1\times10^{16}$ cm^{-3} and $N_{st} = 1\times10^{10}$ cm^{-2} in this simulation. The solid curve represents Q_{Si}, which is observed to scarcely deviate from -2×10^{11} cm^{-2} ($-Q_f$) for the entire range of injection levels. We thus observe the validity of Equation (80) since $Q_{Si} = -Q_f$. Note too in Figure

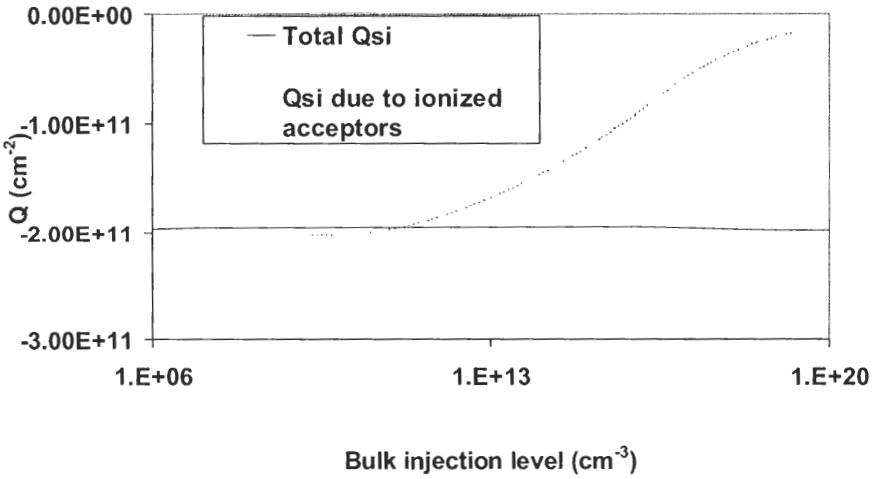

Figure 61. Numerical simulation of Q_{Si} vs. Δn for curve 4 in Figure 12 ($Q_f = 2\times10^{11}$ cm^{-2}). Note that $Q_{Si} \approx -Q_f$ for all injection levels, thereby justifying Equation (80).

61 that at low injection levels, the total Q_{Si} is within 10% of the Q_{Si} due only to ionized acceptors. Q_{Si} due only to ionized acceptors is calculated by using only the last term on the right side of Equation (31)

$$F(\Psi_s,\varphi_n,\varphi_p) = e^{q(\varphi_p-\Psi_s)/kT} - e^{q\varphi_p/kT} + e^{q(\Psi_s-\varphi_n)/kT} - e^{-q\varphi_n/kT} + \frac{q\Psi_s N_A}{kTn_i} \qquad (31)$$

and inserting into Equation (30)

$$Q_{Si} = -\sqrt{\frac{2kTn_i\varepsilon_{Si}}{q^2}F(\Psi_s,\varphi_n,\varphi_p)}\,; \qquad (30)$$

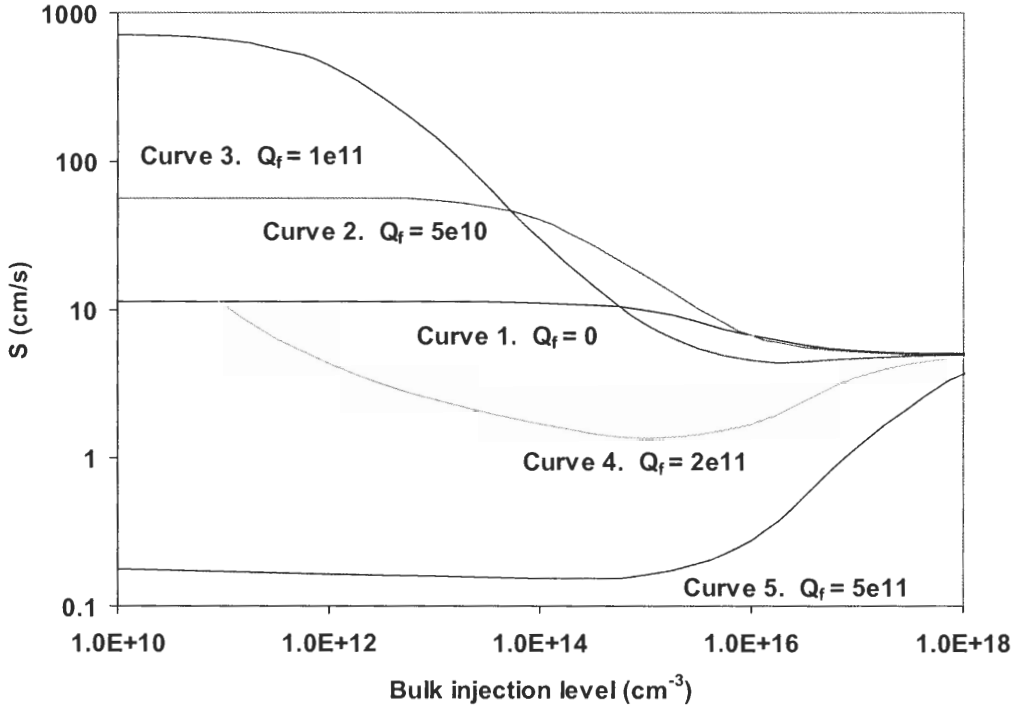

Figure 12. Numerical simulation of surface recombination velocity as a function of injection level for p-type silicon, reproduced from Aberle [9]. Here, $N_A = 1\times10^{16}$ cm^{-3}, $N_{st} = 1\times10^{10}$ cm^{-2} (evenly divided between acceptor and donor states), and $\sigma_n = \sigma_p = 1\times10^{-16}$ cm^2.

total Q_{Si} is calculated using all five terms in Equation (31). Thus the last term in Equation (31), resulting from ionized acceptors, dominates the expression at low injection levels. This observation that Q_{Si} may be dominated by ionized acceptors will be used in Cases A and B below. In contrast, Q_{Si} is dominated by mobile electrons in Cases C and D, which correspond with greater band-bending arising from greater Q_f.

Next, in order to solve for Ψ_s analytically, Equation (30) is equated with Equation (80) and simplified by an appropriate set of assumptions described below. In order to obtain simple analytical approximations that explain the behavior of all curves in Figure

12, four cases have been identified. (The cases correspond with the four questions raised in Sec. 2.2.2.)

Case A: LLI with $p_s >> n_s$ and Q_{Si} due primarily to ionized acceptors.

Case B: LLI with $n_s >> p_s$ and Q_{Si} due primarily to ionized acceptors.

Case C: LLI with $n_s >> p_s$ and Q_{Si} due primarily to mobile electrons.

Case D: HLI with $n_s >> p_s$ and Q_{Si} due primarily to mobile electrons.

Case C was investigated by Kuhlmann [37], resulting in Equation (34).

The first three cases are distinguished by band-bending, resulting from different levels of Q_f. Case A corresponds with the least band-banding and lowest Q_f, while Case C corresponds with the most band-banding and highest Q_f; Case B is an intermediate condition. For example, it is shown below that part of curve 2 ($Q_f = 5\times10^{10}$ cm^{-2}) from Figure 12 can be approximated with Case A, part of curve 4 ($Q_f = 2\times10^{11}$ cm^{-2}) can be approximated with Case B, and part of curve 5 ($Q_f = 5\times10^{11}$ cm^{-2}) can be approximated with Case C.

To compare the analytical approximations with the full numerical solutions, curves 2, 4, and 5 from Figure 12 are reproduced in Figure 62. (Curve 1 is omitted because it represents the flatband situation that can be described analytically without approximation, and curve 3 is omitted because it is similar to curve 2.) The approximations deviate significantly from the numerical solutions, but the order of magnitude and predicted behavior (increasing, decreasing, or constant) are consistently correct. (There is a good reason, discussed below, why the Case A approximation is evidently the least accurate.) Each case will now be considered in turn.

Case A. With $p_s >> n_s$, Q_{Si} is due largely to ionized acceptors because $N_A >> p_s$ for positive Q_f (depletion conditions) [33, 37]. This means that all terms in Equation (31) except the last may be disregarded, since the last term represents Q_{Si} due to ionized acceptors. (This can be concluded from the discussion by Grove and Fitzgerald [33], p. 789.) Then Ψ_s can be written as

$$\Psi_s = \frac{qQ_f^2}{2\varepsilon_{Si}N_A} \tag{81}$$

where we have used $F(\Psi_s, \varphi_n, \varphi_p) = \frac{q\Psi_s N_A}{kTn_i}$ and $Q_{Si} = -Q_f$. Substituting Equation (81)

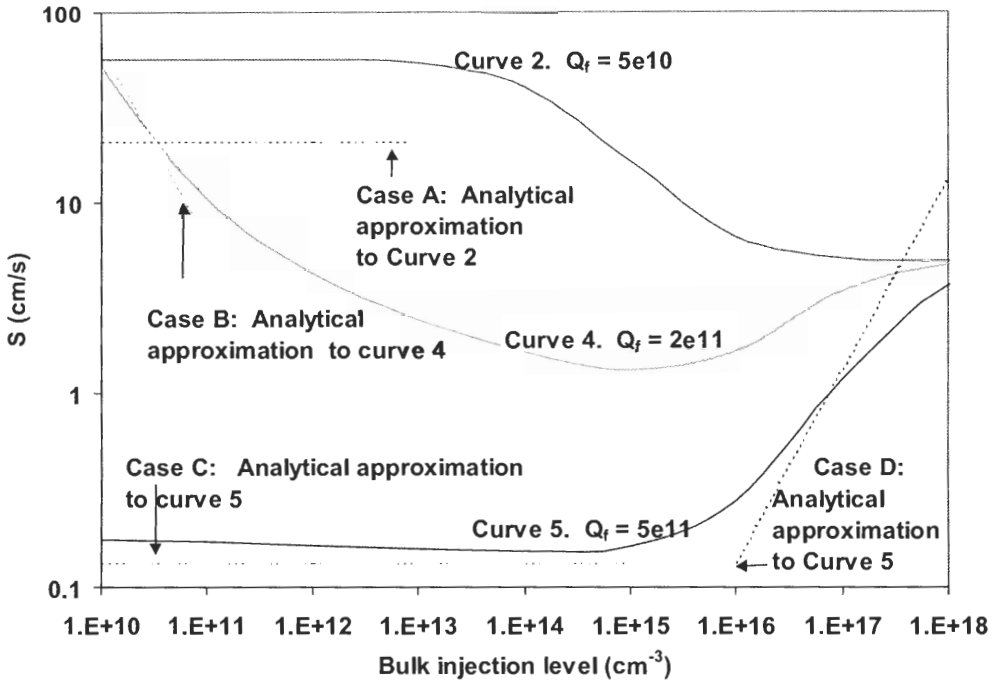

Figure 62. Comparison of three numerical solutions from Figure 12 (curves 2, 4, and 5) with analytical approximations. The Case A approximation is the least accurate because it is the most sensitive to error in Ψ_s, with $S_{eff} \propto e^{\frac{q\Psi_s}{kT}}$. Since Ψ_s is determined approximately, the relatively small error in Ψ_s leads to a larger error in S_{eff} in Case A.

into Equation (33)

$$S_{eff} = \frac{U_s}{\Delta n} = \frac{v_{th} N_{st}[(n_0 + \Delta n)(N_A + \Delta n) - n_i^2]}{\Delta n\left(\frac{(n_0 + \Delta n)e^{q\Psi_s / kt}}{\sigma_p} + \frac{(N_A + \Delta n)e^{-q\Psi_s / kT}}{\sigma_n}\right)} \tag{33}$$

and applying the assumptions of LLI ($N_A >> \Delta n >> n_i >> n_0$) and $p_s >> n_s$ results in

$$S_{eff} = v_{th} N_{st} \sigma_n e^{\frac{q\Psi_s}{kT}} = v_{th} N_{st} \sigma_n e^{\frac{q^2 Q_f^2}{2kT\varepsilon_{Si} N_A}}. \tag{82}$$

This equation explains why curve 2 in Figure 62 is flat at low injection levels. The curve declines at higher injection levels as n_s approaches the same order of magnitude as p_s and Equation (82) loses its validity. The transition from $p_s >> n_s$ to $p_s \sim n_s$ is explained in Figure 63, obtained by numerical calculations. The solid line is electron surface concentration, and the thin dashed line is hole surface concentration. Where n_s approaches p_s and Equation (82) becomes inapplicable, S_{eff} changes with injection level. S_{eff} drops to approach the flatband case (curve 1 in Figure 12) because increasing injection level causes more electrons to accumulate near the interface and lower Ψ_s [9]. Equation (82) also predicts that when $p_s >> n_s$, small increases in Q_f cause large increases in S_{eff}.

Equation (82) shows that for Case A, even though Q_f and Ψ_s are small, S_{eff} is very highly sensitive to Ψ_s, which is obtained approximately through Equation (81). Recall that Q_f appears in Equation (81) as an approximation to Q_{Si} due to ionized acceptors. The relatively small (~20%) error in this approximation leads to a larger error in S_{eff}, in this

case, given the exponential dependence of S_{eff} on Ψ_s. The high sensitivity to Ψ_s explains why the Case A approximation is the least accurate of the four.

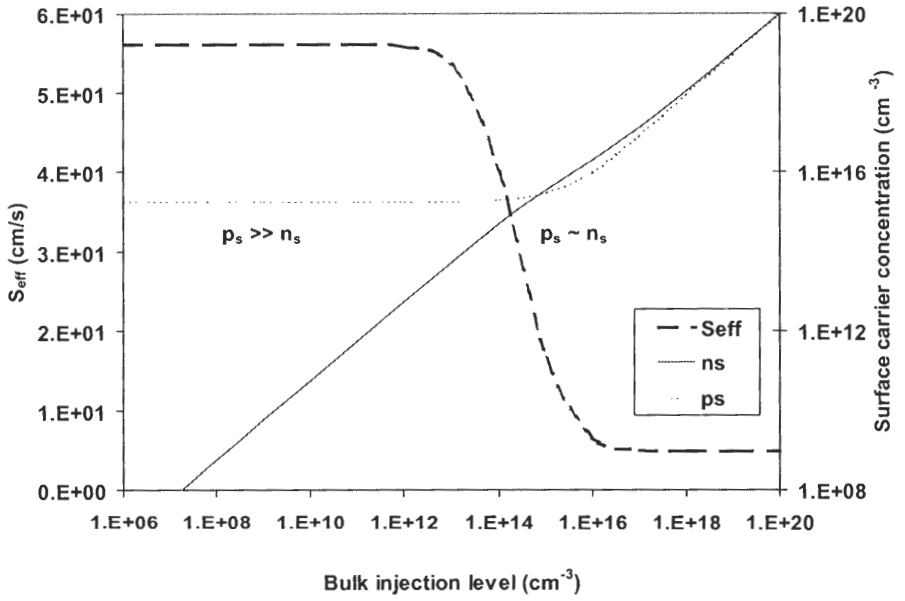

Figure 63. A comparison of electron and hole surface concentrations for curve 2 of Figures 12 and 61 ($Q_f = 5\times10^{10}$ cm^{-2}). S_{eff} is independent of Δn whenever $p_s >> n_s$, as predicted by Equation (82).

Case B. While searching for an explanation for the behavior of curve 4 in Figure 62, it is observed that at very low injection levels, although $n_s >> p_s$, it is still the case that Q_{Si} is due mainly to ionized acceptors. This observation is made by examining the results of the numerical solution in Figure 61. Thus, Equation (81) is still valid. Case B is associated with higher Q_f and Ψ_s than Case A. This switches the carrier concentration from $p_s >> n_s$ to $n_s >> p_s$ while maintaining $F(\Psi_s, \varphi_n, \varphi_p) = \dfrac{q\Psi_s N_A}{kTn_i}$ and $Q_{Si} = -Q_f$.

Solving for S_{eff} again, but now using $n_s >> p_s$, we find

$$S_{eff} = \frac{v_{th} N_{st} \sigma_p N_A e^{\frac{-q^2 Q_f^2}{2\varepsilon_{Si} kTN_A}}}{\Delta n}. \tag{83}$$

This equation adequately describes the injection level dependence of curve 4 of Figure 12 at low injection levels, where Q_{Si} is due to ionized acceptors. At higher injection levels within LLI, Q_{Si} becomes a consequence predominantly of mobile electrons, and Equation (34) takes effect, flattening out the curve.

Case C. When $n_s >> p_s$ and Ψ_s is larger than in Case B (due to higher Q_f), Equation (31) is dominated by the third term on the right instead of the last term. The third term, which dominates when Ψ_s is large, represents charge due to mobile electrons. It is expedient to solve for Ψ_s from Equation (30) as follows [37]:

$$e^{-\frac{q\Psi_s}{kT}} = \frac{2\varepsilon_{Si} kT\Delta n}{q^2 Q_f^2}. \tag{84}$$

Upon substitution of Equation (84) into Equation (33) under the assumptions of low-level injection, Equation (34) can be obtained. (Kuhlmann obtained Equation (34) by considering a voltage applied to a semiconductor in the dark. Here we find the same result by considering an illuminated semiconductor under no applied voltage.)

Case D. The only difference between Case C and Case D is that Case D is in HLI. Equation (84) is still valid because the conditions of inversion and Q_{Si} due primarily to mobile electrons are still used. Using $\Delta n >> N_A$ for the case of high level injection and substituting Equation (84) in Equation (33) results in

$$S_{eff} = \frac{2v_{th}\varepsilon_{Si}\sigma_p kTN_{st}\Delta n}{q^2 Q_f^2}. \tag{85}$$

This equation explains the increase in S_{eff} with Δn observed in curve 5 of Figure 62 in the high-level injection regime.

Thus Equations (82), (83), and (85), introduced here, along with Equation (34) from Kuhlmann, explain the behavior of all sections of all curves in Figures 12 and 62. An additional comparison between analytical approximations and numerical solutions is found in Figure 64, where two numerically computed S vs. N_A curves are compared with the predictions of Equation (34). The agreement is found to be excellent at relatively low doping levels, where the assumption that $n_s >> p_s$ is most accurate.

5.7.2 Comparison of Experimental Data, Analytical Expressions, and Numerical Simulation

Various dielectrics (SiO_2, SiN_x, and SiO_2/SiN_x stack) were deposited on p-type FZ wafers to obtain S_{eff} vs. Δn data for Case B and S_{eff} vs. N_A data for Case C. The effective lifetimes (τ_{eff}) were measured by means of inductively coupled photoconductance decay; τ_{eff} was sufficiently large to satisfy transient conditions. S_{eff} can be calculated from τ_{eff} using standard equations [9, 17], namely

$$S_{eff} = \sqrt{D_n\left(\frac{1}{\tau_{eff}} - \frac{1}{\tau_b}\right)}\tan\left[\frac{W}{2}\sqrt{\frac{1}{D_n}\left(\frac{1}{\tau_{eff}} - \frac{1}{\tau_b}\right)}\right] \approx \frac{W}{2}\left(\frac{1}{\tau_{eff}} - \frac{1}{\tau_b}\right), \qquad (86)$$

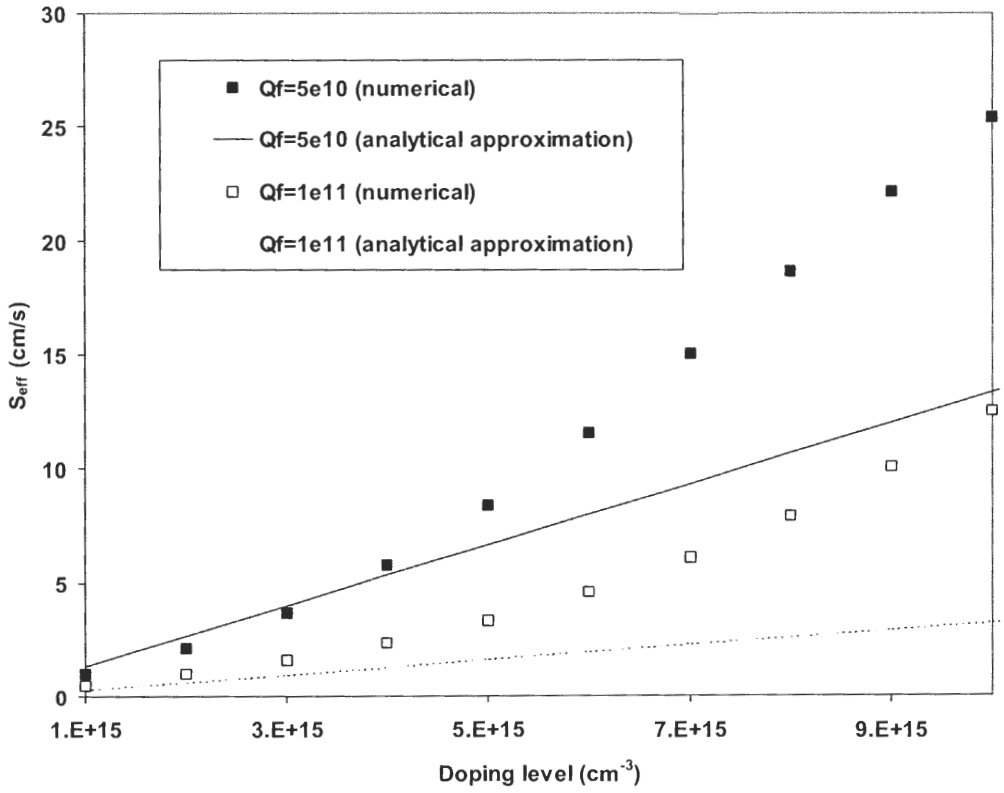

Figure 64. A comparison of analytical approximations and numerical solutions for two S_{eff} vs. N_A curves. Since here $n_s >> p_s$ and mobile electrons dominate Q_{Si} (as confirmed by numerical modeling), the conditions for Case C are met, and Equation (34) is the appropriate analytical approximation. The approximation is most accurate at low doping levels, where the assumption that $n_s >> p_s$ is most accurate (again, as confirmed by numerical modeling).

where the simplified approximation on the right is valid for low S_{eff}. In calculating S_{eff}, bulk lifetime (τ_b) was estimated using an equation often employed in the literature [20, 25]:

$$\tau_b = \frac{\tau_{b,\max}}{1 + N_A / N_{ref}} \qquad (1)$$

where we have set $\tau_{b,max} = 4$ ms and $N_{ref} = 7\times10^{15}$ cm^3.

Case B. A conventional furnace oxide (CFO) was grown on a 2.9 Ω-cm float zone wafer. After a forming gas anneal (FGA), τ_{eff} was measured by inductively coupled photoconductance decay. S_{eff} was calculated from τ_{eff} and is shown in Figure 65. A numerical fit and analytical approximation to the fit are also shown. The values of Q_f and N_{st} used in fitting attempts were chosen with the help of Equation (83): if the fit needed to be elevated to higher values, for example, either N_{st} was raised moderately or Q_f was lowered slightly, as suggested by Equation (83). Equation (83) was chosen because the measured data exhibit Case B behavior: S_{eff} is inversely proportional to Δn.

To obtain a good numerical fit, Q_f was set at 7.6×10^{10} cm^{-2}, and N_{st} was set at 5×10^{10} cm^{-2}. Both capture cross-sections were set equal to 10^{-16} cm^2. The same parameter values were used in the analytical approximation and the numerical simulation. The numerical simulation gives a good fit to the data. The analytical approximation

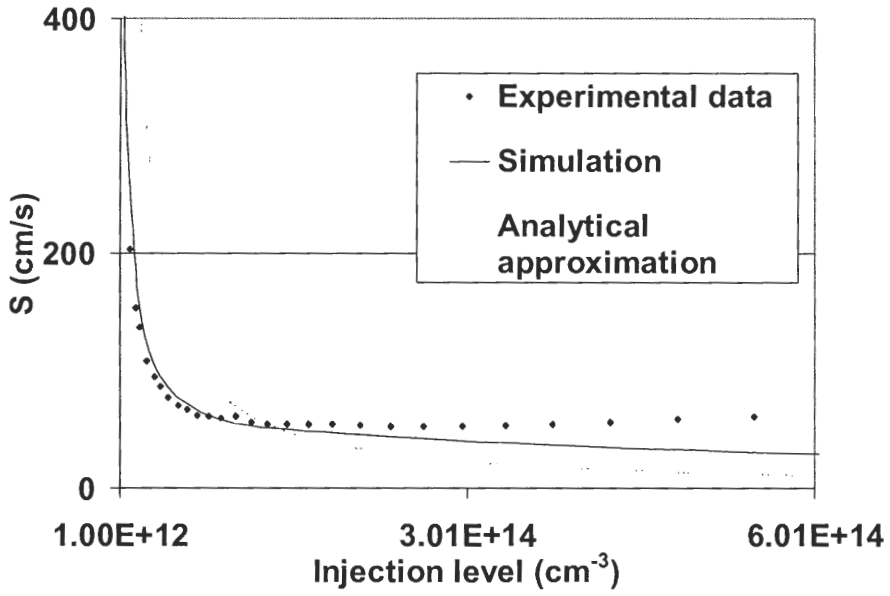

Figure 65. Case B: comparison of experimental, numerical, and analytical values of S_{eff}. This measurement was done on a 2.9 Ω-cm float zone wafer passivated by silicon dioxide.

predicts the right trend for S vs. Δn, but with a somewhat inferior fit.

Case C. Two sets of p-type float zone silicon wafers with of six different resitivities ranging from 0.7 Ω-cm to 10 Ω-cm were cleaned and passivated as follows: An approximately 10 nm oxide was grown on the first set of wafers. After FGA, the effective lifetimes were measured. Then about 80 nm of SiN_x was deposited on both sides of the same wafers, forming a SiO_2/SiN_x stack. The second set of wafers received SiN_x deposition only, at a thickness of about 85 nm. All wafers were given a FGA, effective lifetimes were measured, and S_{eff} was calculated using Equation (86).

The experimental results are represented by the symbols in Figure 66. There is a clear trend toward increasing S_{eff} as N_A increases. The lines in Figure 66 are numerical fits, using the values of Q_f and N_{st} shown in the table. The fits are not unique, but are intended merely to illustrate the compatibility of the computation of U_s based on mid-gap traps with experimental results. The values of Q_f and N_{st} used in preliminary fitting attempts were chosen with the help of Equation (34): the slopes of the experimental S_{eff} vs. N_A curves were calculated, and Equation (34) was used to find approximately which combinations of σ_p, Q_f, and N_{st} would result in the same slopes. These initial values were adjusted to obtain better fits. Equation (34) was chosen because the data exhibit Case C behavior: S_{eff} increases roughly linearly with Δn for the data in Figure 66.

The N_{st} and Q_f values obtained by the fit suggest that CFO has low Q_f and N_{st}, nitride has high Q_f and N_{st}, and the oxide/nitride stack has low N_{st} and high Q_f. The data indicate that the nitride, with high N_{st}, shows a stronger doping dependence of S_{eff}. The oxide and the oxide/nitride stack have smaller N_{st} and smaller doping dependence of S_{eff}, but the oxide/nitride stack gives smaller values of S_{eff} due to higher Q_f.

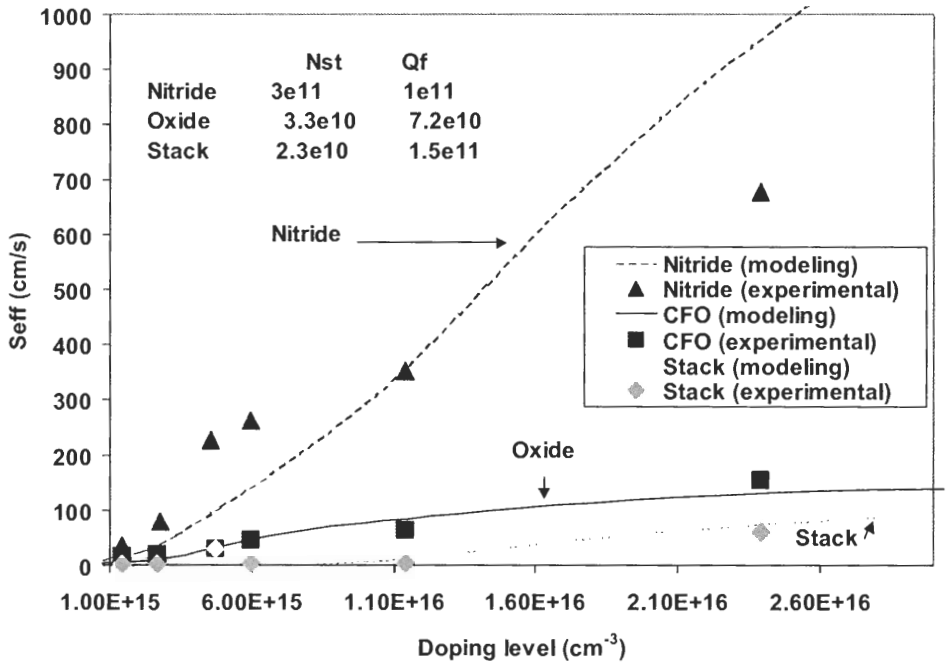

Figure 66. Case C: comparison of experimental and numerical values of S_{eff}. Both capture cross-sections were set equal to 10^{-16} cm^2. The values chosen for N_{st} and Q_f are shown in the table.

5.8 Conclusions

While confirming that the conventional method of iodine passivation can reduce S below 2 cm/s on float zone, we demonstrated that the same iodine solution can fail to passivate string ribbon silicon well enough to determine S for a dielectric. Our sensitivity analysis has shown that the method of using a white light spectrum and an IR spectrum to obtain information about τ_b and S has serious limitations: only a lower bound can be placed on τ_b for τ_b greater than about 10 μs, and only an upper bound can be placed on S for S less than about 1000 cm/s. Thus, both τ_b and S must be somewhat poor in order for their values to be extracted within about an order of magnitude. Fortunately, although

monocrystalline τ_b is too good to be extracted with precision using the two-spectrum method, it can be well determined by the conventional iodine passivation method. The two-spectrum method was applied to float zone and HEM wafers of different resistivity. Only an upper limit to S (165 cm/s) was inferred for the easily passivated float zone wafer, as predicted by our sensitivity analysis. Also consistent with the sensitivity analysis is the fact that both upper and lower limits were inferred for S on the less effectively passivated HEM wafers: 1200 cm/s < S < 4200 cm/s for the 1.4 Ω-cm wafer, and 3000 cm/s < S < 20000 cm/s for the 0.2 Ω-cm wafer. The 0.2 Ω-cm HEM wafer was measured before and after the SiN_x was annealed. As expected, the two-spectrum method provided a τ_b range that remained unchanged, while the S range was higher for the as-grown SiN_x, by a factor of about 3.

The previous results are based on the original two-spectrum method, in which an uncertainty of ±10% is arbitrarily assumed for each τ_{eff} measurement. In this research, two improvements over the original method are introduced. First, instead of using arbitrary 10% uncertainty, repeated measurements are made for each wavelength, and statistical tolerance intervals based on the data are used to set upper and lower bounds to τ_{eff}. Second, a third wavelength is used to narrow the region in the S-τ_b plane consistent with all measurements. Applying this modified method to measured lifetimes, we find that upper S limits for float zone are often under 100 cm/s. However, for identically passivated cast mc-Si samples, the upper S limit often approached 500 cm/s or higher. For identically passivated string ribbon, the upper S limit was extremely high. This suggests, but does not conclusively prove, that different materials may respond differently to identical passivation. For float zone and cast mc-Si, higher resistivity

tended to have better upper limits to S. For string ribbon, no resistivity trend was apparent.

Three new analytical approximations to S_{eff}, Equations (82), (83), and (85), were derived after identifying four cases satisfying different conditions: LLI with $p_s >> n_s$ and Q_{Si} due primarily to ionized acceptors, LLI with $n_s >> p_s$ and Q_{Si} due primarily to ionized acceptors, LLI with $n_s >> p_s$ and Q_{Si} due primarily to mobile electrons, and HLI with $n_s >> p_s$ and Q_{Si} due primarily to mobile electrons. (The third case had previously been treated by Kuhlmann.) The progression from the first to the third case listed above is marked by increased Q_f and band-bending. Understanding the three new equations, along with Equation (34), permitted the explanation of every section of the S_{eff} vs. Δn and S_{eff} vs. N_A curves obtained by numerical procedures. A comparison between the analytical approximations and numerical solutions indicated that Case A is least accurate because it is most sensitive to error in Q_f. Equations (34) and (83) aided in fitting numerical calculations to experimental data for the dielectric passivation of p-type float zone silicon.

CHAPTER 6

IMPACT OF DIELECTRIC, BACK Al COVERAGE, AND BULK RESISTIVITY ON PROCESS-INDUCED BULK-LIFETIME ENHANCEMENT IN CAST AND RIBBON mc-Si

As described in Chapter 2, τ_b in mc-Si is known to respond dramatically to processing. Phosphorous diffusion getters the bulk defects, silicon nitride supplies hydrogen to passivate the bulk defects as well as the surface, and aluminum enhances this hydrogenation and also serves as a gettering site. The experiments described in this chapter seek to answer three important questions.

First, is aluminum-enhanced hydrogenation less effective in bifacial cells with only partial aluminum coverage? If high lifetimes can only be achieved with full aluminum coverage, the appeal of bifacial cells and dielectric rear passivation is greatly diminished.

Second, does the oxide in the oxide/nitride stack impede the flow of hydrogen from the nitride layer to the bulk, reducing bulk passivation? Does stack passivation results in better surface passivation but worse bulk passivation than the nitride alone?

Third, how do final bulk lifetimes depend on resistivity as well as dielectric layer and aluminum coverage in processed cast and string ribbon mc-Si?

6.1 Experiment

To answer these questions, a large and systematic study was conducted on six wafers each of 0.3 Ω-cm, 0.5 Ω-cm and 2 Ω-cm Eurosolare cast mc-Si and 0.8-1.4 Ω-cm, 1.8-2.2 Ω-cm, and 4.4-5.6 Ω-cm string ribbon silicon. The cast mc-Si wafers of a given resistivity were adjacent slices from the same ingot and thus displayed the same pattern of grain boundaries. The wafers were cleaned and immersed in the iodine solution described previously. Since no S was computed in this experiment, the iodine solution reduced surface recombination adequately to detect differences and changes in τ_b. As-grown lifetime was measured on three spots of each cast mc-Si wafer, four spots on each string ribbon wafer of 1.8-2.2 Ω-cm and 4.4-5.6 Ω-cm, and two spots on each very small 0.7-1.1 Ω-cm string ribbon wafer. The same spots were measured on each wafer after processing. All the wafers were cleaned and processed according to Figure 67.

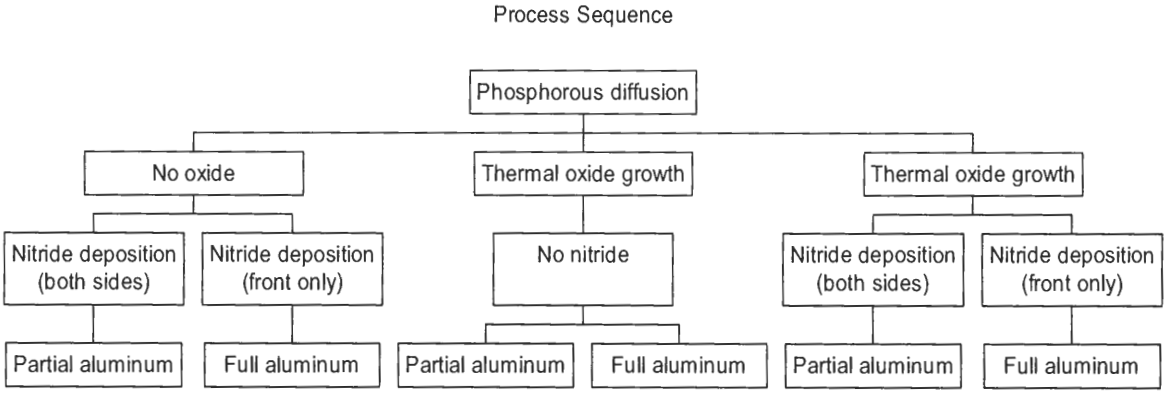

Figure 67. Process sequence for cast and string ribbon mc-Si of three resistivities.

First, all wafers went through a conventional furnace diffusion at 900°C for 20 minutes. This step forms the emitter in solar cell fabrication. Next, the wafers were divided into three groups, corresponding with three promising dielectric passivation schemes. Silicon nitride was deposited on one third of the wafers, a conventional thermal

oxide was grown on both sides on one third, and the remaining wafers were given first an oxide and then a nitride to form the oxide/nitride stack. Next, aluminum was screen-printed on the rear of each wafer. As shown in Figure 67, half the wafers received an aluminum grid (about 19% aluminum coverage), and the other half received full aluminum. The aluminum grid corresponds with bifacial solar cells with dielectric rear passivation, and the full aluminum corresponds with the aluminum back surface field. All wafers were fired in a belt furnace at 850°C for two minutes; this high-temperature anneal formed the aluminum back-surface field and promoted nitride-induced hydrogenation.

Next, the aluminum, dielectrics, and emitter were etched from the wafers. The wafers were once again cleaned and immersed in iodine and the final lifetimes were measured to assess the collective impact of dielectrics, aluminum, and resistivity. The final cast-mc-Si lifetimes in Figures 68-70 indicate a number of clear trends. The bulk lifetime exhibited a pronounced dependence on resistivity, with τ_b characterized as follows: for the 2 Ω-cm material, τ_b frequently exceeded 30 μs and sometimes 90 μs; a range of 10 μs to 30 μs was common in 0.5 Ω-cm material; and τ_b rarely exceeded 10 μs in the 0.3 Ω-cm material.

Another trend revealed in cast mc-Si is that the nitride dielectric usually corresponds with the highest τ_b, while stack corresponds with the lowest. The oxide usually corresponds with the intermediate τ_b. This defies the expectation that the oxide should yield the lowest τ_b because no hydrogen was supplied by a nitride layer. It is surprising that the stack passivation resulted in lower τ_b than either dielectric alone. We

propose two possible explanations, one based on gettering, and the other based on hydrogenation.

The first possible explanation is that gettering, not hydrogenation, may be largely responsible for the differences in τ_b in cast mc-Si. It is known, for example, that even a simple oxide can be an efficient gettering sink [75]. We further speculate that the stress exerted by the dielectric layer contributes to the effectiveness of gettering at that layer. The oxide layer exerts tensile stress on the silicon matrix (a magnitude of 3.5×10^8 Pa is cited in the literature), and the nitride layer exerts compressive stress on the silicon matrix (again, with a magnitude 3.5×10^8 Pa cited in the same paper) [76]. Since the oxide and nitride layers exert opposite and roughly equal stress, it may be that the stress exerted by the oxide/nitride stack is lower than the stress exerted by either dielectric alone. If lower stress means less gettering, this could explain why the stack-passivated cast mc-Si wafers had lower τ_b than the wafers coated by either dielectric alone.

An alternative explanation is that hydrogenation is responsible for the observed differences in τ_b. For nitride-coated wafers, it is clear that the nitride layer supplies hydrogen that is drawn through the bulk under the influence of vacancies injected at the opposite surface during aluminum alloying. For oxide-coated wafers, we speculate that hydrogen may be supplied by small amounts of water vapor in the tube furnace. If the wafers are coated with oxide only, the hydrogen is drawn through the bulk as described above. However, if nitride is deposited on top of the oxide, we speculate that the high temperature during deposition releases the hydrogen. Without vacancies at the rear or the very high temperatures of aluminum alloying, the hydrogen is released into the ambient rather than driven through the bulk. Furthermore, the new hydrogen deposited in the

nitride layer may be blocked by the oxide from diffusing into the bulk during aluminum alloying [77]. Consequently, less hydrogen may be available to passivate the bulk in the stack-passivated case than in the case of either dielectric alone. This possibility is purely speculative at this time.

Figures 68-70 reveal that for the 2 Ω-cm material, full Al gives higher τ_b than partial Al. This suggests that reducing Al coverage lessens gettering and/or hydrogenation [78]. Such a trend is not clear in the lower resistivities, suggesting that there may be a dopant-defect interaction unsusceptible to gettering.

Tables 7-9 show the percentage change from as-grown τ_b to final τ_b. As-grown τ_b for 0.3 Ω-cm, 0.5 Ω-cm, and 2 Ω-cm cast mc-Si material fell in the respective ranges of 3-5 μs, 10-30 μs, and 30-50 μs. In all cases for the 0.3 Ω-cm material, τ_b is improved through processing. In contra0st, τ_b for the 0.5 Ω-cm and 2 Ω-cm material usually showed degradation through processing in this experiment. This seems to indicate that there may be a competition between gettering/hydrogenation and contamination; low-lifetime materials are most easily improved through gettering and hydrogenation, while high-lifetime materials are most susceptible to contamination. Still, with full aluminum on the back, final τ_b was greatest for 2 Ω-cm, followed by 0.5 Ω-cm and 0.3 Ω-cm. With partial aluminum this trend was not as clear.

Figures 68-70 show that nitride passivation was most effective in enhancing lifetime. This trend was confirmed upon repeating the experiment, giving the data of Figure 71. Again, nitride tends to give the highest τ_b, and stack tends to give the lowest. This is true for partial as well as full aluminum on the rear. The missing bar corresponds with a wafer lost during processing.

Results for string ribbon are compiled in Figure 72. Consistent with the results for cast mc-Si, nitride on string ribbon seems to give significantly higher lifetime than the other two dielectrics. Figure 73 shows that in all cases a significant increase in τ_b was observed. The greatest improvement exceeded 1200% for one nitride-passivated spot with partial aluminum, and the lowest improvement was about 70% for one stack-passivated and one oxide-passivated spot with partial aluminum. Aside from the outlying 1200% data point, Figure 73 indicates that full aluminum generally results in higher lifetime than partial aluminum. This is consistent with the data in [78].

Figure 73 shows that nitride confers higher lifetime than the other dielectrics, and full aluminum confers better improvement than partial aluminum. Both these observations were reproduced in an additional experiment with results shown in Figures 74 and 75. In Figure 75, improvement in τ_b approaches 2000% for one nitride-coated spot with full aluminum.

6.2 Conclusions

We investigated processing schemes combining oxide, nitride, or oxide/nitride dielectric coatings with full or partial aluminum coverage. In spite of considerable scatter in lifetime data due to inhomogeneity in these materials, some interesting trends were observed. For Eurosolare cast mc-Si, τ_b increases strongly with increasing resistivity. Processing tends to reduce this trend, raising τ_b for the lowest resistivity and often lowering τ_b for higher resistivity. In most cases, nitride-coated wafers gave the highest τ_b, while stack-coated wafers gave the lowest. For the 2 Ω-cm material, full Al gave higher τ_b than partial aluminum. With full aluminum on the back, 2 Ω-cm cast mc-Si

gave the highest final lifetime, followed by 0.5 Ω-cm and 0.3 Ω-cm materials, regardless of the front dielectrics. In string ribbon, all processing combinations improved τ_b, with improvement usually highest for full aluminum and sometimes exceeding 1000%.

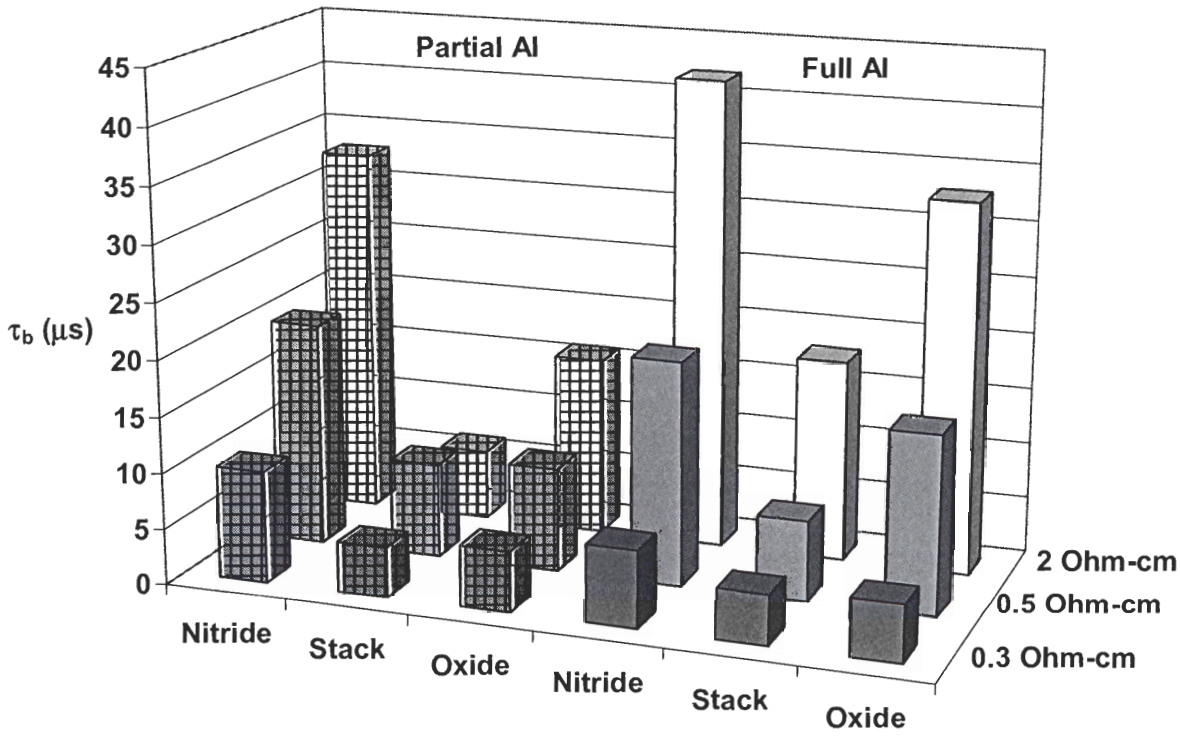

Figure 68. Final τ_b for spot A in cast mc-Si after a two-minute heat treatment at 850°C in a belt furnace. As-grown τ_b for 0.3 Ω-cm, 0.5 Ω-cm, and 2 Ω-cm materials were 3-5 µs, 10-30 µs, and 30-50 µs respectively.

Table 7. Percentage change in τ_b for spot A in cast mc-Si.

	Partial Aluminum			Full Aluminum		
	Nitride	Stack	Oxide	Nitride	Stack	Oxide
2 Ω-cm	-25	-85	-67	-18	-66	14
0.5 Ω-cm	25	-51	-45	54	-49	14
0.3 Ω-cm	113	5	15	52	2	41

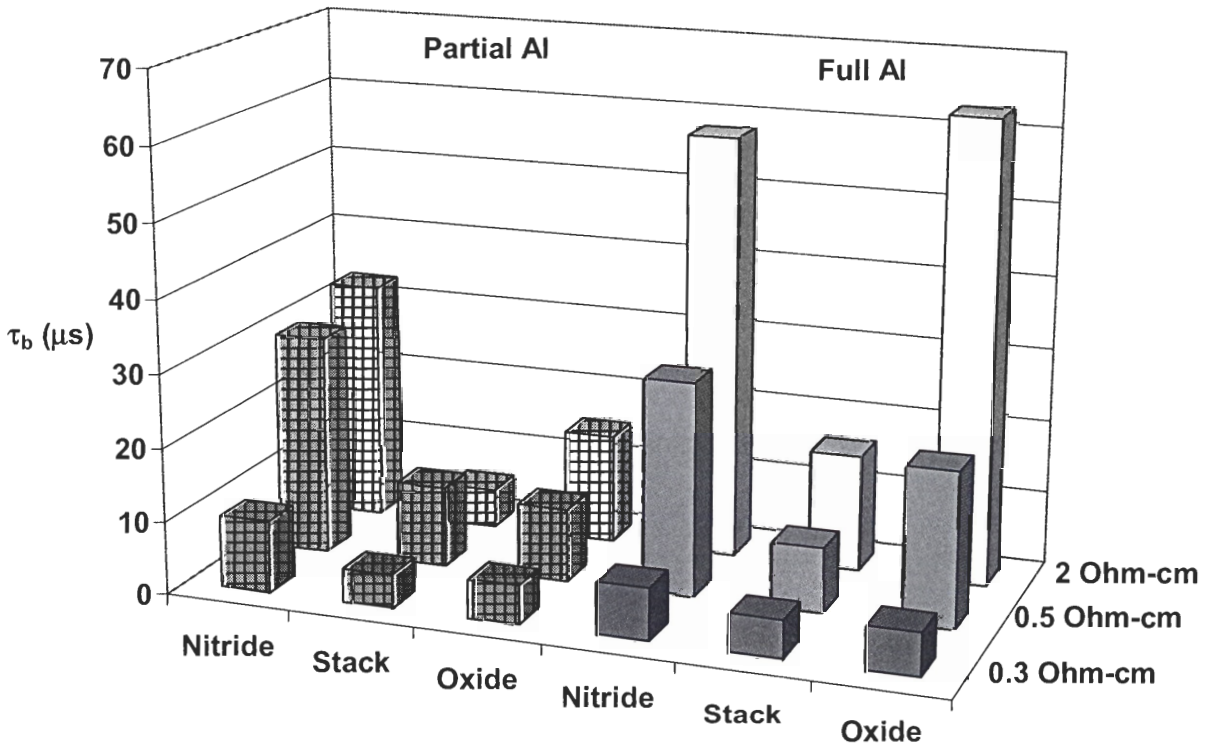

Figure 69. Final τ_b for spot B in cast mc-Si after a two-minute heat treatment at 850°C in a belt furnace.

Table 8. Percentage change in τ_b for spot B in cast mc-Si.

	Partial Aluminum			Full Aluminum		
	Nitride	Stack	Oxide	Nitride	Stack	Oxide
2 Ω-cm	-25	-88	-72	16	-69	66
0.5 Ω-cm	36	-54	-62	53	-58	-5
0.3 Ω-cm	158	21	47	103	46	81

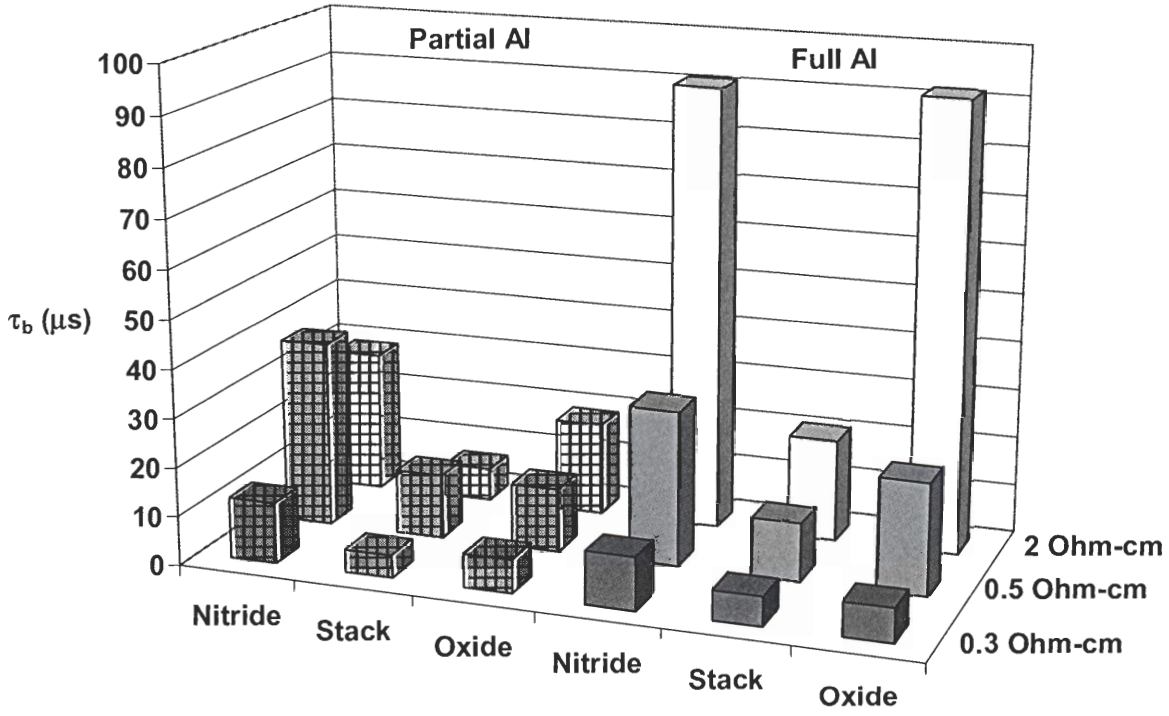

Figure 70. Final τ_b for spot C in cast mc-Si after a two-minute heat treatment at 850°C in a belt furnace.

Table 9. Percentage change in τ_b for spot C in cast mc-Si.

	Partial Aluminum			Full Aluminum		
	Nitride	Stack	Oxide	Nitride	Stack	Oxide
2 Ω-cm	0	-79	-53	139	-42	188
0.5 Ω-cm	58	-52	-57	39	-54	-15
0.3 Ω-cm	218	12	74	176	62	106

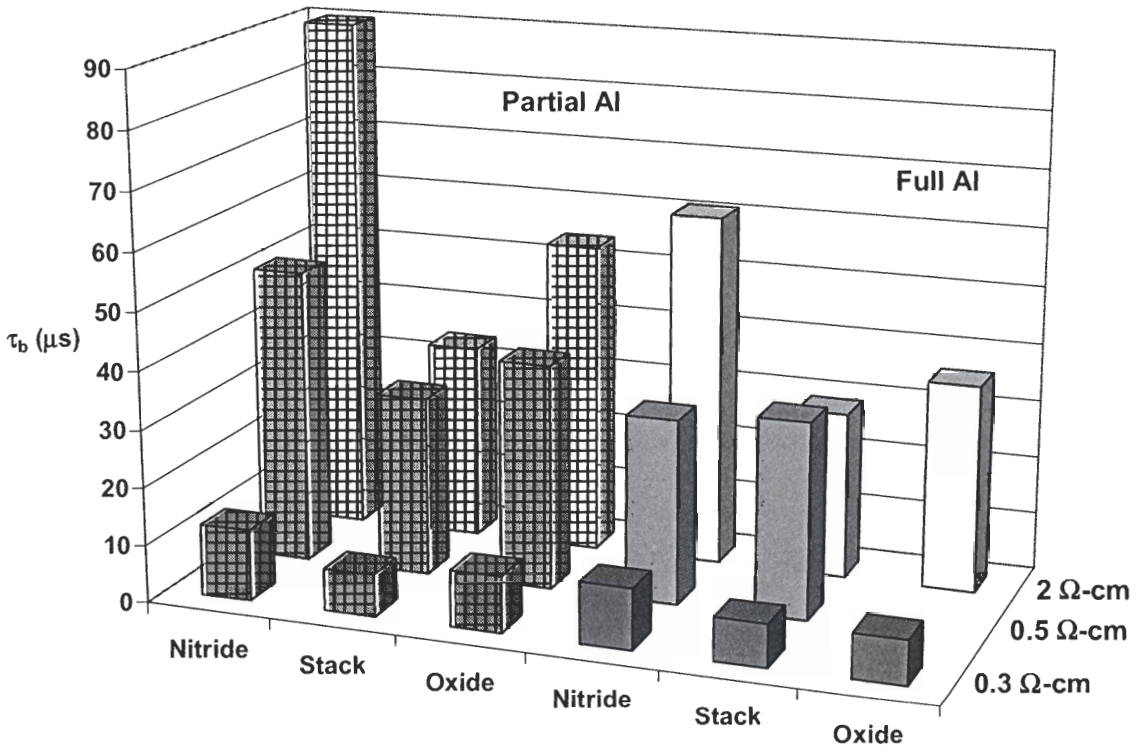

Figure 71. Additional experiment showing the effect of dielectric passivation, back aluminum coverage, and resistivity on the final τ_b in cast mc-Si after a 850°C heat treatment for two minutes.

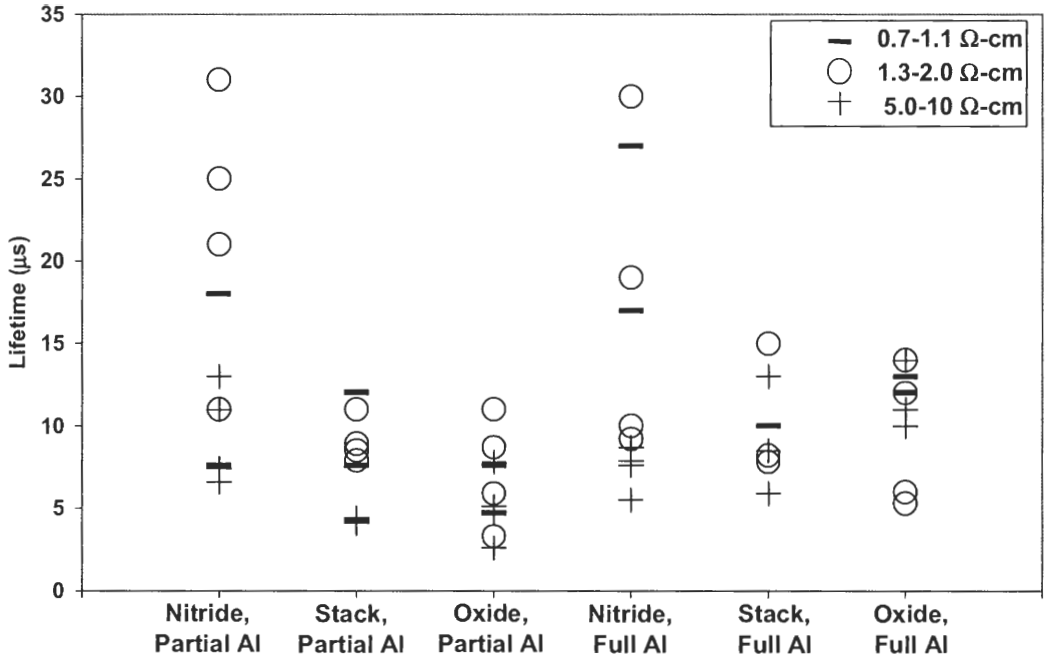

Figure 72. Final τ_b of multiple spots measured on string ribbon wafers. All samples were subjected to a 850°C heat treatment for two minutes.

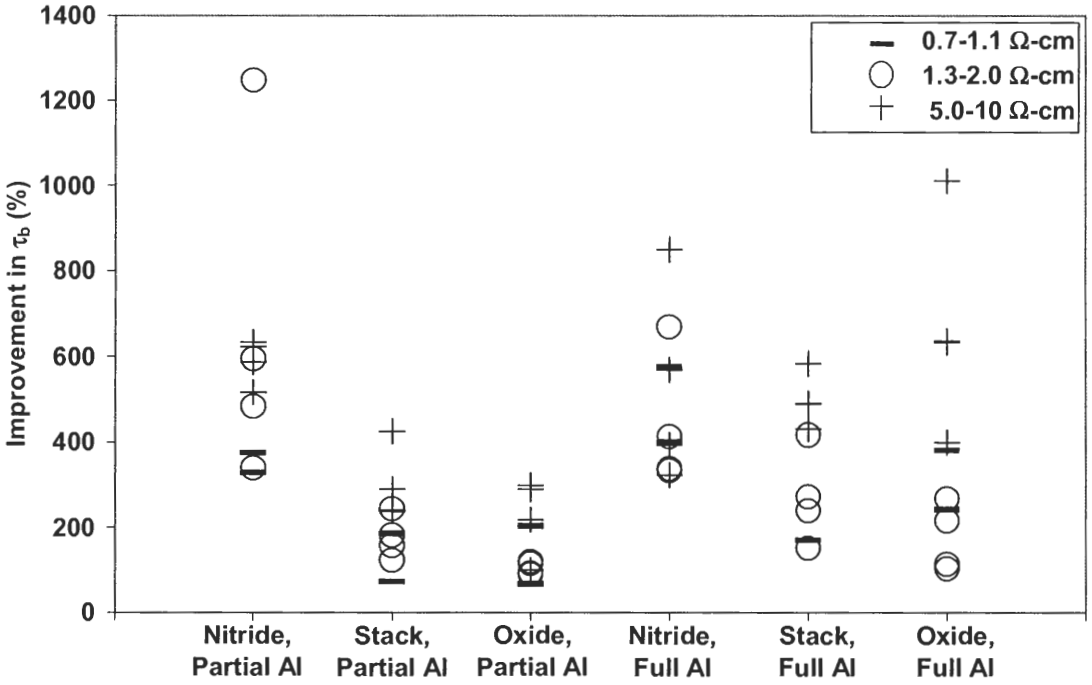

Figure 73. Percent improvement calculated from the final τ_b of Figure 72 and as-grown τ_b.

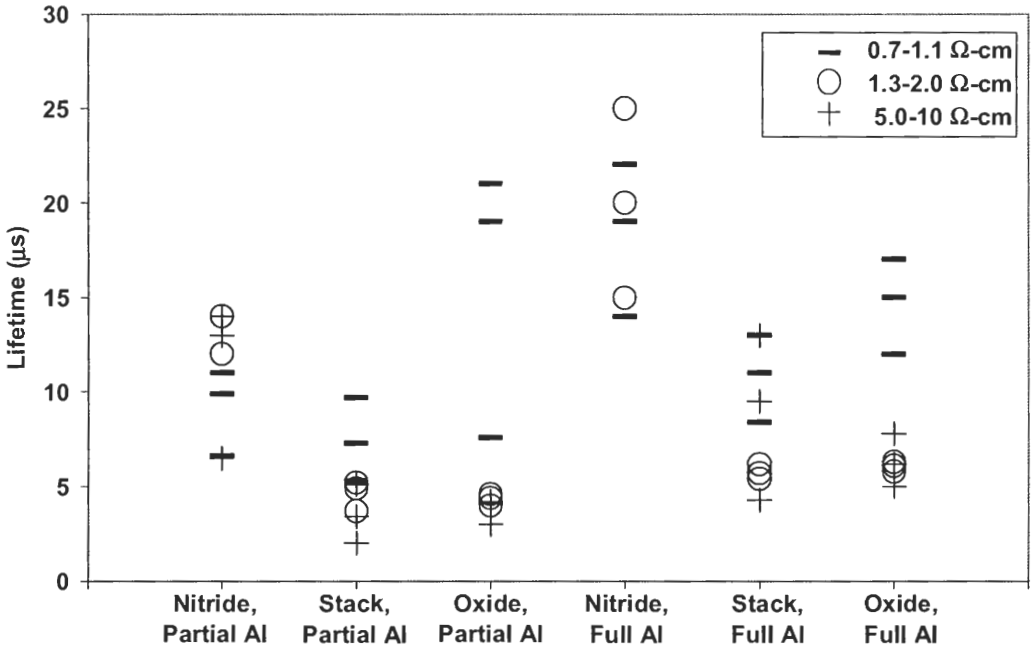

Figure 74. Additional experiment with string ribbon to reproduce the trends observed in Figure 72.

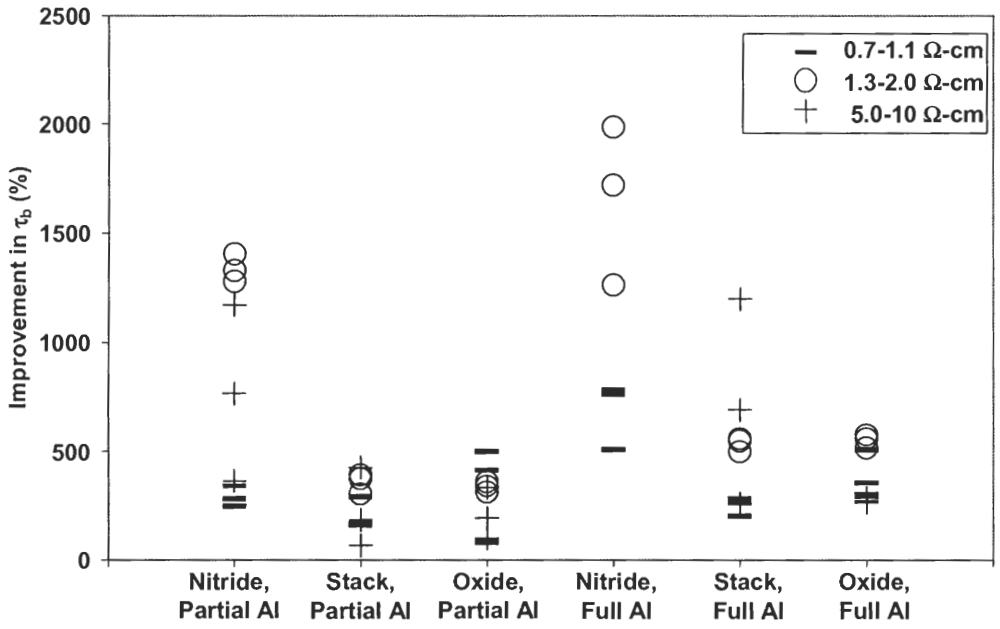

Figure 75. Percent improvement calculated from the final τ_b of Figure 74 and as-grown τ_b.

CHAPTER 7

SIMULATION OF THE DOPING DEPENDENCE OF CELL EFFICIENCY BASED ON EXPERIMENTALLY DETERMINED DOPING DEPENDENCE OF S AND τ_b

In this chapter, the bulk lifetimes measured in Task 4 and the surface recombination velocities measured in Task 3 will be used in device simulations to predict the doping dependence of V_{oc}, J_{sc}, and cell efficiency. The device simulations will be performed using the PC-1D software.

7.1 Development of a Two-Dimensional Model To Account for the Impact of Gridlines on S

It is important to recognize that S on the highly doped emitter of the device is essentially independent of bulk doping level. To study the bulk-doping dependence of S for dielectric passivation, the non-diffused rear surface must be passivated by the dielectrics under investigation. Metal grid contacts can be punched through the rear dielectric to make solar cells. Since the rear surface then has the same appearance as the front surface, with a metal grid over a dielectric, this structure is called bifacial.

The S results obtained in Ch. 5 were measured on test structures consisting of silicon wafers coated with the passivating dielectric. No metal was present. It has been shown that the necessary formation of rear metal gridlines can adversely affect S [29, 79]. Thus, if the S measurements on the simple test structures are to be predictive of solar cell

performance, the impact of the metal grid must be included in the calculations. This is attempted in this chapter by developing a two-dimensional model for finding an average or effective S for use in the one-dimensional program PC-1D.

An empirical relationship among S for the dielectric (S_d), S for the metal (S_m), and the resulting average, effective S ($S_{eff.av}$) was deduced [79]:

$$S_{eff.av} = S_d + \frac{r}{1+\alpha\left(\frac{d}{L}\right)^2}\left(S_m - S_d\right), \tag{87}$$

where r is the metallization fraction, d is the line spacing, L is the diffusion length, and α is an adjustable empirical parameter. While an excellent fit to measured data was achieved using Equation (87), this equation has no predictive value, since α is a case-specific parameter that can only be determined by fitting the equation to a particular set of results.

To approach $S_{eff.av}$ from first principles, in this chapter a two-dimensional numerical model based on fundamental physics will be established and applied in this chapter. We will assume that S for the dielectric (S_d) in the non-metallized regions is unaffected by the metallization. In fact, metal contacts have in some cases been shown to shunt the inversion layer created by the dielectric charge [80]. By ignoring the possibility of this parasitic shunting, we will effectively be computing a lower limit to $S_{eff.av}$. Methods for preventing such shunting are described in [80, 81].

The structure to be modeled is divided into identical elementary cells, as shown in Figure 76. According to the geometry of Figure 76, the line spacing is 2b and the metallization fraction is r = (b – a)/b. W is the thickness of the wafer. We will solve the two-dimensional, steady-state continuity equation [35]

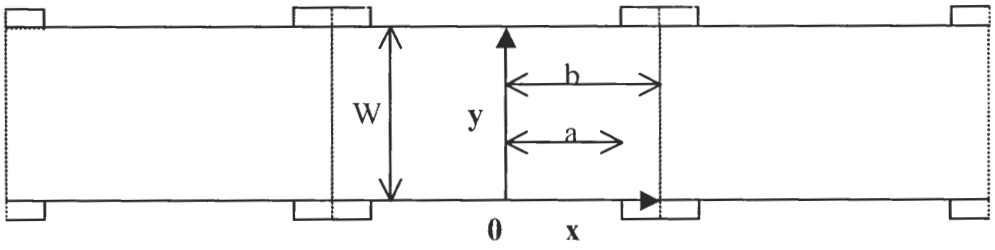

Figure 76. Illustration of elementary cell: $-b \le x \le b$ and $0 \le y \le W$.

$$0 = D\left(\frac{\partial^2 \Delta n}{\partial x^2} + \frac{\partial^2 \Delta n}{\partial y^2}\right) - \frac{\Delta n}{\tau_b} + G\,, \tag{88}$$

where D is the diffusion coefficient, Δn is the excess carrier concentration, τ_b is the bulk lifetime, and G is the generation rate. G will be assumed uniform, which is approximately true for long-wavelength illumination. There seems to be little reason to suspect that $S_{eff.av}$ would depend on wavelength.

The lateral boundary condition is that no current flows from one identical elementary cell into another:

$$\frac{\partial \Delta n(\pm b, y)}{\partial x} = 0\,. \tag{89}$$

The lower and upper boundary conditions are determined by surface recombination:

$$\frac{\partial \Delta n(x,0)}{\partial y} = S \times \Delta n(x,0)\,, \tag{90.a}$$

$$\frac{\partial \Delta n(x,W)}{\partial y} = -S \times \Delta n(x,W)\,, \tag{90.b}$$

where $S = S_d$ for $|x| < a$ and $S = S_m$ for $a < |x| < b$.

Equation (88) is solved using standard finite-difference methods [82]. Specifically, a network of grid points is superimposed on the elementary cell of Figure 76. The distance between adjacent points in the x direction is Δx, and the distance between adjacent points in the y direction is Δy. Each grid point is identified by an ordered pair (p,q), as shown in Figure 77. The objective now is to determine $\Delta n(p,q)$ at all grid points. The differential Equation (88) is replaced by a finite difference equation [82]:

$$0 = D\left(\frac{\Delta n(p+1,q)+\Delta n(p-1,q)-2\Delta n(p,q)}{(\Delta x)^2}+\frac{\Delta n(p,q+1)+\Delta n(p,q+1)-2\Delta n(p,q)}{(\Delta y)^2}\right) - \frac{\Delta n(p,q)}{\tau_b}+G \tag{91}$$

The derivation of Equation (91) based on charge conservation is given in Appendix B. While Equation (91) is valid at all interior grid points, different equations are necessary for charge conservation at all points along $x = \pm b/2$, $y = 0$, and $y = W$. These are derived and shown in Appendix B.

If there are N points (p,q), then there are N unknowns, $\Delta n(p,q)$. For each unknown, there is an equation; for example, Equation (91) is used for each interior grid point. Even for large N, this system of equations can easily be solved using mathematical software; Matlab was used for this task. An example of the resulting Δn surface is shown in Figure 78. The input parameters are $S_d = 100$ cm/s, $S_m = 10^6$ cm/s, $\tau_b = 1$ ms, W = 0.03 cm, D = 30 cm^2/s, gridline spacing d = 0.1 cm, and r = 0.06. Figure 78 clearly shows the large impact of the metallized regions on the whole wafer.

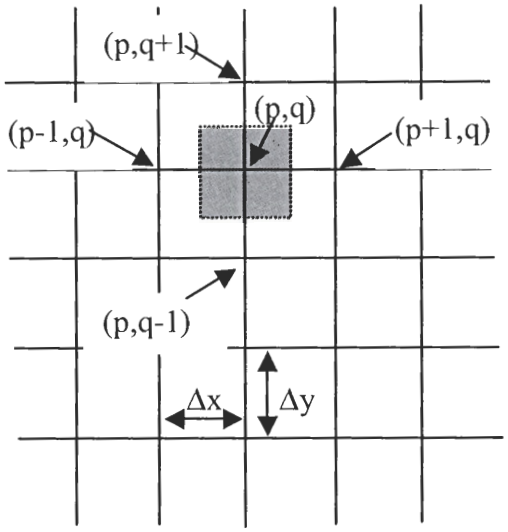

Figure 77. Illustration of grid points for use with finite difference model.

We define $S_{eff.av}$ as the single S value which, when replacing both S_d and S_m, leaves unchanged the average Δn over the entire wafer. Average Δn over the entire wafer determines the measurable effective lifetime, $\tau_{eff} = \Delta n_{av}/G$. Δn_{av} is computed numerically by integrating under the surface of Figure 78. The choice of G is arbitrary in this case; Δn_{av} is proportional to G, and the computed τ_{eff} is thus independent of G. The resulting τ_{eff} is plugged into Equation (23), the equation for steady-state, uniform generation. This gives the single $S_{eff.av}$ value which, when replacing both S_d and S_m, results in the same τ_{eff} and Δn_{av}. Using this definition of $S_{eff.av}$ and the input parameters listed above, we find $S_{eff.av} = 440$ cm/s.

The gridlines model was tested by setting $S_m = S_d$, which produces a one-dimensional problem. This one-dimensional problem was solved both analytically and with the gridlines model, and agreement was excellent.

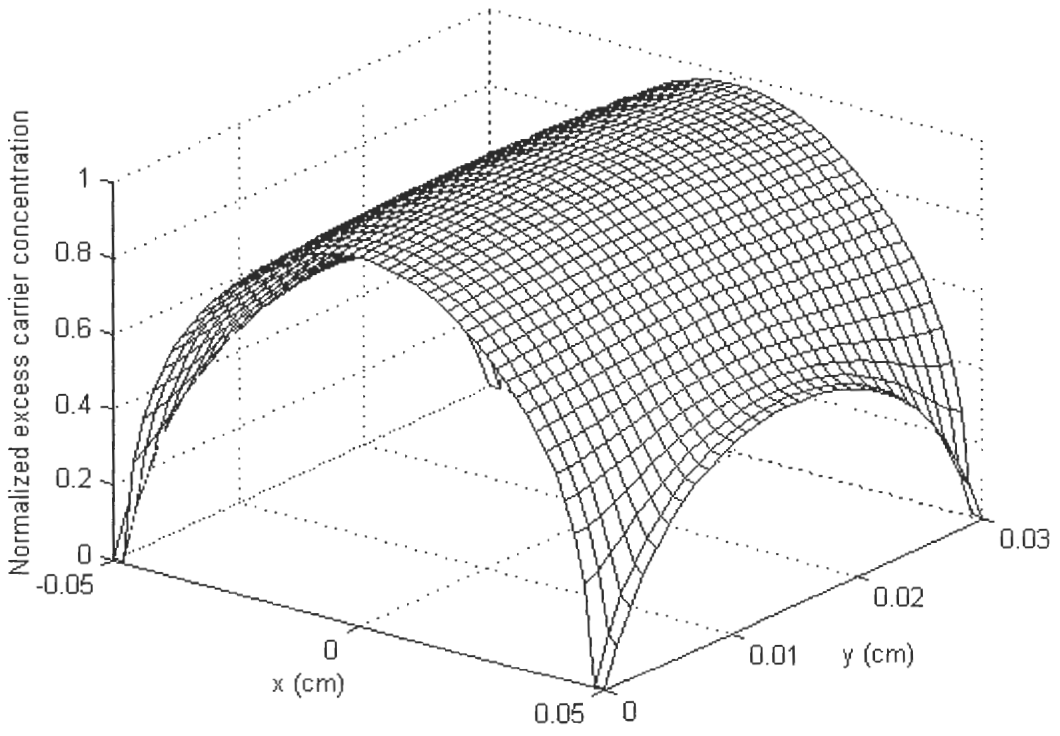

Figure 78. $\Delta n(x)$ surface obtained by finite difference solution to Equation (88).

7.2 Device Simulations

In this section, the gridlines model developed above will be used to input S_d from the experiments of Ch. 5 will be used in the gridlines model to obtain $S_{eff.av}$ for use in PC-1D. The PC-1D simulations are then used to predict cell parameters such as V_{oc}, J_{sc}, and cell efficiency for string ribbon and cast mc-Si bifacial cells. In Chapters 5 and 6, three dielectrics were investigated: nitride, oxide/nitride stack, and oxide. In cell modeling and fabrication, only nitride and stack will be used because the nitride layer serves as an indispensable anti-reflection coating.

To use this gridlines model as a tool to predict cell efficiency, some of the inputs, such as wafer thickness, must be obtained from measurements on the actual wafers on which cells will be fabricated. For more clarity, the source of each input into the gridlines model is indicated below:

d: The distance between gridlines will be 0.2 cm for all cells fabricated.

r: The linear metallization fraction will be 0.1 for all cells fabricated.

S_m: The surface recombination velocity for the metal-silicon interface is set to 10^6 cm/s, a commonly cited value [83].

W: This is the thickness of the wafer on which cells will be fabricated.

D: This is the diffusion coefficient, calculated from the resistivity of the wafer on which cells will be fabricated. For a given material, roughly the same three resistivities were used in the S experiments of Chapter 5, the τ_b experiments of Chapter 6, and the cell fabrication in Chapter 8.

τ_b: For a given material (string ribbon or cast mc-Si), resistivity, and dielectric (nitride or stack), we use from Chapter 6 both the lowest and highest τ_b measured following gettering with partial aluminum, as shown in Figures 68-70 and 72.

S_d: For a given material, resistivity, and dielectric, we use from Chapter 5 both the lowest lower limit to S (always 0) and the highest upper limit to S.

Thus there are twelve total cases being simulated: nitride and stack for three resistivities (0.8-1.2 Ω-cm, 1.4-1.7 Ω-cm, and 5.2-6.6 Ω-cm) of string ribbon, and nitride and stack for three resistivities (0.25-0.26 Ω-cm, 0.44-0.45 Ω-cm, and 2.2-2.3 Ω-cm) of

cast mc-Si. For each of these twelve cases, $S_{eff.av}$ is calculated from four conditions chosen to represent the widest possible range of experimental values from Chapters 5 and 6: highest S and highest τ_b, highest S and lowest τ_b, lowest S and highest τ_b, and lowest S and lowest τ_b. The same four conditions for each of the same twelve cases are subsequently used in device simulations in PC-1D, with $S_{eff.av}$ from the gridlines model supplied as the rear S for the devices. Other inputs into PC-1D include W, D, and τ_b as described above, and typical values for emitter profile, reflectance, and series and shunt resistances. Figure 79 explains the sources of the inputs to PC-1D.

Figure 80 summarizes the results of the gridlines model. $S_{eff.av}$ is shown as a function of S_d. When $S_d = 0$, the impact of the metal gridlines is to cause $S_{eff.av}$ to range from 160 cm/s to 430 cm/s; this variation is due entirely to differences in W, τ_b, and N_A. For S_d above 1000 cm/s, the gridlines have a very small effect.

The results of the device simulations are presented in Table 10 and will be compared with experimental cell data in the next chapter. The ranges in bulk resistivity (ρ) shown in Table 10 represent the ranges measured on the wafers used to fabricate solar cells. The ranges in V_{oc}, J_{sc}, and cell efficiency are PC-1D simulation results based on the variation in S and τ_b found in earlier tasks.

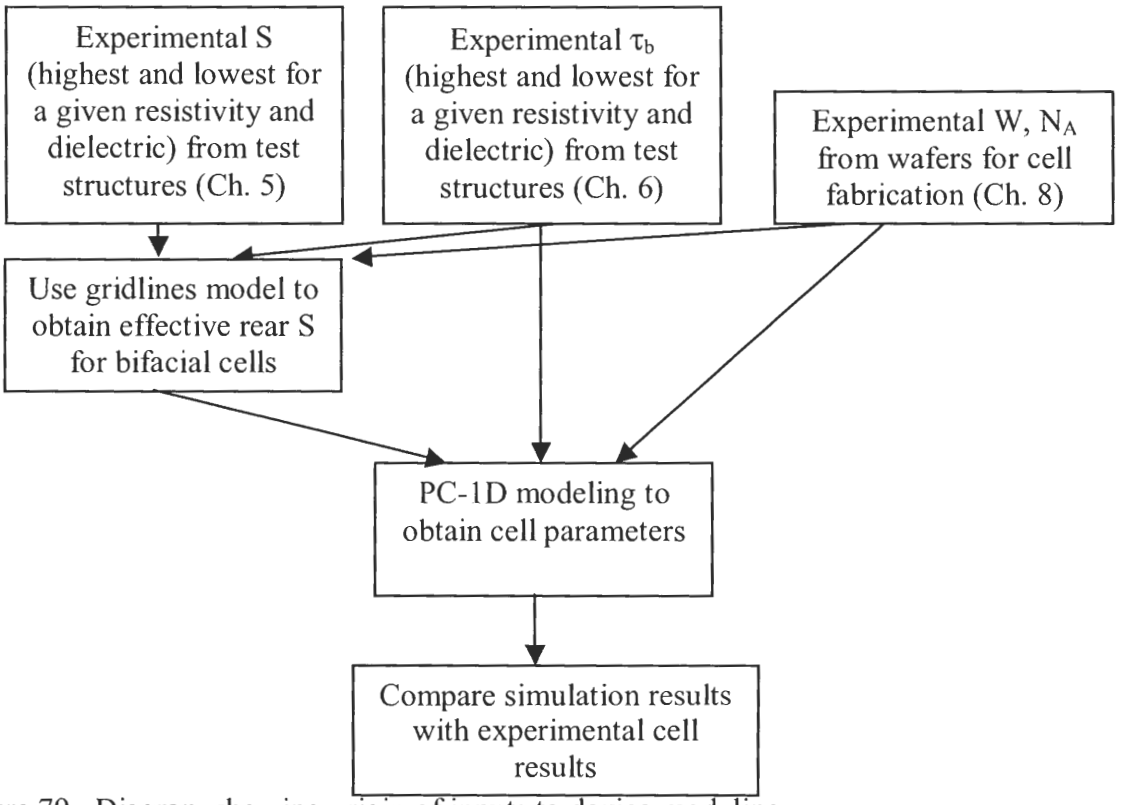

Figure 79. Diagram showing origin of inputs to device modeling.

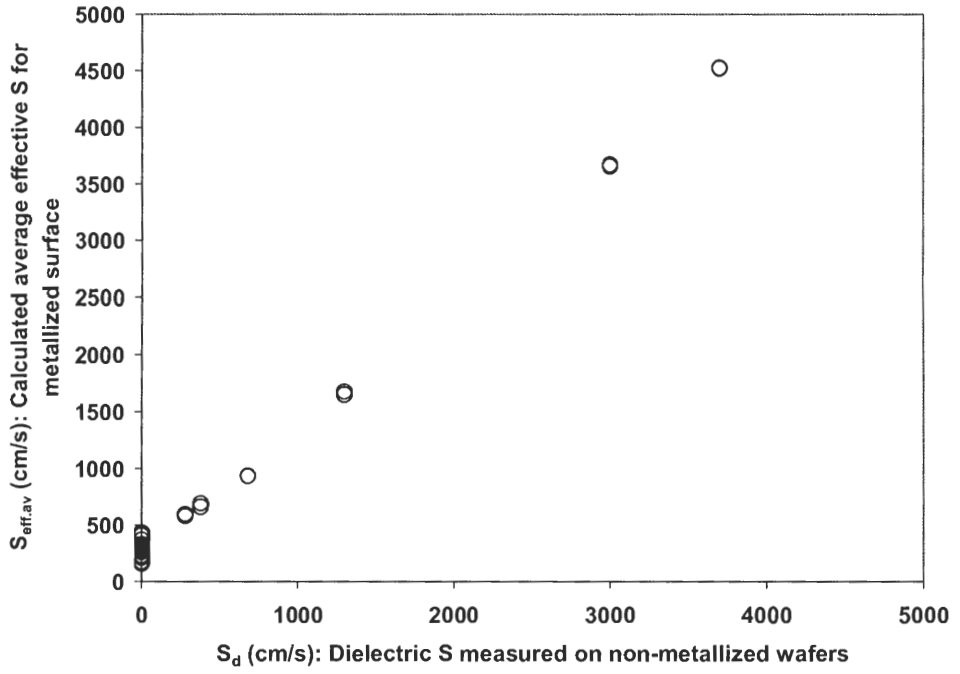

Figure 80. $S_{eff.av}$ results of the gridlines model, shown as a function of experimental S_d values used in the calculations. Only $S_d < 5000$ cm/s results are shown in this figure.

Table 10. V_{oc}, J_{sc}, and cell efficiency of device simulations based on experimental τ_b from Task 4 and experimental S from Task 3. Experimental S was adjusted to account for gridlines using the model described in this chapter.

Material	Dielectric	ρ (Ω-cm)	V_{oc} (mV)	J_{sc} (mA)	Efficiency (%)
Cast mc-Si	Nitride	0.25-0.26	625-627	29.2-29.6	14.3-14.5
Cast mc-Si	Nitride	0.44-0.45	623-628	30.3-31.2	14.7-15.3
Cast mc-Si	Nitride	2.2-2.3	596-601	31.1-31.5	14.5-14.8
Cast mc-Si	Stack	0.25-0.26	621	28.2	13.7
Cast mc-Si	Stack	0.44-0.45	617-620	29.4-30.0	14.2-14.5
Cast mc-Si	Stack	2.2-2.3	576-579	29.2-29.5	13.2-13.4
String ribbon	Nitride	0.8-1.2	600-612	29.2-30.7	13.7-14.7
String ribbon	Nitride	1.4-1.7	612	27.2-27.8	13.0-13.3
String ribbon	Nitride	5.2-6.6	554-566	29.5-30.7	12.7-13.5
String ribbon	Stack	0.8-1.2	600-607	29.3-30.2	13.8-14.4
String ribbon	Stack	1.4-1.7	611-612	26.9-27.2	12.9-13.0
String ribbon	Stack	5.2-6.6	549-551	29.0-29.2	12.3-12.5

7.3 Results and Conclusions

In Table 10, the ρ ranges are the measured resistivity ranges of wafers subsequently used for cell fabrication. The ranges in V_{oc}, J_{sc}, and efficiency are simulation results based on using the highest and lowest measured τ_b and S for the given resistivity and dielectric. A number of trends can be seen in the simulation results. For cast mc-Si, V_{oc} tends to increase as resistivity decreases, as predicted by Equation (38); lower resistivity means higher N_A, lower J_{0b}, and higher V_{oc}. For string ribbon, the highest V_{oc} is predicted for the middle resistivity (0.44-0.45 Ω-cm) because S and τ_b were considerably worse for the lowest resistivity (0.25-0.26 Ω-cm). For the cast material, J_{sc} tends to increase with increasing resistivity. This is due to the tendency of τ_b to increase with increasing resistivity, as found in Figures 68-71. No such J_{sc} vs. ρ trend is seen for string ribbon because no τ_b vs. ρ trend was found in Figure 72. Finally, for both nitride

and stack passivation, the middle resistivity (0.44-0.45 Ω-cm) is predicted to give the best efficiency for cast mc-Si, and the low resistivity (0.8-1.2 Ω-cm) is predicted to give the best efficiency for string ribbon. The conformity of these predictions with experimental cell results will be tested in the next chapter.

CHAPTER 8

FABRICATION AND CHARACTERIZATION OF MULTICRYSTALLINE SILICON SOLAR CELLS TO TEST RESULTS OF DEVICE SIMULATIONS

In the previous chapter, device simulations were performed using the values of τ_b and S determined from experimental test structures. In this chapter, we describe the fabrication and characterization of complete solar cells to test the predictions of the simulations.

8.1 Cell Fabrication

Bifacial solar cells were fabricated on three resistivities (0.8-1.2 Ω-cm, 1.4-1.7 Ω-cm, and 5.2-6.6 Ω-cm) of string ribbon and three resistivities (0.25-0.26 Ω-cm, 0.44-0.45 Ω-cm, and 2.2-2.3 Ω-cm) of cast mc-Si. For each resistivity, two wafers were used: one for nitride-passivated bifacial cells, and one for stack-passivated bifacial cells.

All the wafers were cleaned in standard solutions. Next, approximately 3000 Å of a masking oxide was deposited on the rear of the wafers. Phosphorous diffusion was then effected in a tube furnace, producing an emitter sheet resistance of roughly 40 Ω/cm on the front of the wafers. The masking oxide and phosglass were removed. The wafers designated for stack passivation underwent a furnace oxidation for 10 minutes at 925°C. Next, all the wafers were sent to Evergreen Solar for low-frequency nitride deposition on the front. When the wafers returned, high-frequency nitride was deposited on the rear.

Aluminum gridlines were screen-printed on the rear, followed by alloying for 60 s at 740°C in a rapid thermal processing (RTP) unit. Then silver gridlines were screen-printed on the front, and the wafers were fired in a belt-line furnace; the 30 inches of heated zones were set to 825°C, and the belt speed was 80 inches per minutes. Finally, the wafers underwent a forming gas anneal (FGA) for 20 minutes at 400°C.

Nine 2cm×2cm cells were fabricated on each cast mc-Si wafer. The smaller string ribbon wafers accommodated four or six cells. Each wafer may be characterized by the best cell parameters or the parameters averaged over all its cells. Since many wafers had one or many cells that "failed" through junction shunting, local contamination, poor contact formation, or other problems, the average parameters are dominated by the "failed" cells. Therefore, the parameters of the best cell on each wafer are used to characterize the wafer and test the predictions of the previous chapter.

8.2 Results and Conclusions

The V_{oc}, J_{sc}, and efficiency of the best cell on each wafer are compared with the device simulations in Figures 81-84. As explained in the previous chapter, the upper and lower lines for V_{oc}, J_{sc}, and cell efficiency are PC-1D simulation results based on the variation in S and τ_b found in earlier tasks. The four cases are nitride- and stack-passivated string ribbon and cast mc-Si cells.

Examination of Figures 81.a, 82.a, 83.a, and 84.a shows that V_{oc} is fairly well predicted by the simulations. The predictions for cast mc-Si were more closely matched than those for string ribbon. In particular, the highest V_{oc} was predicted for the highest resistivity in cast mc-Si, whereas the highest V_{oc} was predicted for the intermediate

resistivity in string ribbon (Chapter 7). Experimentally, the highest V_{oc} was measured on the lowest resistivity for both materials. This suggests that rear S for these cells may have been poor, according to the simulation results of Chapter 3 shown in Figures 20, 24, and 27.

Figures 81.b, 82.b, 83.b, and 84.b show that the measured and predicted J_{sc} did not show as good a match as V_{oc}. This is probably because J_{sc} depends strongly on τ_b, which could vary significantly from spot to spot in multicrystalline materials. τ_b measurements from Task 4 indicate that τ_b variation is more pronounced in string ribbon than cast mc-Si. For example, consider the wafers of roughly 2 Ω-cm. To examine spatial variation in τ_b, 2-4 spots were measured after gettering on each of six string ribbon wafers (Figure 72), and three spots were measured after gettering on each of six cast mc-Si wafers (Figures 68-70). The spread in the three or four measurements on each wafer gives an indication of the variability of τ_b on that wafer. We can calculate the standard deviation in the τ_b measurements of a particular wafer, as a percentage of the mean τ_b on the wafer. For string ribbon, the percent standard deviation ranges from 13% to 49%. For cast mc-Si, the spread is appreciably smaller, ranging from 6% to 38%. Higher variability in τ_b in string ribbon may help account for the larger discrepancy between predicted and measured J_{sc} in this material.

In Figures 81.c, 82.c, 83.c, and 84.c, the efficiency prediction curves typically take the shape of the J_{sc} curves from Figures 81.b, 82.b, 83.b, and 84.b. The measured efficiency vs. resistivity trend, however, usually follows the measured J_{sc} vs. resisitivity trend. The discrepancy between predicted and measured J_{sc} therefore carries over into a discrepancy between predicted and measured cell efficiency. An interesting and

unexpected observation is that in all cases, the resistivity giving the best measured J_{sc} also gives the best measured efficiency. Specifically, for both nitride- and stack-passivated string ribbon wafers, the intermediate resistivity (1.4-1.7 Ω-cm) gives the best J_{sc} and efficiency. For the nitride-passivated cast mc-Si cells, the highest resistivity (2.2-2.3 Ω-cm) is the best, whereas the intermediate resistivity is the best for stack-passivated cast mc-Si cells.

In our measurements of multicrytalline bifacial cells, the resistivity dependence of V_{oc} is so slight that the J_{sc}-vs.-resistivity trend predicts the efficiency-vs.-resistivity trend. If this were shown to be true in general for multicrystalline bifacial cells, then the prediction of J_{sc} would be much more important than the prediction of V_{oc}. In this case, characterization of τ_b, which largely influences J_{sc}, should have a much higher priority than characterization of S, which largely influences V_{oc}. In these devices, bulk lifetime was not very high; therefore, surfaces were not as important as τ_b. However, if gettering and passivation can enhance the lifetime so that diffusion length is 2-3 times the cell thickness, then we should see S dominating V_{oc} and V_{oc} dominating the efficiency.

In Figures 83 and 84, we observe the tendency for J_{sc} to increase with increasing resistivity in cast mc-Si. This conforms with the previously observed improvement in τ_b and S at higher resistivity. However, V_{oc} decreases at higher resistivity. This can be explained by reviewing the basic equations

$$V_{oc} = \frac{kT}{q} \ln\left(\frac{J_{sc}}{J_0} + 1\right) \tag{5}$$

and

$$J_{0b} = \frac{qD_n n_i^2}{L_n N_A} F_p . \tag{38}$$

Equation (5) shows that V_{oc} tends to decrease as J_0 increases. In Equation (38), the component of J_0 due to the base tends to increase as N_A decreases. If the improvements in diffusion length and surface quality at higher resistivity do not overcome this reduction in N_A, then J_{0b} will indeed increase and V_{oc} will decrease at higher resistivity.

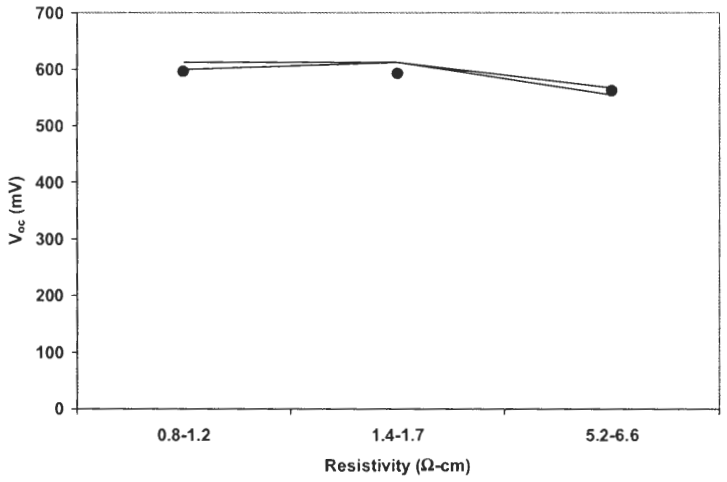

a.

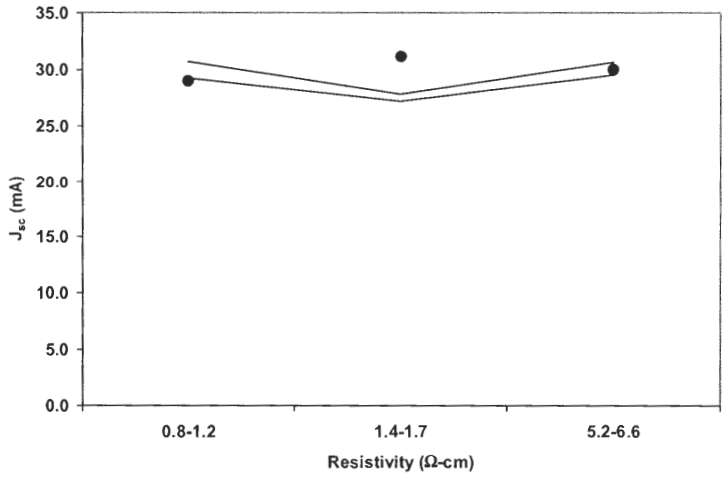

b.

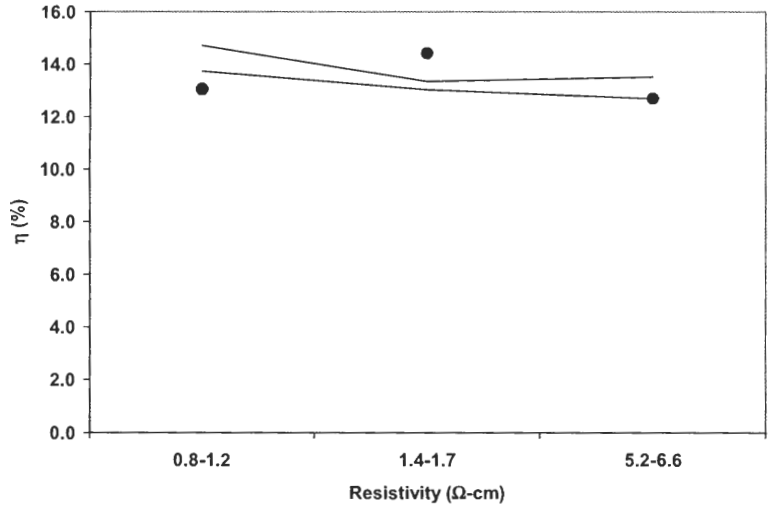

c.

Figure 81. Measured V_{oc} (a), J_{sc} (b), and cell efficiency (c), shown as dots, compared with simulation, shown as lines, for nitride-passivated string ribbon wafers.

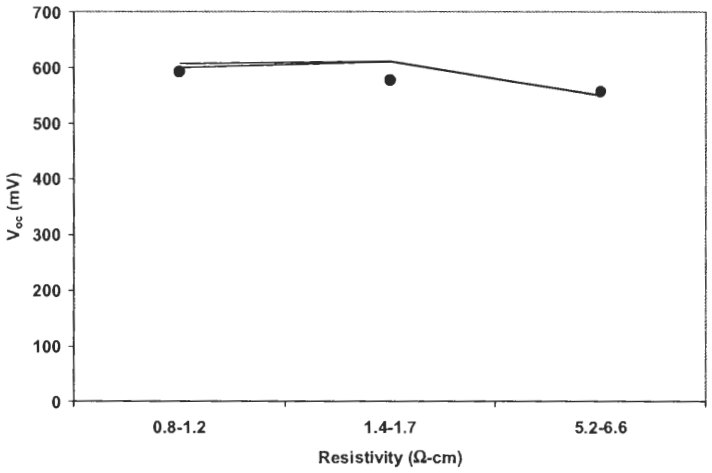

a.

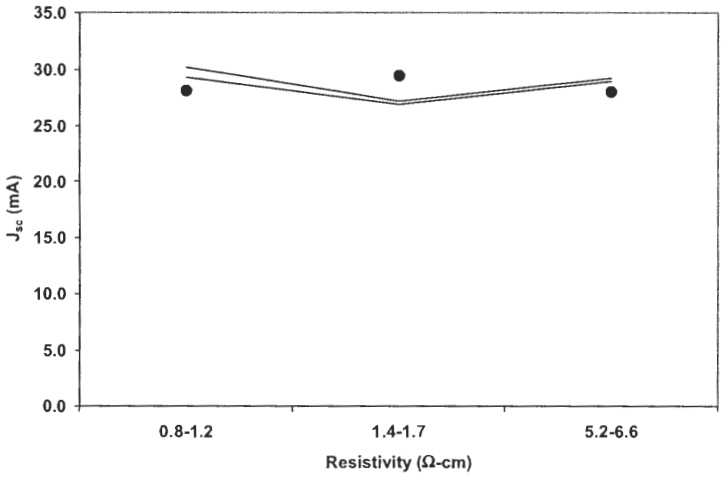

b.

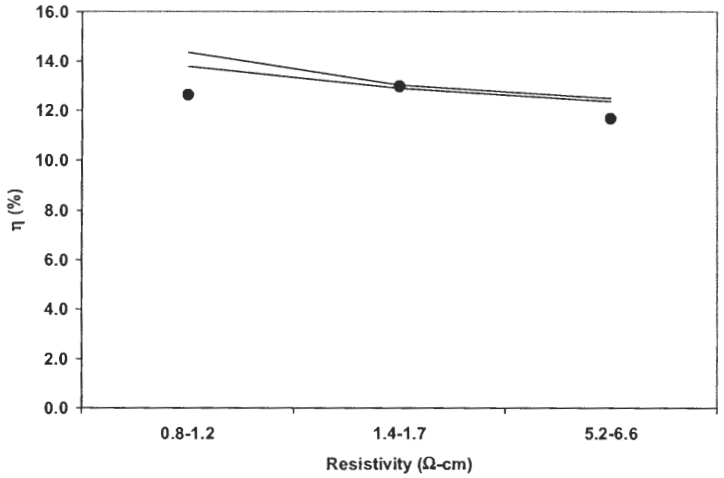

c.

Figure 82. Measured V_{oc} (a), J_{sc} (b), and cell efficiency (c), shown as dots, compared with simulation, shown as lines, for stack-passivated string ribbon wafers.

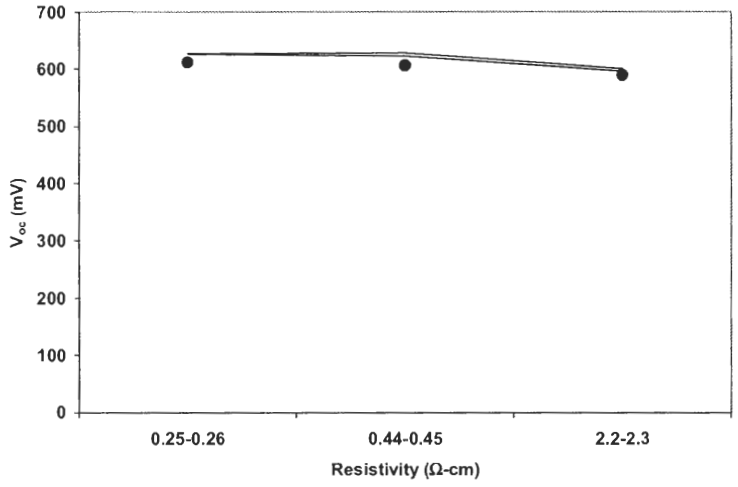

a.

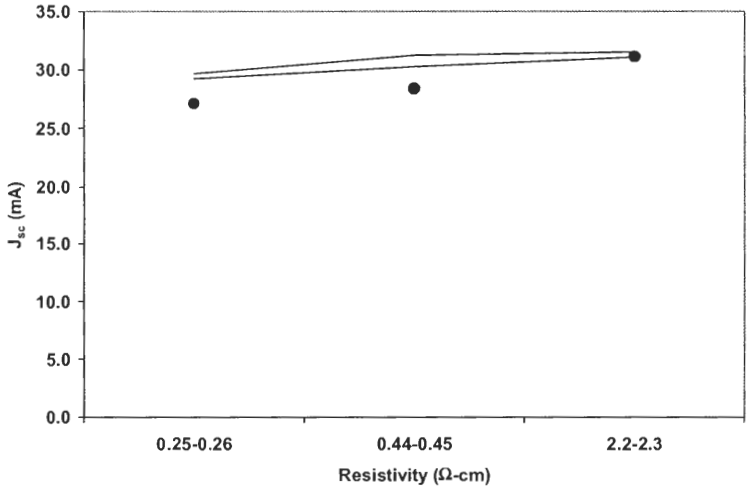

b.

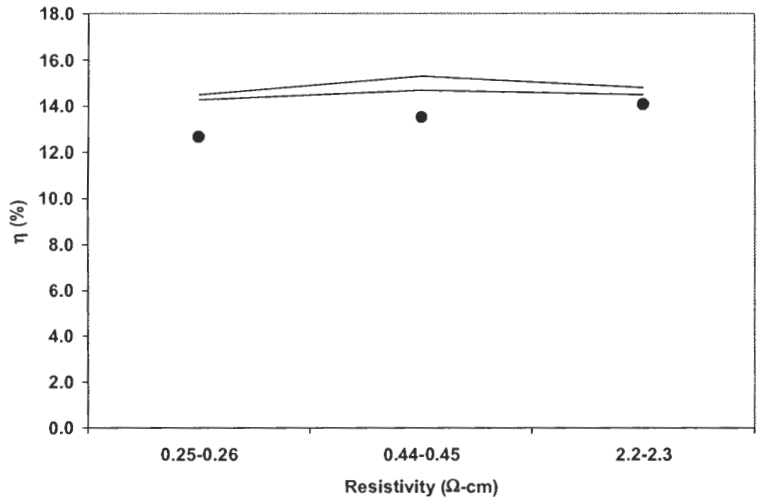

c.

Figure 83. Measured V_{oc} (a), J_{sc} (b), and cell efficiency (c), shown as dots, compared with simulation, shown as lines, for nitride-passivated cast mc-Si wafers.

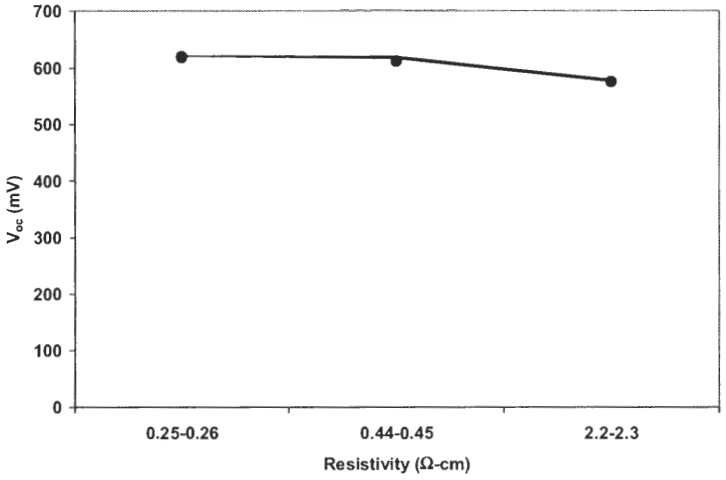

a.

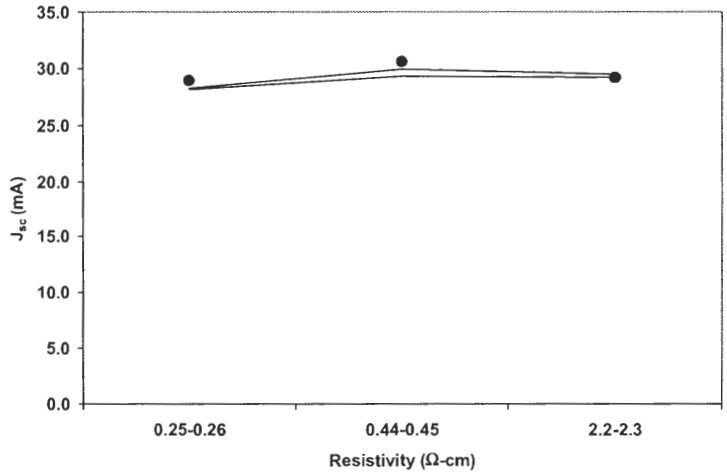

b.

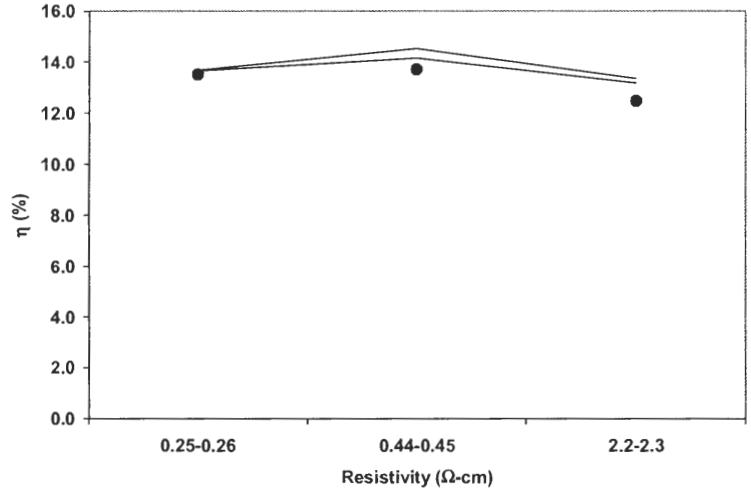

c.

Figure 84. Measured V_{oc} (a), J_{sc} (b), and cell efficiency (c), shown as dots, compared with simulation, shown as lines, for stack-passivated cast mc-Si wafers.

CHAPTER 9

FUTURE WORK

To determine with certainty whether multicrystalline materials have higher S than identically passivated monocrystalline materials, it will be necessary to apply a technique with greater precision than the two- and three-wavelength analyses considered previously. In this research, the technique using a passivating iodine solution was demonstrated to succeed for high-lifetime areas measured through high-resolution mapping. Thus, high-resolution lifetime mapping may be a good technique for extracting S using an iodine solution without the disturbing influence of low-lifetime areas. If S for multicrystalline materials is shown conclusively to exceed S for monocrystalline materials, the observation should be clarified by investigating the role of defects at the silicon-dielectric interface.

Identical S on both sides of the wafers is assumed in the derivation of all the expressions we have discussed (general, steady-state, and transient) linking S, τ_b, and τ_{eff}. Frequently, test structures are prepared with identical passivation on both sides of the wafer to satisfy this assumption. More versatile equations can be derived to allow S_1 and S_2 on the two sides to differ. The transient case has already been addressed in the literature; the steady-state condition apparently has not.

Further investigation of the dopant-defect interaction should be pursued to understand why low-resistivity multicrystalline materials have anomalously low lifetimes. This is a familiar observation, but the microscopic details of the interaction are not well understood.

Another future research activity may be collaboration with industry to characterize τ_b, S, and cell parameters for very many wafers of a given resistivity and processing condition. Industry, unlike small research laboratories, has the resources to process and characterize a large number of wafers for every condition of interest. This is necessary to understand the variability in the materials, since the quality of non-uniform multicrystalline wafers may vary from wafer to wafer.

APPENDIX A

ANALYTICAL SOLUTION OF CONTINUITY EQUATION WITH TIME-VARYING ILLUMINATION OF ARBITRARY SPECTRAL CONTENT

Many of the details omitted in the derivation of Equation (52) are supplied in this appendix. For convenience, all relevant equations given in the text are reproduced here.

The continuity equation governing excess minority carrier concentration in a semiconductor wafer in low-level-injection is as follows:

$$\frac{\partial \Delta n}{\partial t} = D\frac{\partial^2 \Delta n}{\partial x^2} - \frac{\Delta n}{\tau_b} + G, \tag{A1}$$

with the boundary conditions

$$D\frac{\partial \Delta n(-W/2,t)}{\partial x} = S\Delta n(-\frac{W}{2},t) \tag{A2.a}$$

and

$$-D\frac{\partial \Delta n(W/2,t)}{\partial x} = S\Delta n(\frac{W}{2},t), \tag{A2.b}$$

when surface recombination velocity is the same on both sides of the wafer.

The time- and position- dependent generation rate is known to be

$$G(x,t) = \left[ke^{-\alpha x} + kRe^{\alpha(x-W)}\right]e^{-t/\tau_f}, \tag{A3}$$

where

$$k \equiv \frac{N_{ph}\alpha(1-R)e^{-\alpha W/2}}{1-(Re^{-\alpha W})^2}. \tag{A4}$$

The single value of α in Equation (A3) implies monochromatic illumination. Later we will explain how to extend the analysis to illumination by a full spectrum of light. Let the initial condition be equilibrium: $\Delta n(x,0) = 0$.

To begin the derivation of $\Delta n(x,t)$, take the Laplace transform of Equation (A1):

$$s\overline{\Delta n} = D\frac{d^2\overline{\Delta n}}{dx^2} - \frac{\overline{\Delta n}}{\tau_b} + \frac{ke^{-\alpha x} + kRe^{\alpha(x-W)}}{s+1/\tau_f}, \tag{A5}$$

which is an ordinary differential equation in x whose solution is

$$\overline{\Delta n} = A\cosh\left[\left(\frac{s+1/\tau_b}{D}\right)^{1/2} x\right] + B\sinh\left[\left(\frac{s+1/\tau_b}{D}\right)^{1/2} x\right] + C_1 e^{-\alpha x} + C_2 e^{\alpha x}. \tag{A6}$$

The constants C_1 and C_2 may be obtained by substituting Equation (A6) into Equation (A5). The first two terms of Equation (A6) cancel with their derivatives in Equation (A5), eliminating the constants A and B. C_1 and C_2 are then found to be

$$C_1 = \frac{k}{(s+1/\tau_f)(s+1/\tau_b - \alpha^2 D)}. \tag{A7a}$$

$$C_2 = \frac{kRe^{-\alpha W}}{(s+1/\tau_f)(s+1/\tau_b - \alpha^2 D)} \tag{A7b}$$

In order to find the constants A and B, we take the Laplace transform of the boundary conditions (A2):

$$D\frac{\partial\overline{\Delta n}(-W/2,s)}{\partial x} = S\overline{\Delta n}(-\frac{W}{2},s) \tag{A8a}$$

and

$$-D\frac{\partial\overline{\Delta n}(W/2,s)}{\partial x} = S\overline{\Delta n}(\frac{W}{2},s). \tag{A8b}$$

Substitution of Equation (A6) into Equation (A8a) and making using of the odd and even parity of sinh and cosh yields

$$-DA\sinh\left[\left(\frac{s+1/\tau_b}{D}\right)^{1/2}x\right]\left(\frac{s+1/\tau_b}{D}\right)^{1/2}+DB\cosh\left[\left(\frac{s+1/\tau_b}{D}\right)^{1/2}x\right]\left(\frac{s+1/\tau_b}{D}\right)^{1/2}$$
$$-\alpha DC_1e^{\alpha W/2}+\alpha DC_2e^{-\alpha W/2}$$
$$=SA\cosh\left[\left(\frac{s+1/\tau_b}{D}\right)^{1/2}x\right]-SB\sinh\left[\left(\frac{s+1/\tau_b}{D}\right)^{1/2}x\right]+SC_1e^{\alpha W/2}+SC_2e^{-\alpha W/2} \tag{A9a}$$

Similarly, substitution of Equation (A6) into Equation (A8b) yields

$$-DA\sinh\left[\left(\frac{s+1/\tau_b}{D}\right)^{1/2}x\right]\left(\frac{s+1/\tau_b}{D}\right)^{1/2}-DB\cosh\left[\left(\frac{s+1/\tau_b}{D}\right)^{1/2}x\right]\left(\frac{s+1/\tau_b}{D}\right)^{1/2}$$
$$+\alpha DC_1e^{-\alpha W/2}-\alpha DC_2e^{\alpha W/2}$$
$$=SA\cosh\left[\left(\frac{s+1/\tau_b}{D}\right)^{1/2}x\right]+SB\sinh\left[\left(\frac{s+1/\tau_b}{D}\right)^{1/2}x\right]+SC_1e^{-\alpha W/2}+SC_2e^{\alpha W/2} \tag{A9b}$$

Addition of Equations (A9) eliminates the constant B and allows A to be found:

$$A=-\frac{\left[\alpha D\sinh\left(\frac{\alpha W}{2}\right)+S\cosh\left(\frac{\alpha W}{2}\right)\right](C_1+C_2)}{D\left(\frac{s+1/\tau_b}{D}\right)^{1/2}\sinh\left[\left(\frac{s+1/\tau_b}{D}\right)^{1/2}\frac{W}{2}\right]+S\cosh\left[\left(\frac{s+1/\tau_b}{D}\right)^{1/2}\frac{W}{2}\right]} \tag{A10a}$$

Substraction of Equation (A9.b) from Equation (A9.a) eliminates A and allows B to be found:

$$B=\frac{\left[\alpha D\cosh\left(\frac{\alpha W}{2}\right)+S\sinh\left(\frac{\alpha W}{2}\right)\right](C_1-C_2)}{D\left(\frac{s+1/\tau_b}{D}\right)^{1/2}\cosh\left[\left(\frac{s+1/\tau_b}{D}\right)^{1/2}\frac{W}{2}\right]+S\sinh\left[\left(\frac{s+1/\tau_b}{D}\right)^{1/2}\frac{W}{2}\right]} \tag{A10b}$$

Finally, substitution of Equations (A7) and (A10) into Equation (A6) allows the full Laplace transform to be found:

$$\overline{\Delta n}(x,s) = -\frac{\cosh\left[\left(\frac{s+1/\tau_b}{D}\right)^{1/2}x\right]\left[D\alpha\sinh\left(\frac{\alpha W}{2}\right)+S\cosh\left(\frac{\alpha W}{2}\right)\right]k(1+Re^{-\alpha W})}{\left(s+\frac{1}{\tau_f}\right)\left(s+\frac{1}{\tau_b}-D\alpha^2\right)\left\{D\left(\frac{s+1/\tau_b}{D}\right)^{1/2}\sinh\left[\left(\frac{s+1/\tau_b}{D}\right)^{1/2}\frac{W}{2}\right]+S\cosh\left[\left(\frac{s+1/\tau_b}{D}\right)^{1/2}\frac{W}{2}\right]\right\}}$$
$$+\frac{\sinh\left[\left(\frac{s+1/\tau_b}{D}\right)^{1/2}x\right]\left[D\alpha\cosh\left(\frac{\alpha W}{2}\right)+S\sinh\left(\frac{\alpha W}{2}\right)\right]k(1-Re^{-\alpha W})}{\left(s+\frac{1}{\tau_f}\right)\left(s+\frac{1}{\tau_b}-D\alpha^2\right)\left\{D\left(\frac{s+1/\tau_b}{D}\right)^{1/2}\cosh\left[\left(\frac{s+1/\tau_b}{D}\right)^{1/2}\frac{W}{2}\right]+S\sinh\left[\left(\frac{s+1/\tau_b}{D}\right)^{1/2}\frac{W}{2}\right]\right\}}$$
$$+\frac{ke^{-\alpha x}+kRe^{\alpha(x-W)}}{\left(s+\frac{1}{\tau_f}\right)\left(s+\frac{1}{\tau_b}-D\alpha^2\right)} \qquad \text{(A11)}$$

$$\overline{\Delta n_1}(x,s) = -\frac{\cosh\left[\left(\frac{s+1/\tau_b}{D}\right)^{1/2}x\right]\left[D\alpha\sinh\left(\frac{\alpha W}{2}\right)+S\cosh\left(\frac{\alpha W}{2}\right)\right]k(1+Re^{-\alpha W})}{\left(s+\frac{1}{\tau_b}-D\alpha^2\right)\left\{D\left(\frac{s+1/\tau_b}{D}\right)^{1/2}\sinh\left[\left(\frac{s+1/\tau_b}{D}\right)^{1/2}\frac{W}{2}\right]+S\cosh\left[\left(\frac{s+1/\tau_b}{D}\right)^{1/2}\frac{W}{2}\right]\right\}}$$

In order to find the inverse Laplace transform of Equation (A11), define

(A12a)

and

$$\overline{\Delta n_2}(x,s) = \frac{\sinh\left[\left(\frac{s+1/\tau_b}{D}\right)^{1/2}x\right]\left[D\alpha\cosh\left(\frac{\alpha W}{2}\right)+S\sinh\left(\frac{\alpha W}{2}\right)\right]k(1-Re^{-\alpha W})}{\left(s+\frac{1}{\tau_b}-D\alpha^2\right)\left\{D\left(\frac{s+1/\tau_b}{D}\right)^{1/2}\cosh\left[\left(\frac{s+1/\tau_b}{D}\right)^{1/2}\frac{W}{2}\right]+S\sinh\left[\left(\frac{s+1/\tau_b}{D}\right)^{1/2}\frac{W}{2}\right]\right\}}$$

(A12b)

and

$$\overline{\Delta n_3}(x,s) = \frac{ke^{-\alpha x} + kRe^{\alpha(x-W)}}{\left(s+\frac{1}{\tau_f}\right)\left(s+\frac{1}{\tau_b}-D\alpha^2\right)}, \tag{A12c}$$

so that Equation (A11) may be written

$$\overline{\Delta n}(x,s) = \frac{\overline{\Delta n_1}(x,s)}{s+1/\tau_f} + \frac{\overline{\Delta n_2}(x,s)}{s+1/\tau_f} + \overline{\Delta n_3}(x,s). \tag{A13}$$

Equation (A13) has three terms. The inverse Laplace transform of the third term may be found in a table:

$$\Delta n_3(x,t) = \frac{\left(ke^{-\alpha x} + kRe^{\alpha(x-W)}\right)\left(e^{-t/\tau_f} - e^{-t/\tau_b+\alpha^2 Dt}\right)}{-1/\tau_f + 1/\tau_b - \alpha^2 D}. \tag{A14}$$

The inverse Laplace transform of the first two terms in Equation (A13) is more complicated. To begin, consider

$$\overline{\Delta n_1}(x, s-1/\tau_b+\alpha^2 D) = \frac{-\cosh\left[\left(\frac{s+\alpha^2 D}{D}\right)^{1/2} x\right]\left[D\alpha\sinh\left(\frac{\alpha W}{2}\right) + S\cosh\left(\frac{\alpha W}{2}\right)\right]k(1+Re^{-\alpha W})}{s\left\{D\left(\frac{s+\alpha^2 D}{D}\right)^{1/2}\sinh\left[\left(\frac{s+\alpha^2 D}{D}\right)^{1/2}\frac{W}{2}\right] + S\cosh\left[\left(\frac{s+\alpha^2 D}{D}\right)^{1/2}\frac{W}{2}\right]\right\}} \tag{A15}$$

The inverse transform of Equation (A15) may be obtained by using the expansion theorem

$$f(t) = L^{-1}\left[\frac{\varphi(s)}{\psi(s)}\right] = \sum_{i=1}^{\infty}\frac{\varphi(s_i)}{\psi'(s_i)}e^{s_i t}, \tag{A16}$$

where s_n are the roots of $\psi(s)$. Equation (A16) is valid whenever the Taylor series expansion

$$\frac{\varphi(s)}{\psi(s)} = \frac{A_0 + A_1 s + A_2 s^2 + \cdots}{B_0 + B_1 s + B_2 s^2 + \cdots} \tag{A17}$$

is such that $A_0 \neq 0$ and $B_0 = 0$. The objective in manipulating Equation (A11) via Equations (A12) and (A15) was to obtain a factor of s in front of the denominator in order to satisfy the condition $B_0 = 0$.

To apply Equation (A16) to Equation (A15), we must find the roots of $\psi(s)$, here defined as the denominator of Equation (A15). It is clear that one root is s = 0. It order to find the other roots, it is expedient to define

$$\mu \equiv j\left(\frac{s+\alpha^2 D}{D}\right)^{1/2}\frac{W}{2}, \tag{A18}$$

with $j = (-1)^{1/2}$. Substitution of Equation (A18) into $\psi(s)$ and setting $\psi(s)$ to zero yields

$$-\frac{2\mu D}{W}\sin\mu + S\cos\mu = 0\,. \tag{A19}$$

Upon rearrangement, Equation (A19) yields

$$\cot\mu = \frac{2D}{WS}\mu\,. \tag{A20}$$

Rearrange Equation (A18) to give

$$s = -\frac{4\mu^2 D}{W^2} - \alpha^2 D\,. \tag{A21}$$

We have thus found all the roots of the denominator $\psi(s)$ of Equation (A15): one rational root s = 0, and an infinite sequence of irrational roots given by Equation (A21), where μ is given by the positive solutions of Equation (A20). (The negative solutions of Equation (A20), when inserted in Equation (A21), give the same values of s as the positive solutions, since μ is squared in Equation (A21). Thus, the negative solutions of Equation (A20) must be omitted to avoid finding redundant values of s.)

We can now apply Equation (A16). For the root s = 0, we find

$$\varphi(0) = -\cosh(\alpha x)\left[\alpha D \sinh(\alpha W/2) + S\cosh(\alpha W/2)\right]k(1+Re^{-\alpha W}) \tag{A22}$$

and

$$\psi'(0) = \alpha D \sinh(\alpha W/2) + S\cosh(\alpha W/2). \tag{A23}$$

(In order to verify Equation (A23), one may take the derivative of the denominator of Equation (A15) and set s = 0.) Similarly, for the irrational roots s_n,

$$\varphi(s_i) = -\cosh(2x\mu_i/W)\left[\alpha D \sinh(\alpha W/2) + S\cosh(\alpha W/2)\right]k(1+Re^{-\alpha W}) \tag{A24}$$

and

$$\psi'(s_i) = -\left(\frac{\mu_i}{2} + \frac{\alpha^2 W^2}{8\mu_i}\right)\left(\frac{2\mu_i D}{W}\cos\mu_i + \left(\frac{2D}{W} + S\right)\sin\mu_i\right). \tag{A25}$$

(The algebra leading to Equation (A25) is complicated, but the reader may verify the result by taking the derivative of the denominator of Equation (A15) and defining μ according to Equation (A21).)

Thus the Laplace transform of Equation (A15) is

$$\begin{aligned} L^{-1}\left[\overline{\Delta n_1}(x, s-1/\tau_b + \alpha^2 D)\right] &= -G_0 e^{-\alpha W/2}\cosh(\alpha x) \\ &+ \sum_{i=1}^{\infty} \frac{k(1+Re^{-\alpha W})\cos\left(\frac{2\mu_i x}{W}\right)\left[D\alpha\sinh\left(\frac{\alpha W}{2}\right) + S\cosh\left(\frac{\alpha W}{2}\right)\right]e^{-4D\mu_i^2 t/W^2 - \alpha^2 Dt}}{\left(\frac{\mu_i}{2} + \frac{W^2\alpha^2}{8\mu_i}\right)\left(\frac{2D\mu_i}{W}\cos\mu_i + \left(S + \frac{2D}{W}\right)\sin\mu_i\right)} \end{aligned} \tag{A26}$$

We now make use of the shifting property of Laplace transforms

$$f(t) = L^{-1}\left[F(s-a)\right]e^{-at} \tag{A27}$$

where a = $1/\tau_b$ - $\alpha^2 D$ to find

$$\Delta n_1(x,t) = -k(1+Re^{-\alpha W})\cosh(\alpha x)e^{t\alpha^2 D - t/\tau_b} + \sum_{i=1}^{\infty} \frac{k(1+Re^{-\alpha W})\cos\left(\frac{2\mu_i x}{W}\right)\left[D\alpha\sinh\left(\frac{\alpha W}{2}\right)+S\cosh\left(\frac{\alpha W}{2}\right)\right]e^{-4D\mu_i^2 t/W^2 - t/\tau_b}}{\left(\frac{\mu_i}{2}+\frac{W^2\alpha^2}{8\mu_i}\right)\left(\frac{2D\mu_i}{W}\cos\mu_i+\left(S+\frac{2D}{W}\right)\sin\mu_i\right)} \quad \text{(A28)}$$

Next we note that the first term of Equation (A13) is $\overline{\Delta n_1}$ multiplied by $1/(s+1/\tau_f)$. In order to find the inverse Laplace transform of this product, we use convolution:

$$L^{-1}[F_1(s)F_2(s)] = \int_0 f_1(t-t')f_2(t')dt' \quad \text{(A29)}$$

To use this equation, substitute as follows:

$$L^{-1}\left[\frac{1}{s+1/\tau_f}\overline{\Delta n_1}(s)\right] = \int_0 e^{(t'-t)/\tau_f}\Delta n_1(x,t')dt' \quad \text{(A30)}$$

where we have used

$$L^{-1}\left[\frac{1}{s+1/\tau_f}\right] = e^{-t/\tau_f}. \quad \text{(A31)}$$

Insertion of Equation (A28) into Equation (A30) yields the inverse Laplace transform of the first term in Equation (A13):

$$L^{-1}\left[\frac{\overline{\Delta n_1}}{s+1/\tau_f}\right] = -\frac{k(1+Re^{-\alpha W})\cosh(\alpha x)\left(e^{-\alpha^2 Dt - t/\tau_b} - e^{-t/\tau_f}\right)}{1/\tau_f + \alpha^2 D - 1/\tau_b} + \sum_{i=1}^{\infty} \frac{k(1+Re^{-\alpha W})\cos\left(\frac{2\mu_i x}{W}\right)\left[D\alpha\sinh\left(\frac{\alpha W}{2}\right)+S\cosh\left(\frac{\alpha W}{2}\right)\right]\left(e^{-4D\mu_i^2 t/W^2 - t/\tau_b} - e^{-t/\tau_f}\right)}{\left(\frac{1}{\tau_f}-\frac{1}{\tau_b}-\frac{4D\mu_i^2}{W^2}\right)\left(\frac{\mu_i}{2}+\frac{W^2\alpha^2}{8\mu_i}\right)\left(\frac{2D\mu_i}{W}\cos\mu_i+\left(S+\frac{2D}{W}\right)\sin\mu_i\right)} \quad \text{(A32)}$$

When the procedure outlined in Equations (A15-A32) is performed for the second term in Equation (A13), the inverse Laplace transform of this second term is found as

$$L^{-1}\left[\frac{\overline{\Delta n_2}}{s+1/\tau_f}\right]=\frac{k(1-Re^{-\alpha W})\sinh(\alpha x)\left(e^{-\alpha^2 Dt-t/\tau_b}-e^{-t/\tau_f}\right)}{1/\tau_f+\alpha^2 D-1/\tau_b}$$
$$+\sum_{i=1}^{\infty}\frac{G_0 e^{-\alpha W/2}\sin\left(\frac{2\nu_i x}{W}\right)\left[D\alpha\cosh\left(\frac{\alpha W}{2}\right)+S\sinh\left(\frac{\alpha W}{2}\right)\right]\left(e^{-4D\nu_i^2 t/W^2-t/\tau_b}-e^{-t/\tau_f}\right)}{\left(\frac{1}{\tau_f}-\frac{1}{\tau_b}-\frac{4D\nu_i^2}{W^2}\right)\left(\frac{\nu_i}{2}+\frac{W^2\alpha^2}{8\nu_i}\right)\left(-\frac{2D\nu_i}{W}\sin\nu_i+\left(S+\frac{2D}{W}\right)\cos\nu_i\right)} \tag{A33}$$

where ν_i are the positive solutions of

$$\tan\nu=-\frac{2D}{WS}\nu\,. \tag{A34}$$

The final solution $\Delta n(x,t)$ is found by summing Equations (A14), (A32), and (A33). Remarkably, Equation (A14) cancels with the first term in Equation (A32) and the first term in Equation (A33), after using the identity

$$-\cosh(\alpha x)+\sinh(\alpha x)=-e^{-\alpha x}\,. \tag{A35}$$

We finally obtain the solution:

$$n(x,t)=\sum_{i=1}^{\infty}\frac{k(1+Re^{-\alpha W})\cos\left(\frac{2\mu_i x}{W}\right)\left[D\alpha\sinh\left(\frac{\alpha W}{2}\right)+S\cosh\left(\frac{\alpha W}{2}\right)\right]\left(e^{-4D\mu_i^2 t/W^2-t/\tau_b}-e^{-t/\tau_f}\right)}{\left(\frac{1}{\tau_f}-\frac{1}{\tau_b}-\frac{4D\mu_i^2}{W^2}\right)\left(\frac{\mu_i}{2}+\frac{W^2\alpha^2}{8\mu_i}\right)\left(\frac{2D\mu_i}{W}\cos\mu_i+\left(S+\frac{2D}{W}\right)\sin\mu_i\right)}$$
$$+\sum_{i=1}^{\infty}\frac{k(1-Re^{-\alpha W})\sin\left(\frac{2\nu_i x}{W}\right)\left[D\alpha\cosh\left(\frac{\alpha W}{2}\right)+S\sinh\left(\frac{\alpha W}{2}\right)\right]\left(e^{-4D\nu_i^2 t/W^2-t/\tau_b}-e^{-t/\tau_f}\right)}{\left(\frac{1}{\tau_f}-\frac{1}{\tau_b}-\frac{4D\nu_i^2}{W^2}\right)\left(\frac{\nu_i}{2}+\frac{W^2\alpha^2}{8\nu_i}\right)\left(-\frac{2D\nu_i}{W}\sin\nu_i+\left(S+\frac{2D}{W}\right)\cos\nu_i\right)} \tag{A36}$$

where, again, μ_i and ν_i are the positive roots (which must be computed numerically) of

$$\cot\mu = \frac{2D}{WS}\mu \tag{A37a}$$

and

$$\tan\nu = -\frac{2D}{WS}\nu\,. \tag{A37b}$$

In order to extend Equation (A36) to the case of illumination by a spectrum of wavelengths, simply sum the solutions obtained for all values of α, each with a corresponding value of k. This follows from the linearity of the continuity equation, Equation (1). To prove in this specific case that Equation (A36) can be summed over wavelength for a spectrum of illumination, it will suffice to show that

$$\overline{\Delta n}(x,s) = \sum_{\lambda}\overline{\Delta n_{\lambda}}(x,s)\,, \tag{A38}$$

where each $\overline{\Delta n_{\lambda}}(x,s)$ is the Laplace transform under monochromatic illumination given in Equation (A11). For a spectrum of illumination, Equation (A3) becomes

$$G(x,t) = \sum_{\lambda}\left[k_{\lambda}e^{-\alpha_{\lambda}x} + k\lambda Re^{\alpha\lambda(x-W)}\right]e^{-t/\tau_f}\,, \tag{A39}$$

and otherwise the continuity equation and boundary conditions remain the same. Equation (A39) assumes that each wavelength of illumination has the same time dependence.

Equation (A5), the Laplace transform of the continuity equation, becomes

$$s\overline{\Delta n} = D\frac{d^2\overline{\Delta n}}{dx^2} - \frac{\overline{\Delta n}}{\tau_b} + \sum_{\lambda}\frac{k_{\lambda}e^{-\alpha_{\lambda}x} + k\lambda Re^{\alpha_{\lambda}(x-W)}}{s+1/\tau_f}\,, \tag{A40}$$

and its solution, Equation (A6), becomes

$$\overline{\Delta n} = A\cosh\left[\left(\frac{s+1/\tau_b}{D}\right)^{1/2}x\right] + B\sinh\left[\left(\frac{s+1/\tau_b}{D}\right)^{1/2}x\right] + \sum_{\lambda}\left(C_{1,\lambda}e^{-\alpha_{\lambda}x} + C_{2,\lambda}e^{\alpha_{\lambda}x}\right). \tag{A41}$$

By the orthogonality of the exponential terms, each term in the sum over λ in Equation (A41) must independently solve Equation (A40); therefore, Equation (A7) gives the values of $C_{1,\lambda}$ and $C_{2,\lambda}$. This already shows that the third line of Equation (A11) becomes a sum of monochromatic terms over the spectrum of illumination. Now we must show that A and B in Equation (A11) become sums over A_λ and B_λ. By inserting Equation (A41) into the Laplace transforms of the boundary conditions, Equations (A7) and (A8), it can be shown after some algebra that

$$A = -\frac{\sum_{\lambda}\left[\alpha_\lambda D \sinh\left(\frac{\alpha_\lambda W}{2}\right) + S\cosh\left(\frac{\alpha_\lambda W}{2}\right)\right]\left(C_{1,\lambda} + C_{2,\lambda}\right)}{D\left(\frac{s+1/\tau_b}{D}\right)^{1/2}\sinh\left[\left(\frac{s+1/\tau_b}{D}\right)^{1/2}\frac{W}{2}\right] + S\cosh\left[\left(\frac{s+1/\tau_b}{D}\right)^{1/2}\frac{W}{2}\right]} \quad \text{(A42a)}$$

and

$$B = \frac{\sum_{\lambda}\left[\alpha_\lambda D \cosh\left(\frac{\alpha_\lambda W}{2}\right) + S\sinh\left(\frac{\alpha\lambda W}{2}\right)\right]\left(C_{1,\lambda} - C_{2,\lambda}\right)}{D\left(\frac{s+1/\tau_b}{D}\right)^{1/2}\cosh\left[\left(\frac{s+1/\tau_b}{D}\right)^{1/2}\frac{W}{2}\right] + S\sinh\left[\left(\frac{s+1/\tau_b}{D}\right)^{1/2}\frac{W}{2}\right]}. \quad \text{(A42b)}$$

Thus, each line in Equation (A11) becomes a sum over wavelength of the monochromatic terms, and Equation (A38) is verified.

APPENDIX B

DERIVATION OF FINITE DIFFERENCE EQUATIONS

The derivations given in this appendix follow the similar treatment for heat conduction given in [82].

Consider the interior point (p,q) shown in Figure B1. Equation (91) will be derived through charge conservation: the net flow of carriers into the shaded box in Figure B1 must equal recombination within the box minus generation within the box. The number current density in the x direction is given by $-D(\partial\Delta n/\partial x) \approx -D\Delta n/\Delta x$. Thus, the flow of carriers through the left side of the box ($F_{p-1,q}$), per unit depth perpendicular to the figure, is

$$F_{p-1,q} = D\Delta y \frac{\Delta n(p-1,q) - \Delta n(p,q)}{\Delta x}. \qquad \text{(B1)}$$

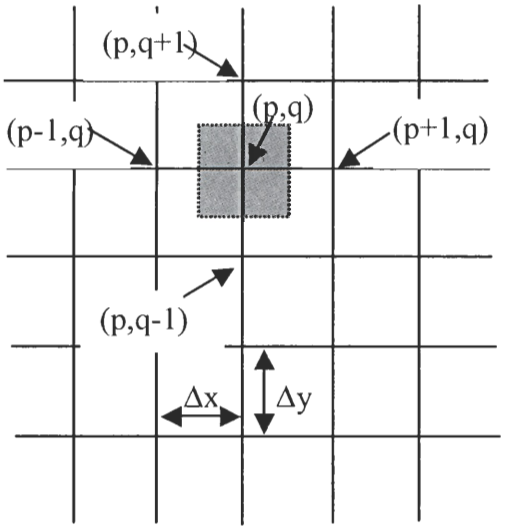

Figure B1. Illustration of an interior point.

$F_{p-1,q}$ is negative if the carrier gradient causes diffusive current to the left. Δy appears in Equation (B1) because the current density is multiplied by length of the surface it flows through, and Δy is the length of the left side of the gray box. Equation (B1) can be easily modified to create $F_{p+1,q}$, $F_{p,q-1}$, and $F_{p,q+1}$. The generation and recombination within the box, per unit depth, are $G\Delta x\Delta y$ and $\Delta x\Delta y\Delta n(p,q)/\tau_b$, respectively. Then, charge conservation in the box gives

$$\begin{aligned} &D\Delta y\frac{\Delta n(p-1,q)-\Delta n(p,q)}{\Delta x}+D\Delta y\frac{\Delta n(p+1,q)-\Delta n(p,q)}{\Delta x}\\ &+D\Delta x\frac{\Delta n(p,q-1)-\Delta n(p,q)}{\Delta y}+D\Delta x\frac{\Delta n(p,q+1)-\Delta n(p,q)}{\Delta y}\\ &+G\Delta x\Delta y-\frac{\Delta x\Delta y\Delta n(p,q)}{\tau_b}=0 \end{aligned} \tag{B2}$$

If Equation (B2) is divided by $\Delta x\Delta y$, Equation (91) is obtained after slight rearrangement.

Next, consider a point along a lateral boundary of the elementary cell, Figure B2. The lateral boundary condition is that no current flows from one identical elementary cell to another, so there is no current from the right into the gray box in Figure B2. Equation (B1) still gives the current from the left, but the current from above and below flow through a surface of length $\Delta x/2$. The current from above, for example, is

$$F_{p,q+1}=D\frac{\Delta x}{2}\frac{\Delta n(p,q+1)-\Delta n(p,q)}{\Delta y}. \tag{B3}$$

The generation is the box is $\Delta x(\Delta y/2)G$, and the recombination is similarly modified. Charge conservation for a box containing a point on the lateral boundary on the right is then

$$
\begin{aligned}
& D\Delta y \frac{\Delta n(p-1,q)-\Delta n(p,q)}{\Delta x} \\
& + D\frac{\Delta x}{2}\frac{\Delta n(p,q-1)-\Delta n(p,q)}{\Delta y} + D\frac{\Delta x}{2}\frac{\Delta n(p,q+1)-\Delta n(p,q)}{\Delta y} \\
& + G\frac{\Delta x}{2}\Delta y - \frac{\Delta x \Delta y \Delta n(p,q)}{2\tau_b} = 0
\end{aligned}
\tag{B3}
$$

A point on a boundary on the left is treated similarly.

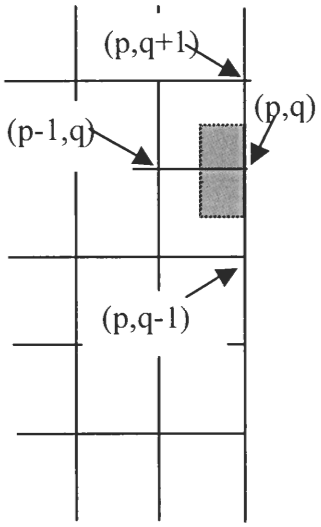

Figure B2. Illustration of a point on a lateral boundary.

A point on the lower boundary, as shown in Figure B3, loses carriers through surface recombination. The recombination current into the surface, per unit depth, is ΔxSΔn(p,q). Otherwise, charge conservation yields a result similar to Equation (B3):

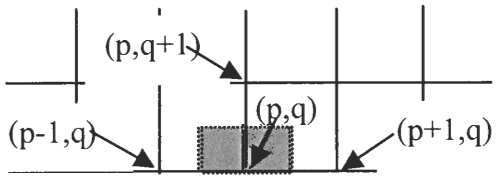

Figure B3. Ilustration of a point on a lower boundary.

$$D\frac{\Delta y}{2}\frac{\Delta n(p-1,q)-\Delta n(p,q)}{\Delta x}+D\frac{\Delta y}{2}\frac{\Delta n(p+1,q)-\Delta n(p,q)}{\Delta x}$$
$$-S\Delta x\Delta n(p,q)+D\Delta x\frac{\Delta n(p,q+1)-\Delta n(p,q)}{\Delta y} \quad . \tag{B4}$$
$$+G\Delta x\frac{\Delta y}{2}-\frac{\Delta x\Delta y\Delta n(p,q)}{2\tau_b}=0$$

A point on the upper boundary is treated similarly.

The final case to consider is a corner, as shown in Figure B4. Charge conservation yields

$$D\frac{\Delta y}{2}\frac{\Delta n(p-1,q)-\Delta n(p,q)}{\Delta x}$$
$$-S\frac{\Delta x}{2}\Delta n(p,q)+D\frac{\Delta x}{2}\frac{\Delta n(p,q+1)-\Delta n(p,q)}{\Delta y} \quad . \tag{B5}$$
$$+G\frac{\Delta x}{2}\frac{\Delta y}{2}-\frac{\Delta x\Delta y\Delta n(p,q)}{4\tau_b}=0$$

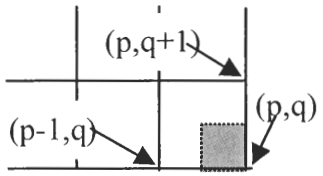

Figure B4. Illustration of a point on a corner.

APPENDIX C

CHARACTERISTICS OF AN ILLUMINATED p-n JUNCTION DIODE

The basic structure of a solar cell is shown in Figure C1. The minority carriers generated by photon absorption diffuse through the material until they encounter the depletion region ($-w_p < x < w_n$ in Figure C1). The electric field in the depletion region sweeps the electrons to the n^+ emitter and the holes to the p base. This reduces the width of the depletion region, thereby lowering the band bending and forward biasing the device.

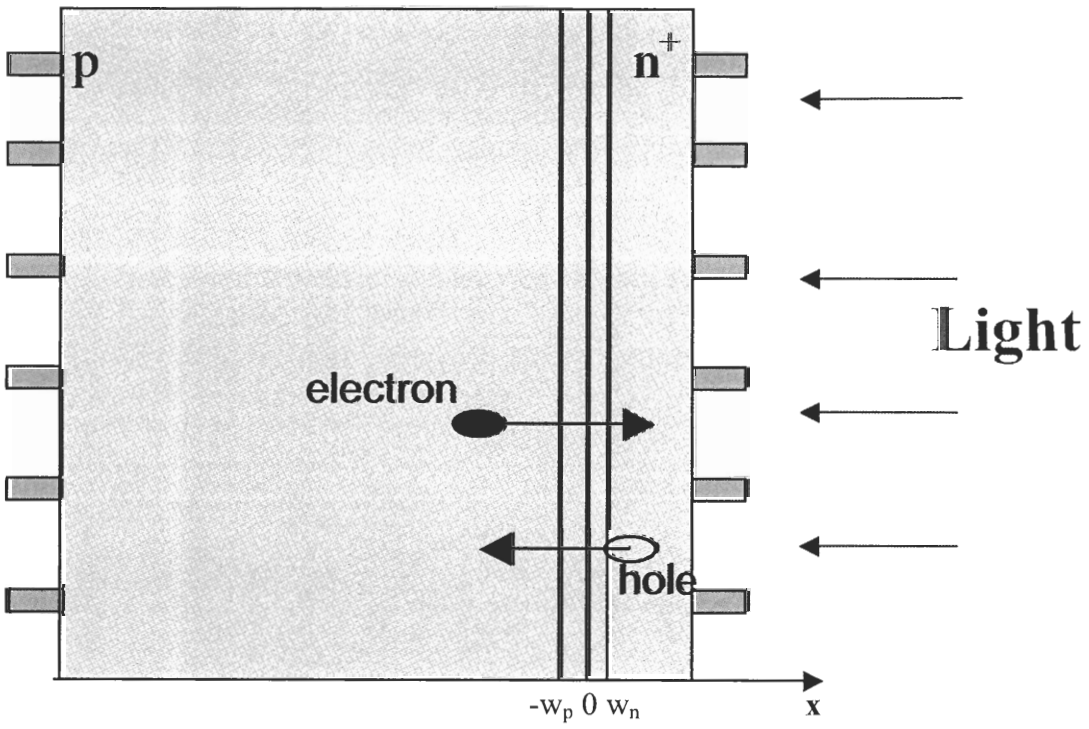

Figure C1. Solar cell structure.

Device simulation software exists for the accurate and realistic modeling of solar cells. However, it is instructive to investigate the basic features analytically. The structure under consideration consists of p-type material with doping level N_A at positions $x < 0$ and n-type material with doping level N_D at positions $x > 0$. If we imagine bringing together the p-type and n-type materials after an initial separation, then the depletion approximation [8] suggests that all the mobile holes between some position $x = -w_p$ and $x = 0$ rush to recombine with all the mobile electrons from $x = 0$ to $x = w_n$. The ionized dopant atoms left behind are responsible for a space-charge region from $x = -w_p$ to $x = w_n$. The first integral of the charge density is proportional to the electric field, which points in the negative x-direction at all positions in the space-charge region (also called the depletion region). Arising from the electric field is a potential difference across the depletion region. In the absence of an external voltage across the structure, the potential difference across the depletion region is [8]

$$\psi_0 = \frac{kT}{q} \ln\left(\frac{N_A N_D}{n_i^2}\right). \tag{C1}$$

If an external voltage V exists across the structure, with higher potential on the p-type side, then the voltage across the depletion region is reduced to $(\psi_0 - V)$.

By solving the Poisson equation with appropriate boundary conditions, $\psi(x)$ can be found as [84]

$$\psi(x) = \begin{cases} \dfrac{qN_A}{2\varepsilon_{Si}}(x + w_p)^2 & -w_p < x < 0 \\ \psi_0 - V - \dfrac{qN_D}{2\varepsilon_{Si}}(x - w_n)^2 & 0 < x < w_n \end{cases}. \tag{C2}$$

By requiring $\psi(x)$ and the electric field to be continuous at x = 0, the edges of the depletion region can be obtained [84]:

$$w_n = \left(\frac{2\varepsilon_{Si} N_A (\psi_0 - V)}{qN_D (N_A + N_D)} \right)^{1/2} \tag{C3}$$

and

$$w_p = \left(\frac{2\varepsilon_{Si} N_D (\psi_0 - V)}{qN_A (N_A + N_D)} \right)^{1/2}. \tag{C4}$$

Assuming uniform generation G, which self-biases the diode in forward bias, the steady-state continuity equation can be used to determine the carrier concentrations for three regions: the p-type region, the depletion region, and the n-type region. Beginning with excess electrons on the p-type side, we can write the steady-state continuity equation as [8]

$$\frac{d^2 \Delta n}{dx^2} = \frac{\Delta n}{L_e^{\ 2}} - \frac{G}{D_e}. \tag{C5}$$

The general solution for $x < -w_p$ is

$$\Delta n = G\tau_e + A \exp[(x + w_p)/L_e] + B \exp[-(x + w_p)/L_e] \tag{C6}$$

where A and B are constants. B is clearly 0 to prevent Δn from diverging as x becomes very negative. A is found from the law of junction, requiring [8]

$$\Delta n(-w_p) = \frac{n_i^{\ 2}}{N_A} \left[e^{qV/kT} - 1 \right]. \tag{C7}$$

Equation (C7) is derived by equating the drift and diffusion currents in the depletion region. Although this assumption is not exact for $V \neq 0$, it reflects the fact that the net current is the small difference between the drift and diffusion currents [8]. Combining Equations (C6) and (C7) gives

$$n(x) = \frac{n_i^2}{N_A} + G\tau_e + \left[\frac{n_i^2}{N_A}(e^{qV/kT} - 1) - G\tau_e\right]\exp[(x + w_p)/L_e]. \tag{C8}$$

To find n(x) in the depletion region, we again use the assumption that diffusion and drift current there are the same [8]:

$$-q\mu_e nE = qD_e\frac{dn}{dx} \tag{C9}$$

which becomes, through the Einstein relation [8],

$$-E(x)dx = \frac{kT}{q}\frac{dn}{n}. \tag{C10}$$

Integrating both sides and recognizing that ψ(x) is the integral of –E(x):

$$\begin{aligned} -\int_x^{w_n} E(x')dx' &= \frac{kT}{q}\int_{n(x)}^{N_D}\frac{dn}{n} \\ \psi(w_n) - \psi(x) &= \frac{kT}{q}\ln\frac{N_D}{n(x)} \\ \psi_0 - V - \psi(x) &= \frac{kT}{q}\ln\frac{N_D}{n(x)} \end{aligned} \tag{C11}$$

Finally, solving for n(x) gives

$$n(x) = N_D\exp[q[\psi(x) - \psi_0 + V]/kT], \tag{C12}$$

where ψ(x) is given in Equation (C2).

The last region where we must solve for n(x) is the n-type side. Charge conservation in this region gives Δn(x) = Δp(x), where Δp(x) is obtained in this region through an equation similar to Equation (C6):

$$\Delta p(x) = G\tau_h + \left[\frac{n_i^2}{N_D}(e^{qV/kT} - 1) - G\tau_h\right]\exp[-(x - w_n)/L_h]. \tag{C13}$$

By following a similar analysis for holes in the three regions of interest, we find

$$p(x) = \begin{cases} N_A + \Delta n & x < -w_p \\ N_A \exp[-q\psi(x)/kT] & -w_p < x < w_n \\ \dfrac{n_i^2}{N_D} + G\tau_h + \left[\dfrac{n_i^2}{N_D}(e^{qV/kT} - 1) - G\tau_h\right]\exp[-(x - w_n)/L_h] & x > w_n \end{cases}$$

(C14)

For accuracy exceeding the simple analytical model, the device simulation software PC-1D can be used to plot n(x) and p(x), as shown in Figure C2. Here, we choose V = 0, signifying short-circuit conditions. We can see from the slope of the minority carrier profiles that minority carriers are traveling by diffusion into the depletion region.

We can compute the quasi-fermi levels by using the equations [52]

$$\varphi_n = \psi - \frac{kT}{q}\ln\frac{n}{n_i} \qquad \text{(C15)}$$

and

$$\varphi_p = \frac{kT}{q}\ln\frac{p}{n_i} - \psi\,. \qquad \text{(C16)}$$

For short-circuit conditions, PC-1D produces Figure C3.

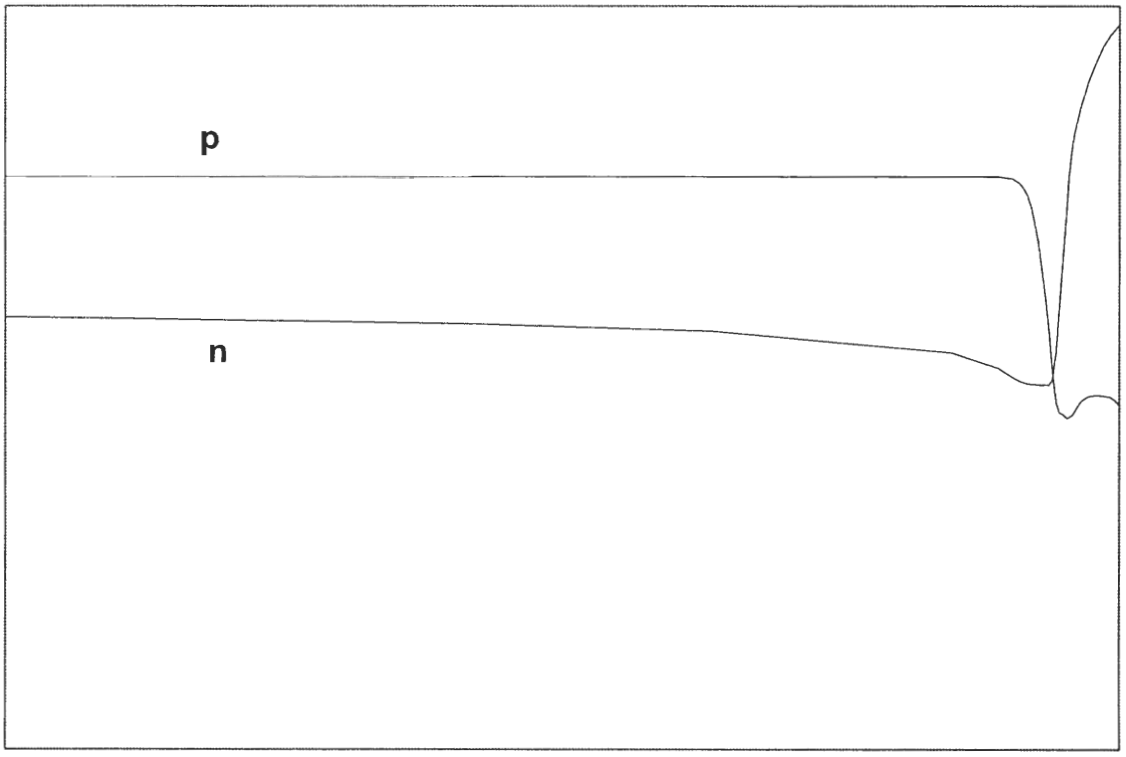

Figure C2. Carrier concentrations in short-circuit conditions.

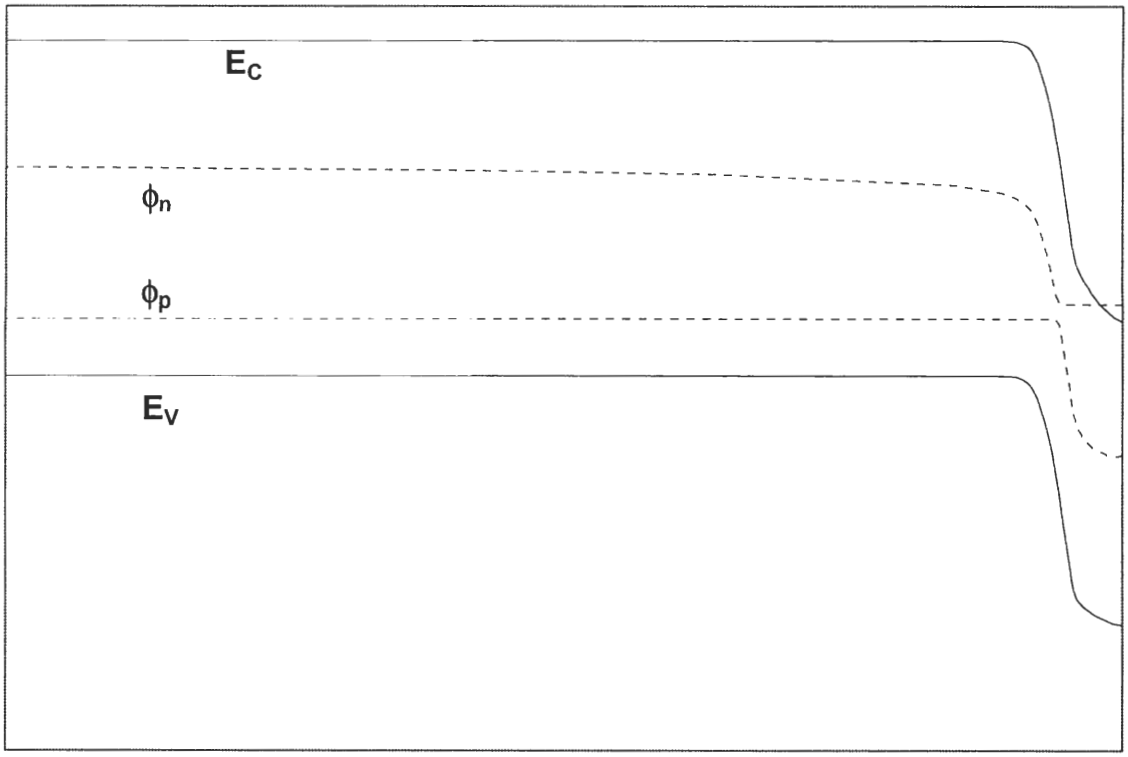

Figure C3. Band diagram for short-circuit conditions.

To plot the results for open-circuit conditions, we set I = 0 in [8]

$$I = I_0(e^{qV/kT} - 1) - I_L, \qquad \text{(C17)}$$

where $I_L = qAG(L_e + W + L_h)$; W is the width of the depletion region. Equation (C17) is a statement of the superposition principle: the current due to illumination ($-I_L$) is added to the standard diode equation to find the total current. The V_{oc} carrier concentrations are computed with PC-1D and shown in Figure C4.

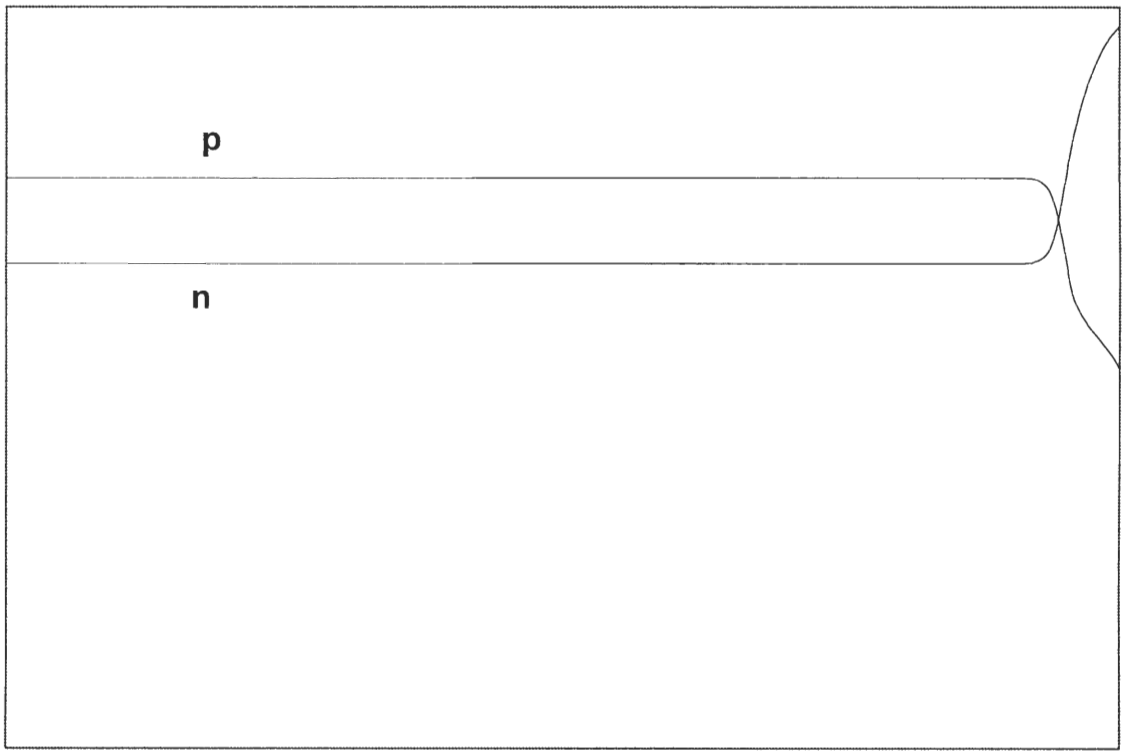

Figure C4. Carrier concentrations for open-circuit conditions.

The band diagram for open-circuit conditions is shown in Figure C5. The quasi-Fermi levels are essentially flat, indicating the absence of a current.

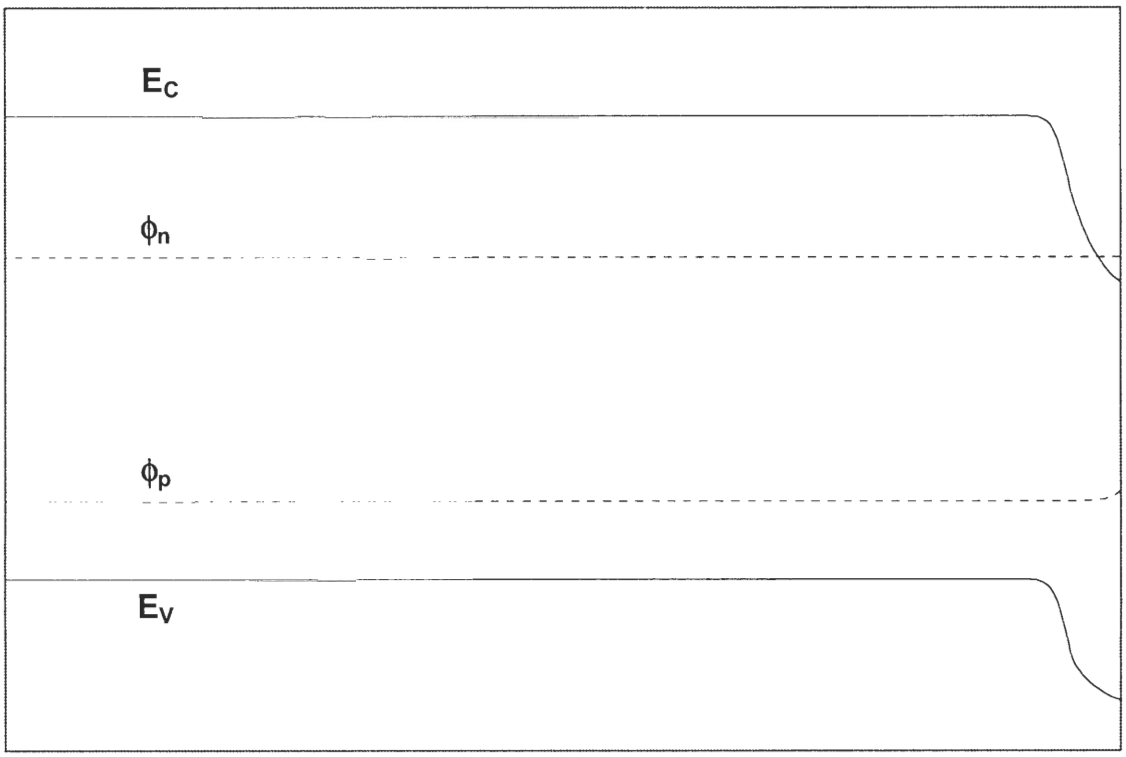

Figure C5. Band diagram for open-circuit conditions.

REFERENCES

[1] J. Szlufcik, S. Sivoththaman, J. F. Nijs, R. P. Mertens, and R. van Overstraeten, "Low-cost industrial technologies of crystalline silicon solar cells," *Proc. IEEE,* vol. 85, pp. 711-730, May 1997.

[2] A. Rohatgi, A. Ebong, V. Yelundur, and A. Ristow, "Rapid thermal processing of next generation silicon solar cells," in *Proc. 10th International Workshop on the Physics of Semiconductor Devices*, New Delhi, 1999, pp. 14-18.

[3] *PV Roapmap*, National Center for Photovoltaics, Department of Energy, 2000.

[4] P. Maycock, ed. *PV News*, Feb. 2003.

[5] A. Rohatgi, W. A. Doolittle, and A. W. Smith, "Doping and oxygen dependence of efficiency of EFG silicon solar cells," in *Proc. 21st IEEE PVSC*, Kissimmee, FL, 1990, pp. 581-587.

[6] A. G. Aberle, T. Lauinger, J. Schmidt, and R. Hezel, "Injection-level dependent surface recombination velocities at the silicon-plasma silicon nitride interface," *Appl. Phys. Lett.*, vol. 21, pp. 2828-2830, May 22, 1995.

[7] M. Bail and R. Brendel, "Separation of bulk and surface recombination by steady state photoconductance," *16th European Photoltaic Solar Energy Conference*, Glasgow, UK, 2000.

[8] M. A. Green, *Solar Cells.* The University of New South Wales: Kensington, NSW, 1992.

[9] A. Aberle, *Advanced Surface Passivation for Crystalline Silicon Solar Cells*, University of New South Wales, Sydney, Australia, 1999.

[10] A. Rohatgi, P. Rai-Choudhury, and D. L. Meier, "Surface-passivated high-efficiency silicon solar cells," in *Proc. Seventeenth IEEE Photovoltaics Specialists Conf.*, 1984, pp. 409-414.

[11] S. K. Datta, K. Mukhopadhyay, P. K. Pal, and H. Saha, "Analysis of thin silicon solar cells for high efficiency," *Sol. En. Mat. and Solar Cells*, vol. 33, pp. 483-497, Aug. 1994.

[12] H. Nagel, C. Berge, and A. Aberle, "Generalized analysis of quasi-steady-state, quasi-transient measurements of carrier lifetimes in semiconductors," *J. Appl. Phys*, vol. 86, pp. 6218-6221, Dec. 1, 1999.

[13] R. Sinton, A. Cuevas, and M. Stuckings, "Quasi-steady-state photoconductance, a new method for solar cell material and device characterization," in *Proc. 25th IEEE PVSC*, 1996, pp. 457-460.

[14] Nagel et al., "Relationship between effective carrier lifetimes in silicon determined under transient and steady-state illumination," in *16th European Photoltaic Solar Energy Conference*, Glasgow, UK, 2000.

[15] D. E. Kane and R. M. Swanson, "Measurement of the emitter saturation current by a contactless photoconductivity decay method," in *Proc. 18th IEEE PVSC*, 1985, pp. 578-583.

[16] A. B. Sproul, "Dimensionless solution of the equation describing the effect of surface recombination on carrier decay in semiconductors," *J. Appl. Phys.*, vol. 76, pp. 2851-2854, Sept. 1, 1994.

[17] K. L. Luke and L. Cheng, "Analysis of the interaction of a laser pulse with a silicon wafer: Determination of bulk lifetime and surface recombination velocity," *J. Appl. Phys.*, vol 61, pp. 2282-2293, March 15, 1987.

[18] A. Cuevas and R. Sinton, "Prediction of the open-circuit voltage of solar cells from the steady-state photoconductance," *Prog. in PV*, vol. 5, pp. 79-90, 1997.

[19] D. MacDonald and A. Cuevas, "Trapping of minority carriers in multicrystalline silicon," *Appl. Phys. Lett.*, vol. 74, pp. 1710-1712, March 22, 1999.

[20] J. R. Elmiger, R. Schieck, M. Kunst., "Recombination at the silicon nitride/silicon interface," *J. Vac. Sci. Technol. A*, vol. 15, pp. 2418-2425, Jul/Aug 1997.

[21] H. M'Saad, J. Michel, J. J. Lappe, and L. C. Kimerling, "Monitoring and optimization of silicon surface quality," *J. Electrochem. Soc.*, vol. 142, pp. 2833-2835, Aug. 1995.

[22] E. Yablonivitch *et al.*, "Unusually low surface-recombination velocity on silicon and germanium surfaces," *Phys. Rev. Lett.*, vol. 57, pp. 249-252, July 14, 1986.

[23] E. Gaubas and J. Vanhellemont, "A simple technique for the separation of bulk and surface recombination parameters in silicon," *J. Appl. Phys.*, vol. 80, pp. 6293-6297, Dec. 1, 1996.

[24] H. Ostendorf and A. L. Endros, "Simultaneous mapping of bulk and surface recombination in silicon," *Appl. Phys. Lett.*, vol. 71, pp. 3275-3277, Dec. 1, 1997.

[25] A. G. Aberle, S. Glunz, and W. Warta, "Impact of illumination level and oxide parameters on Shockley-Read-Hall recombination at the Si-SiO_2 interface," *J. Appl. Phys.*, vol. 71, pp. 4422-4431, May 1, 1992.

[26] S. Bowden, F. Duerinckx, J. Szlufcik, and J. Nijs. "Rear surface passivation of multicrystalline silicon solar cells," in *16th European Photoltaic Solar Energy Conference*, Glasgow, UK, 2000.

[27] A. Cuevas, M. Stocks, D. McDonald, M. Cerr, and C. Samundsett, "Recombination and trapping in multicrystalline silicon," *IEEE Trans. on Electron Dev.*, vol. 46, pp. 2026-2034, Oct. 1999.

[28] A. Rohatgi and S. Narasimha, "Design, facbrication, and analysis of greater than 18% efficient multicrystalline silicon solar cells," *Solar Energy Mat. and Solar Cells*, vol. 48, pp. 187-197.

[29] S. Narasimha, *Understanding and application of screen-printed metallization, aluminum back surface fields, and dielectric surface passivation for high-efficiency silicon solar cells*, Ph.D. Thesis, Georgia Institute of Technology, 1999.

[30] A. G. Aberle, "Surface passivation of crystalline silicon solar cells: a review," *Progress in Photovoltaics*, vol. 8, pp. 473-487, 2000.

[31] M. Stocks, A. Blakers, and A. Cuevas, "Multicrystalline silicon solar cells with low rear surface recombination," in *26th IEEE PVSC*, 1997, pp. 67-70.

[32] H. Morita, A. Sato, H. Washida, T. Kato, and A. Onoe, "Efficiency improvement of solar cell utilizing plasma-deposited silicon nitride," *Japanese J. Appl. Phys.*, vol. 21, supplement 21-2, pp. 47-51, 1982.

[33] D. J. Fitzgerald and A. S. Grove, "Surface recombination in semiconductors," *Surface Science*, vol. 9, pp. 347-369, 1968.

[34] R. B. M. Girisch, R. P. Mertens, and R. F. de Keersmaecker, "Determination of Si-SiO_2 interface recombination parameters using a gate-controlled point-junction diode under illumination," *IEEE Trans. Electron Dev.*, vol. 35, pp. 203-221, Feb. 1988.

[35] S. M. Sze, *Physics of Semiconductor Devices*, New York: John Wiley and Sons, 1981.

[36] A. S. Grove and D. J. Fitzgerald, "Surface effects on p-n junctions: characteristics of surface space-charge regions under non-equilibrium conditions," *Solid-State Electronics*, vol. 9, pp. 783-806, 1966.

[37] B. Kuhlmann, *Charakterisierung und mehrdimensionale Simulation von MIS-Inversionsschichtsolarzellen ("Characterization and multi-dimensional simulation of MIS inversion-layer solar cells")*, Ph.D. thesis (in German), University of Hannover, Germany, 1998. Trans. by J. Moschner.

[38] J. Jeong, M. D. Rosenblum, J. P. Kalejs, and A. Rohatgi, "Hydrogenation of defects in edge-defined film-fed grown aluminum-enhanced plasma-enhanced chemical vapor deposited silicon nitride multicrystalline silicon," *J. Appl. Phys.*, vol. 87, pp. 7551-7557, 2000.

[39] H. E. Elgamel, A. Rohatgi, Z. Chen, C. Vinckier, J. Nijs, and R. Mertens, "Optimal surface and bulk passivation of high efficiency multicrystalline silicon solar cells," in *Proc. 24th IEEE PVSC*, 1994, pp. 1323-1326.

[40] R. Ludemann, "Hydrogen passivation of multicrystalline silicon solar cells," *Materials Science & Engineering B*, vol. 58, pp. 86-90, 1999.

[41] J. I. Pankove and N. M. Johnson, *Hydrogen in Semiconductors.* New York: Academic, 1991.

[42] D. L. Meier, J. Hwang, and R. B. Campbell, "The effect of doping density and injection level on minority-carrier lifetime as applied to bifacial dendritic web silicon solar cells," *IEEE Trans. on Electron Dev.*, vol. 35, pp. 70-79, Jan. 1988.

[43] F. Duerinckx, *et al.*, "Increase in efficiency and material yield by use of PECVD silicon nitride in a simple screen printing process on Solarex material," in *Proc. 26th IEEE PVSC*, 1997, p. 259.

[44] P. Sana, A. Rohatgi, J. P. Kalejs, and R. Bell, "Gettering and hydrogenation of edge-defined film-fed grown multicrystalline silicon solar cells by Al diffusion and forming gas anneal," *Appl. Phys. Lett.*, vol. 64, p. 97, 1994.

[45] A. Rohatgi, *et al.*, "Gettering and passivation for high efficiency multicrystalline silicon solar cells," *Optoelectron., Devices Technol.*, vol. 9, p. 523-36, Dec. 1994.

[46] M. Spiegel, *et al.*, in *Proc. 2nd World Conf. on PV Solar Energy Conversion*, Vienna, 1998, p. 1685.

[47] R. Ludemann, A. Hauser, and R. Schindler, in *Proc. 2nd World Conf. on PV Solar Energy Conversion*, Vienna, 1998, p. 1638.

[48] H. Nagel, J. Schmidt, A. G. Aberle, and R. Hezel, in *Proc. 14th European Photovoltaics Solar Energy Conference*, Barcelona, 1997, p. 762.

[49] L. Cai and A. Rohatgi, "Effect of post-PECVD photo-assisted anneal on multicrystalline silicon solar cells," *IEEE Trans. Electron Dev.*, vol. 44, pp. 97-103, Jan. 1997.

[50] V. Yelundur *et al.*, "Al-enhanced SiN_x induced hydrogen passivation of string ribbon silicon," *J. Electronic Mat.*, vol. 30, pp. 526-531, May 2001.

[51] D. Kendall, Conference of Physics and Application of Lithium Diffused Silicon, NASA, Goddard Space Flight Center, Dec. 1969.

[52] K. Brennan, *The Physics of Semiconductors*, New York: Cambridge University Press, 1999.

[53] A. Ebong, M. Hilali, A. Rohatgi, D. Meier, and D. S. Ruby, "Belt furnace gettering and passivation of n-web silicon for high efficiency screen-printed front surface field solar cells," in *Proc. 10th Workshop on Crystalline Silicon Solar Cell Materials and Processes*, Colorado, August 2000, pp. 234-235.

[54] B. R. Bathey, *et al.*, "R&D toward a 15+% efficiency solar cell manufacturing line for EFG silicon wafers," in *Proc. 28th IEEE PVSC*, Anchorage, 2000, pp. 194-197.

[55] W. A. Smith and A. Rohatgi, "Modeling the effect of trap levels on the optimum resistivity of silicon solar cells," in *Proc. 20th IEEE PVSC*, Las Vegas, 1988, pp. 729-734.

[56] G. Augustine, A. Rohatgi, and N. M. Jokerst, "Base doping optimization for radiation-hard Si, GaAs, and InP solar cells," *IEEE Trans. Electron Dev.*, vol. 39, pp. 2395-2400, Oct. 1992.

[57] S. K. Pang, A. W. Smith, and A. Rohatgi, "Effect of trap location and trap-assisted Auger recombination on silicon solar cell performance," *IEEE Tran. Electron Dev.*, vol. 42, pp. 662-668, April 1995.

[58] S. Rein, W. Warta, and S. G. Glunz, "Investigation of carier lifetime in p-type CZ-silicon: specific limitations and realistic prediction of cell performance," in *Proc. 28th IEEE PVSC*, Anchorage, 2001, pp. 57-60.

[59] W. Shockley and W. T. Read, Jr., "Statistics of the Recombinations of Holes and Electrons," *Phys. Rev.*, vol. 87, pp. 835-842, Sept. 1, 1952.

[60] A. Aberle, W. Warta, J. Knobloch, and B. Voss, "Surface passivation of high efficiency silicon solar cells," in *21st IEEE PVSC*, Kissimmee, FL, 1990, pp. 233-238.

[61] F. M. Schuurmans, A. Schonecker, J. A. Eikelboom, W. C. Sinke, "Crystal-orientation dependence of surface recombination velocity for silicon nitride passivated silicon wafers," in *Proc. 25th IEEE PVSC*, 1996.

[62] S. K. Datta, K. Mukhopadhay, P. K. Pal, and H. Saha, "Analysis of thin silicon solar cells for high efficiency," *Sol. En. Mat. and Solar Cells*, vol. 33, pp. 483-497, Aug. 1994.

[63] S. Karazhanov, "Temperature and doping level dependence of solar cell performance including excitons," *Sol. En. Mat. and Solar Cells*, vol. 63, pp. 149-163, July 1, 2000.

[64] A. Goetzberger , J. Knobloch, and B. Voss, *Crystalline Silicon Solar Cells*. John Wilyey & Sons: New York, 1998.

[65] J. D. Moschner *et al.*, "Comparison of front and back surface passivation schemes for silicon solar cells," in *Proc. 2nd World Conference on Photovoltaic Solar Energy Conversion*, 1998, pp. 1894-1897.

[66] S. Narasimha and A. Rohatgi, "Effective passivation of the low resistivity silicon surface by a rapid thermal oxide/plasma silicon nitride stack," *Appl. Phys. Lett.*, vol. 72, pp. 1872-1874, 1998.

[67] A. Rohatgi, S. Narasimha, D. S. Ruby, "Effective passivation of the low resistivity silicon surface by a rapid thermal oxide/PECVD silicon nitride stack and its application to passivated rear and bifacial Si solar cells," in *Proc. 2nd World Conference on Photovoltaic Energy Conversion*, 1998, pp. 1566-1569.

[68] J. R. Davis and A. Rohatgi, "Theoretical considerations for back surface field solar cells," in *Proc. IEEE PVSC*, 1980, pp. 569-573.

[69] M.P. Godlewski, C.R. Baraona, and H.W. Brandhorst, "Low-High Junction Theory Applied to Solar Cells," in *Proc. 10th IEEE Photovoltaic Specialists Conf.,* IEEE, New York, 1973, pp. 40-49.

[70] O. Palias, J. Gervais, L. Clerc, S. Martinuzzi, "High resolution lifetime scan maps of silicon wafers," *Materials Science and Engineering B*, vol. 71, pp. 47-50, 2000.

[71] S. Martinuzzi and M. Stemmer, "Mapping of defects and their recombination strength by a light-beam-induced current in silicon wafers," *Materials Science and Engineering B*, vol. 24, pp. 152-158, 1994.

[72] A. V. Luikov, *Analytical Heat Diffusion Theory*. New York: Academic Press, 1968.

[73] G. Hahn and W. Meeker, *Statistical Intervals: A Guide for Practitioners*, New York: John Wiley & Sones, Inc., 1991.

[74] J. Walsh, "Distribution-free tolerance intervals for continuous symmetrical populations," *Ann. Math. Statist.*, vol. 33, pp. 1167-1174, 1962.

[75] K. Leo, R. Schindler, J. Knobloch, and B. Voss, "Titanium gettering in silicon: Investigation by deep level transient spectroscopy and secondary ion mass spectroscopy," *J. Appl. Phys.*, vol. 62, pp. 3472-3474, Oct. 15, 1987.

[76] W. Jung, A. Misiuk, J. Bak-Misiuk, and M. Rozental, "Effect of stress exerted by Si_3N_4 and SiO_2 insulation layers on donor generation in surface layer of Czochralski-grown silicon," in *Proc. of the Internation Society for Optical Engineering*, 1999, pp. 218-221.

[77] N. H. Nickel, W. B. Jackson, I. W. Wu, C. C. Tsai, and A. Chiang, "Hydrogen permeation through thin silicon oxide films," *Phys. Rev. B*, vol. 52, pp. 7791-7794, Sept. 15, 1995.

[78] V. Yelundur, A. Rohatgi, J.-W. Jeong, and J. I. Hanoka, "Improved string ribbon silicon solar cell performance by rapid thermal firing of screen printed contacts," *IEEE Trans. on Electron Dev.*, vol. 49, pp. 1405-1410, 2002.

[79] J. Schmidt, T. Lauinger, A. Aberle, and R. Hezel, "Record low surface recombination velocities on low-resistivity silicon solar cell substrates," in *Proc. 25th IEEE PVSC*, 1996, pp. 413-416.

[80] S. Dauwe, L. Mittelstadt, A. Metz, and R. Hezel, "Experimental evidence of parasitic shunting in silicon nitride rear surface passivated solar cells," *Prog. Photovolt. Res. Appl.*, vol. 10, pp. 279-291, 2002.

[81] L. Mittelstadt, A. Metz, and R. Hezel, "Thin multicrystalline silicon solar cells with silicon nitride front and rear surface passivation," in *Proc. 29th IEEE PVSC*, 2002.

[82] S. Kakac and Y. Yener, *Heat Conduction*, Washington, DC: Taylor and Francis, 1993.

[83] E. L. Heasel, "Recombination beneath ohmic contacts and adjacent oxide covered regions," *Solid-State Electronics*, vol. 22, pp. 89-93, 1979.

[84] J. R. Hook and H. E. Hall, *Solid-State Physics*, New York: John Wiley & Sons, 1994.

PUBLICATIONS FROM THIS WORK

JOURNAL PAPERS

1. **J. Brody**, A. Rohatgi, and A. Ristow, "Review and comparison of equations relating bulk lifetime and surface recombination velocity to effective lifetime measured under flash lamp illumination," *Solar Energy Materials and Solar Cells*, vol. 77, pp. 293-301, May 2003.

2. **J. Brody** and A. Rohatgi, "Sensitivity analysis of two-spectrum separation of surface and bulk components of minority carrier lifetimes," *Solid-State Electronics*, vol. 46, pp. 859-866, April 2002.

3. **J. Brody** and A. Rohatgi, "Analytical approximation of effective surface recombination velocity of dielectric-passivated p-type silicon," *Solid-State Electronics*, vol. 45, pp.1549-1557, Sept. 2001.

4. **J. Brody**, A. Rohatgi, and V. Yelundur, "Bulk resistivity optimization for low-bulk-lifetime silicon solar cells," *Progress in Photovoltaics*, vol. 9, pp. 273-285, July-Aug. 2001.

5. A. Ebong, **J. Brody**, A. Rohatgi, and T. Williams, "Optimization of front metal contact firing scheme to achieve high fill factors on screen printed silicon solar cells," *Solar Energy Materials and Solar Cells*, vol. 65, pp. 613-619, Jan. 2001.

REFEREED CONFERENCE PAPERS

1. **J. Brody**, P. Geiger, G. Hahn, and A. Rohatgi, "Comparison of dielectrics and iodine solution for monocrystalline and multicrystalline surface passivation," in *3rd World Conf. on PV Energy Conversion*, 2003.

2. **J. Brody** and A. Rohatgi, "Comparison of Dielectric Surface Passivation of Monocrystalline and Multicrystalline Silicon," in *Proc. 29th IEEE PVSC*, 2002.

3. A. Ebong, **J. Brody**, A. Ristow, A. Rohatgi, and D. Meier, "Optimization of front metal contact firing scheme to achieve high fill factors on screen printed silicon solar cells," in *Technical Digest, 9th International Photovoltaic Science and Engineering Conference*, 1999, pp. 765-766.

WORKSHOP PAPERS

1. **J. Brody**, A. Rohatgi, and A. Ristow, "Guidelines for more accurate determination and interpretation of effective lifetime from measured quasi-steady-state photoconductance," in *11th Workshop on Crystalline Silicon Solar Cell Materials and Processes*, Estes Park, Colorado, 2001, pp. 163-167.

2. A. Ebong, **J. Brody**, A. Ristow, A. Rohatgi, and D. Meier, "Gettering, hydrogenation and resistivity dependence of minority carrier lifetime in dendritic web ribbon silicon," in *9th Workshop on Crystalline Silicon Solar Cell Materials and Processes*, Beaver Run, Colorado, 1999, pp. 189-192.

VITA

Jed Brody was born and raised near Philadelphia and spent much of his youth reading science fiction, playing the flute, juggling, and climbing trees. He earned his B.S. in Physics at Haverford College. He spent the next two years as a Peace Corps volunteer in Benin, West Africa, teaching high school physics and chemistry in French. His graduate research was done in the University Center of Excellence for Photovoltaics Research and Education at the Georgia Institute of Technology. *Creative Loafing* published his story "The Kid Who Ate Paste" as the second-place winner of a fiction contest. He has joined the physics faculty at Emory University as a Lecturer and Director of Advanced (instructional) Laboratories.